



2021

INTERACTIONS OF LIGNIN DIMERS WITH ENGINEERED SURFACES AND MODEL CELL MEMBRANES FOR DESIGN OF LIGNIN-BASED MATERIALS

Mahsa Moradipour

University of Kentucky, massie.moradipour@gmail.com

Author ORCID Identifier:

<https://orcid.org/0000-0003-4853-0599>

Digital Object Identifier: <https://doi.org/10.13023/etd.2021.394>

[Right click to open a feedback form in a new tab to let us know how this document benefits you.](#)

Recommended Citation

Moradipour, Mahsa, "INTERACTIONS OF LIGNIN DIMERS WITH ENGINEERED SURFACES AND MODEL CELL MEMBRANES FOR DESIGN OF LIGNIN-BASED MATERIALS" (2021). *Theses and Dissertations--Chemical and Materials Engineering*. 135.
https://uknowledge.uky.edu/cme_etds/135

This Doctoral Dissertation is brought to you for free and open access by the Chemical and Materials Engineering at UKnowledge. It has been accepted for inclusion in Theses and Dissertations--Chemical and Materials Engineering by an authorized administrator of UKnowledge. For more information, please contact UKnowledge@lsv.uky.edu.

STUDENT AGREEMENT:

I represent that my thesis or dissertation and abstract are my original work. Proper attribution has been given to all outside sources. I understand that I am solely responsible for obtaining any needed copyright permissions. I have obtained needed written permission statement(s) from the owner(s) of each third-party copyrighted matter to be included in my work, allowing electronic distribution (if such use is not permitted by the fair use doctrine) which will be submitted to UKnowledge as Additional File.

I hereby grant to The University of Kentucky and its agents the irrevocable, non-exclusive, and royalty-free license to archive and make accessible my work in whole or in part in all forms of media, now or hereafter known. I agree that the document mentioned above may be made available immediately for worldwide access unless an embargo applies.

I retain all other ownership rights to the copyright of my work. I also retain the right to use in future works (such as articles or books) all or part of my work. I understand that I am free to register the copyright to my work.

REVIEW, APPROVAL AND ACCEPTANCE

The document mentioned above has been reviewed and accepted by the student's advisor, on behalf of the advisory committee, and by the Director of Graduate Studies (DGS), on behalf of the program; we verify that this is the final, approved version of the student's thesis including all changes required by the advisory committee. The undersigned agree to abide by the statements above.

Mahsa Moradipour, Student

Dr. Barbara L. Knutson, Major Professor

Dr. Stephen E. Rankin, Director of Graduate Studies

INTERACTIONS OF LIGNIN DIMERS WITH ENGINEERED SURFACES AND
MODEL CELL MEMBRANES FOR DESIGN OF LIGNIN-BASED MATERIALS

DISSERTATION

A dissertation submitted in partial fulfillment of the
requirements for the degree of Doctor of Philosophy in the
College of Engineering
at the University of Kentucky

By

Mahsa Moradipour

Lexington, Kentucky

Co- Directors: Dr. Barbara L. Knutson, Professor of Chemical Engineering
and Dr. Stephen E. Rankin, Professor of Chemical Engineering

Lexington, Kentucky

2021

ABSTRACT OF DISSERTATION

INTERACTIONS OF LIGNIN DIMERS WITH ENGINEERED SURFACES AND MODEL CELL MEMBRANES FOR DESIGN OF LIGNIN-BASED MATERIALS

Capitalizing on byproducts of industrial and agricultural economies is among the utmost goals of sustainability. Of particular interest for commercial upgrading is lignin, a phenolic biopolymer found in the cell walls of plants which is the second most abundant biopolymer on Earth after cellulose. Due to its heterogeneous structure, deconstructing lignin to selected small molecules for use as chemicals or advanced materials has been elusive. This work capitalizes on a “bottom up” approach to the synthesis of lignin oligomers of known bond chemistry to better understand their interfacial interactions.

The potential pharmacological mechanism of lignin deconstruction components and their toxicological effect on biological systems is currently relatively unexplored. Herein, the interaction of three lignin-derived small molecules (lignin dimers with varying chemical functionality) with lipid bilayers (model cell membranes) was investigated via quartz crystal microbalance with dissipation monitoring (QCM-D) studies of binding and differential scanning calorimetry (DSC) measurements of the change in lipid bilayer phase behavior as a function of dimer concentration. Our results demonstrate that minor differences in structure of lignin molecules have a significant impact on their ability to penetrate into model cell membranes.

To show that the lignin oligomers under investigation have the potential to impart surfaces with lignin-like properties (e.g. pharmacological and toxicological properties), a hydrophobic lignin dimer which was previously shown to interact strongly with model cell membrane was chemically modified to covalently attach to mesoporous silica nanoparticles (MSNPs). The ability of lignin dimer-functionalized particles to interact with and disrupt lipid bilayers was compared to MSNPs functionalized with eugenol, a natural aromatic pharmaceutical found in cloves. While eugenol-grafted particles showed evidence of weak interactions with the bilayer, dimer-grafted particles with the same concentration caused considerable lipid mass loss associated with disruption of up to ~93% of the membrane, suggesting higher biocidal activity.

The structure of lignin suggests that it is not only a potential therapeutic and pharmacological substance, but also a promising source of aromatic chemicals. Developing methods to selectively separate and purify lignin oligomers from the complex lignin depolymerization mixture remains an ongoing challenge. Binding of β -cyclodextrin (CD) (a truncated cone-shaped molecule with a hydrophilic exterior and a hydrophobic cavity) to three lignin dimers with different chemical structures was studied using Isothermal

Titration Calorimetry (ITC). The thermodynamic parameters (K , ΔH , ΔS , and ΔG) of formation of dimer: β -CD complexes were measured and compared. The results demonstrated that differences in the thermodynamics of CD-lignin interactions can be used to develop selective separation strategies for lignin-derived small molecules. For example, binding with β -CD of a dimer containing a bb bond is entropically driven (due to hydrophobic effects) while favorable enthalpy of interactions drives binding of a dimer with a different bond (bO4). A surface modification technique was also proposed to attach β -CD directly to mesoporous silica nanoparticles, with a goal of using the silica particles for selective capture of lignin-derived small molecules.

In sum, this work established structure–function relationships for well-defined lignin derivatives at biologically relevant surfaces. A strategy to create lignin-conjugated silica surfaces was developed and it was shown that bio-inspired materials comprising lignin small molecules have the potential to serve as a platform for novel antimicrobial coatings and therapeutic carriers. Moreover, the potential of β -cyclodextrin to selectively separate lignin oligomers from lignin deconstruction mixture was studied, and a strategy to create immobilized cyclodextrin-functionalized surfaces was proposed.

KEYWORDS: Lignin Dimers, Model Cell Membranes, Functionalized Silica Nanoparticle, Quartz Crystal Microbalance, Isothermal Titration Calorimetry, β -cyclodextrin

Mahsa Moradipour

09/13/2021

INTERACTIONS OF LIGNIN DIMERS WITH ENGINEERED SURFACES AND
MODEL CELL MEMBRANES FOR DESIGN OF LIGNIN-BASED MATERIALS

By
Mahsa Moradipour

Barbara L. Knutson, Ph.D.

Co-Director of Dissertation

Stephen E. Rankin, Ph.D.

Co-Director of Dissertation

Stephen E. Rankin, Ph.D.

Director of Graduate Studies

September 13, 2021

Date

DEDICATION

To my mom, Maryam Rajabi and my dad, Alireza Moradipour, without whose never-failing support and encouragement, I would not have made it this far.

ACKNOWLEDGMENTS

I am forever grateful to my advisors, Prof. Barbara Knutson and Prof. Stephen Rankin for their endless support, patience, motivation, and guidance during my graduate studies. I sincerely thank them for providing me with an opportunity to join their group and for their immense guidance, encouragement, and constructive criticism which helped me grow as a research scientist and expand my scientific vision towards much wider perspectives.

I would also like to extend my sincere gratitude to my other doctoral committee members, Prof. Bert Lynn and Prof. Thomas Dziubla, not only for their insightful advice and encouragement during my proposal defense and annual committee meetings, but also for their challenging questions which incited me to broaden my perspective on my research. I also thank Prof. Jian Shi for being my external examiner for this dissertation and providing valuable feedback.

I would like to express my appreciation to our collaborators at the University of Kentucky (UK) and Louisiana State University (LSU), whose contribution was invaluable for the completion of this work. Prof. Bert Lynn's lab at the Chemistry Department at UK has collaborated in the synthesis of lignin dimers and I appreciate the efforts of Poorya Kamali and Dr. Shardrack Asare in synthesizing lignin oligomers. Thanks should also go to Kimmy Dean from Dr. Lynn's lab for contributing in the work of measuring the thermodynamics of the interactions of lignin dimers with cyclodextrins. I also wish to thank Prof. Dorel Moldovan and his team including Dr. Xinjie Tong and Dr. Brian Novak at LSU for performing the molecular dynamic simulation studies for our collaborative projects and for their enthusiasm and efforts toward completion of our joint projects.

I gratefully acknowledge the assistance of Dr. Dali Qian and Dr. Nicholas Briot of Electron Microscopy Center for their help in performing XPS characterization as well as TEM and SEM imaging. Many thanks should also go to Stephen Johnson from TA Instruments for hours of help and assistance with troubleshooting ITC. I also appreciate the guidance received from Brian Wajdyk at the Center for Nanoscale Science and Engineering (CeNSE) for the studies performed using QCM-D.

I cannot thank my fellow labmates enough for their joyful presence, the stimulating discussions, and for all the fun we have had in all these years. Particularly helpful to me during my Ph.D. was Dr. Arif Khan whose work was heavily engaged with that of mine. Additionally, Dr. Yuxin He, Andrew Drake, Sayma Afrin, Rebecca Pike, Aniruddha Shirodkar, Joshua Garay, and Ramy Ghanim each played an undeniable role in making my Ph.D. an unforgettable experience. I would also like to recognize the assistance that I received from Dr. Shanshan Zhou, Dr. Kwabena Darkwah, Dr. Syed Islam, and Dr. Suraj Nagpure during the initiation of my graduate research.

The completion of my dissertation would not have been possible without the hard work put up by the undergraduate students trained on different projects under my mentorship. Efforts put by Rachel Monroe, Meghan Mace, and Delaney Weber were critical for the projects to progress and succeed. I also had the great pleasure of mentoring the NSF REU undergraduate students Audrey Fetsko of University of Notre Dame and Emily Chase of The University of Tennessee at Chattanooga in the summer of 2017 and 2018, respectively.

I would like to acknowledge and appreciate the funding and financial supports received from the National Science Foundation (NSF) EPSCoR Track-2 RII, award NO.

OIA1632854 and partially from National Science Foundation REU Program at University of Kentucky, grant NO. 1460486.

Last but not least, I would like to thank my family: my parents and my brother, for their profound belief in me and my work, and for their unwavering support throughout my graduate studies. Neither of my accomplishments in life would have been possible without their unfailing support and continuous encouragement. Also, the support and endorsement that I received from my friends, especially the Johnsons has been nothing short of amazing.

TABLE OF CONTENTS

ACKNOWLEDGMENTS	iii
LIST OF TABLES	x
LIST OF FIGURES	xi
CHAPTER 1. INTRODUCTION.....	1
CHAPTER 2. BACKGROUNDS.....	7
2.1 Lignin.....	7
2.1.1 Lignin and its small molecule derivatives	7
2.1.2 Lignin depolymerization.....	12
2.1.3 Lignin-based nano-structured materials.....	14
2.2 Liposomes and supported lipid bilayers	16
2.2.1 Differential Scanning calorimetry (DSC) for studying the thermal behavior of lipid bilayers	21
2.2.2 Quartz Crystal Microbalance with Dissipation (QCM-D) for studying supported lipid bilayers.....	24
2.2.3 Interaction of lipid bilayers with small molecules.....	30
2.2.4 Interactions of lipid bilayers with silica nanoparticles	34
2.3 Cyclodextrins	35
2.3.1 Interactions of cyclodextrins with small molecules and formation of “host- guest” complexes	37
2.3.2 Isothermal Titration Calorimetry (ITC)	42
2.3.3 Cyclodextrin-based surfaces and materials.....	48
CHAPTER 3. THE EFFECTS OF LIGNIN DIMERS ON THE GEL-TO-FLUID PHASE TRANSITION IN DPPC BILAYERS	52
3.1 Summary	52
3.2 Introduction.....	53
3.3 Materials and Methods.....	57
3.3.1 Chemicals and Reagents	57
3.3.2 G- β O4'-G and <i>benz</i> G- β O4'-G Lignin Dimers Synthesis	57

3.3.3	Differential Scanning Calorimetry.....	58
3.3.4	Partition Coefficient from DSC	59
3.4	Results and Discussion	59
3.4.1	DSC Measurements of Transition Temperature	59
3.5	Conclusion	65
CHAPTER 4. INTERACTION OF LIGNIN DIMERS WITH MODEL CELL MEMBRANES: A QCM-D STUDY.....		67
4.1	Summary	67
4.2	Introduction.....	67
4.3	Materials and Methods.....	72
4.3.1	Chemicals and Reagents	72
4.3.2	Quartz Crystal Microbalance with Dissipation (QCM-D).....	73
4.4	Results and Discussion	75
4.5	Conclusion	85
CHAPTER 5. INTERACTION OF LIGNIN-DERIVED DIMER AND EUGENOL- FUNCTIONALIZED SILICA NANOPARTICLES WITH SUPPORTED LIPID BILAYERS.....		87
5.1	Summary	87
5.2	Introduction.....	88
5.3	Materials and Methods.....	92
5.3.1	Chemicals and Reagents	92
5.3.2	Synthesis of G-eug Dimers	93
5.3.3	Synthesis of Mesoporous Silica Nanoparticles (MSNPs).....	93
5.3.4	Thiol Functionalization of Bare MSNPs.....	94
5.3.5	Attachment of Eugenol or G-eug Dimer to SH-MSNPs.....	94
5.3.6	Characterization of MSNPs	95
5.3.7	Thiol Quantification of the SH-MSNPs.....	95
5.3.8	Verification of Eugenol or G-eug Dimer Surface Attachment	96
5.3.9	Quantification of the Attached Molecules by Thermogravimetric Analysis (TGA).....	97

5.3.10	Particle-Lipid Bilayer Interactions Measured by QCM-D.....	97
5.4	Results and Discussion	99
5.4.1	Characterization of Bare and Thiol-Functionalized MSNPs	99
5.4.2	Characterization of Eugenol-MSNPs and G-eug Dimer-MSNPs.....	102
5.4.3	Interaction of Particles and Lipid Bilayers	105
5.5	Conclusion	113
CHAPTER 6. THERMODYNAMIC INTERACTIONS OF LIGNIN DIMERS WITH β -CYCLODEXTRIN		115
6.1	Summary	115
6.2	Introduction.....	116
6.3	Materials and Methods.....	119
6.3.1	Chemicals and Reagents	119
6.3.2	G- β O4'-G Lignin Dimer Synthesis.....	119
6.3.3	Isothermal Titration Calorimetry (ITC)	120
6.3.4	ITC Data Analysis and Fitting of Binding Models.....	120
6.4	Results and Discussion	122
6.4.1	β -CD-Dimer Binding Thermodynamic Parameters	122
6.4.2	Effect of i-PrOH on the Binding Thermodynamic Parameter	132
6.5	Conclusion	134
CHAPTER 7. SYNTHESIS OF β -CYCLODEXTRIN-FUNCTIONALIZED MESOPOROUS SILICA NANOPARTICLES		135
7.1	Summary	135
7.2	Introduction.....	136
7.3	Materials and Methods.....	139
7.3.1	Chemicals and Reagents	139
7.3.2	Synthesis of Mesoporous Silica Nanoparticles (MSNPs).....	140
7.3.3	Amine Functionalization of Bare MSNPs	140
7.3.4	Attachment of β -cyclodextrin to MSNPAs.....	141
7.3.5	Nanoparticle Characterization	142
7.3.6	UV-vis and Solution Depletion Studies with Pinoresinol.....	143

7.3.7	Fluorescence and Solution Depletion Studies Using TNS	144
7.4	Results and Discussion	144
7.4.1	Characterization of The Particles.....	144
7.4.2	UV-vis and Solution Depletion Studies Using Pinoresinol	148
7.4.3	Fluorescence and Solution Depletion Studies Using TNS	151
7.5	Conclusion	155
CHAPTER 8. CONCLUSIONS AND FUTURE DIRECTIONS		157
APPENDICES		164
APPENDIX A. SUPPLEMENTARY MATERIALS FOR CHAPTER 4.....		164
APPENDIX B. SUPPLEMENTARY MATERIALS FOR CHAPTER 5		168
APPENDIX C. SUPPLEMENTARY MATERIALS FOR CHAPTER 6.....		171
APPENDIX D. SUPPLEMENTARY MATERIALS FOR CHAPTER 7.....		174
APPENDIX E. Alternative β -CD Functionalization Technique Based on Thiol-ene Click Chemistry		184
APPENDIX F. Functionalizing Silica Coated QCM Substrates with Thiol Functional Groups Through Hydroxylation of MPTMS		192
REFERENCES		206
VITA.....		226

LIST OF TABLES

Table 2.1 Experimental affinity constant (K) and thermodynamic parameters (ΔH , ΔS , and ΔG) of 1:1 inclusion complexation of small guest molecules with β -CD in aqueous solutions at T=298 K.....	41
Table 2.2 Details and observed results of conventional and non-conventional titration protocols used in ITC studies on β -cyclodextrin complexes described by Bertaut et al. [136]......	47
Table 3.1 DSC liquid crystalline to gel transition temperature in DPPC in the presence of lignin GG dimers.....	62
Table 3.2 Log(K) from DSC and MD.....	65
Table 3.3 DSC liquid crystalline to gel transition temperature in DPPC in the presence of lignin GG dimers.....	66
Table 4.1 Quantitative QCM-D results of the lignin GG dimers' interactions with the synthetic DPPC lipid bilayers with 1 hr of exposure at a concentration of 0.1 mg/mL of dimer solutions.....	84
Table 5.1 BET surface area, BJH average pore diameter and pore size distribution obtained from nitrogen adsorption, and zeta potential values measured in PBS at pH 7.4 for bare MSNPs, SH-MSNPs, eugenol-MSNPs, and G-eug dimer-MSNPs.....	101
Table 6.1 Thermodynamic parameters for β -CD interaction with lignin GG dimers as determined using a one-binding site model through ITC at T=298 K. (confidence level=95%).....	129
Table 7.1 BET surface area, BJH average pore diameter and pore size distribution obtained from nitrogen adsorption.....	146

LIST OF FIGURES

Figure 1.1 Plant structural material, adapted from Figueiredo et al. [1].....	1
Figure 2.1 Distribution of various bonding motifs in a softwood lignin structure. Reproduced from Ref. [17] (Zakzeski et al., Chemical reviews 110.6 (2010)), with permission from American Chemical Society, copyright 2010.....	8
Figure 2.2 Lignin's three monomers (monolignols) and their corresponding structures: H, G, and S.....	9
Figure 2.3 Exemplary lignin dimers : (I) guaiacyl-syringyl dimer of β -O-4, (II) guaiacyl-guaiacyl dimer of β - β (pinoresinol), (III) podophyllotoxin, (IV) β -5 phenylcoumaran dimer, (V) 4-O-5 (diaryl ether) linked guaiacyl-type thioacidolysis dimer, (VI) 5-5 (biaryl) linked guaiacyl-type thioacidolysis dimer.	11
Figure 2.4 Different components of a phospholipid molecule in a lipid bilayer sheet.	17
Figure 2.5 Different model cell membranes	19
Figure 2.6 Schematic illustration of the different states of the lipid bilayer during the phase transition: gel-crystalline state ($T < T_p$), rippled phase ($T_p \leq T < T_m$), and the liquid-crystalline state ($T \geq T_m$).....	20
Figure 2.7 Schematic of a Differential Scanning Calorimeter (DSC) adapted from Spink [90].....	22
Figure 2.8 DSC heating scan of phase transition of pure DPPC liposomes in PBS over the temperature range of 25-55 °C with scan rate of 1 °C/min.....	23
Figure 2.9 Schematic of a Quartz Crystal Microbalance with Dissipation (QCM-D) with a lipid bilayer as the adhered layer on a gold (Au) sensor.....	26
Figure 2.10 Chemical structures of 1) α -CD, b) β -CD, c) γ -CD [adapted from Wikipedia], and d) Schematic of the 3D structure of a β -CD molecule.	37
Figure 2.11 Schematic of the 1:1 and 1:2 complex formation of CDs with guest molecules	39
Figure 2.12 Schematic of an Isothermal titration calorimeter (ITC)	44
Figure 2.13 Typical ITC data obtained for the binding interaction of ibuprofen (0.5 mM) to β -CD (5 mM) in PBS at $T=298$ K, (a) exothermic heat releases upon injection of 3.7 μ L aliquots of β -CD into ibuprofen solution versus time, (b) heat of dilution of β -CD (5 mM) in PBS, (c) integrated heat profile after subtraction of dilution heat plotted against molar ratio of β -CD and ibuprofen.....	46
Figure 2.14 Schematic representations of different cyclodextrin-functionalized structures: (a) CD- coated substrates, (b) CD-coated porous particles, and (c) CD-based polymer matrices. Adapted from Bibby et al [152].	50
Figure 3.1 Chemical structures of the three β O4-linked lignin dimers and the lipid DPPC.	56
Figure 3.2 DSC heating scans for mixtures of DPPC with (a) G- β O4'-G, (b) G- β O4'- <i>trunc</i> G, (c) <i>benz</i> G- β O4'-G. The mole fraction of the dimers is indicated beside each scan.	61
Figure 3.3 Linear regression of changes in main phase transition temperature (ΔT_m) of the DPPC/dimer samples vs. dimer concentration, Cs. (a) G- β O4'-G (b) G- β O4'- <i>trunc</i> G (c) <i>benz</i> G- β O4'-G.....	63

Figure 4.1 Chemical structures of the three β O4-linked lignin dimers used in the experiments and simulation, and the lipids DPPC and DOPC.	71
Figure 4.2 Representative QCM-D results for solvent-assisted DPPC lipid bilayer formation on a gold sensor. (a) Frequency shifts divided by the overtone number($n=3$), and (b) dissipation shifts at the third overtone ($n=3$). The parts of the graphs separated by the vertical dashed lines denote the introduction of flowing PBS, isopropanol ('i-PrOH'), 0.5 mg/mL DPPC lipid in isopropanol ('DPPC'), and finally PBS. Insets show schematics of lipid deposition and bilayer formation during the process.	77
Figure 4.3 (a) Changes in frequency divided by the overtone ($n=3$), and (b) changes in dissipation with time as G- β O4'- <i>trunc</i> G dimer solutions of variable concentration (0.01, 0.02, and 0.1 mg/mL) flow over a DPPC lipid bilayer. The vertical dashed lines denote time frames over which solutions of lignin dimer with different concentrations was introduced, followed by PBS. Time of zero corresponds to the initial DPPC bilayer, the introduction of the 0.01 mg/mL dimer solution started at $t=12$ min, followed by the introduction of 0.02 mg/mL solution after 60 minutes and 0.1 mg/mL after 60 additional minutes. Flow at 0.1 mg/mL was continued for 176 minutes before rinsing with PBS for 115 min. Frequency data are presented for the third overtone ($n=3$).	79
Figure 4.4 Interactions of G- β O4'-G (red), G- β O4'- <i>trunc</i> G (black), <i>benz</i> G- β O4'-G (blue) dimers with supported DPPC lipid bilayers on gold-coated quartz crystal sensors obtained by QCM-D. (a) Changes in frequency divided by the overtone ($n=3$), (b) changes in dissipation. Time is measured starting from dimer injection onto an existing bilayer ('Lignin dimers'), followed by the PBS rinse ('PBS'). $\Delta f/3$ and ΔD are shifted to a value of 'zero' at time 'zero' corresponding to the initial DPPC bilayer. Data are presented for the third overtone ($n=3$).	82
Figure 5.1 Grafting of the silica nanoparticles with thiol, eugenol, and G-eug dimer.	92
Figure 5.2 Electron microscope images of synthesized MSNPs: (a) scanning electron (SEM) image and (b) transmission electron (TEM) image.	100
Figure 5.3 TGA of bare MSNPs, SH-MSNPs, eugenol-MSNPs, and G-eug dimer-MSNPs.	105
Figure 5.4 DPPC lipid bilayer formation on gold coated quartz crystal obtained by QCM-D in terms of frequency shifts at third overtone.	108
Figure 5.5 Change in frequency with the introduction of different concentrations of G-eug dimer-MSNPs on supported DPPC lipid bilayers on a gold QCM sensor. Time is measured from particle injection onto an existing bilayer ('Nanoparticles'), followed by the PBS buffer rinse ('PBS'). Δf is normalized to a value of 'zero' corresponding to the initial DPPC bilayer.	109
Figure 5.6 Change in (a) frequency and (b) dissipation with the introduction of SH-MSPNs, eugenol-MSNPs, G-eug dimer-MSNPs at 0.5 mg/mL on supported DPPC lipid bilayers on a gold QCM sensor. Time is measured from particle injection onto an existing bilayer ('Nanoparticles'), followed by the PBS buffer rinse ('PBS'). Δf and ΔD are normalized to a value of 'zero' corresponding to the initial DPPC bilayer.	111
Figure 6.1 Heat of dilution of β -CD (5 mM) into (a) ACN/water (10% v/v), and (b) i-PrOH/water (10% v/v) at $T=298$ K.	124

Figure 6.2 Raw heat rate with time for β -CD (5 mM) interaction with (a) G- $\beta\beta$ -G (0.5 mM), (b) G- β O4'- <i>trunc</i> G (0.7 mM), and (c) G- β O4'-G (0.5 mM) and integrated heat profiles after subtraction of dilution heat plotted against molar ratio of β -CD to the lignin dimers: (d) G- $\beta\beta$ -G, (e) G- β O4'- <i>trunc</i> G, and (f) G- β O4'-G in ACN/water mixture at T=298 K. First injection points were eliminated from thermodynamic analysis. Data points above integrated heat (μ J)= 0 (illustrated in pale gray) are automatically not included in the fitting model.....	126
Figure 6.3 Raw heat rate with time for β -CD (5 mM) interaction with lignin GG dimers for (a) G- $\beta\beta$ -G (0.5 mM), (b) G- β O4'- <i>trunc</i> G (0.7 mM), and (c) G- β O4'-G (0.5 mM) and integrated heat profiles after subtraction of dilution heat plotted against molar ratio of β -CD to the lignin dimers: (d) G- $\beta\beta$ -G, (e) G- β O4'- <i>trunc</i> G, and (f) G- β O4'-G in i-PrOH/water mixture at T=298 K. First injection points were eliminated from thermodynamic analysis. Data points above integrated heat (μ J)= 0 (illustrated in pale gray) are automatically not included in the fitting model.	127
Figure 7.1 Schematics of the synthesis of β -CD-functionalized silica nanoparticles (CD-MSNPs).....	139
Figure 7.2 Expanded FTIR spectra of MSNPAs, CD-MSNPs, and β -CD in the range of 500-2500 cm^{-1}	147
Figure 7.3 TGA of bare MSNPs, MSNPAs, and CD-MSNPs.....	148
Figure 7.4 Comparison between MSNPAs and CD-MSNPs in terms of pinoresinol adsorption in two different media, ACN/water (pH=5.8) and ACN/acetate buffer (pH=3.7). Data points and lines represent experimental values and corresponding Langmuir linear fit, respectively.	151
Figure 7.5 The emission fluorescence spectra of MSNPA and CD-MSNPs in acetate buffer (1 mg/mL, pH=3.7) before and after adding TNS (10^{-5} M) to the suspensions. $\lambda_{\text{excitation}}=366$ nm. For “MSNPA with TNS” in the ~421-456 nm range, the fluorescence intensity readings were outside of the dynamic range (overflow), hence the datapoints in that range are shown as a flat horizontal line.....	153

CHAPTER 1. INTRODUCTION

The fundamental concept of sustainability includes the need to provide the food, energy, and water needed to supply the world population while preserving the resources for future generations. In that event, capitalizing on materials considered byproducts of industrial and agricultural economies is amongst the utmost goals of sustainable practices. Sustainable and biodegradable polymers are promising candidates for energy sources and materials synthesis due to their abundance, biocompatibility, biodegradability, renewability, and low production expenses [1, 2]. A distinct type of sustainable biopolymer is lignocellulosic biomass which consists of three major parts: cellulose, hemicellulose, and lignin (**Figure 1.1**). After cellulose, lignin is the second most abundant biopolymer on Earth which comprises 15–30% of biomass [3]. Lignin, which is found in structure of vascular plants and some algae, accounts for antimicrobial properties and structural rigidity of the plants, as well as the water passage within their cell walls [1, 4, 5].

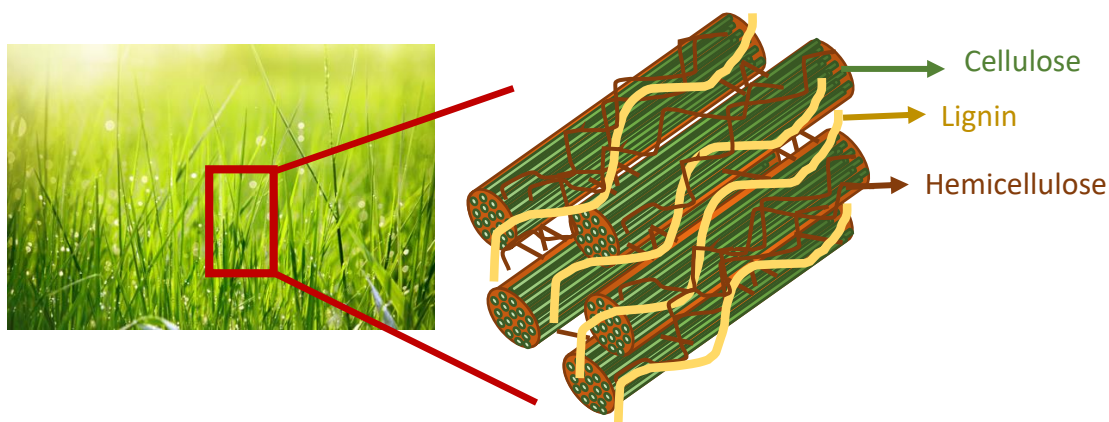


Figure 1.1 Plant structural material, adapted from Figueiredo et al. [1].

Every year nearly 50 million tons of lignin is produced as a byproduct in paper and pulping processes in form of kraft lignin and liginosulfonate [2, 5]. Around 98% of the lignin produced in the paper and pulping industry is burned as fuel for energy compensation in the paper mills, whereas only ~2% of it is utilized for making value-added products (e.g. chemicals, adhesives, dispersants, and surfactants) [6, 7]. For instance, only 1-2% of the lignin produced from the sulfite pulp industry is exploited in producing liginosulfonates [7]. However, the aromatic structure of lignin makes it a potential renewable feedstock for aromatic molecules traditionally manufactured by the petroleum industry [5, 8]. Aromatic compounds which are commonly used in the preparation of drugs, food, fragrance and essential oils are of great commercial interest [9, 10]. Fully harnessing lignin and attempting to break it down for use in applications such as energy storage, commodity chemical feedstocks, aromatics, surfactants, polymer composites, UV stabilizers, coatings, and biomedical products is advantageous and profitable. However, the goal of breaking lignin down and using it for these applications is challenging due to lignin's heterogeneous macromolecular structure, complicated distribution of inter-unit bonds, and insolubility in water and most solvents.

Lignin is made up of three monomers which can bind together in various ways to make lignin-derived small molecules known as lignin oligomers. These oligomers can be obtained from “breaking down” lignin or synthesized through “building up” chemistry. Currently, lignin deconstruction into smaller units is being practiced as an approach to design advanced functional materials, materials interfaces for separations and catalysis, and chemical feedstocks. However, due to its extremely stable and complex polyphenolic structure, lignin is very difficult to break down. In spite of many proposed lignin

depolymerization methods, deconstruction of the polymeric lignin usually lacks specific “target” chemicals because of the difficulty in identifying the critical series of monolignols and bonding motifs to achieve a desired property for a functional material interface or as a chemical precursor. Thus, this dissertation will be centered on utilizing “built-up” lignin oligomers for modifying interfacial surface chemistry, one route to creating advanced lignin-based materials.

The dissertation is divided into eight chapters starting with this **Chapter 1**, where a concise introduction of this research is explained together with describing the scope of the study and the outline of the dissertation.

In **Chapter 2**, a comprehensive background and literature review for the dissertation subjects is provided, including challenges associated with lignin depolymerization, production and applications of lignin-derived small molecules and nanostructured materials, liposomes and supported lipid bilayers as model cell membranes, and cyclodextrins as host molecules to separate and protect lignin small molecules. Descriptions for techniques such as Differential Scanning calorimetry (DSC), Quartz Crystal Microbalance with Dissipation (QCM-D), and Isothermal Titration Calorimetry (ITC) have also been provided in **Chapter 2**.

Chapters 3 and 4 of this dissertation are focused on characterizing the interactions of lignin-derived small molecules, more specifically, dimers of coniferyl alcohol (GG lignin dimers) with lipid bilayers as simplified model systems for the basic functions of biological membranes. Limited information is available about how variations in structure of lignin oligomers alter the way they interact with cell membranes. Knowledge about the interaction of lignin oligomers with cell membranes is crucial for recognizing their

toxicological impacts on biological systems and for designing lignin-based materials with potential pharmacological and therapeutic properties such as coated surfaces and functionalized nanoparticles. In **Chapter 3**, the effect of the incorporation of three dimers of coniferyl alcohol (GG lignin dimers) on the structure of a dipalmitoyl phosphatidyl choline (DPPC) lipid bilayer was interpreted from changes in the gel-to-fluid phase transition at a limit of infinite dilution using differential scanning calorimetry (DSC). This work is published in *The Journal of Physical Chemistry B* (Tong et al., J. Phys. Chem. B 129, 8247-8260 (2019) [11]) and reproduced here with permission from the American Chemical Society. In **Chapter 4**, the concentration dependence of the uptake of the same three dimers in DPPC and (1,2-dioleoyl-sn-glycero-3-phosphocholine) DOPC bilayers and their corresponding effect on lipid bilayer disorder were studied using a quartz crystal microbalance with dissipation (QCM-D). A manuscript on this chapter has been published in *Biointerphases* and is reproduced from Moradipour et al., *Biointerphases* 16, (2021) [12], with the permission of AIP Publishing.

As a result of the lack of well-defined lignin small molecules and corresponding surface functionalization approaches, the potential to impart surfaces with particular lignin-like pharmacological and toxicologic features remains mostly uninvestigated. In **Chapter 5**, a hydrophobic lignin dimer which in **Chapters 3 and 4** was shown to interact with model cell membranes was chemically modified to covalently attach to mesoporous silica nanoparticles (MSNPs). In **Chapter 5**, allyl-modified guaiacyl β O4 lignin dimer and eugenol, a known natural antimicrobial, were separately attached to MSNPs (~150 nm diameter with 4.5 nm pores) via click chemistry. The interaction of the functionalized MSNPs with phospholipid bilayers of DPPC (representing model cell membranes) was

measured using QCM-D. The ability of the dimer-functionalized particles to interact with and perturb DPPC bilayers is compared to that of eugenol-functionalized particles. A manuscript based on this chapter was published in *Colloids and Surfaces B: Biointerfaces* (Moradipour et al., Colloids Surf. B, 191, (2020) [13]), and is reproduced with permission from Elsevier.

The structure of lignin suggests that it is a promising source of aromatic chemicals. Potential approaches to selectively separate and purify lignin oligomers from the multi-component lignin deconstruction mixture is still ongoing. We hypothesized that cyclodextrin (CD)-lignin interactions can be used to establish selective separation and protection strategies for lignin-derived small molecules. Exploring the interaction of lignin oligomers with CDs in solution provides necessary groundwork for generating selective immobilized CD-silica surfaces. In **Chapter 6**, thermodynamics of β -cyclodextrin (β -CD) binding with three dimers including two derivatives of β O4 dimers of coniferyl alcohol (GG lignin dimer) as well as pinoresinol (G- $\beta\beta$ -G) are measured by Isothermal Titration Calorimetry (ITC). The thermodynamic parameters (enthalpy, entropy, stoichiometry and free energy of binding) are evaluated by fitting single distinct binding site model to the isotherms derived from raw heat curves during injection. The results are interpreted in terms of the nature of binding (enthalpy or entropy driven), location of the dimers with respect to the cyclodextrin molecules, and equilibrium stoichiometric binding ratio.

In **Chapter 7**, a method for fabrication of β -cyclodextrin (β -CD) functionalized mesoporous silica nanoparticles (MSNPs) through the covalent attachment of β -CD is proposed. The MSNPs were initially functionalized with (3-aminopropyl)triethoxysilane (APTES). The silane coating on the surface of the particles derived from the hydrolysis of

APTES acts as a coupling agent and provides amine group ($-\text{NH}_2$) for attaching the β -CD molecules. To attach β -CD to the amine group ($-\text{NH}_2$), commercially available mono-2-O-(p-toluenesulfonyl)- β -CD (6-TsO- β -CD) was stirred with the amine-functionalized MSNPs in N-methylpyrrolidone (NMP) in presence of Potassium Iodide (KI). The grafted β -CD moieties can function as inclusion sites and hosts for lignin dimers. Possessing an average loading capacity of 0.042 mmol β -CD/g particles, the resultant nanoparticles could potentially serve as a biocompatible platform for selective separation, loading, and delivery of lignin dimers.

The dissertation concludes in **Chapter 8** by summarizing highlights and suggestions for expanding this work in new directions. Future directions include transferring the lignin dimer functionalization strategy from silica nanoparticles to silica thin films and ceramics. Modifying the film with organolignols by grafting via silanol functional groups would impart the surfaces with lignin-like characteristics for a broader application range. Additionally, the future directions involve using the specificity of the host-guest complexation of CDs with monolignols and dimers for separation enrichment of specific lignin dimers from lignin deconstruction mixtures. Success of this project would provide an inexhaustible source of valuable aromatic chemicals (lignin dimers) from agricultural and industrial byproduct lignin.

CHAPTER 2. BACKGROUNDS

2.1 Lignin

2.1.1 Lignin and its small molecule derivatives

Lignin is a cross-linked polyphenolic polymer (**Figure 2.1**) with high molecular weight of 600–15000 kDa made up of three phenylpropane aromatic lignin monomers - sinapyl, coniferyl, and *p*-coumaryl alcohol - which are also called monolignols (**Figure 2.2**) [3, 14]. Lignin's three monomers are linked together through aromatic ether bonding motifs and non-aromatic carbon-carbon bonds [15]. The key structural units within each monomer are a phenolic ring and a three-carbon side chain attached in the position para to the phenolic hydroxyl group [16]. Three types of aromatic structures are found in lignin, syringyl (S), guaiacyl (G), and *p*-hydroxyphenyl (H) units as shown in **Figure 2.2**. Lignin is a promising precursor for synthesizing low molecular weight molecules such as aromatics (e.g. phenol, vanillin, guaiacol, benzene and toluene), aldehydes (e.g. vanillin aldehyde and syringaldehyde), acids (e.g. vanillic acid and syringic acids), dimethyl sulfide, dimethyl sulfoxide and etc. [1, 17]. The most prevalent linkage between the monolignols is a β -O-4 ether linkage which comprises more than half of the linkage structures in lignin [1]. Coupling of two or three of monomeric units of S, G, and H through aldol reaction (β -O-4 linkage) forms a lignin dimer or trimer of β -O-4, respectively. An example of a guaiacyl-syringyl dimer of β -O-4 [18] is shown as (I) in **Figure 2.3**. Other lignin bonding motifs are α -O-4 (ether), 5-5 (biphenyl), β - β (resinol), 4-O-5 (diphenyl ether), β -5 (phenylcoumaran), and β -1 (diphenyl methane) [1] some of which are shown in **Figure 2.3**.

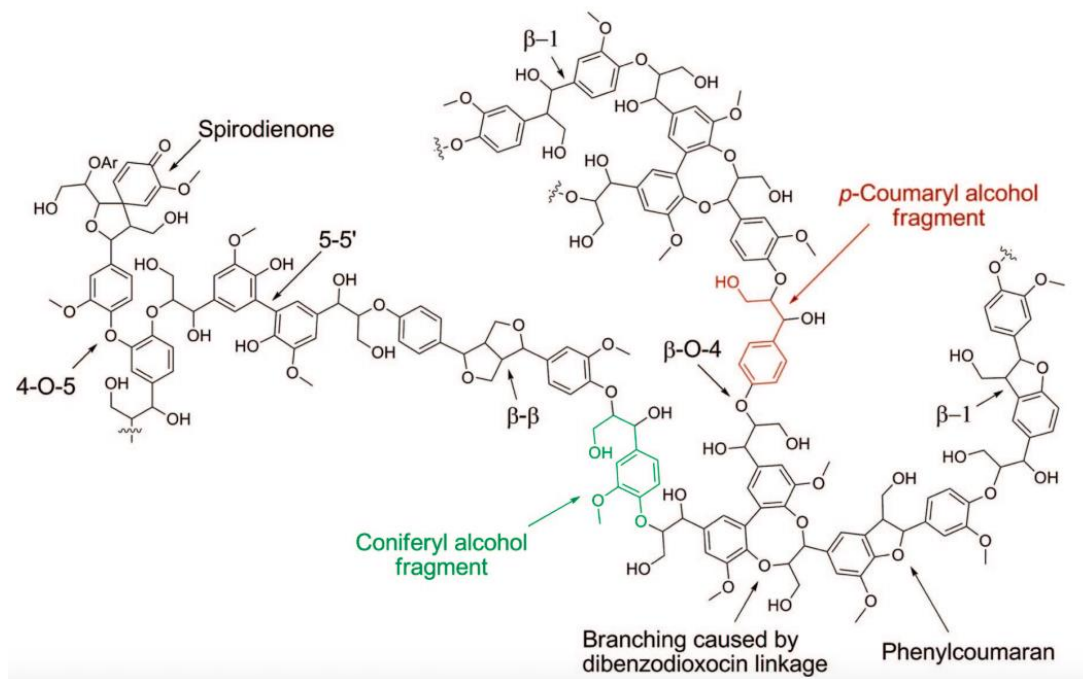


Figure 2.1 Distribution of various bonding motifs in a softwood lignin structure. Reproduced from Ref. [17] (Zakzeski et al., Chemical reviews 110.6 (2010)), with permission from American Chemical Society, copyright 2010.

Some lignans and lignin-derived small molecules possess anticancer [19], antiviral [19, 20], and antimicrobial [20, 21] properties and can hinder activities of specific enzymes. Thus they are potential promising alternatives to current petroleum-based small molecules used in various industries such as pharmacological and medical industries [20, 22]. For instance, pinoresinol is a β - β dimer of coniferyl alcohol, which comprises at least 2 % of softwood lignin and is frequently found in wood, fibrous plants, roots, leaves, and the reproductive organs and seeds of several plants. It is mainly identified as a defensive compound possessing anthelmintic and antifungal properties [22-24]. Moreover, podophyllotoxin (a dimeric lignin small molecule) and its derivatives (etoposide and teniposide) are used broadly in anticancer as well as antiviral treatments [19, 24]. Structures of both pinoresinol and podophyllotoxin are shown in **Figure 2.3** (II) and (III) respectively.

Additionally, **Figure 2.3** (IV) shows the structure of β -5 phenylcoumaran dimer which is a resultant compound of dimerization of two dehydrogenated coniferyl alcohol monomers through the β -5 linkage [25].

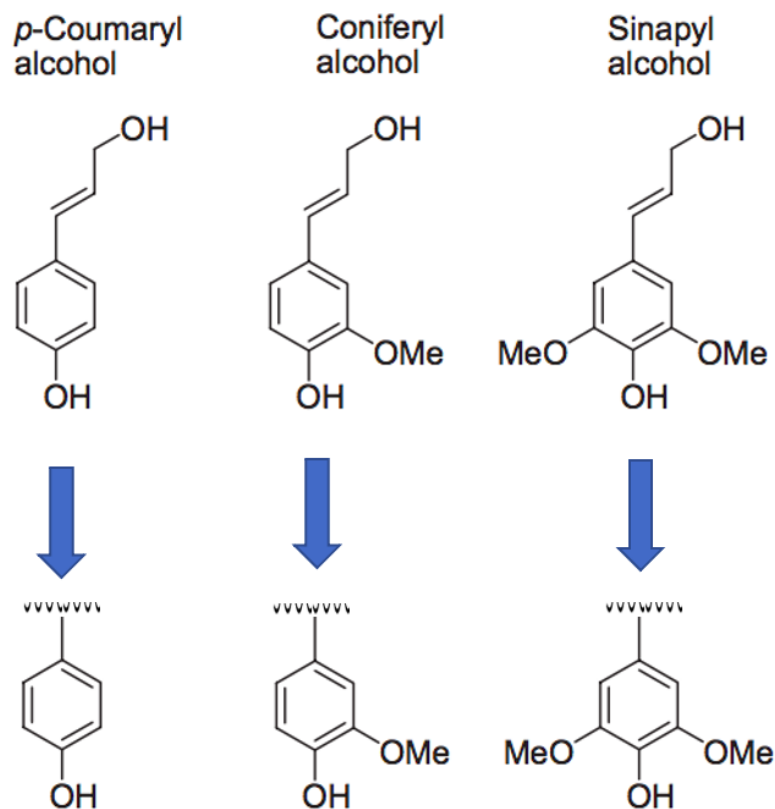


Figure 2.2 Lignin's three monomers (monolignols) and their corresponding structures: H, G, and S

Current production of lignin-derived small molecules is based on a top-down approach, in which lignin is broken down and desired compounds are isolated from the deconstruction mixture. For instance, phenols are produced through alkaline hydrolysis of lignin, organic acids (toluic, formic, acetic, benzoic, and methoxybenzoic) are provided by oxidation of lignin, and vanillin is commercially isolated via the oxidation of lignin under

alkaline conditions. In intensive oxidizing conditions, vanillin may be oxidized to vanillic acid. Dimethyl sulfoxide is prepared by oxidation of sulfated lignin and dimethyl sulfide is isolated from the reaction of kraft lignin with molten sulfur under basic conditions, where two methyl groups are passed on from lignin to sulfur [4]. Zhang et al. synthesized a non-phenolic lignin dimer of β -O-4, namely 1-methoxy-2-(4-methoxyphenethoxy)benzene, through pyrolysis [26]. Yue et al. identified and quantified several guaiacyl-based lignin dimers released by thioacidolysis from softwood with various linkages such as 4-O-5, and 5-5 shown as (V) and (VI) in **Figure 2.3**, respectively [23]. Goñi et al. identified thirty lignin-derived phenolic dimers as products of alkaline CuO oxidation reactions in presence of twenty four different vascular plant materials under alkaline conditions. The lignin dimer products were characterized by five different kinds of bonding motifs between phenolic units such as direct 5-5-ring-ring bonding, α -1-monoketone, β -1-diketone, α -5-monoketone, and α -2-methyl sidechain-ring couplings [27]. Njiojob and co-workers proposed a method for the stereoselective synthesis of enantiomerically pure β -O-4 lignin dimer model compounds with decent yields. Their method can be employed for enzymatic, microbial, and chemical studies of lignin deconstruction [28]. However, obtaining lignin-derived small molecules by breaking down lignin is severely hindered by the extreme chemical heterogeneity of lignin, which limits both the ability to target a desired chemical product profile during deconstruction and the ability to analyze the products of deconstruction. An alternative to breaking down lignin would be a “building up” approach in which lignin-mimetic monolignol chemistry is used to synthesize and characterize lignin sequences with known bonding. For instance, Asare et al. provided a generalized route for the organic synthesis of various β -O-4 dimers from different monolignols [29]. In this

dissertation, synthesized lignin dimers from the “building up” approach served as a starting point for investigations of interfacial surface chemistry of lignin and its derivatives.

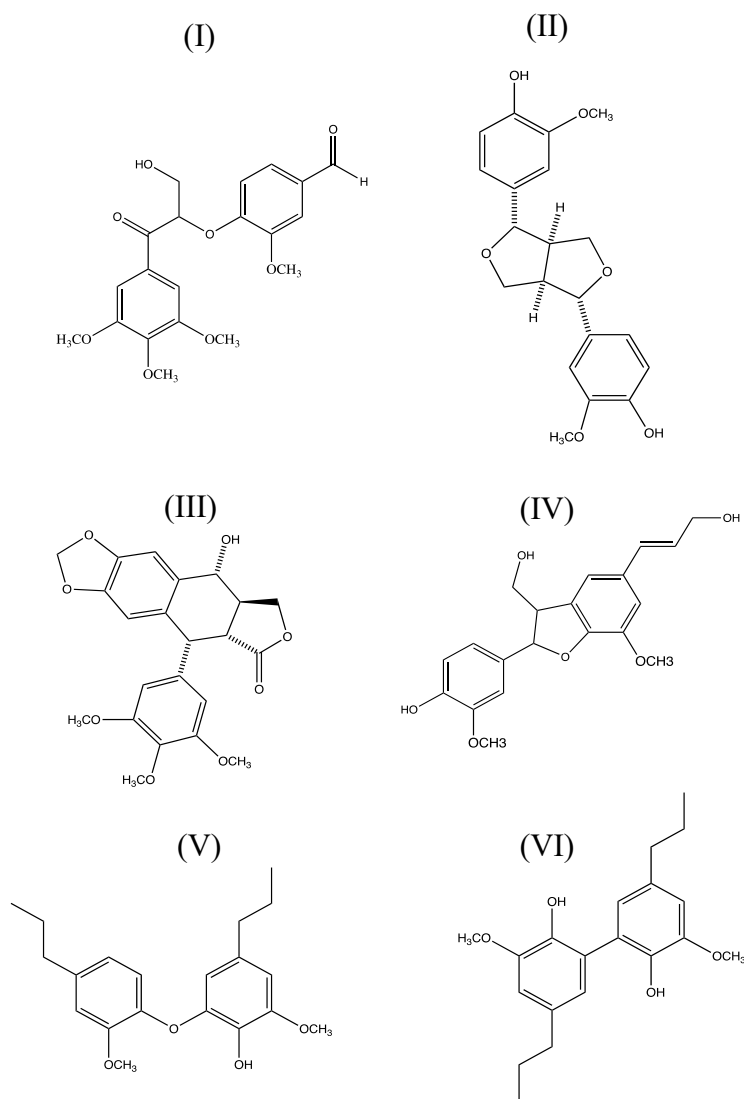


Figure 2.3 Exemplary lignin dimers : (I) guaiacyl-syringyl dimer of β -O-4, (II) guaiacyl-guaiacyl dimer of β - β (pinoresinol), (III) podophyllotoxin, (IV) β -5 phenylcoumaran dimer, (V) 4-O-5 (diaryl ether) linked guaiacyl-type thioacidolysis dimer, (VI) 5-5 (biaryl) linked guaiacyl-type thioacidolysis dimer.

2.1.2 Lignin depolymerization

Lignin's monomers (sinapyl, coniferyl, and *p*-coumaryl alcohol) are randomly arranged and distributed within the lignin macromolecule, leading to the irregular structure as well as variable molecular weight of lignin [6]. The complexity in structure and bonding motifs of lignin depends mostly on the plant source and the isolation process [30]. Lignin is categorized into three kinds: softwood lignin (woody gymnosperms) which consists of mostly coniferyl alcohol, hardwood lignin (woody angiosperms) which is comprised of coniferyl and sinapyl alcohols, and grass lignin which has all three alcohols in its structure [15]. The stability of the polyphenolic structure of lignin has made it very arduous to be broken down or modified. Aggressive reaction conditions are needed to transform or depolymerize crude lignin (usually in form of kraft lignin and lignosulfonate), some of which often result in production of undesired amounts of byproducts such as sulfur [5]. Some of the processes for lignin depolymerization are pyrolysis, hydrolysis, gasification, hydrogenation, oxidation, enzymatic oxidation, and microbial conversion [17], a few of which are explained below.

Pyrolysis is a commonly used thermal decomposition treatment which is conducted in the absence of oxygen, and changes lignin into different solid (char), liquid (oils) and gas products. Though not necessary, pyrolysis can be performed in the presence of catalysts such as zeolites, metals, and metal oxides. Pyrolysis is performed in two ways depending on the temperature of the reaction and the heating rate. In conventional (slow) pyrolysis

lignin is heated to ~ 500 °C and the heating rate is slow, whereas in the flash (fast) pyrolysis temperature can go up to ~ 1000 °C, with a higher heating rate [1, 26].

In hydrothermal degradation (hydrolysis), water-based solutions (e.g. 50/50 (v/v) water/ethanol, phenol, acetone or formic acid) in a temperature range of 280 to 400 °C and pressure range of 20–25 MPa are used to depolymerize lignin [1]. In this process, the presence of H^+ and OH^- moieties improves and speeds up the acid and base-catalyzed hydrolysis reactions. Throughout hydrolysis, different compounds (e.g. phenols, catechol, guaiacol and other methoxy phenols) are generated by cleavage of ether bonds, some of which break down even further by hydrolysis of methoxy groups, with the benzene ring remaining intact [31].

Gasification includes a series of consecutive hydrolysis, polymerization, hydrogenation, water–gas shift, steam reforming, and methanation reactions at high temperature of at least 700 °C and high pressure of 15–27.5 MPa. The major products of lignin gasification are gases such as carbon dioxide, hydrogen, carbon monoxide, and methane. The presence of catalysts such as bases (e.g. NaOH, KOH) and base salts (e.g. Na_2CO_3) is necessary for this process [1].

Despite the natural resistance of lignin against microbial attacks, its degradation can occasionally takes place through oxidative enzymes (oxidoreductases) such as laccases and peroxidases produced by some bacteria and fungi [1]. Wood-rotting fungi such as white-rot and brown-rot basidiomycetes are known for their ability to cause lignocellulose decay. White-rot basidiomycetes are the most common wood-rotting organisms and produce laccases or ligninolytic peroxidases to oxidize lignin and form aromatic radicals. White–rot fungi have also been efficiently utilized in pretreatment of the lignocellulosic

biomass to deconstruct lignin and to facilitate the enzymatic access to cellulose in the biomass for separation of bio-moieties from hemicellulose and cellulose [32]. Brown-rot fungi, which comprises less than 10% of wood-rotting basidiomycetes depolymerize lignin into aromatic compounds as well [33]. However, during the pretreatment of lignocellulose, the brown-rot fungi first attack the cellulose, whereas the white-rot fungi attack both cellulose and lignin via lignin degradation pathways created by enzymes [32].

2.1.3 Lignin-based nano-structured materials

Renewable resources including lignin have been progressively utilized for production of value-added nanostructured materials (mostly within 1-100 nm) such as nanoparticles and nanocomposites [34]. Lignin-conjugated nanoparticles have been investigated for drug delivery and therapeutic applications [35-39], and in making adhesives [40, 41], reinforcements [35], antioxidants [42, 43], antimicrobials [44-46], pollutant removers [47, 48], and UV blockers [49, 50]. Because of lignin's biodegradability and biocompatibility, nanoparticles made from lignin have less environmental and health hazards compared to nanoparticles made from metals and semiconductors (such as silver, TiO₂ and ZnO) and therefore are attractive candidates for biomedical, and therapeutic applications and for delivery of drug compounds [51, 52]. As an example, Figueiredo et al. developed lignin nanoparticles with low cytotoxicity and remarkable capacity to effectively load poorly water-soluble drugs [39]. Furthermore, Byrne et al. observed that poly(lactic-co-glycolic acid) (PLGA) nanoparticles conjugated with lignin and loaded with anticancer drugs have an improved delivery to the breast cancer cells compared to lignin-free PLGA nanoparticles loaded with the same drug [38].

Owing to its polyphenolic structure and possessing multiple oxygen-containing functional groups, lignin acts as a barrier against degradation of the plant and invasion of microorganisms [53]. Moreover, lignin's phenol groups scavenge free radicals and serve for antioxidant purposes [17, 30]. The antimicrobial and antioxidant properties have made lignin a versatile material for use in food packaging [54-56], antioxidants [57-61], UV-protectants [62-64], antimicrobial coatings [65, 66], wound healing [67], and tissue engineering [68-70].

Bionanocomposites are the materials which are mainly made from sustainable substances as fillers and hydrocarbon-based polymers as matrix. Lignin holds the potential to be used as filler for fabricating biodegradable nanocomposites because of its abundance, biodegradability, cost effectiveness, and relative lightweight [71, 72]. Moreover, lignin improves the resistance against UV and thermal oxidation when incorporated into different polymer matrices such as poly(lactic acid) (PLA), polypropylene (PP), polyethylene (PE), and polystyrene (PS) [17, 30]. Kai et al. fabricated biocompatible nanofibrous composites by using alkylated lignin (10–50%), PLA, and poly(L lactide) (PLLA) as precursors. The antioxidant assay proved that because of the radical scavenging ability of lignin, the addition of lignin to PLA reduced the oxidative stress caused by PLA. The nanofibers were tested in presence of human cells and it was revealed that there is a promising balance between the cytotoxicity and the antioxidant activity, making the nanofibers excellent potential biomedical materials [61]. Yang et al. synthesized nanocomposite films by adding lignin nanoparticles to a PLA-based matrix for manufacturing antimicrobial food packaging. Biocidal and antibacterial activities of the fabricated nanocomposites were evaluated against the food borne bacterial pathogen; *Pseudomonas syringae* pv. *tomato*

(Pst). The results demonstrated the efficacy of the lignin nanoparticles in decreasing bacteria proliferation even at a high bacteria concentration [55].

2.2 Liposomes and supported lipid bilayers

As part of evaluating the potential pharmacological activity of lignin oligomers, studies of their interactions with lipid bilayers will be featured as part of this dissertation. Lipid bilayers are the basic structural units of the biological cell membranes [73]. Lipid bilayers compromise the outer layer around the biological cells, which acts as a barrier against the migration of unwanted moieties to the inside of the cells and keeps the desired moieties inside the cells [74]. Actual cellular membranes have a complicated heterogeneous structure consisting of lipids, proteins, and carbohydrates which are not homogeneously distributed in the membrane [73, 75]. Along with lipids, proteins are major constituents of the cell membrane and play multiple roles in their biological function (e.g. enzymatic catalysis of some chemical reactions at the membrane) [76]. Moreover, the covalent attachment of carbohydrates to the lipids and proteins complicates the membrane's structure [76]. This complexity of the cell membrane structure as well as the extremely dynamic nature of the interactions of lipids with proteins and other moieties in the cell membrane make the investigation of the interactions with compounds and drug delivery systems very challenging [73]. Use of model cell membranes (e.g. lipid monolayers or lipid bilayers in form of liposomes or supported bilayers) has been suggested as a solution to bypass the complications associated with studying the actual cell membrane environment [73]. Lipid bilayers are thin organic membranes (a few nanometers in width) composed of two layers of fatty molecules called lipids [74]. There are $\sim 5 \times 10^6$ lipid molecules per μm^2 area of the lipid bilayer sheet. Phospholipids are the most common

lipid molecules and contain a polar head group and two hydrophobic hydrocarbon fatty acid tails [74]. As illustrated in **Figure 2.4**, the lipid molecule is amphiphilic, meaning that one end of the molecule is hydrophilic (heads) while the other end is hydrophobic (tails). The phosphate-containing hydrophilic heads are exposed to the aqueous bulk medium at each surface of the bilayer, whereas the hydrophobic tails which are typically fatty acid chains are protected from water buried in the interior. One tail typically has one or more carbon double bonds which make it unsaturated, whilst the other tail is saturated and lacks the double bonds [74, 77].

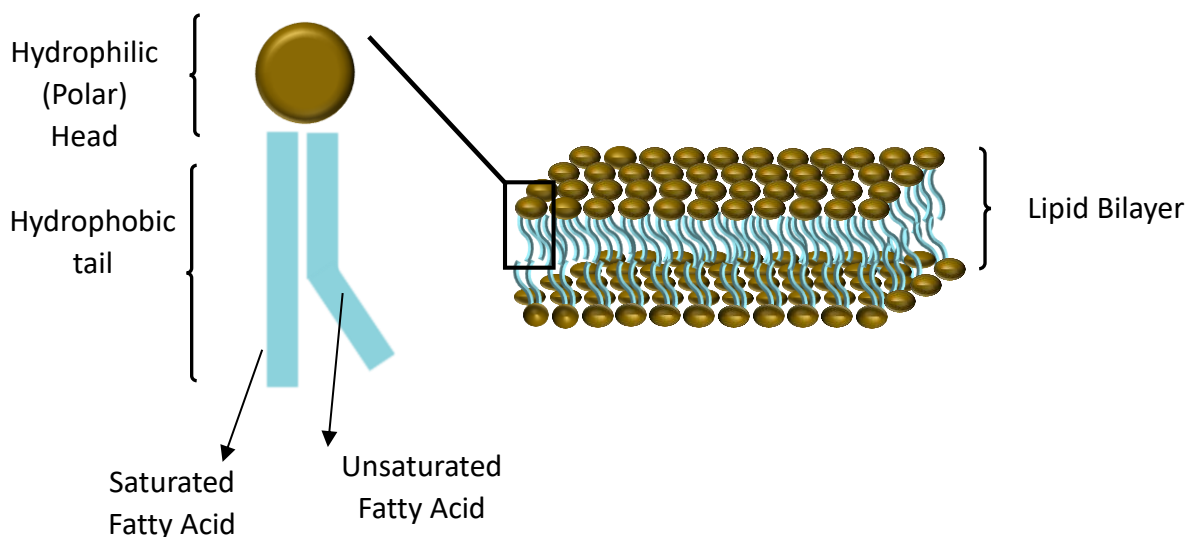


Figure 2.4 Different components of a phospholipid molecule in a lipid bilayer sheet.

Phospholipids create enclosed vesicles in aqueous medium called liposomes (**Figure 2.5**) [74]. A liposome (or a lipid vesicle) is a self-assembled lipid bilayer which has engulfed a compartment of the surrounding bulk medium and formed a colloidal sphere as small as tens of nanometers or as large as tens of microns [78]. The former is referred to as small unilamellar vesicles (SUV's), and the latter is referred to as giant unilamellar vesicles (GUV's) [78, 79]. Liposomes possess several physicochemical features similar to

cellular membranes, including chemical composition, permeability, interacting with different moieties, and osmotic activity [80]. Because of their amphiphilic nature, simplicity of surface modification, biocompatibility, and ability to solubilize hydrophobic molecules liposomes are widely used in cell studies, drug delivery, gene delivery, cancer chemotherapy, cosmetic industry, etc. [78, 79, 81].

Supported lipid bilayers (SLBs) are two-dimensional lipid bilayer films prepared on the surface of a solid support such as glass, quartz, mica, gold, and silicon surfaces (**Figure 2.5**) [82]. Alongside liposomes, SLBs are amongst the most common model cell membrane systems [83]. SLBs can be created by various methods including the Langmuir-type deposition methods (Langmuir–Blodgett or Langmuir–Schäffer), solvent-assisted formation, and the fusion of liposomes on solid surfaces [83-86]. SLBs on solid substrates are utilized for cell studies, manufacturing catalytic surfaces, sensors, and as insulating layers with thicknesses in order of nanometers on conductive surfaces [87]. The growing interest in SLBs is due to their numerous advantages. In contrast to unsupported free-floating vesicles, supported lipid bilayers allows the use of surface sensitive imaging techniques such as fluorescent microscopy, Surface Plasmon Resonance (SPR), and Total Internal Reflection Fluorescence (TIRF) microscopy. Moreover, the use of the solid supports preserves the geometry, stability and the integrity of the membrane tethered to it and allows for other characterization techniques such as Quartz Crystal Microbalance studies (QCM) and Atomic Force Microscopy (AFM) [79, 85]. However, using SLBs as model cell membranes has some shortcomings. For instance, in cell studies, SLBs do not resemble the curvature of actual cell membranes. Furthermore, restrictions of the mobility

of the SLB lipids affect the diffusion coefficient and makes it nearly two times less than that of liposomes [88].

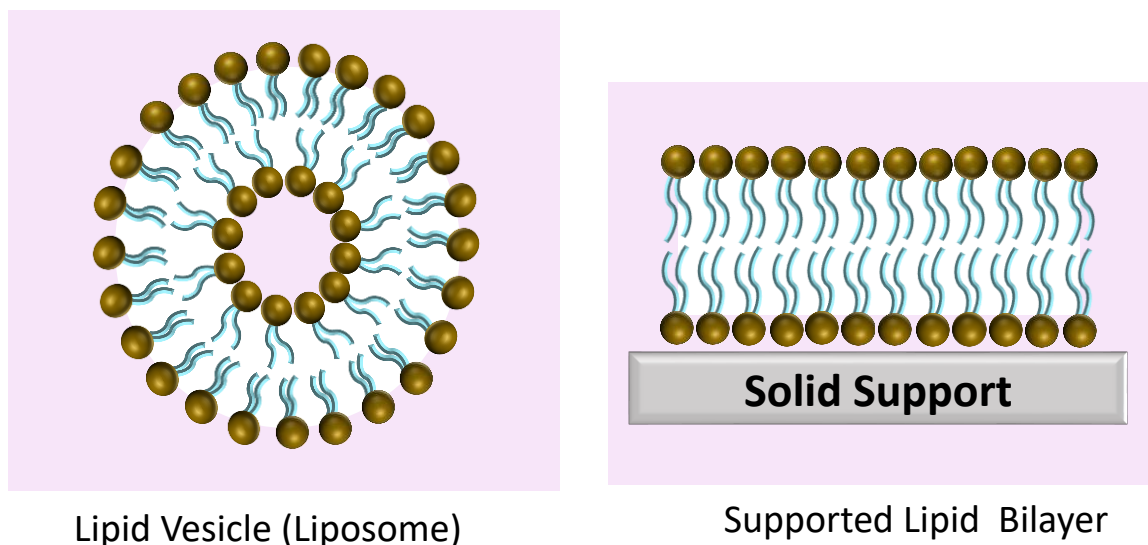


Figure 2.5 Different model cell membranes

The phase transition in lipid bilayers can take place by either increasing the temperature, or by varying the ionic strength or the pH of the bulk aqueous solution [89]. When thermal energy is added to a lipid bilayer, the hydrophobic van der Waals interactions between lipid acyl chains are weakened which leads to an increase in the dynamic and mobility of the tails of the lipid molecules and ultimately affects the stability of the system [80]. The phase transition of lipid bilayers occurs as a result of melting or disarrangement of the hydrocarbon chains of lipid molecules [90]. The lipid bilayer phase transition temperature (T_m), also known as the gel to fluid crystal phase transition temperature, is the temperature below which the bilayer has ordered two-dimensional crystal-like gel state and above which it has a disordered fluid-like state (**Figure 2.6**) [90].

The phase transition temperature and enthalpy of the transition depend on factors including the length of the hydrocarbon chains, the type of the phospholipid head group and the ionic strength of the bulk solution [89]. For lipids with shorter hydrocarbon chains or with double bonds in the chains, T_m is usually lower [74]. For some lipids, periodic ripples in the bilayer occur at a temperature below T_m , which is referred to as the pre-transition temperature (T_p). As seen in **Figure 2.6**, at temperatures between T_p and T_m of most of the lipids, the gel state and fluid state exist simultaneously [91]. A decrease in the T_m of a lipid bilayer exposed to an exogenous compound is associated with an increase in fluidity, mobility, and disorder of the lipid bilayer and is an indication of strong interaction with the compound. Similarly, a decrease in the enthalpy (ΔH) of the lipid bilayer once exposed to a solute is typically a sign of strong interactions of the solute with the acyl chain of lipid bilayers [92]. The changes in T_m the phase transition and the enthalpy per mol of lipids can be measured through calorimetric methods such Differential Scanning Calorimetry (DSC) [80].

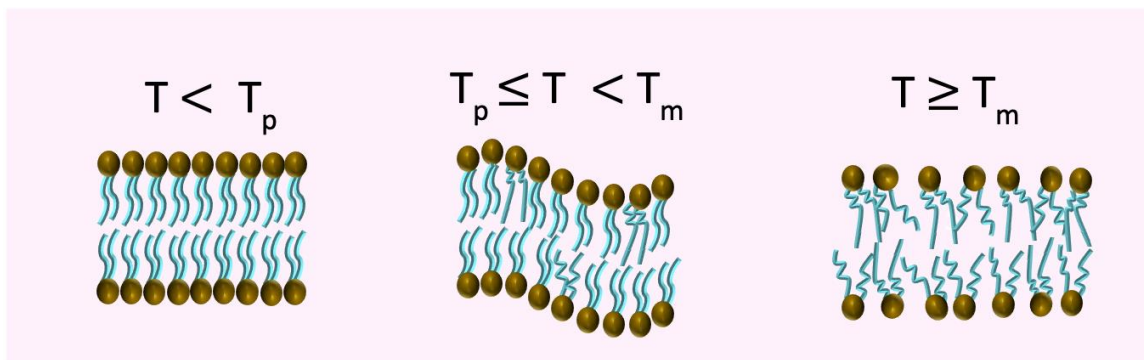


Figure 2.6 Schematic illustration of the different states of the lipid bilayer during the phase transition: gel-crystalline state ($T < T_p$), rippled phase ($T_p \leq T < T_m$), and the liquid-crystalline state ($T \geq T_m$)

2.2.1 Differential Scanning calorimetry (DSC) for studying the thermal behavior of lipid bilayers

Differential scanning calorimetry (DSC) is a characterization technique, frequently used to study the thermodynamic properties and thermal behavior of polymers, proteins, lipid membranes, etc [80]. For instance, the denaturation temperature of proteins, glass transition temperature of polymers, heat capacity of dilute biopolymer solutions, and phase transition temperature of lipid membranes can be determined using DSC [90].

DSC works based on measuring the amount of power required for energy compensation between two identical cells: a reference and sample cell at atmospheric pressure. As illustrated in **Figure 2.7**, in a typical DSC setup, the sample (e.g. liposomes in solution) is put in a pan and placed inside the sample cell, while the reference pan in the reference cell is left empty or filled with the blank solution. Both reference and sample cells are situated inside a shield which controls the temperature range of scanning initially entered in the system by the user. The cells are in thermal contact with the shield and hence get heated as the shield's temperature increases. There are temperature sensors located between the sample and reference cells which ensure that the temperatures of the two cells are similar at all times. If the temperature of the sample cell varies, the cell heater control unit and the computer apply suitable compensating heat to the cell through heaters placed on the cell surfaces to maintain the temperature difference close to zero. The compensating heat flow versus the scanned temperature range is recorded as the calorimetric output signal (**Figure 2.8**) [90].

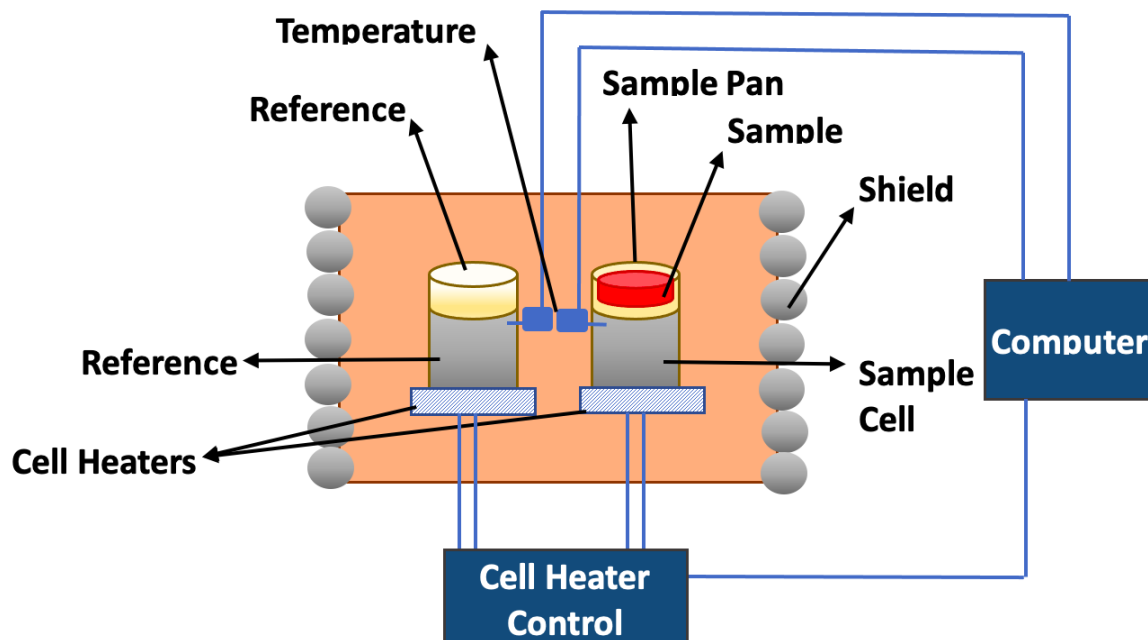


Figure 2.7 Schematic of a Differential Scanning Calorimeter (DSC) adapted from Spink [90]

The phase transition of lipid bilayers can be investigated by calorimetry methods. DSC measures the different characteristic temperatures and ultimately assists with describing the transition process of lipid bilayers. As seen in **Figure 2.8** for phase transition of a model lipid bilayer system, the main phase transition temperature or the melting temperature (T_m) is indicated by an endothermic peak in the heat flow and is the highest temperature peak which can be sharp for small molecules, and broad for larger species such as liposomes. The pretransition temperature (T_p) is a temperature in which a well-arranged bilayer in the gel phase changes into a rippled bilayer and is usually identified by a relatively broad and small shoulder before T_m . The onset temperature (T_{onset}) is the temperature at which the bilayer melting process starts, that is determined by the intersection of the baseline tangent with the tangent of the leading edge of the peak of a

transition. Where the peak transition returns to the baseline is referred to as offset temperature (T_{offset}).

The area under a melting transition curve is the total amount of heat taken up over the course of the melting process [80]. In other words, the changes in the enthalpy of a lipid bilayer are associated with the thermal energy given to it. In **Figure 2.8**, the heating scan showing the phase transition of pure dipalmitoyl phosphatidyl choline (DPPC) liposomes have been measured by DSC and illustrated as a graph of heat flow (μW) versus temperature (over the range of 25-55 °C). The pure DPPC melting temperature or main phase transition temperature (T_m) is identified by an endothermic peak at 42.35 ± 0.15 °C. The corresponding onset (T_{onset}) and offset (T_{offset}) are recorded at 41.16 ± 0.07 , 50.07 ± 0.2 respectively. The peak of the pretransition temperature (T_p) occurs at 37.06 ± 0.06 °C [11, 93].

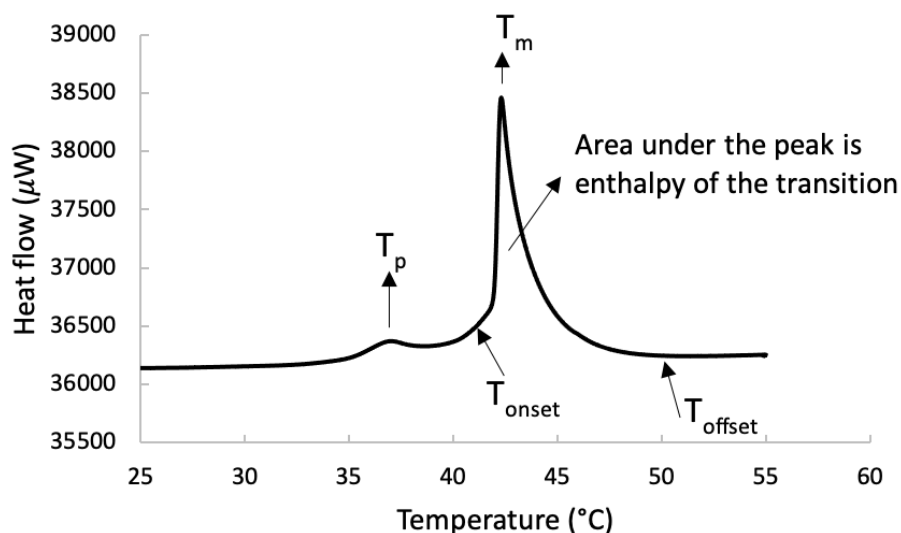


Figure 2.8 DSC heating scan of phase transition of pure DPPC liposomes in PBS over the temperature range of 25-55 °C with scan rate of 1 °C/min.

The partition coefficient of the solutes between the liposomes and aqueous solution (K) is related to the shift in transition temperature relative to pure liposomes. For low solute concentrations, K can be estimated using the relation (**Equation 2.1**) [94]:

$$-\Delta T_m = \left\{ \frac{R \cdot T_m^2}{\Delta H_{lipid}} * \frac{K}{55.5 + C_{lipid} * K} \right\} C_s \quad . \quad (2.1)$$

This equation assumes that at equilibrium, the depression in the main phase transition temperature is directly proportional to the amount of the solute that partitions into the lipid bilayer [93]. In this equation, ΔT_m is the difference between the transition temperature of the sample and pure liposomes, T_m is the transition temperature of pure liposomes, R is the ideal gas constant, ΔH_{lipid} is the phase transition enthalpy (kJ/mol), C_{lipid} is the concentration of the lipid in the solvent (M), and C_s is the concentration of the solute in the solvent (M). To solve for the partition coefficient, the entire constant in brackets is found using linear regression in the limit of low C_s . The partition coefficient values are usually reported as $\log(K)$.

2.2.2 Quartz Crystal Microbalance with Dissipation (QCM-D) for studying supported lipid bilayers

Quartz Crystal Microbalance (QCM) is a piezoelectric quartz crystal which resonates at a known frequency once subjected to a certain AC voltage. If exogenous species attach or adhere to the crystal's surface and form an adlayer, changes in the resonance frequency of the crystal take place. This phenomenon enables QCM to be utilized as a sensitive mass balance which probes mass changes in order of ng/cm^2 . Quartz Crystal Microbalance with Dissipation (QCM-D) not only measures the changes in resonant frequency (Δf) and subsequently the mass of the adlayer (Δm), but also evaluates

the variations in the viscoelastic properties of the adlayer by monitoring and measuring the changes in the energy loss or dissipation (ΔD) of the system. Once the AC voltage shuts down, the energy dissipation/decay of the crystal's oscillation happens over time depending on the viscoelastic features and bond stiffness of the attached moieties and the contact medium [95, 96]. To calculate the dissipation (ΔD) in QCM-D, the crystal's oscillation decay time (τ) is measured, and is put in **Equation 2.2** [97]:

$$\Delta D = \frac{1}{\Delta f \pi \tau} \quad (2.2)$$

QCM-D is extremely sensitive, simple to operate, and provides interaction monitoring in real time [95]. It also allows the temperature control which facilitates the study of the effect of temperature on the experiment. Bare and/or coated substrates of different materials (silica, oxidized gold, etc) can be used in QCM-D. All these qualities have made the QCM-D a versatile technique for investigating the molecular adsorption/desorption, binding kinetics, model cell interactions, measurements of liquid density and viscosity, and surface functionalization [98]. QCM-D is used in studies related to biomaterials, drug discovery, vacuum science, materials science, gas sensing, electronic semiconductor devices, and optical coatings [99]. As seen in **Figure 2.9**, in a typical QCM-D setup, the sensor; which is a round disk of quartz sandwiched between two metal electrodes (e.g. Au), is placed inside a flow cell which is carefully secured in a closed shield [96]. The sample solution is pumped through an input tube and flows towards the cell chamber. As the solution flows over the substrate, a decrease in the oscillation frequency of the crystal occurs which is an indicator of the addition of mass to the surface of the substrate. The process continues until the desired layer forms on the sensor.

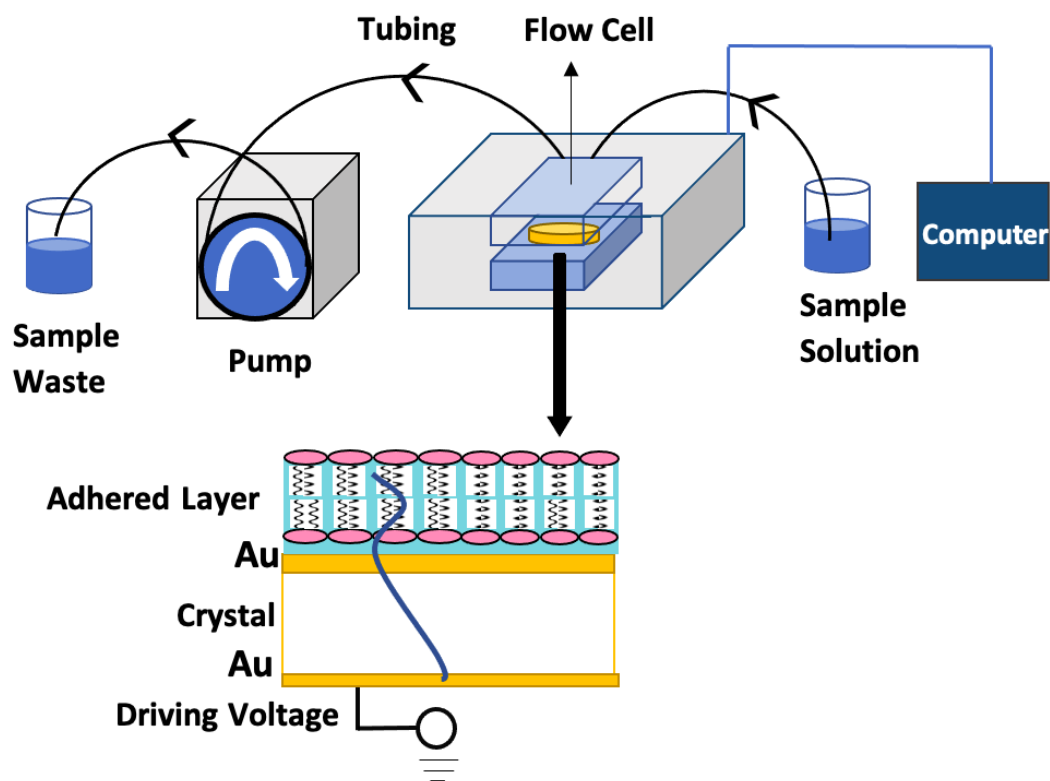


Figure 2.9 Schematic of a Quartz Crystal Microbalance with Dissipation (QCM-D) with a lipid bilayer as the adhered layer on a gold (Au) sensor

The QCM-D technique allows the measurement of frequency and dissipation values at several harmonics/overtones ($n=1, 3, 5, 7, 9, 11, 13$) of the crystal's frequency consecutively on the millisecond time scale [96]. This feature allows for depth profiling and characterizing processes as a function of distance from the surface [100]. The first overtone ($n=1$) is referred to as fundamental frequency ($f_1=5$ MHz) which has the penetration depth of ~ 250 nm in pure water. Usually, results at the first overtone are unreliable because they are affected by the flow of the bulk solution in the QCM flow cell, thus they are not included in the analysis and data interpretation [101]. The magnitude of the overtone is inversely proportional to the distance from the surface being probed; for

example, the third overtone ($n=3, f_3=15$ MHz) is measuring mass changes further from the surface than the seventh overtone ($n=7, f_7=35$ MHz) [38]. For instance, in a process where a species is being adsorbed to a lipid membrane on QCM sensor, similar Δf values at all overtones points out to a process that has the same structural characteristics across the entire thickness of the layer; i.e a vertical transmembrane insertion rather than a simple surface adsorption [100]. The penetration depth (δ) of the QCM-D can be calculated through the expression below:

$$\delta = \sqrt{\frac{\eta}{\pi \rho \Delta f}} \quad (2.3)$$

where η is the shear viscosity and ρ is the density of the layer [97]. One of the simplest equations that relates the oscillation frequency of the sensor to the coupled mass on it is called Sauerbrey equation [99]. In this equation the mass of adlayer per active area ($\Delta m / A$) is measured from the change in frequency (Δf) of the sensor:

$$\frac{\Delta m}{A} = \frac{C \Delta f}{n} \quad (2.4)$$

where C is the material specific Sauerbrey constant and is expressed as:

$$C = \frac{t_q \rho_q}{f_0} \quad (2.5)$$

t_q is the thickness and ρ_q is the density of quartz (-17.7 Hz ng/cm² for a 5 MHz crystal). n is the overtone number at which the frequency is being measured. For Sauerbrey relationship to be applicable, three requirements have to be met: Firstly, the mass of the attached layer should be trivial compared to the mass of the quartz crystal; secondly, the

adhered layer should be rigid; and thirdly, the adhered layer must be evenly spread on the crystal's surface [96]. However, in case of thick and massive films or highly dissipative films with larger dampening effect relative to a rigid film of equal mass, the relationship between Δf and Δm becomes more complex and both the frequency and damping of the sensor should be taken into account [102]. Moreover, in liquid phase, the viscous and elastic factors contribute to the frequency variations and this leads to failure to fulfill the second requirement of the Sauerbrey expression (**Equation 2.4**) as mentioned above [96, 99]. Some of the more realistic models used for interpreting the QCM-D data are Voigt viscoelastic model and power-law model [99]. Sadman et al. studied swelling changes of a thermoresponsive hydrogel to differentiate the three different models of QCM-D: Sauerbrey, Voigt viscoelastic, and power-law models. They observed that at high temperatures the film was rigid and thin, thus the Sauerbrey equation was applicable. As the film cooled down, it swelled and its properties (e.g. thickness) could be calculated only through the Voigt and the power-law models [99]. Voigt viscoelastic model has also been shown to be suitable to measure the thickness of adsorbed protein layers [102].

Synthetic phospholipid bilayers, such as those comprising DPPC, in the form of solution-based vesicles or lipid bilayers on a solid support are frequently used as model cell membranes to interpret the interactions of cells with surfaces. Two commonly employed methods for forming supported lipid bilayers on QCM disks are vesicle fusion and solvent-assisted lipid bilayer (SALB) formation techniques. In vesicle fusion technique, an aqueous buffer solution is first run over the surface to establish a baseline. Next, pre-formed lipid vesicles in the same buffer solution are injected to the sensor and adsorbed on the surface through electrostatic interaction to reach a critical coverage. At

this critical coverage level, vesicles start to fuse, rupture, and release the solvent trapped inside them. Following the vesicles' rupture a planar lipid bilayer forms and spreads on the solid support [86]. Despite being simple and very common, vesicle fusion method has some disadvantages. Sometimes, the lipid bilayers formed by this method have defects and holes, the presence of which has been previously observed by AFM [103]. Moreover, formation of lipid bilayers on some surfaces like gold, titanium oxide, and aluminum oxide is not feasible through this technique. Addition of vesicles on such surfaces results in creation of a layer of intact and un-ruptured vesicles sitting next to each other. One way to make the adsorbed vesicles rupture and form the lipid bilayer is by varying experimental factors such as ionic strength, pH of the buffer solution, osmotic shock, and injection of some cations or peptides to the surface. It should be considered that all the mentioned variations cause further complications in the experiment [86].

In SALB formation method, an aqueous buffer solution is initially passed over the QCM sensor to develop a baseline. Next, an organic solvent (e.g. isopropanol) is passed over the surface which causes drastic shifts in Δf and ΔD . After the frequency and dissipation signals stabilize, the lipids which had been dissolved in the same organic solvent are introduced to the surface and lead to small shifts of Δf and no significant shifts in ΔD . Lastly, the initial aqueous buffer solution is flowed into the system again which causes a dramatic decrease of the frequency and increases of the dissipation as a lipid bilayer forms. SALB method has numerous benefits compared to vesicle fusion. For example, it can be performed on various types of sensors such as gold, and also it is simpler because it does not include preparation of vesicles in advance or addition of any exogenous components (e.g. membrane-active peptides) [86]. As interpreted from the Sauerbrey

equation (**Equation 2.4**), the mass of the bilayer formed on a sensor is proportional to the decrease in an oscillating crystal's resonance frequency (Δf). The QCM-D response of the energy dissipation (ΔD) describes the variation in the viscoelasticity or rigidity of the film coated on the surface. High values of dissipation are the result of deformation of a soft film, whereas low dissipation describes films that are nondeformable and rigid. In relation to SLBs, an increase in dissipation indicates the loosening or thickening of the lipid bilayer. In the presence of molecules or nanoparticles, an increase in dissipation suggests that the molecules or the particles have adhered to the bilayer, leading to hydrodynamic effects that increase dissipation loss with the surrounding medium.

2.2.3 Interaction of lipid bilayers with small molecules

Small molecules with different levels of hydrophobicity, polarity, size, and charge interact with cell membranes and impact the membrane properties. The cell membrane is selectively permeable due to its hydrophobic interior; meaning that it allows hydrophobic compounds to partition into the membrane from outside of the cell, while many hydrophilic moieties are barred from entering the cell and need particular mechanisms to find their way inside the membrane [104][105]. The study of the interaction between cell membranes and small compounds is crucial for recognizing the pharmacological performance mechanism of some drugs and to elucidate their toxicological impacts on biological systems [94, 105]. For instance, the mode of action of small pharmaceutical compounds such as tranquillizers, anesthetics, narcotics, and antidepressants is based on their transport through the hydrophobic interior of the cell membrane [106]. Moreover, the mechanism of action of antibacterial therapeutics (e.g. aminoglycosides) is better understood if their interaction with microorganisms' cell membrane is first investigated [101]. Small compounds might

also fortify the properties of the lipid bilayer and enable cells to tolerate harsh condition with extreme temperatures or hydration levels [107].

A commonly practiced method for exploring cell membrane interactions is octanol/water partitioning and calculating the n-octanol–water partition coefficient. In this method, the octanol phase is thought to simulate the hydrophobic interior of the lipid bilayer. However, this technique is arduous, has slow equilibration and lengthy phase separation, and is limited because it does not account for polar interactions of the molecules with the hydrophilic head groups of the lipids [104, 108]. Use of phospholipid liposomes and supported lipid bilayers as model systems for investigating the interaction of small molecules (e.g. drugs) with biological membranes is a more versatile alternative [92]. Fujisawa et al. employed liposomes of dipalmitoyl phosphatidyl choline (DPPC) and dimyristoyl phosphatidyl choline (DMPC) to investigate the interaction of phenol and its derivatives (m-cresol, p-chlorophenol and eugenol) by using DSC [105]. From a decrease in the gel to liquid-crystalline phase transition temperature (T_m) and decrease in phase transition enthalpies (ΔH) of both DMPC and DPPC liposomes, they concluded that m-cresol and p-chlorophenol are biologically more active and had a greater impact on the lipid bilayers relative to phenol itself [105]. Eugenol, (a model allyl-containing phenolic compound and natural antimicrobial) also showed a substantial effect on the liposomes because of being high hydrophobic [105]. In a different study, Fujisawa et al. utilized DSC to study the interaction of 37 different types of mono-, di-, tri-methacrylates with the same DPPC model system and observed that compounds with hydroxy, carbonyl, amino and phenyl groups caused larger changes in T_m and ΔH [92]. Moreover, dimethacrylates with short-chain substituents; and aliphatic trimethacrylates also caused significant decrease in

T_m and ΔH . On the contrary, methacrylates with simple alkyl ester linkage and dimethacrylates with bisphenol A groups caused the smallest perturbation in the bilayer. Their results also demonstrated that phospholipid bilayers (more specifically acyl chains of DPPC liposomes) have high affinity towards double bonds in compounds [92].

A powerful technique for studying and quantifying interaction of small molecules with lipid bilayers supported on solid surfaces is QCM-D [88]. Joshi et al. utilized QCM to investigate the adsorption of aminoglycosides (kanamycin A and neomycin B) onto model bacterial cell membranes tethered on gold, and monitored similar rates of membrane diffusion for both aminoglycosides followed by bilayer destruction once a critical concentration was achieved [101]. Kannisto et al. investigated the adsorption of two small-molecule compounds, propranolol and tetracaine, onto lipid bilayers adhered on silica support through QCM and calculated the adsorbed mass of the solutes as a function of their concentration in the aqueous solution, and also measured the effect of the solutes on the bilayer viscoelasticity [108]. Wargenau et al. explored the cell membrane penetration ability of lipid-soluble compounds (vanillin, gallic acid and protocatechualdehyde) to penetrate cell membranes [109]. They used supported DMPC lipid bilayers on QCM-D silica substrates as their model cell membranes. Although these low molecular weight solutes did not measurably change the mass density of the supported lipid bilayer membrane, uptake in the bilayer changed their gel–fluid phase transitions [109]. Gallic acid and protocatechualdehyde decreased the gel–fluid phase transition temperature (by establishing interactions within the fluid phase of the bilayer), while vanillin increased it (by creating an energy-favorable dissolution effect in the gel phase rather than in the fluid phase) [109].

Monolignols (coniferyl alcohol, p-coumaryl alcohol and sinapyl alcohol) as well as some other phenolic compounds work together to build the lignin macromolecule mainly in the plants' cell walls or in the cell wall/plasma membrane interface. Thus, investigating the passage of lignin monomers and phenolic compounds through the plant cell membrane is of great importance [104]. Moreover, lignin-derived small molecules are thought to act as antimicrobial agents against microbes, therefore, estimating the partitioning of these lignin precursors and derivatives into appropriate model cell membranes of microorganisms is important. However, only a few studies directly have focused on partitioning of lignin derived small molecules into cell membranes. Boija et al. employed octanol/water partitioning measurements as well as Immobilized Liposome Chromatography (ILC) to investigate the interaction of eight lignin monomer and dimer model compounds with multilamellar liposomes [104]. Their results indicate that up to three hydroxyl groups can be present on a molecule before the membrane penetration capacity of the compound is restricted [110]. Correspondingly, diffusion of lignin precursors is a potential membrane transport mechanism in plant cells, because the number of hydroxyl groups in the lignin model compounds does not exceed the allowed limit of three [110]. Their results demonstrate that all lignin precursors partitioned well into the octanol phase, and that the hydrophobicity of the compounds together with the possibility of the polar interactions with the hydrophilic phospholipid head groups play important roles in diffusion of the lignin compounds into the liposomes [104].

2.2.4 Interactions of lipid bilayers with silica nanoparticles

Silica nanoparticles are being widely used in a broad spectrum of applications including drug and gene delivery [111], tissue engineering [112], biomedical imaging [113], biosensing and detection [113], and environmental remediation [114]. To better understand the mechanism of action of silica nanoparticles as selective cell targeting agents (e.g. drug carriers, tumor destructors, or antimicrobial agents) investigating the interaction of nanoparticles with cells and particularly cell membranes is crucial [115]. Because of the complicated and dynamic nature of the actual biological membranes, model biological membranes comprised of synthetic lipid bilayers are frequently used as simpler substitutes for cell membranes [116]. The interaction of lipid bilayers and nanoparticles involves many types of driving forces such as Van der Waals, electrostatic, and hydrophobic interaction forces; the interplay among which can be regulated by adjusting various factors such as pH, temperature, and ionic strength [117]. The magnitude of the Van der Waals forces between a liposome and a silica particle depends on the diameter of the particle, the outer diameter and the thickness of the liposome, and the distance between the surfaces of the two objects [117]. The electrostatic double-layer interactions are also functions of distance between surfaces of liposomes and nanoparticles. Hydrophobic interactions occur when phospholipid bilayers are subjected to an exogenous force or stress, and as a result widen laterally and subject fractions of their hydrophobic part to the bulk medium [117]. For instance, hydrophobic tailored silica nanoparticles which have a higher affinity to the acyl-chains in the interior of the bilayer interact strongly with the lipid bilayers [117].

Use of SLBs as model cell membranes through methods such as QCM-D and AFM allows for relatively simple investigation of the interaction of nanoparticles onto the bilayer and changes in the bilayer order and integrity [88]. There is growing interest in employing QCM-D to study the interaction of nanoparticles with lipid bilayers [95]. QCM-D is a versatile technique to investigate the deposition and disruptive interactions of nanoparticles with lipid bilayers due to its simplicity of operation and availability of multiple types of model sensor surfaces [95]. Previously, by forming a bilayer directly on a coated quartz crystal sensor, QCM-D has been used to investigate the adherence and uptake of NPs to SLBs [54], the structural rearrangement of NPs adsorbed to the SLBs [55], and the disruption of bilayers by NPs [118, 119]. Liu and Chen studied the interaction of silica nanoparticles (less than 150 nm) with DOPC lipid bilayers in presence of phosphate ions (vital components in biological medium) and observed that silica nanoparticles attach and associate well with the bilayer but do not cause any disruption in the structure of the bilayer [120].

2.3 Cyclodextrins

Another aspect of lignin oligomer interfacial behavior addressed in this dissertation is their interaction with cyclodextrins as potential separation media. Cyclodextrins (CDs) are cyclic oligosaccharides obtained from enzymatic deconstruction of starch, and were discovered by Villiers in 1891 [121]. Naturally occurring CD molecules can contain six (α -CD), seven (β -CD), and eight (γ -CD) (α -1,4)-linked α -D-glucopyranose units connected through -1,4- glycosidic linkages (**Figure 2.10a-c**) [122-124]. The structure of CDs resembles a hollow truncated cone with a hydrophilic exterior containing the hydroxyl groups and a hydrophobic interior composed of carbon backbones of glucopyranose units

[123, 125]. This specific truncated cone-like shape (**Figure 2.10d**) allows the CDs to include “guest” molecules in their cavities and enables them to act as “hosts” binding to the less polar or hydrophobic section of the guest molecules [124, 126, 127].

CDs can be used in a wide range of applications such as pharmacy (used as stabilizers and solubilizers of poorly water-soluble drugs for parenteral administration, nasal sprays and eye drops, or to decrease local drug irritation), food industry (used as flavor and odor stabilizer and to mask undesirable flavors and odors), cosmetics (stabilizers of chemically unstable compounds, to lengthen the action, decrease local irritation, and remove displeasing smells), gene delivery, cancer therapy, and chromatographic separations as well as selective adsorption [121, 123, 124, 128].

Among the three major CDs (α CD, β -CD and γ CD), β -CD has the optimum cavity size for many moderately sized molecules, is very facile to produce, and has a relevantly low price (with an annual production of ~10,000 tons and commodity price of ~5 USD per kg in 2007). β -CD comprises ~55% of the cyclodextrins used in marketed medicines followed by its derivative, hydroxypropyl- β -CD, in the second place (~16%) [123].

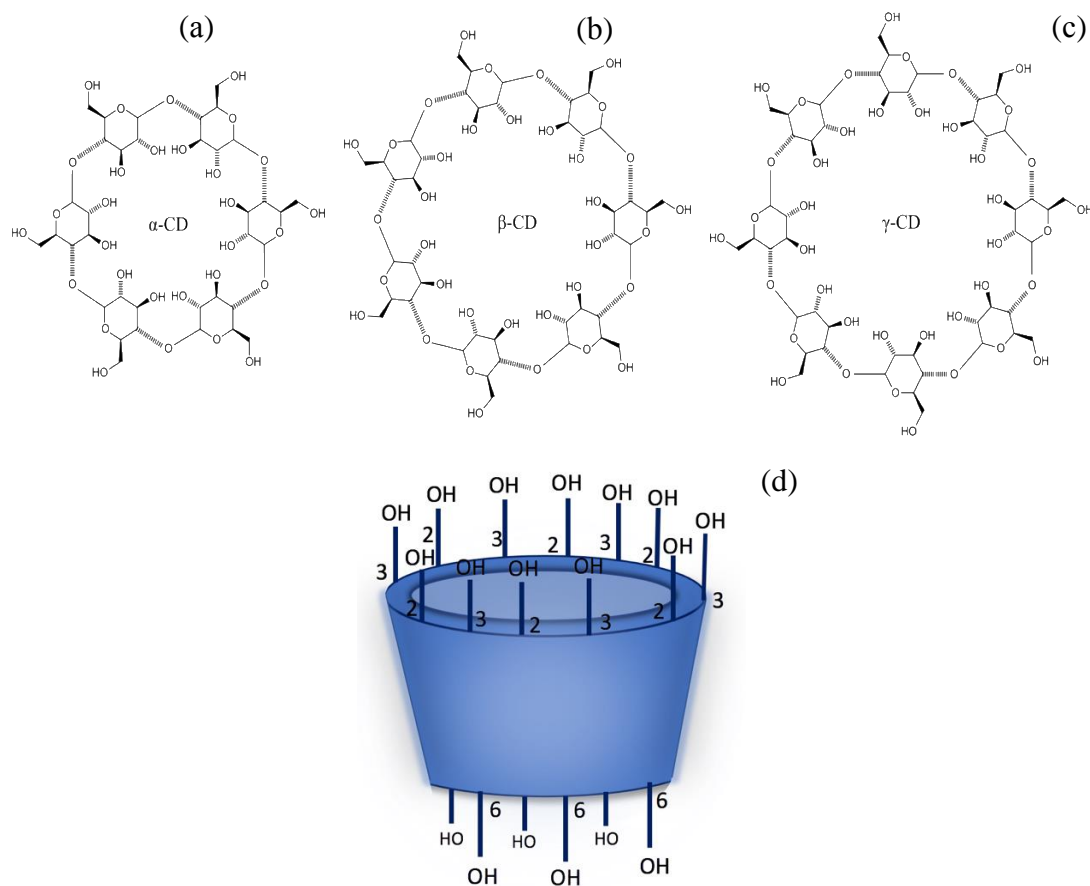


Figure 2.10 Chemical structures of a) α -CD, b) β -CD, c) γ -CD [adapted from Wikipedia], and d) Schematic of the 3D structure of a β -CD molecule.

2.3.1 Interactions of cyclodextrins with small molecules and formation of “host-guest” complexes

Inclusion complexes in a solution containing CDs (host) and other molecules (guest) form when water molecules placed inside the hydrophobic interior of the CD's cavity are substituted by a guest molecule. In the inclusion complex formation process, no covalent bonds are created or broken, and the guest and host molecules are in dynamic equilibrium with the complex [122]. On the other hand, the hydroxy groups on the exterior of the cyclodextrins can form hydrogen bonds with other molecules and create non-inclusion-based (exclusion) complexes [121, 122]. The prevalent type of cyclodextrin

complex stoichiometry is the 1:1 guest/CD in which one guest molecule (G) binds to one CD molecule (**Figure 2.11**):



the affinity constant (K1) can be expressed as:

$$K1 = \frac{[G.CD]}{[G].[CD]} \quad (2.7)$$

where [G], [CD], and [G.CD] represent the equilibrium concentration of the guest, the cyclodextrin, and the inclusion complex, respectively. The interaction of the guest and the CD molecule is stronger, and the complex is more stable, when K value is larger. The value of K1 is normally between 50 and 2000 M⁻¹ with an average of 490 M⁻¹ for β-CD [129]. The next common sequential guest/CD complex is the 1:2 G/CD complex which forms when an existing 1:1 G.CD complex and an additional cyclodextrin molecule bind together [129]:



the affinity constant (K2) can be expressed as:

$$K2 = \frac{[G.CD_2]}{[G.CD].[CD]} \quad (2.9)$$

where [G.CD], [CD], and [G.CD₂] represent the equilibrium concentration of the corresponding species.

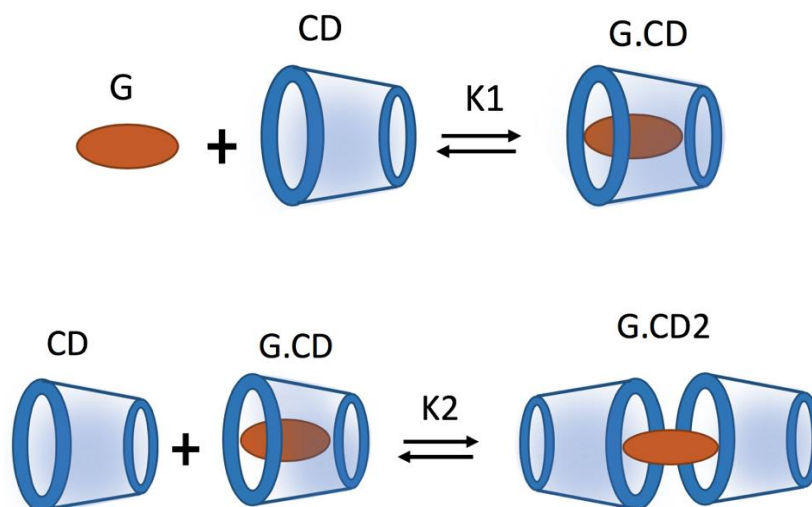


Figure 2.11 Schematic of the 1:1 and 1:2 complex formation of CDs with guest molecules

Measuring and analyzing the affinity constant (K), stoichiometry (N), and the thermodynamic parameters (inclusion enthalpy ΔH , inclusion entropy ΔS , and Gibbs free energy ΔG) of the interaction of CDs with guest molecules allows for determination of the kind of forces involved in the complex formation process [125]. Some of the important phenomena that play roles in complex formation are Van der Waals interactions, hydrophobic interactions, electrostatic (Coulombic) forces, charge-transfer interactions, the release of conformational strain, and hydrogen bonding [123, 125, 130]. Enthalpic and entropic contributions (which are frequently termed as driving factors) together compromise the Gibbs free energy ($\Delta G = \Delta H - T\Delta S$) [125]. The affinity constants (K) and thermodynamic parameters for the 1:1 complex formation resulted from interaction of β -CD with some example drugs and small molecules in aqueous solution are presented in **Table 2.1**. Inclusion complex formation of the CDs in aqueous solutions consist of the replacement and rearrangement of the water molecules (around 15-25 water molecules that initially filled the slightly apolar cavity of the CD) by a less polar hydrophobic guest

molecule which is able to create a more stable lower energy state [125, 131]. In order for the ΔG of the CD-guest interactions to be negative, usually a combination of multiple phenomena (hydrophobic interactions, electrostatic interactions, van der Waals forces, hydrogen bonding, dispersive interactions, and charge-transfer interaction) happen simultaneously [122, 132].

Table 2.1 Experimental affinity constant (K) and thermodynamic parameters (ΔH , ΔS , and ΔG) of 1:1 inclusion complexation of small guest molecules with β -CD in aqueous solutions at T=298 K

Guest molecule	Medium	Affinity constant, (K) M ⁻¹	ΔH kJ/mol	ΔG kJ/mol	T ΔS kJ/mol	ΔS J/K.mol	Driving factor	ref
Brompheniramine	water	1440 \pm 75	-15.48 \pm 0.21	-18.03	2.55	8.56	Enthalpy	[133]
Cyclopentolate	water	2040 \pm 120	-27.45 \pm 0.38	-18.87	8.58	28.79	Enthalpy	[133]
Scopolamine	water	1520 \pm 110	-4.35 \pm 0.50	-18.16 \pm 0.21	13.81	46.34	Entropy	[134]
Homatropine hydrobromide	water	1210 \pm 92	-1.63 \pm 0.17	-18.08 \pm 0.21	15.94	53.49	Entropy	[134]
Atropine sulfate	water	6060 \pm 190	-4.90 \pm 0.42	-21.59 \pm 0.17	16.69	56.00	Entropy	[134]
Paconol	water	3330	-3.35 \pm 0.49	-20.1	16.8	56.38	Entropy	[135]
Acetovanillone	water	937.7	-3.92 \pm 0.13	-17.0	13.1	43.96	Entropy	[135]
Ibuprofen	Phosphate buffer	9558 \pm 129	-13.92 \pm 0.05	-22.71	8.79	29.50	Enthalpy	[136]
2-naphthalene-sulfonate	water	234423	-29.33 \pm 0.25	-30.67	1.34	4.5	Entropy	[137]
(+)-usnic acid (UA)	Phosphate buffer	153 \pm 9	-19.76 \pm 0.91	-12.46	-7.28	-24.43	Enthalpy	[138]
2-Carboxybenzoyl-D-glutamic acid	Phosphate buffer	84 \pm 2	-11.2 \pm 0.1	-10.98 \pm 0.06	-0.22 \pm 0.15	-0.74 \pm 0.5	Enthalpy	[139]
3-Carboxybenzoyl-D-glutamic-L-tyrosine	Phosphate buffer	116 \pm 3	-14.8 \pm 0.2	-11.78 \pm 0.07	-3 \pm 0.2	-10.06 \pm 0.7	Enthalpy	[139]

For interaction of some hydrophobic compounds with CDs, a relationship between enthalpy and entropy (called enthalpy–entropy compensation) has been proposed, in which

an increase or decrease in ΔH is compensated by a similar increase or decrease in $T\Delta S$, such that the resultant change of ΔG is small [130, 139]. Thus, the entire CD/guest complexation thermodynamic mechanism may alter without the value of the Gibbs free energy being dramatically affected. Solvent restructuring, which is a driving force in complex formation, rearrangement of solvent molecules near solute surfaces, and the dehydration of hydrophobic surface in general are mentioned as the main reasons for the enthalpy–entropy compensation phenomena [122, 130, 140, 141]. While nearly complete compensation for hydrophobic surfaces has been observed, hydrophilic surfaces demonstrate a lesser extent of compensation [122, 130]. Enthalpy–entropy compensation is typically shown by a graph of $T\Delta S$ versus ΔH or vice versa. In either cases, the datapoints have to lie on a straight line with slope and intercept of α and $T\Delta S_0$ respectively [140]. The slope of the line (α) represents the contribution of enthalpy to the changes in ΔG , while the intercept ($T\Delta S_0$) denotes the stability of the inclusion complex when no enthalpic stabilization is present ($\Delta H=0$) [142]. Schönbeck et al. used a series of three host molecules (natural β -CD, randomly substituted (2-hydroxypropyl)- β -CD (HP093), and randomly substituted (2-hydroxypropyl)- β -CD (HP063)), and observed that for 1-adamantanol and 1-adamantanemethanol molecules, the complexes with those three CD hosts lie on almost straight lines with a slope around 0.67 which means that about 67% of the destabilizing effects caused by an escalation in ΔH is compensated by increased $T\Delta S$ [130].

2.3.2 Isothermal Titration Calorimetry (ITC)

A broad spectrum of methods (e.g. nuclear magnetic resonance, chromatography, phase solubility, molecular mechanics, affinity capillary electrophoresis, fluorescence, potentiometric titration, spectroscopy, and calorimetry) has been utilized to measure the

affinity constants (K) and the thermodynamic parameters (ΔH , ΔS , and ΔG) of the binding of the CDs with the guest molecules, among which Isothermal Titration Calorimetry (ITC) stands out due to its high sensitivity (measuring affinity constants as low as 10 M^{-1} and as high as 10^7 M^{-1}) as well as the ability to provide a comprehensive thermodynamic description of the inclusion process and simultaneous measurement of the binding parameters (K , ΔH , ΔG , ΔS , and n) in a single experiment [125, 136, 143, 144].

As seen in **Figure 2.12**, the ITC instrument consists of two identical cells in an adiabatic jacket, the sample cell and the reference cell, with both kept at a constant temperature. The reference cell is usually filled with water or the buffer used in the experiment, and works only as a temperature reference. One of the reactants is placed in the sample cell, and the other one in the injection syringe. Throughout the experiment, the syringe injects the titrant reactant (usually termed as a ligand) into the sample cell sequentially and stirs the solution in the sample cell simultaneously to ensure maximum interaction. After every injection, the binding reaction between the ligand and the sample inside the cell (the receptor) occurs, and the ligand/receptor complex is formed, which results in the release or absorption of a certain amount of heat, leading to a temperature difference between the reference cell and the sample cell. The instrument measures the amount of power needed to keep the temperature of the two cells at the same level (temperature difference being close to zero) and restores the temperature balance.

The heat signals are recorded in form of peaks as illustrated in **Figure 2.13a** for interaction of ibuprofen with β -CD, for example. Integrating the area under the peaks after subtracting the heat of the dilution (**Figure 2.13b**) which is the heat generated or taken up when the ligand is injected into the solvent only, determines the amount of heat related to

each injection. The areas under each peak should be then normalized per mole of ligand titrated in every injection, and be plotted versus the molar ratio of the ligand to that of the receptor in the sample cell as demonstrated in **Figure 2.13c**. The integrated heat profile is referred to as an isotherm. Finally, a suitable model should be selected to fit the isotherm which allows for determining the thermodynamic parameters of the binding including affinity constant (K), stoichiometry (N), and the thermodynamic parameters (ΔH , ΔS , and ΔG) [125, 143]. Thermodynamic parameters of binding (association/dissociation constant (K_a/K_d), stoichiometry (N), and enthalpy change (ΔH)) are directly determined by non-linear least squares error fitting [144, 145], while ΔG and ΔS are calculated through thermodynamic relations presented in **Equations 2.10** and **2.11**:

$$\Delta G = -RT \times \ln(K_a) \quad (2.10)$$

$$\Delta G = \Delta H - T\Delta S \quad (2.11)$$

where T is the isothermal temperature of the experiments and R is the gas constant (8.314 J/K.mol).

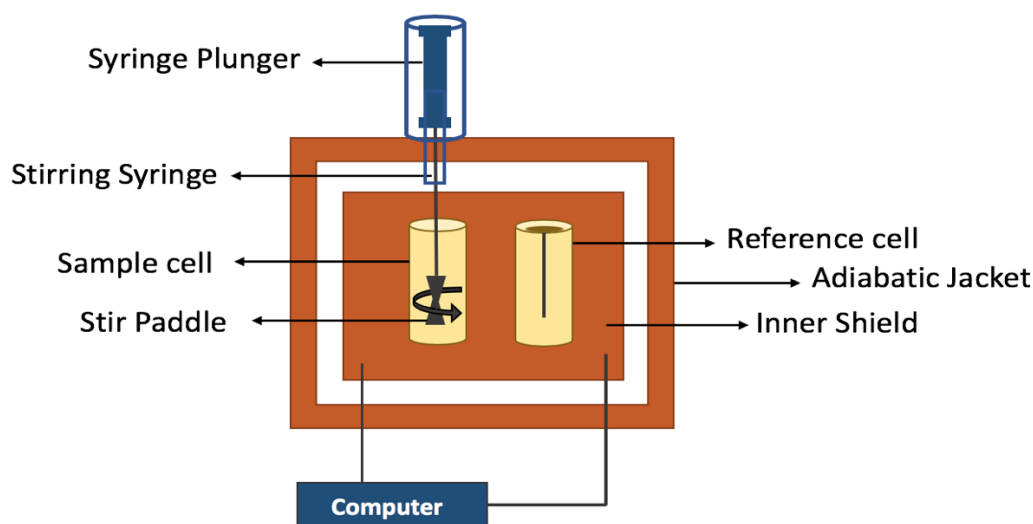


Figure 2.12 Schematic of an Isothermal titration calorimeter (ITC)

The models that are usually used to describe guest-CD interactions are either a one-site or two-site binding models. In the one-site independent binding model, also known as the Wiseman Isotherm, a Langmuir type equilibrium is considered between a ligand and receptor with single set of identical binding sites [144].

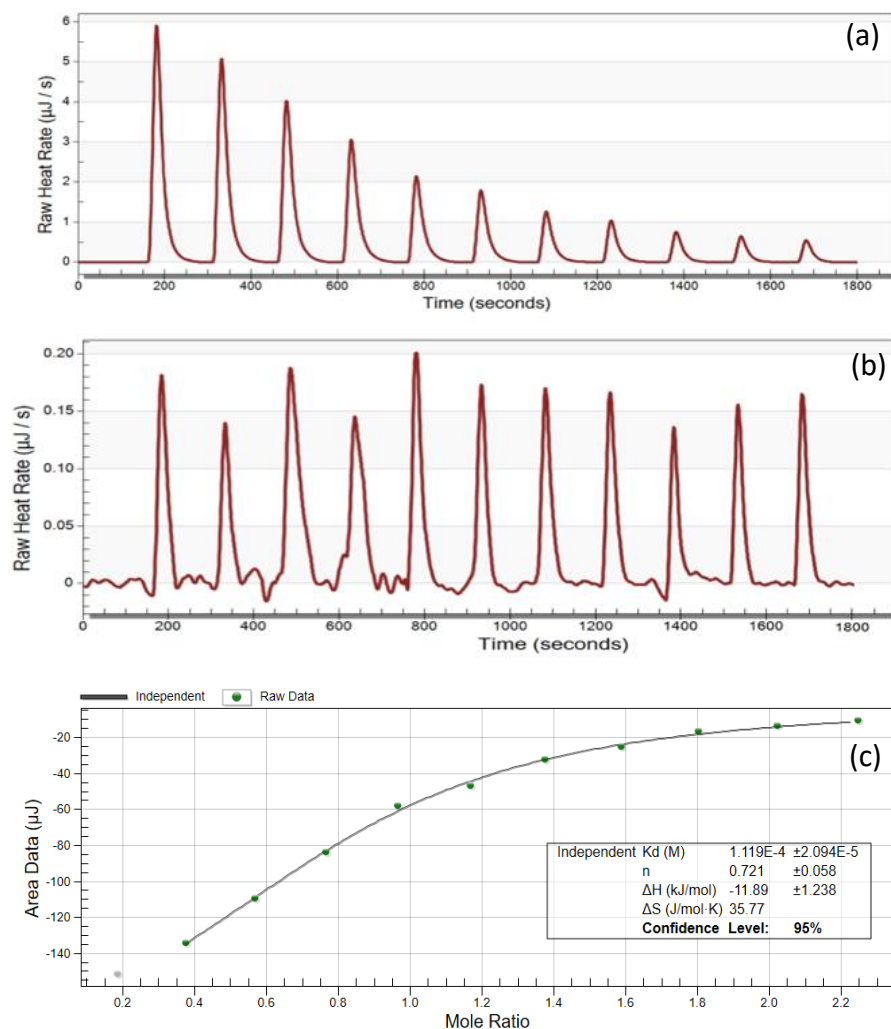


Figure 2.13 Typical ITC data obtained for the binding interaction of ibuprofen (0.5 mM) to β -CD (5 mM) in PBS at $T=298$ K, (a) exothermic heat releases upon injection of $3.7 \mu\text{L}$ aliquots of β -CD into ibuprofen solution versus time, (b) heat of dilution of β -CD (5 mM) in PBS, (c) integrated heat profile after subtraction of dilution heat plotted against molar ratio of β -CD and ibuprofen.

Bertaut et al. compared the efficiency of conventional and non-conventional ITC protocols to study 1:1 β -CD inclusion complexes using ibuprofen as the model guest molecule. In their work, 8 protocols were studied: classic titration protocol, reverse titration protocol, release protocol, dilution protocol, attenuated titration protocol, attenuated reverse titration protocol, annihilated release protocol, and annihilated dilution protocol

[136]. The details of the protocols and observed results have been summarized in **Table 2.2**. Bertaut et al. concluded that despite the pervasiveness of the classic titration protocol (where ibuprofen is injected is injected into β -CD in the cell) in ITC studies on cyclodextrin complexes, non-conventional protocols, particularly the release protocol (where a mixture of β -CD and ibuprofen is injected into the blank buffer in the cell) and/or a combination of both release and classic titration protocols can increase the accuracy and efficiency of the experiment. In the case of guest molecules with small affinity towards cyclodextrins, coupling of experiments such as reverse titration (where β -CD is injected into ibuprofen in the cell) and annihilated release (where a mixture of β -CD and ibuprofen is injected into ibuprofen in the cell) has been shown to enhance the thermodynamic characterization [136]. The classical titration protocol and the single site binding model are used in **Chapter 6** for the analysis of thermodynamic interactions between β -CD and lignin dimers.

Table 2.2 Details and observed results of conventional and non-conventional titration protocols used in ITC studies on β -cyclodextrin complexes described by Bertaut et al. [136].

Protocol	Classic titration	Reverse titration	Release	Dilution	Attenuated titration	Attenuated reverse titration	Annihilated release	Annihilated dilution
Syringe content	β -CD	Ibuprofen	β -CD + Ibuprofen	Buffer	β -CD	β -CD + Ibuprofen	β -CD + Ibuprofen	Ibuprofen
Cell content	Ibuprofen	β -CD	Buffer	β -CD + Ibuprofen	β -CD + Ibuprofen	β -CD	Ibuprofen	β -CD + Ibuprofen
Isotherm description	Exothermic/ diminishing	Exothermic/ flat	Endothermic/ diminishing	Endothermic/ flat	Exothermic/ diminishing	Exothermic/ flat	Zero/flat	Zero/flat
Observed results	Formation of inclusion compounds, release of heat	Release of small and constant heat	Consumption of heat, partial dissociation of the complex in the cell	Small and equal endothermic peaks, partial dissociation of inclusion compounds	Exothermic peaks, release of attenuated heat, increase in concentration of inclusion compounds	Exothermic peaks, release of attenuated heat, increase in concentration of inclusion compounds	No heat generated or consumed, no formation or dissociation of components was observed	No heat generated or consumed, no formation or dissociation of components was observed

2.3.3 Cyclodextrin-based surfaces and materials

CDs are promising candidates for delivery, detection, selective adsorption, or chromatographic separations of hydrophobic guest molecules (including lignin oligomers) owing to their host-guest inclusion complex formation properties. The growing interest in polymer-CD interactions has created a platform for designing CD-based drug delivery systems such as nanoparticles and hydrogels [125]. Early applications of CD-functionalized materials focused on chromatographic separations and selective adsorption based on the hydrophobic and tunable inner surface of CDs. More recent work with CD-based materials focused on drug delivery of hydrophobic drugs and gating systems based on CDs [146-148]. One way to take advantage of CD's unique properties is to immobilize them onto stationary phases and solid materials. Immobilized CDs have several advantages over homogeneous free CD dispersions such as: 1) the supported guest molecules trapped inside the CD cavities are less likely to react with radical species in the reaction media, 2) the inclusion complexes can be extracted from the guest reaction mixture and be put with an appropriate solvent for further separation, and 3) immobilized CD molecules can be reutilized. There are some methods available for immobilization of the CDs and fabrication of CD-based solid materials for separation and delivery. One of these methods includes surface-functionalization of substrates and porous as well as nonporous nanomaterials with CDs (**Figure 2.14a-b**). Chen et al. [149], and Xavier et al. [150] fabricated β -CD-coated silver nanoparticles and used those for probing and entrapment of phenol and aromatic compounds (e.g. resorcinol, hydroquinone, and pyrocatechin) as well as toxic melamine, respectively. Additionally, hybrid iron oxide mesoporous silica nanoparticles modified

with β -CD have been used as catalysts for conversion of benzyl alcohol to benzaldehyde, and also for adsorption of bisphenol A from polluted water [151].

Another commonly used method is incorporation of CDs in polymers by conjugating the CDs through chemical cross-linkers to the polymer chains (**Figure 2.14c**) [152]. β -CD-ionic liquid polymer (CD-ILP) was manufactured by reacting β -CD with 1-benzylimidazole (BIM) to make β CD-BIMOTs and polymerizing it via toluene diisocyanate (TDI) linker to form insoluble CD-ILP (β -CD-BIMOTs-TDI). Both the β -CD-BIMOTs-TDI polymer and native β -CD polymer (β CD-TDI) demonstrated promising uptake and removal capacity towards phenols and arsenate [153]. CD-based nanosponges which are nanostructured cross-linked polymers, typically acquired by having CDs reacting with a cross-linker, benefit from properties of both polymers (e.g. large molecular weight) and those of the CDs (molecular solubility and stabilization, increasing loading capacity, providing controlled and prolonged release, decreasing the toxicity of the cross-linker, etc.) [154, 155]. These CD-based nanosponges have been widely used in drug delivery to solubilize and stabilize the pharmaceutical compounds such as anti-diabetes repaglinide [155], anti-cancer curcumin [156], and anti-inflammatory meloxicam [157]. Furthermore, grafting hydrogels with CDs fortifies the properties of the hydrogels and protects and regulates the delivery of bioactive compounds, thus improves the hydrogels' functionality as biomedical implants material, wound dressing material, and drug carriers [158].

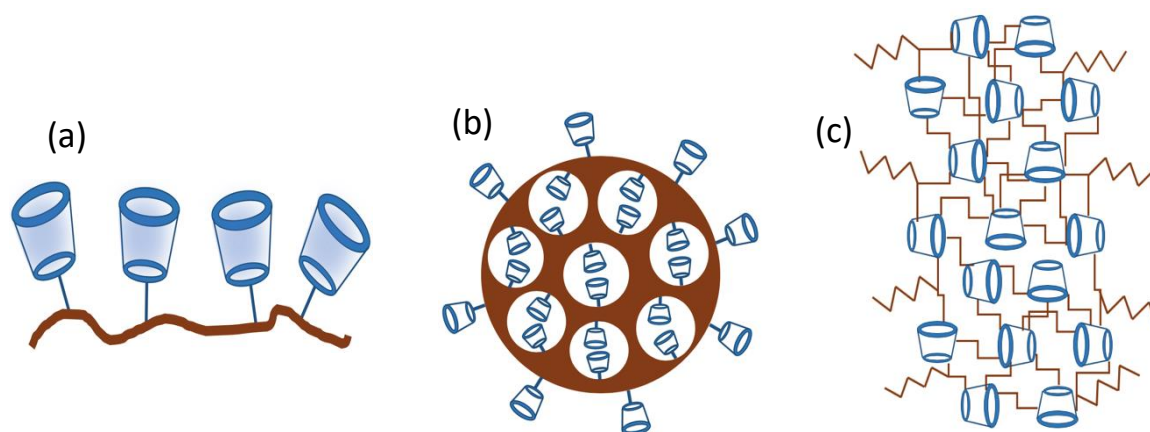


Figure 2.14 Schematic representations of different cyclodextrin-functionalized structures: (a) CD- coated substrates, (b) CD-coated porous particles, and (c) CD-based polymer matrices. Adapted from Bibby et al [152].

After the porous silica materials were developed, many studies focused on sensing, separation and catalytic applications of CDs supported on porous silica [152, 159-161]. Porous silica is non-toxic, cost-effective, has high specific surface area (up to $\sim 1000 \text{ m}^2/\text{g}$), controlled pore geometry, tunable pore size, and vast possibilities of functionalization via the reaction of terminal silanol groups with silane compounds [162-165]. All of these properties make porous silica supports promising candidates for immobilizing CDs. There are two approaches to develop CD-functionalized silica material with first one involving the coating and grafting reactions and the second one including sol–gel or self-assembly processes. Functionalizing the external surface of silica with CD facilitates enhanced access to the binding sites [165]. However, the drawback of this method is the inconsistent and irregular dispersal of CD molecules on the surface. Additionally, CD-coated silica materials obtained via this approach have limited cyclodextrin loading which can negatively affect the adsorption capacities [165]. In the second method, the CD moieties

are confined within the framework of nanoporous silicas. These materials possess both high cyclodextrin group loadings and robust structures [152, 165].

CHAPTER 3. THE EFFECTS OF LIGNIN DIMERS ON THE GEL-TO-FLUID PHASE TRANSITION IN DPPC BILAYERS

3.1 Summary

High resolution differential scanning calorimetry (DSC) was used to investigate the effect of three lignin dimers on the gel to fluid phase transition in DPPC lipid bilayers. The goal of this research is to begin to understand the partitioning of model lignin dimers into lipid bilayers and its effects on the gel to fluid transition temperature (T_m). The long-term objective is to establish structure–function relationships for well-defined lignin derivatives at biologically relevant surfaces. This work uses a newly synthesized guaiacylglycerol guaiacol ester with a hydroxypropenyl (HOC_3H_4-) group resembling natural lignin (GG dimer), compared with a truncated GG dimer without the HOC_3H_4- and benzyl-modified GG dimers. The DSC results show that the dimer most like natural lignin (with a hydroxypropenyl tail) has $\log K = 2.72 \pm 0.05$ and has little effect on the T_m value. In contrast, the truncated dimer, which has been used as a representative GG dimer in prior studies, partitions into the bilayer and shifts T_m because of its increased lipophilicity (DSC $\log K = 3.45 \pm 0.20$). Similarly, modification of the natural GG dimer by benzylation of the phenol makes it lipophilic (DSC $\log K = 3.38 \pm 0.28$), causing it to partition into the bilayer, as seen in shifts in T_m . The success at predicting the structural effects of lignin dimers on lipid bilayers advances the applications of lignin small molecules for the design and selection of alternative lignin small-molecule derivatives based on their ability to penetrate cell membranes.

3.2 Introduction

Lignin is one of the most abundant biopolymers in nature and is found mostly in cell walls of plants. It is a polymer composed of the aromatic monomers (so-called monolignols) p-coumaryl alcohol, coniferyl alcohol, and sinapyl alcohol that bind to each other via radical coupling and form a complex, heterogeneous structure. In plants, lignin plays important roles in structuring cell walls and preventing water penetration through the xylem. It has also been documented to have important roles in plant and tree defense against microbial attack [105]. Because it is naturally biodegradable, biocompatible, and has good stability and low toxicity, lignin derivatives are under investigation for multiple pharmacological and biomedical applications [166]. It has also been proven that lignin and its derivatives (a.k.a. “lignins”) have antioxidant and antibacterial properties and they have already been used for the treatment of various diseases including diabetes, HIV, and cancer [166, 167]. The use of lignin nanoparticles (LNPs) in drug delivery has been reported in many studies [39, 168]. Besides benefits to human health, purified lignin and specific lignins have the potential to improve livestock intestine morphology and to control pathogens [169]. In many of these applications, the effects of lignins could be explained by the antioxidant capacity conferred by the phenolic character of its constituents [170]. It has been documented that low-molecular-weight oligomers derived from guaiacyl units are central to the antioxidant properties of lignin [171]. Often, in these applications, lignin absorbs into or binds to cell membranes or to membrane embedded molecular structures, such as proteins. For this reason, the investigation of the interaction of lignins with cell membranes is of critical importance.

Cell membranes are primarily comprised of lipids. In the physiological state, lipid

bilayers are in their fluid state and this fluidity is pivotal to cell functions. The gel-fluid transition temperature (T_m) of lipid bilayers is the temperature where the lipids change from a gel phase where they are tightly packed in ordered domains to a more loosely packed fluid phase. Interactions between compounds such as drugs and lipid bilayers can affect their structure and permeability, and therefore T_m . Conversely, important changes in lipid and bilayer dynamics occur near the transition. For example, it was reported that the protein-mediated exchange of lipids between vesicles was greatly increased near the transition temperature [172]. Lipid transfer processes are essential to biological function.

Additive-induced changes in T_m depend on both the molecular structure and concentration of the additives as well as the identity of the lipids since these factors determine the location and concentration of the additives in the bilayer. This is supported by multiple experimental investigations. Mahendra examined the effect of a variety of small molecules including alkanols, fatty acids, detergents, and ionophores on dipalmitoyl lecithin bilayer phase behavior [106]. The plant-derived flavonoids quercetin, hesperetin, and naringenin were reported to lower T_m of 1,2-dipalmitoyl-sn-glycero-3-phosphocholine (DPPC) liposomes, while rutin (also a flavonoid) did not [173]. Prenyl-modified isoflavones had a more noticeable effect on T_m of DPPC than non-prenylated ones [174]. T_m was reduced by more than 10 K with broader transition peaks when adding a high concentration (20%) of isoflavone. Ojogun et al. investigated the partitioning and phase behavior of a series of nicotinic acid esters (nicotines) between aqueous solution and DPPC membrane bilayers [93]. High concentrations of nicotines increased the main phase transition temperature and decreased the membrane partition coefficient. Zhao et al. investigated the effects of cholesterol and paclitaxel on the phase behavior of DPPC

liposomes, finding that both fluidize the bilayer [175]. Given that some lignin derivatives have polyphenolic drug-like structures, it is of interest to investigate their partitioning into lipid bilayers through effects on T_m .

There is little existing work related to the interaction of lignin dimers and derivatives with lipid bilayers, and we are not aware of any study of their effect on the gel-fluid transition temperature. The transport of lignin monomers across the plant cell membrane has been studied and seems to involve ATP-binding cassette transporters [176-179]. Boija and Johansson studied the partitioning of monolignol and dilignol model substances in liposomes using immobilized liposome chromatography and concluded that passive diffusion of some lignin precursors may be possible [105]. None of the compounds they considered are the same as those we consider here. Here we studied the interaction of three derivatives of β -O-4' linked dimers of coniferyl alcohol (GG) with DPPC bilayers with the aim of developing a molecular-level understanding of how these molecules affect the gel-fluid phase behavior of the bilayers. The derivatives considered are shown in **Figure 3.1** and are the unmodified dimer, a truncated analogue, and a benzyl modified dimer. We investigated the interaction of these molecules with liposomes of DPPC using high resolution differential scanning calorimetry (DSC). The DSC instrument incrementally changes the temperature of a sample and measures the heat flow. DSC allows phase transition temperatures to be identified easily by a peak in the heat flow and we applied it to identify the transition temperature of liposomes between gel and fluid phases [80]. Results from this study were confirmed by Molecular dynamics (MD) simulation performed in Dr. Moldovan's lab at Louisiana State University, and a collaborative manuscript on this study was published in *The Journal of Physical Chemistry B* (Tong et al.,

J. Phys. Chem. B 129, 8247-8260 (2019) [11]) and reproduced here with permission from the American Chemical Society. MD simulation is a useful tool to gain information at the microscopic level and has contributed to understanding lipid bilayer phase behavior. Gel–fluid transition temperatures calculated from MD simulations showed the same trend as DSC results, and the simulations also helped to explain how the lipids were affected by the lignin dimers.

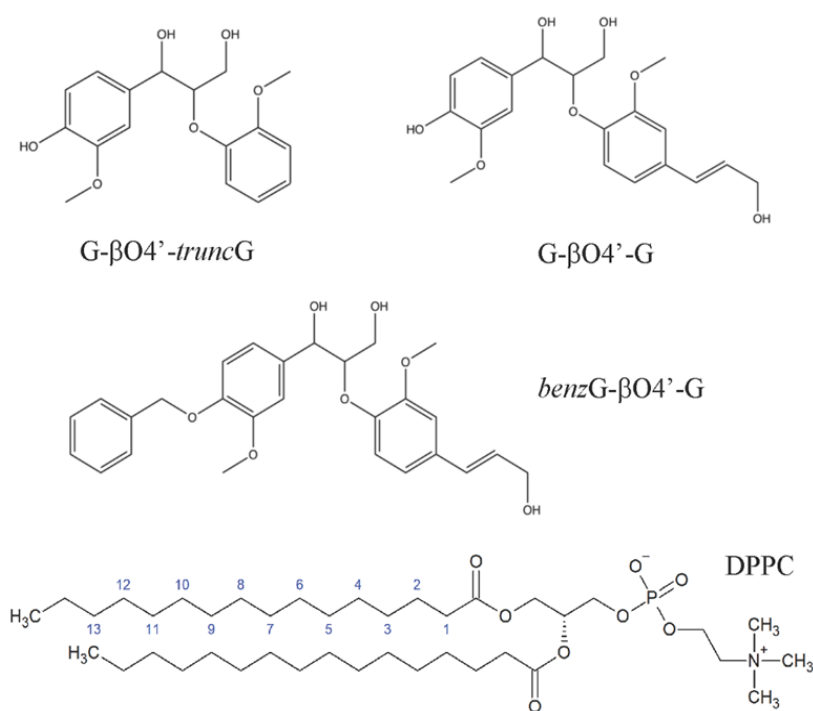


Figure 3.1 Chemical structures of the three β O4-linked lignin dimers and the lipid DPPC.

3.3 Materials and Methods

3.3.1 Chemicals and Reagents

Isopropanol (99%), chloroform (99.8%), and deionized water (ASTM type II) were purchased from VWR International; phosphate-buffered saline (PBS) from Sigma Aldrich; 1,2-dipalmitoyl-sn-glycero-3-phosphocholine (DPPC) from Avanti Polar Lipids (Alabaster, USA); and guaiacylglycerol- β -guaiacyl ether which is referred to as G- β O4'-*trunc*G dimer ($\geq 97\%$) from TCI America. All chemicals were used as received without further purification.

3.3.2 G- β O4'-G and *benz*G- β O4'-G Lignin Dimers Synthesis

The structures of the three lignin dimers used in the study are summarized in **Figure 3.1**. The G- β O4'-G and *benz*G- β O4'-G lignin dimers were synthesized by Dr. Lynn's group at University of Kentucky. The synthesis of 1-(4-hydroxy-3-methoxyphenyl)-2-[2-methoxy-4-(3-hydroxyprop-1-en-1-yl)phenoxy]propane-1,3-diol, which is abbreviated as G- β O4'-G dimer is described by Asare et al. [29]. This dimer has the same β -O-4' linked units in the core as the commercially available G- β O4'-*trunc*G dimer (guaiacylglycerol- β -guaiacyl ether), but with a 3-hydroxyprop-1-enyl tail. The synthesis of benzyl-modified GG dimer; 1-(4-benzyloxy-3-methoxyphenyl)-2-[2-methoxy-4-(3-hydroxyprop-1-en-1-yl)phenoxy]propane-1,3-diol (*benz*G- β O4'-G), is described by Tong et al. and proceeded with a small modification of the G- β O4'-G synthesis method such that the phenol group in the A ring of vanillin was protected with a benzyl group instead of the triisopropylsilyl group that was used for G- β O4'-G [11].

3.3.3 Differential Scanning Calorimetry

To perform DSC experiments, DPPC liposomes in solution were made with varying amounts of lignin GG dimers following the traditional thin-film method described elsewhere [93, 175]. Initially, GG dimers were mixed with 10 mg of DPPC to obtain mixtures of DPPC/dimer with dimer mole fraction ranging from 0 up to 0.40. Then, each one of the mixtures were dissolved in 1 mL of chloroform separately. The chloroform was then evaporated using a nitrogen gas stream to form lipid films in the bottom of the vials. To ensure that the chloroform evaporated completely, the vials were placed inside a vacuum chamber overnight. In the next step, lipids were rehydrated by addition of 1 mL of PBS buffer, making them rearrange into bilayers. Next, the bilayers were agitated and detached from the vial surfaces to form liposomes. Finally, the liposomes were extruded sequentially through a 200 nm polycarbonate membrane at a temperature above the gel-fluid transition temperature of the lipid ($T_m = 315.3 \pm 0.15$ K) to make unilamellar liposomes of uniform size. Extrusion using membranes with 200 nm pore size yields homogeneous liposomes with an average diameter of ~260 nm in the final suspension [180, 181]. This protocol was conducted for making DPPC/G- β O4'-*trunc*G, DPPC/G- β O4'-G, and DPPC/*benz*G- β O4'-G mixtures in all of which various amounts of the lignin dimers were added to 10 mg of DPPC in 1 mL of PBS. 500 μ L of the DPPC/dimer solutions were weighed into 1 mL ampoules of a multi-cell differential scanning microcalorimeter (MC-DSC, TA Instruments, New Castle, DE), and the ampoules were placed inside the machine. Samples were first heated to 328 K, then cooled to 283 K and finally reheated from 283 K to 328 K at 1 K/min. The main phase transition temperature of the samples was determined using *Nano-Analyzer* software.

3.3.4 Partition Coefficient from DSC

The partition coefficient of the dimers between the DPPC liposomes and aqueous solution (K) is related to the shift in transition temperature relative to pure DPPC liposomes. For low concentrations, K was estimated using **Equation 3.1** as shown below:

$$-\Delta T_m = \left\{ \frac{R \cdot T_m^2}{\Delta H_{DPPC}} * \frac{K}{55.5 + C_{DPPC} \cdot K} \right\} C_s \quad . \quad (3.1)$$

Equation 3.1 assumes that at equilibrium, the depression in the main phase transition temperature is directly proportional to the amount of the dimer that partitions into the lipid bilayer [93]. In this equation, ΔT_m is the difference between the transition temperature of the sample and pure DPPC liposomes, T_m is the transition temperature of pure liposomes, R is the ideal gas constant, ΔH_{DPPC} is the phase transition enthalpy (31.4 kJ/mol), C_{DPPC} is the concentration of DPPC in PBS (0.0136 M), and C_s is the concentration of the dimers in PBS (M) [94]. Solvent (PBS) is assumed to have the molar concentration of water (55.5 M). To solve for the partition coefficient, the entire constant in brackets was found using linear regression in the limit of low C_s . The partition coefficient values are reported as $\log(K)$.

3.4 Results and Discussion

3.4.1 DSC Measurements of Transition Temperature

Differential scanning calorimetry (DSC) is a robust screening tool to study the lipid phase transitions as well as lipid-drug interactions, and is frequently used to identify the change in the thermodynamic lipid phase transition as a function of the concentration of

components incorporated in the lipid bilayer [182]. Internalization of a solute in the lipid bilayer leads to a change in phase transition temperature (T_m) of the lipid bilayer [183, 184]. The main phase transition temperature (T_m) of the lipid is a temperature at which the lipid membrane changes from a highly ordered 2D crystal-like gel state to a fluid-like state, and the pre-transition temperature (T_p) is a temperature in which a flat membrane in the gel phase changes into a rippled bilayer [91]. The DSC instrument allows phase transition temperatures to be identified easily by a peak in the heat flow and, therefore, was applied to identify the gel-fluid transition temperature of liposomes in samples with and without lignin dimers [80].

Figure 3.2 shows the DSC results measured for lignin dimer/liposome systems in PBS buffer (pH 7.4) on the second heating scan, after first heating from room temperature, cooling to 283K, and heating again. The transition temperatures are consistent with the first heating scan (not shown), indicating that no significant artifacts of liposome preparation affected the results. The pure DPPC melting temperature (T_m) is indicated by a prominent endothermic peak at 315.5 ± 0.15 K, and the pure lipid also exhibits a pre-transition at $T_p=310.8$ K [93]. When a component incorporates into the lipid bilayer, a characteristic shift in the location of the endothermic peak related to the T_m happens, the magnitude of which depends on the concentration of the added component and strength of its interaction with the membrane [183, 184]. The peaks in the heating thermograms for G- β O4'-G in **Figure 3.2a**, show that by increasing its mole fraction in the bilayer from $X_{\text{dimer}} = 0$ to $X_{\text{dimer}} = 0.33$, the main phase transition temperature is decreased from 315.5 K to 314.7 K. In contrast, the results for DPPC/G- β O4'-*trunc*G (**Figure 3.2b**) show more significant shifts in T_m ; as the dimer concentration increases from $X_{\text{dimer}} = 0$ to $X_{\text{dimer}} =$

0.36, T_m is decreased from 315.5 K to 313.4 K. In the case of *benzG*- β O4'-G, the peaks in the heating thermographs (**Figure 3.2c**) also show a large effect on the gel-to-fluid phase transition; as dimer concentration increases from $X_{\text{dimer}} = 0$ to $X_{\text{dimer}} = 0.4$, T_m is decreased from 315.5 K to 311.5 K.

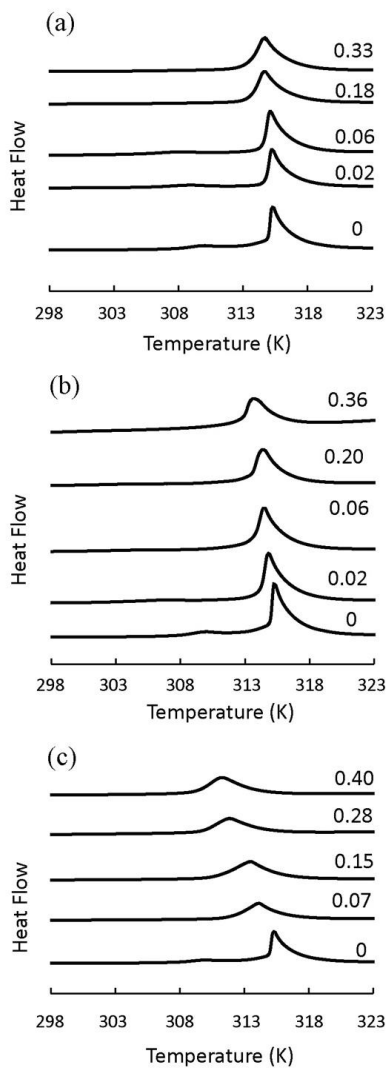


Figure 3.2 DSC heating scans for mixtures of DPPC with (a) G- β O4'-G, (b) G- β O4'-*truncG*, (c) *benzG*- β O4'-G. The mole fraction of the dimers is indicated beside each scan.

At higher concentrations of the dimers, the depressions calculated from **Table 3.1** deviate from a linear trend with C_s [94]. This is most likely caused by interactions among dimers that can cause clustering and significant perturbations of the gel phase. In contrast, there are negligible solute-based variations of the phases and solute–solute interactions in dilute solutions [185]. Therefore, we limited our measurements to the low concentrations of dimer where a linear relationship between ΔT_m and C_s was observed. The melting temperature of the DPPC/dimer samples for all three lignin GG dimers are included in **Table 3.1**. The results in this table clearly demonstrate that the presence of the G- β O4'-*trunc*G and *benz*G- β O4'-G dimers decreased T_m to a significant extent, while G- β O4'-G had only a slight effect. This suggests that G- β O4'-*trunc*G and *benz*G- β O4'-G partition into the interior hydrocarbon layer of the lipid bilayer to disrupt the order of the gel phase.

Table 3.1 DSC liquid crystalline to gel transition temperature in DPPC in the presence of lignin GG dimers.

G- β O4'-G		G- β O4'- <i>trunc</i> G		<i>benz</i> G- β O4'-G	
X_{dimer}	T_m (K)	X_{dimer}	T_m (K)	X_{dimer}	T_m (K)
0	315.5	0	315.5	0	315.5
0.02	315.4	0.02	315.2	0.07	314.3
0.06	315.3	0.06	314.7	0.15	313.6
0.18	314.8	0.20	314.5	0.28	312.0
0.33	314.7	0.36	313.4	0.40	311.5

The partitioning of components into lipid bilayers and biological membranes is the foundation for drug uptake and passive transport into membranes and plays an important role in the molecular process of drug action [186]. Previously, the partition coefficients of

some natural bioactive phenolic compounds in DPPC bilayers were measured [187]. Some of these plant-derived compounds which are known to have antimicrobial and therapeutic properties (such as eugenol, thymol, and carvacrol) have similar structures to lignin monomers [188-190]. Reiner et al. determined the partition coefficients of eugenol, thymol, carvacrol, propofol, and chlorothymol in DPPC membrane to be $\log(K) = 1.89, 2.64, 2.48, 3.06$ and 3.54 respectively [187]. Here, the membrane partition coefficients of the lignin dimers are determined from **Equation 3.1** using linear regression of T_m versus dimer concentration C_s in the limit of small C_s , as shown in **Figure 3.3**.

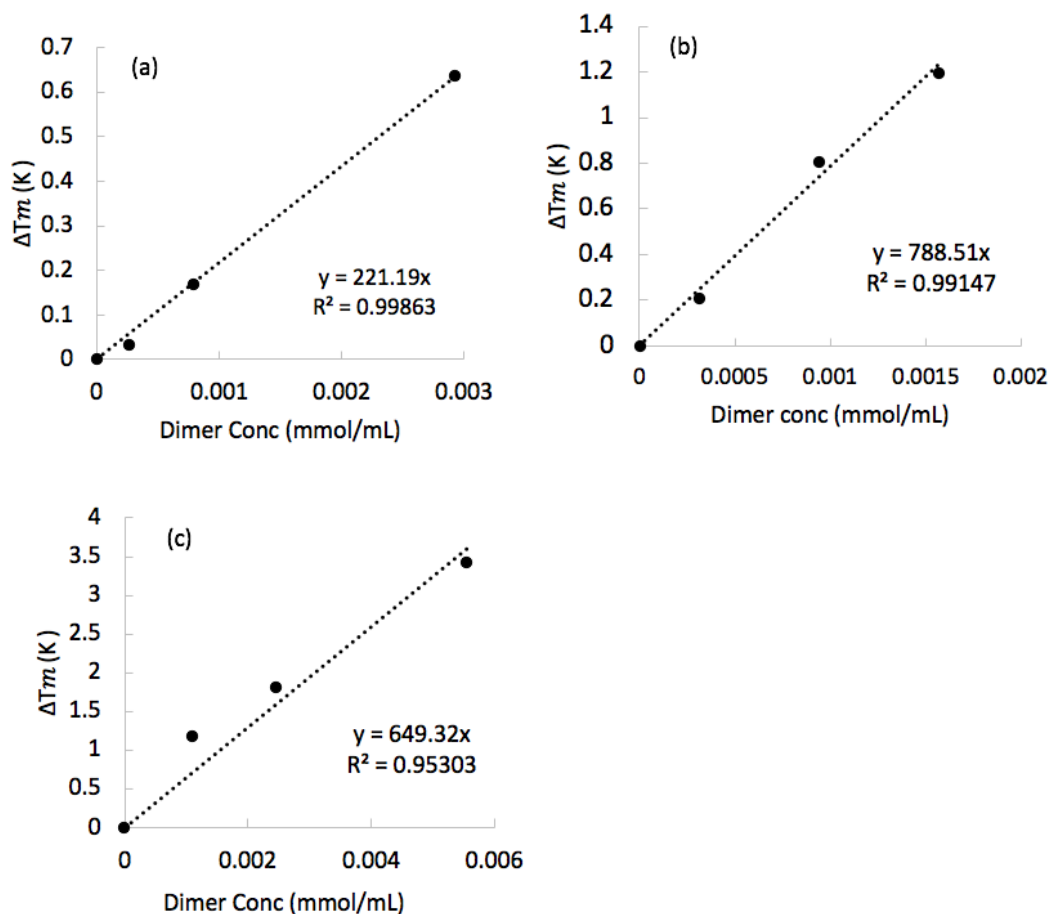


Figure 3.3 Linear regression of changes in main phase transition temperature (ΔT_m) of the DPPC/dimer samples vs. dimer concentration, C_s . (a) G- β O4'-G (b) G- β O4'-truncG (c) benzG- β O4'-G.

As shown in **Figure 3.3**, ΔT increases linearly with increasing dimer concentration within the measured concentration range, and the slope increases with increasing hydrophobicity of the dimers. The results for the partition coefficients of all three lignin GG dimers from DSC and MD are included in **Table 3.2**. Consistent with the slopes in **Figure 3.3**, $\log(K)$ from both DSC and MD is less for G- β O4'-G than for the G- β O4'-*trunc*G and for the *benz*G- β O4'-G dimers (**Table 3.2**). This is consistent with the hydrophilic-lipophilic balance (HLB) of the dimers, which is calculated using the Davies group contribution method to be 8.5 for G- β O4'-*trunc*G, 9.0 for G- β O4'-G, and 5.1 for *benz*G- β O4'-G [191]. This corresponds to water dispersible character for the first two compounds but a high degree of lipophilicity for the latter.

The overall result of this calorimetry study supports the idea that partitioning into the lipid bilayer correlates with hydrophobicity/lipophilicity of the dimers [192]. The dimer most resembling natural lignin, G- β O4'-G, may associate with the bilayer but its hydrophilic nature does not cause bilayer penetration. The commercially available truncated dimer, while it does contain a β -O-4 linker, is more hydrophobic and therefore has the ability to penetrate and disrupt the gel phase of DPPC bilayers. The benzyl derivative shows that it is possible to chemically alter naturally derived lignin compounds such that they are able to penetrate into lipid bilayers as well.

Table 3.2 Log(K) from DSC and MD.

Dimer	G- β O4'-G	G- β O4'- <i>trunc</i> G	<i>benz</i> G- β O4'-G
Experiment (DSC)	2.72 ± 0.05	3.45 ± 0.20	3.38 ± 0.28
Simulation (MD)	-1.42 ± 0.13	3.83 ± 0.29	5.21 ± 0.21

3.5 Conclusion

Interactions between DPPC lipid bilayers and coniferyl alcohol-based lignin GG dimers and their derivatives were studied using differential scanning calorimetry (DSC). Specifically, the systems studied consist of fully hydrated DPPC liposomes in the presence of different concentrations of lignin dimers. Experimental liposome-water partition coefficients for the lignin dimers were obtained through a relationship between the shift in the gel-fluid transition temperature relative to pure DPPC liposomes obtained from DSC measurement. A commercially available truncated G-G dimer with the hydroxyproenyl tail removed, G- β O4'-*trunc*G, and G-G dimers with an added benzyl group, *benz*G- β O4'-G, show a higher affinity for the bilayer interior than G- β O4'-G natural dimers. DSC transition temperature shifts for the G- β O4'-G natural dimer were very small and the partition coefficient for that dimer was smallest (2.72). The partition coefficients obtained using DSC measurements were similar for G- β O4'-*trunc*G (log K = 3.45) and *benz*G- β O4'-G (log K = 3.38).

Molecular Dynamic (MD) simulations performed by Dr. Moldovan's group at Louisiana State University show that the G- β O4'-G dimer associates with the headgroups of the lipid but does not penetrate strongly into the interior of the bilayer [11, 193].

Therefore, this dimer has little effect on the T_m value. In contrast, the $G-\beta O4'-truncG$ dimer partitions into the bilayer because of its increased lipophilicity. Similarly, modification of the natural GG dimer by benzylation of the phenol makes it lipophilic, causing it to partition into the bilayer.

Results from this study enhance our understanding of properties required for lignin derivatives to be developed as potential pharmacological, toxicological and therapeutic agents by providing details of their activity for a model of the cell membrane. These data suggest that the hydroxypropenyl tail may present a barrier to the penetration of lignin oligomers into the cell, and thus may inhibit their pharmacology. This inhibition can be circumvented by removing hydroxypropenyl tails or adding additional hydrophobic groups.

Table 3.3 DSC liquid crystalline to gel transition temperature in DPPC in the presence of lignin GG dimers.

G- $\beta O4'$ -G		G- $\beta O4'-truncG$		<i>benzG</i> - $\beta O4'$ -G	
X_{dimer}	T_m (K)	X_{dimer}	T_m (K)	X_{dimer}	T_m (K)
0	315.5	0	315.5	0	315.5
0.02	315.4	0.02	315.2	0.07	314.3
0.06	315.3	0.06	314.7	0.15	313.6
0.18	314.8	0.20	314.5	0.28	312.0
0.33	314.7	0.36	313.4	0.40	311.5

CHAPTER 4. INTERACTION OF LIGNIN DIMERS WITH MODEL CELL MEMBRANES: A QCM-D STUDY

4.1 Summary

The study of the interaction between cell membranes and small molecules derived from lignin, a protective phenolic biopolymer found in vascular plants, is crucial for recognizing the potential pharmacological mechanism of these aromatic molecules and their toxicological impacts on biological systems. In this work, the interactions of a biomimetic cell membranes – supported 1,2-dipalmitoyl-sn-glycero-3-phosphocholine (DPPC) lipid bilayers– are compared with three β O4 dimers of coniferyl alcohol (G lignin monomer) including a guaiacylglycerol guaiacol ester with a hydroxypropenyl (HOC_3H_4 -) tail (G- β O4'-G), a truncated GG dimer without HOC_3H_4 - (G- β O4'-*trunc*G) and a benzylated GG dimer (*benz*G- β O4'-G). The uptake of the lignin dimers (per mass of lipid) and the energy dissipation of the bilayer (a measure of bilayer disorder) are higher for *benz*G- β O4'-G and G- β O4'-*trunc*G compared to G- β O4'-G in the gel phase DPPC bilayer, as measured using quartz crystal microbalance with dissipation (QCM-D). Similar uptake of G- β O4'-*trunc*G in a fluid phase bilayer of 1,2-dioleoyl-sn-glycero-3-phosphocholine (DOPC) suggests that the bilayer phase does not drastically affect the amount of lignin dimer uptake. Our results demonstrate that minor differences in the structure of lignin derivatives (such as the removal of the hydroxypropenyl tail) have significant impacts on their ability to penetrate into lipid bilayers.

4.2 Introduction

Lignin is a complex phenolic cross-linked polymer that, together with cellulose, acts as the structural material in plants and is important for rigidity and water transport

within plant cell walls [4]. Lignin is the second most abundant biopolymer after cellulose, comprising 15–30% of biomass. However, unlike cellulose, lignin has limited current uses due to the heterogeneity of its structure. While comprised of only three monomers, lignin has a complex structure due to variation in both sequence and types of bonds between monomers. The goal of deconstructing lignin to commercially viable small molecules for use as chemicals or advanced materials has been elusive because of this heterogeneity, leading to much of lignin being discarded as waste or burned for energy, and only a small part being utilized for value-added products [6, 171, 194]. Currently, potential uses of products derived from lignin are being explored for a wide variety of applications. These include using lignin and its small molecule derivatives as commodity chemical feedstocks, reinforcements for polymers, UV protectants, in tissue engineering materials, and as antioxidants and antimicrobials [194-197].

Lignin is composed of three monolignols (the aromatic alcohols *p*-coumaryl alcohol, coniferyl alcohol, and sinapyl alcohol) and every monomer includes a characteristic phenolic ring (*p*-hydroxyphenyl (H), guaiacyl (G) and syringyl (S), respectively) and a hydroxypropenyl group [198]. The monomers can be linked together in many different ways to form dimers, trimers, or more complex oligomers connected by various bonding motifs including β O4, α O4, 4O5, 55, $\beta\beta$, β 5, and β 1 [168, 199]. This variety makes the structure of lignin very complicated and implies that when lignin is deconstructed by methods such as pyrolysis, hydrogenolysis, and hydrolysis, an extremely diverse mixture of lignin-derived molecules is acquired [1, 200]. Finding ways to analyze, separate, and identify small molecule lignin derivatives is arduous because of this complexity. In our previous published work, we proposed a generalized pathway for

synthesizing different β O4 dimers which are potential model compounds in the development of applications, and analytical and separation methods for small lignin-derived molecules [29].

The study of the interaction between cell membranes and small molecules is crucial for recognizing the pharmacological mechanism of some compounds and to elucidate their toxicological impacts on biological systems [94, 105]. For instance, the mode of action of a substantial number of small pharmaceutical drugs such as tranquillizers, anesthetics, narcotics, and antidepressants is based on their transport through the hydrophobic interior of the cell membrane [106]. Phenolic compounds such as lignans have similar structure to lignin oligomers and are of great interest for human therapeutic applications due to possible protective (e.g. antioxidant) or growth-inhibiting (e.g. anticancer) properties [101, 201-204]. Thus, the interaction of compounds derived from lignin with cell membranes is an indicator of lignin's therapeutic or toxic behavior [168, 205] and allows us to identify effective ways to use oligomers of lignin (some of which overlap with lignans [206]) for therapeutic applications with consideration of risk to humans and the ecosystem [119].

The outer leaflet of mammalian cell membranes, facing the extracellular space, is primarily made of phosphatidylcholine (PC), sphingomyelin (SM), phosphatidylethanolamine (PE), and cholesterol [207, 208]. Phosphatidylcholine (PC) and sphingomyelin (SM) are the amplest phospholipids in the human red blood cell (erythrocyte) membrane with PC comprising ~35% of the membrane [209, 210]. Moreover, pulmonary surfactant of all mammalian species embodies substantial amounts (~80%) of PC with nearly 60% of it being in the dipalmitoylated form [211]. Here, 1,2-dipalmitoyl-sn-glycero-3-phosphocholine (DPPC) bilayer has been chosen as a simplified

model system for the basic functions of biological mammalian membranes [118, 212]. Building on our previously published work in dilute systems, here we study the interactions of three β O4 dimers of coniferyl alcohol (GG lignin dimer) including the novel G- β O4'-G and *benz*G- β O4'-G dimers and commercially available G- β O4'-*trunc*G dimer (**Figure 4.1**) with DPPC lipid bilayers. All three monomers are built around two guaiacyl (G) units linked with a β O4 bond. G- β O4'-G has a hydroxypropenyl tail expected to be found in natural lignin, while G- β O4'-*trunc*G is truncated, and *benz*G- β O4'-G has the hydroxypropenyl tail but is benzylated at the phenol end. In **Chapter 3**, the effect of the incorporation of these dimers on the structure of a DPPC lipid bilayer was interpreted from changes in the gel-to-fluid phase transition at a limit of infinite dilution using differential scanning calorimetry (DSC) and molecular dynamics (MD) simulations (performed by Dr. Moldovan's group at Louisiana State University) [11]. *benz*G- β O4'-G and G- β O4'-*trunc*G decreased the bilayer transition temperature significantly relative to pure DPPC, while G- β O4'-G had little effect on transition temperature [11]. In the current contribution, the concentration dependence of the uptake of G- β O4'-G, G- β O4'-*trunc*G and *benz*G- β O4'-G dimer in DPPC bilayers and its corresponding effect on lipid bilayer disorder are investigated using a quartz crystal microbalance with dissipation (QCM-D) as well as MD simulations (performed by Dr. Moldovan's group).

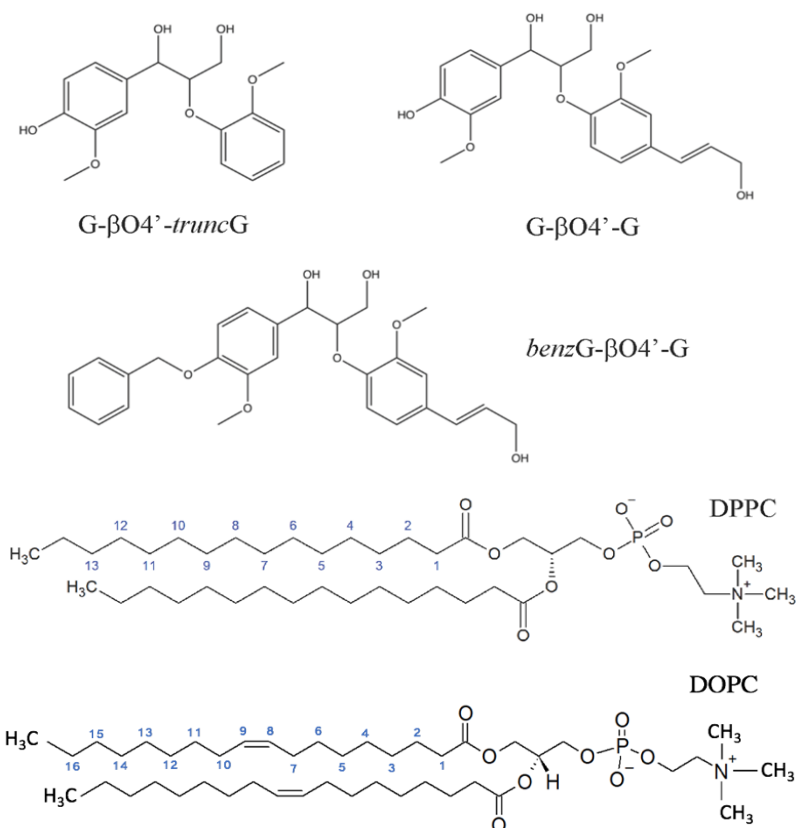


Figure 4.1 Chemical structures of the three $\beta O4$ -linked lignin dimers used in the experiments and simulation, and the lipids DPPC and DOPC.

QCM-D has been widely used as a robust method for investigating and quantifying adsorption of small molecules to lipid bilayers supported on solid surfaces [88]. Previously, Joshi et al. used QCM to study the interaction of aminoglycosides (kanamycin A and neomycin B) with model cell membranes supported on gold, and observed similar rates of membrane penetration for both aminoglycosides followed by bilayer disruption when a critical concentration threshold was reached [101]. Kannisto et al. studied the interaction of two small-molecule drugs, propranolol and tetracaine, with lipid bilayers supported on silica using QCM and successfully measured the adsorbed mass of the compounds as a function of their concentration in the aqueous phase, as well as the impact of the compounds on the bilayer viscoelasticity [108]. Wargenau et al. evaluated the cell

membrane penetration potential of low molecular weight lipid-soluble compounds (vanillin, gallic acid, and protocatechualdehyde) using supported phospholipid bilayers on QCM-D silica sensors. They observed that while the studied compounds did not cause any noticeable mass density changes in the bilayer, they caused significant changes in their gel–fluid phase transitions [109]. Here, lipid bilayers are formed on gold QCM sensors by solvent-assisted deposition from isopropanol followed by injection of lignin dimer aqueous solutions in a flow cell. Changes of dissipation (a measure of bilayer rigidity and disorder) and mass of the lipid bilayer are used to interpret the uptake of the solute into the lipid bilayer. The interactions of silica nanoparticles functionalized with double-bond modified G- β O4'-*trunc*G dimer as well as lignin-graft-PLGA nanoparticles with DPPC lipid bilayers have been studied using QCM-D and presented in our previous publications [13, 38]. In this chapter, we examine the concentration dependence of dimer incorporation on bilayer properties in order to gain new insights into the mechanism of action of lignin oligomers with potential therapeutical or toxic properties at biological interfaces. MD simulation examined the concentration dependence of dimer incorporation on bilayer properties such as molecule positioning, bilayer thickness, and compressibility of dimer/lipid systems. A collaborative manuscript on this chapter has been published in and is reproduced here from Moradipour et al., *Biointerphases* 16, (2021) [12], with the permission of AIP Publishing.

4.3 Materials and Methods

4.3.1 Chemicals and Reagents

Isopropanol (99%) and deionized water (ASTM type II) were purchased from VWR International; phosphate-buffered saline (PBS) from Sigma Aldrich; 1,2-dipalmitoyl-sn-

glycero-3-phosphocholine (DPPC) from Avanti Polar Lipids (Alabaster, USA); and guaiacylglycerol- β -guaiacyl ether which is referred to as G- β O4'-*trunc*G dimer ($\geq 97\%$) and 1,2-didecanoyl-sn-glycero-3-phosphocholine (DOPC) from TCI America. All chemicals were used as received without further purification.

4.3.2 Quartz Crystal Microbalance with Dissipation (QCM-D)

A Quartz Crystal Microbalance with Dissipation (QCM-D; Q-sense E4, Biolin Scientific, Sweden) was employed to monitor the interaction of G- β O4'-G, G- β O4'-*trunc*G, and *benz*G- β O4'-G dimers in PBS (pH of 7.4) with DPPC and DOPC supported lipid bilayers on a gold substrate at 298 ± 0.2 K. The variations in oscillation frequency (Δf) and energy dissipation (ΔD) of the sensor were measured in real-time during the formation of a supported lipid bilayer (SLB), absorption of dimers from 0.1 mg/mL (unless otherwise indicated) solutions of dimers in PBS into the bilayer, and the washing of the bilayer, as discussed below. Both DPPC and DOPC lipid bilayers were created on a QCM-D gold-coated sensor (Nanoscience Instruments, Phoenix, USA) using the solvent assisted lipid bilayer (SALB) formation method reported by Tabaei et al. with slight changes [86]. Initially, PBS solution was passed over the substrate until a steady baseline was reached, followed by isopropanol for ~35 minutes, all at a flow rate of 30 mL/hr. Then, a lipid solution in isopropanol (1.5 mg/mL for both DOPC and DPPC lipid bilayers) was flowed through the QCM-D cell for 60 minutes. Finally, the substrate was rinsed with PBS again, leading to the rearrangement of the lipids adsorbed on the substrate into a SLB [213-215]. After forming the lipid bilayers, a solution containing G- β O4'-G, G- β O4'-*trunc*G, or *benz*G- β O4'-G dimers at a concentration of 0.1 mg/mL was passed through the QCM chamber for 60 minutes at a flow rate of 30 mL/hr. To make the solutions of dimers in

PBS, the dimers were first dissolved in 0.2 mL of isopropanol and then added to 29.8 mL of PBS. Lastly, the substrate was rinsed with PBS for 60 minutes to remove unbound molecules from the surface. At the conditions of this experiment (298 K), the supported DPPC bilayer was in its gel phase. The G- β O4'-*trunc*G dimer solutions (at 0.01, 0.02, and 0.1 mg/mL) were also used to study the interaction with a phosphocholine lipid bilayer, DOPC, in its fluid phase.

QCM-D experimental data collected at the 3rd overtone ($n=3$, 15 MHz) were analyzed by using the Sauerbrey model (**Equation 2.4**), which assumes that the adjacent layer is thin, rigid, and homogenous, and is utilized to determine the mass of lipid bilayers formed on QCM sensors [97, 213, 216]. In **Equation 2.4**, the mass of lipid bilayer per area ($\Delta m/A$) was measured from the change in frequency (Δf). C is the material-specific Sauerbrey constant ($17.7 \text{ ng cm}^{-2} \text{ Hz}^{-1}$), and n is the overtone number at which the frequency is being recorded [217]. The penetration depth of the overtones decreases with increasing overtone number [101, 217]. The fundamental frequency ($n=1$, 5 MHz), which measures a penetration depth of $\sim 250 \text{ nm}$ from the quartz crystal surface, was not considered because this resonance is very sensitive to variations in the bulk solution and prone to producing a noisy response. All the frequency values in this work are divided by the overtone number which is $n=3$ unless otherwise specified. In pure water, the penetration depth for the 3rd overtones is $\sim 145 \text{ nm}$ [97, 218]. The thickness of a hydrated phospholipid bilayer is approximately 8 nm (much lower than the penetration depth at $n=3$; $d/\lambda_3 = 0.055$), so the Sauerbrey equation (**Equation 2.4**) is expected to be applicable [97, 99].

4.4 Results and Discussion

Artificial membranes composed of SLBs have structure and dynamics that mimic the primary characteristics of cell membranes and thus are frequently used as simplified systems for studying membrane thermodynamics and transport processes [103, 219]. The solvent-assisted lipid bilayer (SALB) deposition method was used as the membrane preparation approach here because it has been shown to produce reproducible bilayers on unmodified gold QCM sensors [86]. QCM-D is a highly sensitive method especially for viscous layers containing large amounts of water (e.g. lipid bilayers) and has been used to investigate SLB formation and molecular interactions at lipid bilayer interfaces [217]. In QCM-D, the energy dissipation is recorded as the damping of the resonance when the driving voltage to the sensor is shut off. Variations in dissipation (ΔD) are related to changes in the rigidity or viscoelasticity of the layer adhered on the surface [119]; the deformation of a soft or disordered adlayer on the substrate leads to large dissipation changes whereas non-deformable or rigid adlayers are identified by small dissipation changes.

Here, QCM-D was utilized to examine and quantify adsorption of lignin dimers to supported lipid bilayers. Representative frequency and dissipation plots for the formation of a DPPC supported lipid bilayer using the SALB method at 297 ± 0.2 K are illustrated in **Figure 4.2**, where DPPC is below its gel-fluid phase transition temperature ($T_m = 315.3 \pm 0.15$ K). In **Figure 4.2**, the time axis starts after reaching steady state with PBS flowing over the sensor. PBS is followed by isopropanol, followed by a solution of DPPC in isopropanol (0.5 mg/mL), and finally PBS again. Rinsing with PBS in the final step causes the lipids adsorbed to the sensor from the isopropanol solution to reorganize into a

bilayer,[86] as shown by a sharp increase in frequency and a corresponding sharp decrease in dissipation. The Δf value for the bilayer in **Figure 4.2a** before dividing by the overtone number ($n=3$) is ~ 62 Hz which using the Sauerbrey equation (**Equation 2.4**) corresponds to a mass value of ~ 366 ng/cm², falling within the mass range reported in the literature for a supported lipid bilayer [220, 221]. The ΔD for the gel phase DPPC bilayer in **Figure 4.2b** is 10.6×10^{-6} which is higher than the value reported for fluid phase lipid bilayers (less than 0.5×10^{-6}) [86]; however, it is consistent with the value reported by Lind et al. for gel phase DPPC lipid bilayers in PBS at 298 K ($\sim 6.5 \times 10^{-6}$ at $n = 7$) [222]. The mass of the SLB formed on the sensor was measured from the difference in the frequency of the initial PBS baseline ($t=5$ min) and the baseline in PBS after SLB formation ($t=150$ min) using the Sauerbrey equation (**Equation 2.4**). The DPPC lipid bilayer mass for all SLBs in this work was above 350 ng/cm², which is in agreement with the reported mass for a rigid SLB that completely covers and is well coupled to the sensor [215, 223, 224].

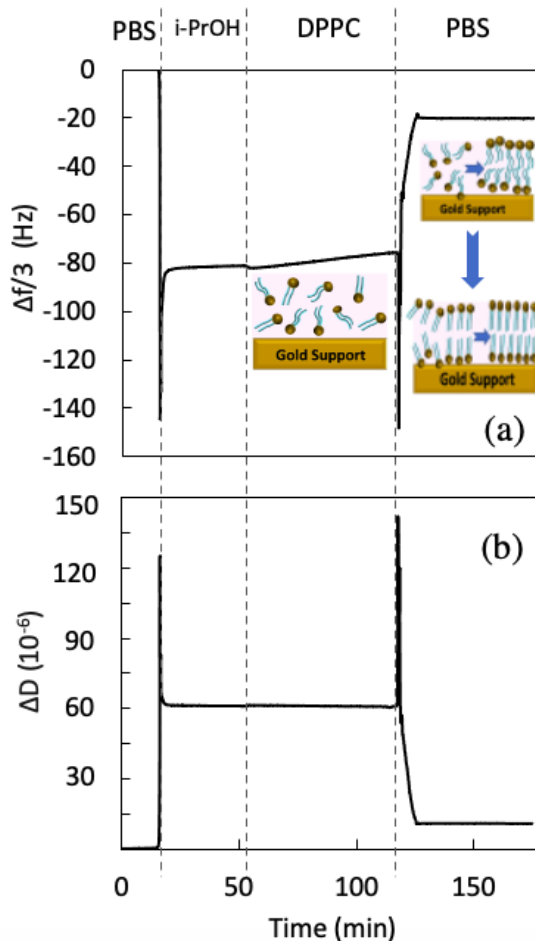


Figure 4.2 Representative QCM-D results for solvent-assisted DPPC lipid bilayer formation on a gold sensor. (a) Frequency shifts divided by the overtone number ($n=3$), and (b) dissipation shifts at the third overtone ($n=3$). The parts of the graphs separated by the vertical dashed lines denote the introduction of flowing PBS, isopropanol ('i-PrOH'), 0.5 mg/mL DPPC lipid in isopropanol ('DPPC'), and finally PBS. Insets show schematics of lipid deposition and bilayer formation during the process.

The amount of the lignin dimers interacting with the bilayer, and consequently the ratio of the mass of the bound dimer to the mass of the lipid bilayer, depends on the concentration of the dimer in solution. Because QCM sensors are sensitive to density and viscosity of fluids, it is conventional to flow dilute solutions (with concentrations in order of 1-1000 μM) over the sensor when studying the adsorption of molecules to lipid bilayers [101, 108, 225]. Concentration-dependent studies of G- $\beta\text{O}4'$ -*trunc*G were conducted

(**Figure 4.3**) to understand the sensitivity of QCM to the contributions of uptake by the SLB as well as bulk solvent properties. In **Figure 4.3**, $t=0$ corresponds to the initial DPPC bilayer and the values of $\Delta f/3$ and ΔD are shifted to 0 at this initial condition. $t=12$ min is the start of the flow of the dimer solution in the QCM cell. QCM-D measurements were carried out using three different concentrations of G- β O4'-*trunc*G solutions in isopropanol/PBS (0.67% v/v) in increasing order (0.01, 0.02, and 0.1 mg/mL). The injection of the dimer solution over the SLB at 0.01 mg/mL for 1 hr results in a decrease in frequency (**Figure 4.3**), which is an indicator of dimer association and incorporation into the lipid bilayer. However, the frequency does not plateau over the 1 hr period of injection, meaning that equilibrium with the SLB is not reached. Similarly, increasing the dimer solution concentration to 0.02 mg/mL for 1 hr results in a further decrease in frequency without evidence of membrane saturation. When the flow is switched to a much more concentrated solution of dimer (0.1 mg/mL), the frequency continues to decrease and begins to level off as a function of time at ~268 min. In the final step, the sensor was rinsed with only PBS solution for ~115 minutes. Thus, the concentration of 0.1 mg/mL was chosen to study the interaction of the dimers with the SLB within a time period of 1 hr, with a goal of achieving measurable equilibrium-like interactions of the bilayer in semi-dilute solutions.

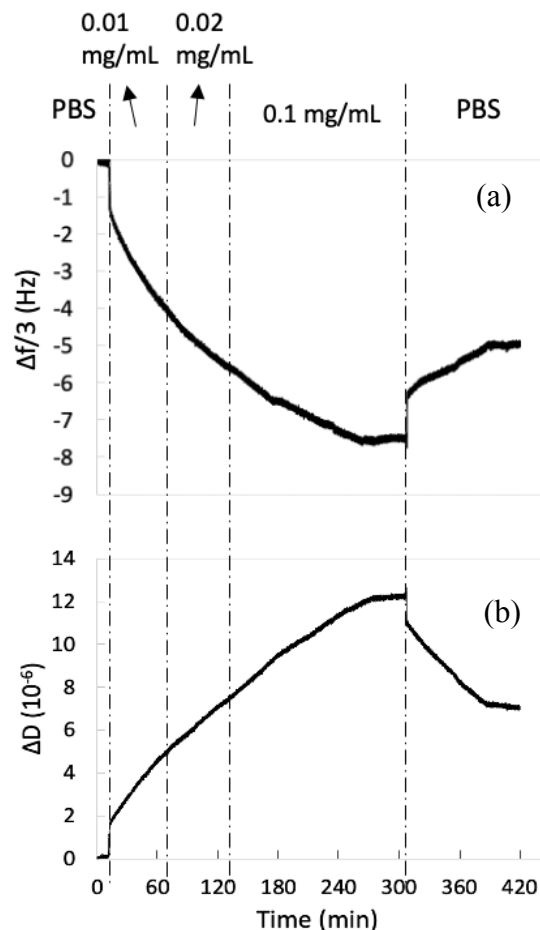


Figure 4.3 (a) Changes in frequency divided by the overtone ($n=3$), and (b) changes in dissipation with time as G- β O4'-*trunc*G dimer solutions of variable concentration (0.01, 0.02, and 0.1 mg/mL) flow over a DPPC lipid bilayer. The vertical dashed lines denote time frames over which solutions of lignin dimer with different concentrations was introduced, followed by PBS. Time of zero corresponds to the initial DPPC bilayer, the introduction of the 0.01 mg/mL dimer solution started at $t=12$ min, followed by the introduction of 0.02 mg/mL solution after 60 minutes and 0.1 mg/mL after 60 additional minutes. Flow at 0.1 mg/mL was continued for 176 minutes before rinsing with PBS for 115 min. Frequency data are presented for the third overtone ($n=3$).

To investigate the effect of modifications of the lignin GG dimer chemical structures on the interactions with phospholipid membranes, 0.1 mg/mL solutions of *benz*G- β O4'-G, G- β O4'-*trunc*G, and G- β O4'-G in isopropanol/PBS (0.67% v/v) were separately introduced to supported DPPC bilayers on QCM sensors. The resulting QCM-

D responses for $\Delta f/3$ and ΔD as functions of time are presented in **Figure 4.4**, in which the time of zero has been set for the fully developed bilayer and a corresponding $\Delta f/3$ value of zero is set. As shown in **Figure 4.4a**, upon introduction of the *benzG*- β O4'-G dimer to the bilayer at ~ 7 min, $\Delta f/3$ drops rapidly due to the change in solvent properties of the semi-dilute isopropanol-dope dimer solution (0.1 mg/mL). Concurrent with the decrease in frequency, a step change followed by a more gradual increase occurs in the dissipation profile (**Figure 4.4b**). Within one hour of initiating *benzG*- β O4'-G dimer flow over the bilayer, $\Delta f/3$ continues to slowly decrease due to the uptake of the dimer by the bilayer (causing an increase in film mass). A subsequent switch to pure PBS solution at ~ 67 min results in a rapid increase in the frequency. This is mainly attributed to difference in the bulk solvent properties and the possible redissolution of some of the dimers. Concurrently, ΔD undergoes a rapid drop immediately after switching to pure PBS and then gradually plateaus at a relatively constant value above the starting value, suggesting that the final SLB is more fluid than the initial bilayer and retains some dimer.

The net frequency change of the bilayer due to the binding and incorporation of the lignin dimers was interpreted from the change in frequency representing the initial DPPC supported bilayer (before ~ 7 min) and the bilayer after rinsing the sensor with pure PBS (at ~ 130 min). *benzG*- β O4'-G and *G*- β O4'-*truncG* displayed similar trends. The net $\Delta f/3$ changes for the *benzG*- β O4'-G and *G*- β O4'-*truncG* were ~ -10.13 and ~ -3.17 Hz, respectively. Similarly, the net ΔD changes of the bilayer for *benzG*- β O4'-G and *G*- β O4'-*truncG* dimers were $\sim 3.4 \times 10^{-6}$ and $\sim 11.5 \times 10^{-6}$, respectively (**Figure 4.4b**). The dissipation shifts measured by QCM-D are an indirect measurement of bilayer fluidity and its viscous losses [221]. The increase of dissipation with the introduction of *benzG*- β O4'-

G and G- β O4'-*trunc*G is consistent with dimers incorporation in the bilayer, and suggests that these hydrophobic dimers ultimately perturb the bilayer's rigidity and correspond to an increase in dissipation loss to the surrounding medium [226]. The results of a separate control experiment presented in the **Appendix Figure A.1a-b** show that the use of a small amount of isopropanol to solubilize the dimers (0.67 vol% in the PBS solution) has a minimal effect on the net frequency (-0.66 Hz) and net dissipation (less than 0.5×10^{-6}) relative to the dimer uptake in the SLBs.

At a concentration of 0.1 mg/mL, the interaction of G- β O4'-G with SLBs is different than *benz*G- β O4'-G and G- β O4'-*trunc*G, as interpreted from their respective frequency and dissipation responses (**Figure 4.4**). As seen in **Figure 4.4a**, G- β O4'-G incorporates more slowly into the membrane. Interestingly, $\Delta f/3$ increases when switching to the PBS buffer, but does not plateau over the one-hour period of buffer rinse. Instead, it trends toward the initial frequency. The reduced changes in net frequency for G- β O4'-G dimer (~ -1.94 Hz) relative to *benz*G- β O4'-G and G- β O4'-*trunc*G and the ability to resolubilize it during rinsing suggest that G- β O4'-G did not associate appreciably with the bilayer interior. The small net changes in ΔD (less than 1×10^{-6}) indicate that the bilayer fluidity of the SLB was largely unaffected by G- β O4'-G dimer addition and subsequent rinsing with PBS. Thus, the time-dependent desorption behavior suggests that G- β O4'-G dimer is not well incorporated in the SLB relative to G- β O4'-G dimer, G- β O4'-*trunc*G.

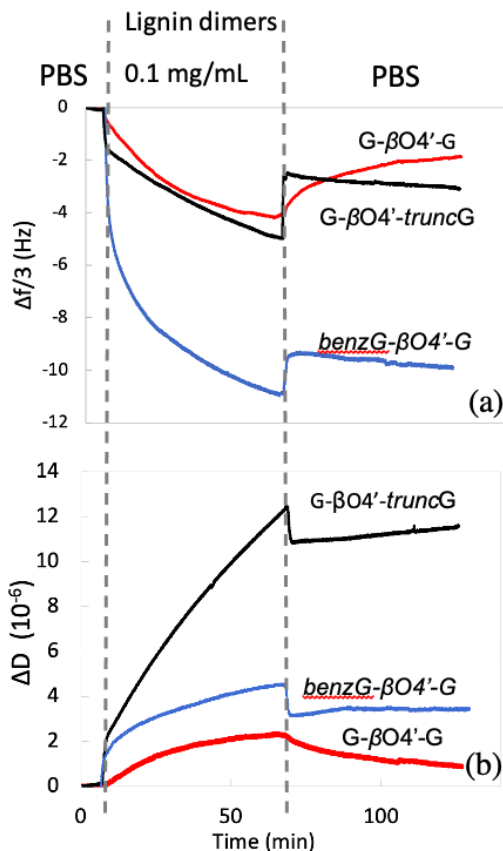


Figure 4.4 Interactions of G- β O4'-G (red), G- β O4'-truncG (black), benzG- β O4'-G (blue) dimers with supported DPPC lipid bilayers on gold-coated quartz crystal sensors obtained by QCM-D. (a) Changes in frequency divided by the overtone ($n=3$), (b) changes in dissipation. Time is measured starting from dimer injection onto an existing bilayer ('Lignin dimers'), followed by the PBS rinse ('PBS'). $\Delta f/3$ and ΔD are shifted to a value of 'zero' at time 'zero' corresponding to the initial DPPC bilayer. Data are presented for the third overtone ($n=3$).

Table 4.1 summarizes the mass of dimers associated with the bilayers after the final PBS rinse relative to the mass of the supported bilayer initially deposited onto the sensor. The results are normalized with respect to bilayer mass because the bilayer mass varied slightly with each bilayer formed using the SALB method (an average of 400 ± 96 ng/cm², consistent with a range reported in literature for mass of the supported phosphatidylcholine lipid bilayers [220, 221] and the observation that DPPC supported lipid bilayers deposited in the gel phase have more variability than those deposited in the fluid phase [222]. The

ratio of adsorbed dimer mass to DPPC bilayer mass follows the trend: $G-\beta O4'-G < G-\beta O4'-truncG < benzG-\beta O4'-G$. This is consistent with the order of increasing equilibrium partitioning of these dilute lignin compounds into phospholipid bilayers [105] as well as their estimated hydrophobicity. Our previous differential scanning calorimetry and MD studies of dimer incorporation in dilute systems also showed enhanced partitioning of the benzylated and truncated GG dimers into DPPC relative to naturally occurring $G-\beta O4'-G$ dimer [11]. $G-\beta O4'-G$ has the most hydroxyl groups (four), one of which is part of the hydroxypropenyl (HOC_3H_4-) tail. The free hydroxyl groups increase the hydrophilicity of the dimer and consequently decrease its penetration depth into the interior of the lipid bilayer, leading to slow diffusion away from the bilayer following the PBS rinse. In a study by Tammela et al., flavonoids with more than three free hydroxyl groups (e.g. luteolin, quercetin, and morin) were reported to initially bind strongly to the heads of the DPPC lipid bilayer via hydrogen bonding, but not to diffuse and transport deeply into the hydrophobic interior of the bilayers compared to more hydrophobic flavonoids [110]. Here, $G-\beta O4'-truncG$ lacks the hydroxypropenyl tail, which increases its hydrophobicity and ultimately leads to more penetration. Similarly, $benzG-\beta O4'-G$ has an added benzyl group at the phenolic end of the dimer which causes an increase in hydrophobicity, allowing it to penetrate deeper into the bilayer. Our previously published PMF calculations for dilute dimeric systems in fluid phase DPPC bilayers illustrated that most of the $G-\beta O4'-G$ dimer resides at or close to the exterior bilayer surface with only a small probability of finding this dimer inside the bilayer [11]. In contrast, most of the $G-\beta O4'-truncG$ is embedded in the bilayer with only a small probability of finding it at the exterior bilayer surfaces. PMF

studies performed by Dr. Moldovan's group also showed that *benzG-βO4'-G* is expected to reside almost exclusively in the bilayer interior [11, 193].

Table 4.1 Quantitative QCM-D results of the lignin GG dimers' interactions with the synthetic DPPC lipid bilayers with 1 hr of exposure at a concentration of 0.1 mg/mL of dimer solutions.

Dimer	G-βO4'-G ^a	G-βO4'- <i>truncG</i> ^b	<i>benzG-βO4'-G</i> ^b
Average ratio of mass of bound dimer to mass of the pure DPPC bilayer	0.10 ± 0.009	0.16 ± 0.03	0.25 ± 0.08

^a Three replicate measurements constitute the basis for these data.

^b Three replicate measurements constitute the basis for these data.

The MD simulation studies by Dr. Moldovan's group were performed at T = 326 K to allow for equilibration within the time scale of the simulations [12, 193]. However, the QCM-D experiments were performed at 297 K, which is below T_m of DPPC (T_m = 315.3 ± 0.15 K), because preliminary experiments indicated that SALB formation of a DDPC bilayer was unsuccessful at 318 K, a temperature above its T_m (data not shown). To show that our QCM results were also valid for fluid bilayers, the interaction of G-βO4'-*truncG* as the model compound with the phosphatidylcholine lipid bilayer, DOPC (T_m = 256.65 K) was investigated at 297 K. Representative QCM-D results for solvent-assisted DOPC lipid bilayer formation on a gold sensor and the resulting frequency and dissipation profiles after introduction of G-βO4'-*truncG* to the bilayer are included in **Appendix Figures A.2** and **A.3**, respectively. The frequency and dissipation values for a DOPC lipid bilayer formed on gold were measured to be -15 ± 1.5 Hz and (0.94 ± 0.2) × 10⁻⁶ respectively (**Appendix Figure A.2a-b**). The net change in frequency due to the incorporation of G-βO4'-*truncG* in the DOPC lipid bilayer in the fluid phase and average ratio of the mass of adsorbed G-βO4'-*truncG* dimer to the mass of the DOPC bilayer were ~-2.33 Hz

(**Appendix Figure A.3a**) and 0.20 ± 0.09 (**Appendix Table A.1**), respectively. These values are consistent with our measurements of G- β O4'-*trunc*G dimer interactions with DPPC bilayers in the gel phase. This suggests that the phase of the lipid bilayer (gel or fluid) does not drastically affect the amount of dimer associated with the membrane. However, the net ΔD changes for the G- β O4'-*trunc*G dimer and the DOPC bilayer were $\sim 1 \times 10^{-6}$ (**Appendix Figure A.3b**), which is substantially lower than what was measured for G- β O4'-*trunc*G dimer and DPPC. The uptake of G- β O4'-*trunc*G dimer has a minimal effect on the fluidity and viscoelastic properties of a bilayer that is already in the fluid phase.

4.5 Conclusion

In this chapter, the interactions of supported DPPC lipid bilayers with concentrated amounts of the three β O4' linked dimers of coniferyl alcohol and its derivatives (GG lignin dimers) are investigated using results from QCM-D.

QCM-D provides a bulk description of the effect of the increased amounts of dimers on the bilayer and revealed that a truncated GG dimer with the hydroxypropenyl tail removed, G- β O4'-*trunc*G, and GG dimers with an added benzyl group, *benz*G- β O4'-G, penetrated more deeply into the bilayer interior. This conclusion is based on the greater increases in the mass of dimer incorporated and the dissipation (viscoelasticity) of the thin film on the gold support for these two variants. On the contrary, the guaiacylglycerol guaiacol ester with a hydroxypropenyl (HOC_3H_4 -) tail (G- β O4'-G) demonstrated relatively weak affinity towards the interior of the lipid bilayer as inferred from smaller shifts in

frequency (mass) and dissipation (viscoelasticity) measured before and after dimer exposure.

MD simulations of lignin GG dimers with DPPC lipid bilayers (performed by Dr. Moldovan's group) qualitatively explained the QCM-D results indicating that G- β O4'-G does not accumulate to a significant extent in the bilayer interior while the more hydrophobic G- β O4'-*trunc*G and *benz*G- β O4'-G are taken up significantly [12, 193]. Density profiles for different concentrations of dimers and PMF results for one concentration indicate that G- β O4'-*trunc*G and *benz*G- β O4'-G were found deeper in the bilayer than G- β O4'-G. Furthermore, results for the ordering of the lipid tails, bilayer thickness, and area per lipid, and bilayer compressibility showed that by promoting disorder in the lipid tails, G- β O4'-*trunc*G and *benz*G- β O4'-G increase the bilayer fluidity more than G- β O4'-G which is consistent with QCM-D dissipation results and **Chapter 3**.

Results from this study enhance our understanding of pharmacological and toxicological effects of lignin derivatives as well as properties required for them to be developed as potential antigrowth and therapeutic agents by providing details of their activity for a model cell membrane. These data suggest that the hydroxypropenyl tail may present a barrier to the penetration of lignin oligomers into the cell, and thus may affect their pharmacology.

CHAPTER 5. INTERACTION OF LIGNIN-DERIVED DIMER AND EUGENOL-FUNCTIONALIZED SILICA NANOPARTICLES WITH SUPPORTED LIPID BILAYERS

5.1 Summary

The potential to impart surfaces with specific lignin-like properties remains relatively unexplored due to the lack of well-defined lignin-derived small molecules and corresponding surface functionalization strategies. Here, allyl-modified guaiacyl β -O-4 eugenol (G-eug) lignin-derived dimer is synthesized and attached to mesoporous silica nanoparticles (MSNPs) via click chemistry. The ability of G-eug lignin-dimer functionalized particles to interact with and disrupt synthetic lipid bilayers is compared to that of eugenol, a natural compound with known therapeutic and antimicrobial properties. Spherical MSNPs (~150 nm diameter with 4.5 nm pores) were synthesized using surfactant templating. Post-synthesis thiol (SH) attachment was performed using (3-mercaptopropyl)trimethoxysilane and quantified by Ellman's test. The resultant SH-MSNPs were conjugated with the G-eug dimers or eugenol by a thiol-ene reaction under ultraviolet light in the presence of a photo initiator. From thermogravimetric analysis (TGA), attachment densities of approximately 0.22 mmol eugenol/g particle and 0.13 mmol G-eug dimer/g particle were achieved. The interaction of the functionalized MSNPs with a phospholipid bilayers of 1,2-dipalmitoyl-sn-glycero-3-phosphocholine (representing model cell membranes) supported on gold surface was measured using Quartz Crystal Microbalance with Dissipation monitoring (QCM-D). Eugenol-grafted MSNPs in PBS (up to 1 mg/mL) associated with the bilayer and increased the mass adsorbed on the QCM-D sensor. In contrast, MSNPs functionalized with G-eug dimer show qualitatively different behavior,

with more uptake and evidence of bilayer disruption at and above a particle concentration of 0.5 mg/mL. These results suggest that bio-inspired materials with conjugated lignin-derived small molecules can serve as a platform for novel antimicrobial coatings and therapeutic carriers.

5.2 Introduction

Lignin, which is the second most abundant natural polymer and constitutes 10 to 40 wt% of plant dry matter, is a significant byproduct of agricultural/forestry processing and biomass conversion. The dominant use of lignin byproduct is as a fuel (combustion), with only a fraction of lignin produced in industry used for other applications, such as structural materials [6, 227]. Lignin is made up of three aromatic phenolic monomers (*p*-coumaryl alcohol, coniferyl alcohol, and sinapyl alcohol), making it a potential viable feedstock for aromatic molecules [8]. Lignin-derived small molecules have the potential to be used in applications including commodity chemical feedstocks, additives, fillers, surfactants, polymer composites, UV stabilizers, hydrogels, antioxidants, and antimicrobial as well as antifouling coatings [1, 194].

Each one of lignin's phenylpropanoid monomers contains a defining phenolic ring (*p*-hydroxyphenyl (H), guaiacyl (G) and syringyl (S), respectively) and a propenol group in the para position to the hydroxyl group. These monomers are arranged randomly within the lignin polymer and connected by different bonding motifs including β -O-4, α -O-4, 4-O-5, 5-5, β - β , β -5, and β -1 [11, 168, 199]. Due to lignin's heterogeneous structure, a highly complex mixture of lignin derivatives are obtained when lignin is deconstructed by methods such as pyrolysis, hydrogenolysis, oxidation, gasification, and hydrolysis [1]. In addition, developing techniques to analyze, separate, and identify small molecule lignin derivatives as targets for applications is difficult due to this complexity. In a previous

article, a generalized route was described for the organic synthesis of various β -O-4 dimers from monolignols that can be used as model compounds in the development of analytical and separation approaches for small lignin-derived molecules [29].

Lignin's highly-branched polyphenolic structure serves to protect the plant against degradation, acting as a shielding layer around the cellulose in primary and secondary cell walls [1]. Few organisms and chemical agents have the ability to degrade lignin. Furthermore, lignin derived from cotton stalks has been shown to have antimicrobial activity against Gram-positive bacteria such as *Bacillus mycoides* and *Bacillus subtilis*, and also some yeasts [228]. All three lignin monomers have been shown to have minimum inhibitory concentrations (MICs) as low as 8 mM against three yeasts: *Saccharomyces cerevisiae*, *Schizosaccharomyces pombe* and *Sporobolomyces roseus* and three bacteria: *Bacillus subtilis subsp*, *Escherichia coli* and *Pseudomonas syringe* [190]. Lignin's protective nature and its antimicrobial properties have generated interest in its use for the production of antimicrobial and antifouling surfaces or coatings for applications such as food production and packaging, biomedical sensors, implants and devices [229]. Moreover, due to the polyphenolic structure, lignin has antioxidant properties. The radical scavenging activity of polyphenolic structures accounts for most of lignin's antioxidant effects [168, 205].

Similarly plant-derived compounds such as eugenol (1-hydroxy-2-methoxy-4-allylbenzene) (**Figure 5.1**), an allyl substituted phenylpropanoid essential oil, have antimicrobial, anti-inflammatory, analgesic, anti-oxidant and anticancer properties [230, 231]. Eugenol is used in the pharmaceutical, agriculture, fragrance, dentistry, food and cosmetic industries. The considerable antimicrobial activity of eugenol, as measured from its MIC, is 2 mM against *Saccharomyces cerevisiae* and *Schizosaccharomyces pombe* yeast, 1 mM against *Sporobolomyces roseus* yeast, and 4 mM or higher against three types

of bacteria: *Bacillus subtilis subsp*, *Escherichia coli* and *Pseudomonas syringe* [190]. In other studies, eugenol has been shown to be able to prevent the growth of *P. aeruginosa* bacteria at 1000 ppm (6.1 mM), and is found to completely inhibit the growth at a concentration of 2000 ppm (12.2 mM) [230, 232]. Eugenol can rapidly incorporate in cell membranes, resulting in membrane swelling [233-235]. The mechanism for the antimicrobial activity of eugenol is based on its disruption of cell membranes, thus increasing non-specific permeability, inhibiting ion transport and the production of intracellular reactive oxygen species (ROS) [236]. The hydroxyl group in eugenol also plays a role in its antimicrobial activity since eugenol derivatives without the hydroxyl group show little to no antibacterial activity [237]. The hydroxyl group is suggested to exchange protons, reducing the pH gradient across the cell membrane [238].

Surface modification of nanoparticles with eugenol cause an increase in the antimicrobial properties of the particles. For instance, eugenol-coated magnetite nanoparticles (Fe_3O_4 NPs) show good antimicrobial effects against both Gram positive (*S. aureus*) and Gram negative (*P. aeruginosa*) bacteria strains [239]. Moreover, grafting chitosan nanoparticles (less than 250 nm in size) with aldehyde-modified eugenol through Schiff base reaction resulted in enhanced antibacterial and antioxidant activities against *E. coli* and *S. aureus* [240]. Jung et al. [241] also grafted the vinyl group of eugenol directly to the amine groups of chitosan hydrogels to obtain antimicrobial surfaces with known eugenol orientation.

In this chapter, we demonstrate a strategy for attaching eugenol and allyl-modified guaiacyl β -O-4 eugenol (G-eug) lignin-derived dimer to mesoporous silica nanoparticles

(MSNPs), and examine the interactions of these functionalized MSNPs with phospholipid bilayers (representative of potential applications in drug delivery and as antimicrobial surfaces [242]). Recent applications of MSNPs in drug delivery and sensing highlight their potential on the basis of the ability to control the shape, size, pore structure and surface functionalization of MSNPs [243-248]. **Figure 5.1** shows the surface functionalization steps for eugenol-MSNPs and G-eug dimer-MSNPs. As synthesized uniform MSNPs were first functionalized with thiol groups (SH) with (3-mercaptopropyl) trimethoxysilane (MPTMS) to form SH-MSNPs. The photoinitiated thiol-ene click reaction between the allyl side chain of eugenol or G-eug dimer and thiol groups (-SH) on MSNPs provides an oriented attachment of the functional group resulting in eugenol-MSNPs and G-eug dimer-MSNPs, respectively. Successful surface functionalization is confirmed by changes in zeta potential, a ferric chloride (FeCl_3) colorimetry test for phenol groups, and the corresponding analysis of the functional groups using UV-vis spectroscopy. The amount of attached functional groups is quantified through thermogravimetric analysis (TGA). The interaction of functionalized MSNPs with phospholipid bilayers supported on the gold surface of a quartz crystal microbalance (QCM-D) sensor is determined from frequency and dissipation changes indicating association with bilayers and the ability of functionalized MSNPs to disrupt the supported bilayer. The attachment of lignin dimers to thiol-functionalized surfaces is expected to be a generalizable approach to utilizing lignin-derived small molecules for molecularly-oriented surface modification, with a goal of investigating and extending the properties of lignin and lignin-derived small molecules to tailored surfaces. A manuscript on this project is published in *Colloids and Surfaces B*:

Biointerfaces (Moradipour et al., Colloids Surf. B, 191, (2020) [13]), which is reproduced with permission from Elsevier.

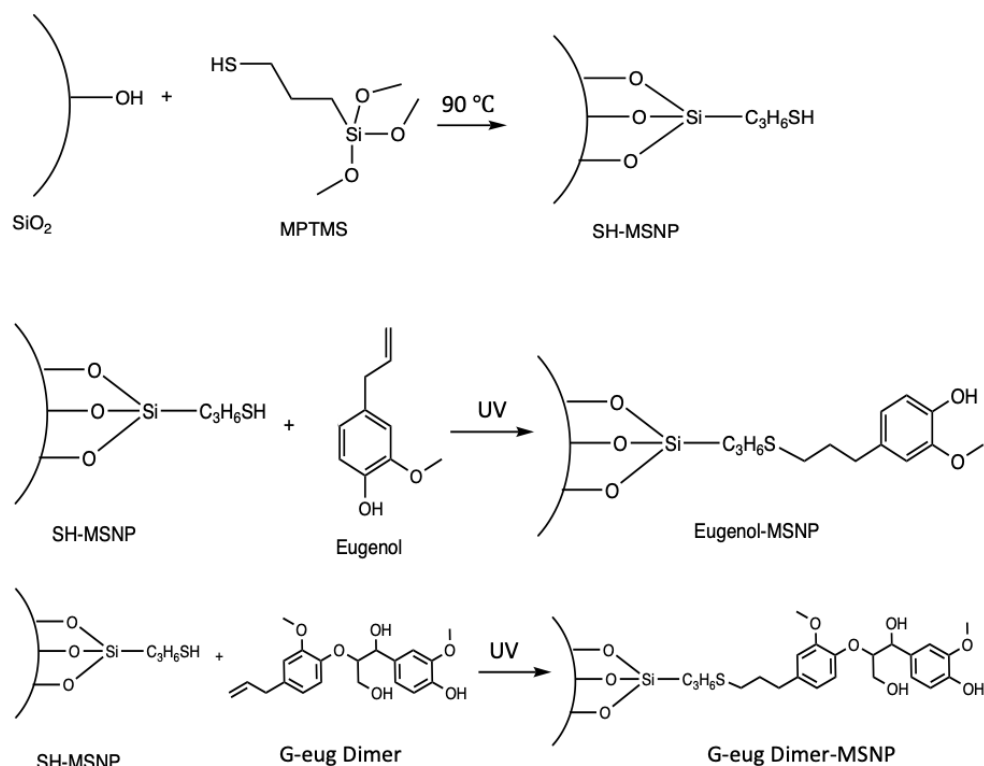


Figure 5.1 Grafting of the silica nanoparticles with thiol, eugenol, and G-eug dimer.

5.3 Materials and Methods

5.3.1 Chemicals and Reagents

Isopropanol (99%), hydrochloric acid (36.5-38%), 200 proof pure ethanol, and deionized water (ASTM type II), were purchased from VWR International. (3-Mercaptopropyl)trimethoxysilane (MPTMS, 95%), eugenol (99%), L-cysteine ($\geq 98\%$), and 5,5'-dithiobis(2-nitrobenzoic acid) (DTNB, Ellman's reagent, 99%) were purchased from Alfa Aesar. 2,2-Dimethoxy-2-phenylacetophenone (DMPA, $\geq 98\%$), and N,N-dimethylhexadecylamine (DMHA, $\geq 98\%$) were purchased from TCI America. Tetraethyl

orthosilicate (TEOS, 98%), and ferric chloride, anhydrous were purchased from Fisher Scientific. Pluronic F-127, tris-HCl buffer and phosphate buffered saline (PBS) was purchased from Sigma Aldrich. NaOH pellets ($\geq 97\%$) were purchased from EMD Millipore. Octadecyltrimethylammonium bromide (OTAB) was purchased from Chem-Impex International. 1,2-Dipalmitoyl-sn-glycero-3-phosphocholine (DPPC) was purchased from Avanti Polar Lipids (Alabaster, USA).

5.3.2 Synthesis of G-eug Dimers

Allyl-modified, 1-(4-hydroxy-3-methoxyphenyl)-2-[2-methoxy-4-(prop-2-en-1-yl)phenoxy]propane-1,3-diol (G-eug) dimer was synthesized by Dr. Lynn's group at University of Kentucky. The synthesis method along with the nuclear magnetic resonance (NMR) and high-resolution mass spectrometry (HR-MS) data for confirming the molecular structure of the G-eug dimer is presented in our published work [13].

5.3.3 Synthesis of Mesoporous Silica Nanoparticles (MSNPs)

MSNPs were synthesized by a surfactant templating sol-gel technique combined with pore swelling under basic conditions using a modified method established by Gu et al. [249]. Initially, 0.4 mL of DMHA, 1.02 g of OTAB and 0.3 g of Pluronic F127 were added to a solution containing 364 mL of DIUF water and 3.5 mL of 2 M NaOH at 80 °C under constant stirring. The solution was allowed to stir for an additional 30 minutes for complete dissolution of the constituents and then 5 mL of TEOS was added dropwise. A white suspension was formed immediately, which was stirred for another 2 h to complete silica condensation and then the solution was cooled to room temperature rapidly. Particles were separated from the solution by high-speed centrifugation at 17,000 rpm for 5 minutes

and washed with ethanol four times with repeated vortex mixing and centrifugation before being dried in an oven at 90 °C overnight. Surfactant templates were removed from the particle pores by our established protocol involving washing with acidic ethanol [243]. Dried as-synthesized particles were re-suspended in 200 mL of 1.5 M HCl in ethanol and allowed to stir for 48 h. Final particles were recovered by repeated high-speed centrifugation and washing with fresh ethanol and ultimately drying at 90 °C.

5.3.4 Thiol Functionalization of Bare MSNPs

Thiol-functionalized MSNPs (SH-MSNPs) were prepared using the method described by Chen et al. [250] with slight modification. 350 mg of bare MSNPs, 36 mL of ethanol and 5 mL of MPTMS were combined in a Teflon autoclave at 90 °C for 48 h. The mixture was allowed to cool to room temperature. The functionalized particles were recovered by centrifugation at 17,000 rpm for five minutes, prior to washing with fresh ethanol with repeated centrifugation and vortex mixing. Finally, SH-MSNPs were allowed to dry in an oven at 50 °C overnight.

5.3.5 Attachment of Eugenol or G-eug Dimer to SH-MSNPs

Allyl-modified, 1-(4-hydroxy-3-methoxyphenyl)-2-[2-methoxy-4-(prop-2-en-1-yl)phenoxy]propane-1,3-diol (G-eug) dimer was synthesized by Dr. Lynn's group at University of Kentucky using their published protocol with slight modifications [29]. The molecular structure of the G-eug dimer was characterized by nuclear magnetic resonance (NMR) and high-resolution mass spectrometry (HR-MS). The description of the synthesis of this dimer along with the NMR and HR-MS data is published by Moradipour et al. [13]. To attach eugenol or G-eug dimer to SH-MSNPs, 0.02 mmol of photo-initiator DMPA was

combined with 3 mL of isopropanol, 0.06 mmol of eugenol or G-eug dimer, and 37.5 mg of SH-MSNPs in a quartz cuvette and the mixture was allowed to stir under UV light (Thorlabs M00284926, $\lambda=365$ nm, 1.2 A) for 24 h. After attachment, the solution was centrifuged at 17,000 rpm for three minutes to recover the particles, which were rinsed with fresh isopropanol at least 5 times to remove unreacted functional groups, and dried in a low temperature oven (50 °C) overnight.

5.3.6 Characterization of MSNPs

Scanning electron microscopy (SEM) images of the particles were taken using Hitachi 4300 SEM instrument to study the morphology and shape of particles. The particle samples were dispersed on a carbon tape attached on a 15 mm aluminum stub, dried in a desiccator and coated with Au-Pd alloy in an Emscope SC400 sputtering system. Transmission electron microscopy (TEM) images were obtained using a JEOL 2010F TEM at a voltage of 200 kV. Samples were prepared by sonicating particles in ethanol to obtain a homogeneous suspension and then dipping a Ted Pella lacey carbon coated copper grid (300 mesh, 01895-F) for 2-3 seconds, and then drying the grid in a desiccator for 3 days prior to analysis. Brunauer-Emmett-Teller (BET) surface area, Barrett, Joyner, Halenda (BJH) average pore diameter, and pore size distribution were measured using nitrogen adsorption at -196 °C with a Micromeritics TriStar 300 instrument. Particles were degassed at 140 °C for 4 h with flowing UHP nitrogen gas prior to analysis.

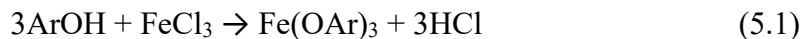
5.3.7 Thiol Quantification of the SH-MSNPs

Thiol quantification of SH-MSNPs was performed using Ellman's test, where the disulfide bond in Ellman's reagent reacts with thiol groups to produce a sulfide possessing

a bright yellow color and having a maximum absorbance at 412 nm [251]. The intensity of this yellow color corresponds to a specific concentration of thiol, which was calibrated using known concentrations of L-cysteine, adapting a method from Leubner et al. [252]. For the measurements, SH-MSNPs and bare MSNPs (control) dispersions (5 mg/mL) were made in DIUF water and 20 μ L of the particles solution was added to 1.38 mL of Tris-HCl buffer solution (pH 7.2) and 100 μ L of Ellman's reagent (1 mM). The mixture was allowed to stir in the dark for 1 h and a 200 μ L aliquot was analyzed by BioTek (Winooski, VT) plate reader. The amount of thiol was calculated by comparing intensity at 412 nm to a calibration curve previously prepared using concentrations from 0 to 10 mM of thiol (L-cysteine) solution in 2 mM increments treated with Ellman's reagent under the same conditions.

5.3.8 Verification of Eugenol or G-eug Dimer Surface Attachment

To verify the attachment of eugenol or G-eug dimer to the thiol-functionalized particles, a FeCl_3 test was used. When a compound containing phenol groups is exposed to FeCl_3 , a reaction between phenol and Fe^{3+} occurs, producing an intensely colored compound (**Equation 5.1**):



where "Ar" represents an aryl group. For an aromatic phenolic compounds, the color change (bright yellow to purple, green, black or blue) on the type of phenolic rings [253, 254]. 15 mg of eugenol-MSNPs and G-eug dimer-MSNPs as well as SH-MSNPs (control) were dispersed in 20 mL of isopropanol separately by sonication, then 1% w/v solution of FeCl_3 was added to each suspension, and mixed for 15 minutes. The resulting

suspensions were centrifuged at 17,000 rpm for 5 minutes to separate the particles and washed repeatedly with fresh isopropanol. The changes in the color that occurred due to the reaction of FeCl_3 and phenol groups were observed.

As another method to confirm phenolic group attachment, the presence or absence of the peak related to phenol group at ~ 282 nm in the absorbance spectra of the functionalized particles in isopropanol was investigated. The UV-vis spectra of particle dispersions were obtained using a HP 8453 UV-vis spectrophotometer, and compared to solutions of eugenol and G-eug dimer.

As a final particle characterization method, dynamic light scattering (DLS) was used for zeta potential measurement using an Anton-Paar Lightsizer 500 equipment. Around 0.1 mg of the particles were sonicated in 1 mL of PBS (pH=7.4) to produce homogeneous suspensions that were analyzed in an Omega cuvette consisting of inverted Ω -shaped capillary.

5.3.9 Quantification of the Attached Molecules by Thermogravimetric Analysis (TGA)

To quantify the amount of eugenol and G-eug dimer attached to the particles, thermogravimetric analysis (TGA) was conducted on the Universal 7A TA Instruments using a temperature ramp of $10^\circ\text{C}/\text{min}$ from 25 to 700°C . Thermal decomposition of bare, thiol-functionalized, eugenol-functionalized, and G-eug dimer-functionalized MSNPs was determined under nitrogen.

5.3.10 Particle-Lipid Bilayer Interactions Measured by QCM-D

The interaction of functional MSNPs with supported DPPC lipid bilayer deposited onto a quartz crystal sensors in PBS solution (pH 7.4) was measured using a Q-sense E4

QCM-D instrument (Biolin Scientific, Sweden) at 20 °C. First, a lipid bilayer was formed on a gold QCM-D substrate using a solvent assisted bilayer formation, as described elsewhere [86]. PBS solution (containing 137 mM NaCl, 2.7 mM KCl and 10 mM phosphate buffer) was passed through the QCM-D chamber for 7 min followed by pure isopropanol for 40 min. Subsequently, a DPPC lipid solution in isopropanol (0.5 mg/mL) was passed over the sensor for 60 min. Finally, PBS was flowed through the QCM chamber to induce formation of a supported lipid bilayer [213-215].

After forming the supported lipid bilayer, PBS solutions containing SH-MSNPs, or eugenol or G-eug dimer grafted MSNPs at different concentrations (0.01, 0.2, and 0.5 mg/mL) were passed through the QCM chamber. After 60 min, PBS solution was flowed through the chamber to remove un-attached particles. The changes in resonance frequency (Δf) and energy dissipation (ΔD) of the sensor were recorded using QTools software.

The mass of the supported lipid bilayer on the sensor was calculated from the change in frequency (Δf) of the QCM sensor using the Sauerbrey equation (**Equation 2.4**), which assumes that the layer is thin and rigid and has been applied previously to lipid bilayers developed on QCM sensors [97, 213, 216]. In this equation, $\frac{\Delta m}{A}$ refers to change in mass (m) adhered per area (A), C is the mass-sensitivity constant ($17.7 \text{ ng cm}^{-2} \text{ Hz}^{-1}$), and n_r refers to the overtone number. The magnitude of the overtone is inversely proportional to the distance from the surface being probed; at the higher overtones (7th and 9th overtone), the sensor probes mass changes closer to the surface than at the lower overtones (3rd and 5th) [101]. In this work, results for the third overtone are reported, as is standard in most QCM literature [215, 255]. The penetration depth for the third overtone

is ~145 nm in pure water, which is much greater than the expected thickness of a lipid bilayer [218]. Assuming a bilayer thickness of 8 nm, $d/\lambda_3 = 0.055$, so the Sauerbrey equation is expected to be applicable [97, 99].

5.4 Results and Discussion

5.4.1 Characterization of Bare and Thiol-Functionalized MSNPs

Mesoporous silica nanoparticles (MSNPs) were synthesized by a surfactant templated sol-gel route using TEOS as silica source with cationic surfactant OTAB as structure directing agent, DMHA as pore expander and Pluronic F127 to control particle size [249]. Templates were removed after synthesis by acidic ethanol wash. Particle size, shape and spherical morphology were observed by SEM (a representative image of template-extracted MSNPs provided in **Figure 5.2a**). The average particle diameter was determined to be 141 ± 28 nm by measuring 20 random particles using ImageJ software. This size is suitable for interaction with lipid bilayer membranes; nanoparticles smaller than 30 nm do not effectively drive the membrane-wrapping process and a larger particle size (above approximately 250 nm) lead to a significant decrease in cellular uptake efficiency [249, 256-258]. The TEM image of the MSNPs (**Figure 5.2b**) depicts an interconnected pore structure throughout the MSNPs. Additionally, the bare MSNPs have a high specific surface area ($842 \text{ m}^2/\text{g}$) and pore volume ($1.64 \text{ cm}^3/\text{g}$) (**Table 5.1**), as determined by nitrogen adsorption, and a pore diameter (~ 4.5 nm) appropriate for loading solutes and small biomolecules [249].

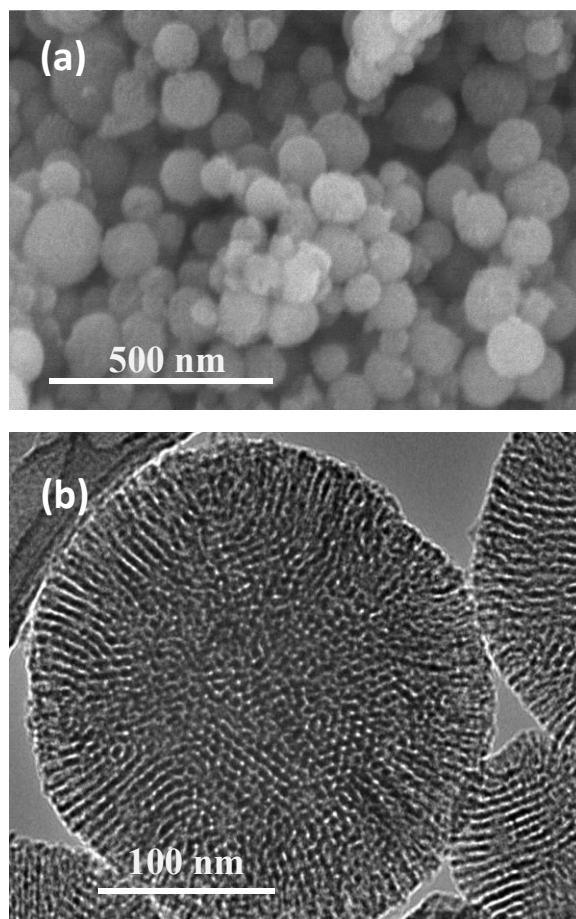


Figure 5.2 Electron microscope images of synthesized MSNPs: (a) scanning electron (SEM) image and (b) transmission electron (TEM) image.

After synthesis, MSNPs were functionalized with thiol groups through the reaction of MPTMS with surface silanol groups. The decrease of surface area, pore volume and average pore diameter are consistent with successful functionalization (**Table 5.1**). The retention of capillary condensation after thiol functionalization in nitrogen adsorption-desorption isotherms suggests that the mesoporosity is still uniform (**Appendix Figure**

B.1). The pore size distribution of SH-MSNPs relative to bare MSNPs, obtained by the Barrett, Joyner and Halenda (BJH) method, indicates that pore sizes were reduced uniformly as a result of functionalization of silica pore walls without significant pore blockage. Additionally, high specific surface area (842 m²/g) and pore volume (1.64 cm³/g), and large average pore diameter (~4.5 nm) of synthesized MSNPs determined by nitrogen adsorption at 77 K as provided in **Table 5.1**, as well as clear capillary condensation at relative pressure 0.5 in adsorption isotherm (type IV) point to uniform mesoporosity and the applicability of the nanoparticles for antimicrobial loading and as delivery vehicle (**Appendix Figure B.1**). Zeta potential measurements provided additional indirect verification of successful thiol attachment. At a pH of 7.4, the surface charge of the particles after thiolation changed to -22.2 ± 0.5 mV from -17.4 ± 0.9 mV of bare MSNPs (**Table 5.1**). The amount of thiol attached to SH-MSNPs was estimated spectroscopically by Ellman's test to be 3.7×10^{-4} moles of thiol groups per gram of SH-MSNPs.

Table 5.1 BET surface area, BJH average pore diameter and pore size distribution obtained from nitrogen adsorption, and zeta potential values measured in PBS at pH 7.4 for bare MSNPs, SH-MSNPs, eugenol-MSNPs, and G-eug dimer-MSNPs.

Particle type	Pore diameter peak ^a (nm)	BJH average pore diameter (nm)	BJH pore volume (cm ³ /g)	surface area (m ² /g)	Zeta potential in PBS, ζ (mV)
Bare MSNPs	3.7 ± 0.4	4.51	1.64	841.6	-17.4 ± 0.9
SH-MSNPs	2.8 ± 0.2	4.12	1.14	566.6	$-22.2 \pm 0.$
Eugenol-MSNPs	2.5 ± 0.3	3.95	1.06	493.0	-12.8 ± 0.5
G-eug dimer-MSNPs	2.8 ± 0.3	3.69	0.71	406.1	-15.5 ± 0.5

^a The ranges are determined from the full width at half maximum (FWHM) of the BJH pore size distribution

5.4.2 Characterization of Eugenol-MSNPs and G-eug Dimer-MSNPs

Eugenol was selected as a model system to demonstrate the orientation-specific functionalization of MSNPs using chemistry that can be extended to allyl-modified lignin dimers. Our method for attaching eugenol and G-eug dimer to SH-MSNPs was inspired by Mangos et al. [245], who attached 11-bromo-1-undecene to thiol-terminated silica nanoparticles through thiol-ene click reactions under UV light. Thiol-ene “click” chemistry reactions have previously been demonstrated for the synthesis of eugenol-containing polymers and networks, including the synthesis of eugenol-ZnO composite materials with antibacterial properties from allyl-eugenol derivatives [231]. Click chemistry and photopolymerization strategies have also been used to synthesize polymer networks, bio-based and dual-curable thermosets, and adhesives from eugenol derivatives [259-261]. Alkene-modified lignin has also been used as an attachment site of thiol-functionalized small molecules (e.g. 1-decanethiol) [262]. The surface properties, attachment density and attachment efficiency are reported here for the use of click chemistry to synthesize oriented eugenol- and G-eug dimer-modified silica surfaces.

Zeta potential measurements performed in PBS (pH 7.4) indirectly confirm the attachment of eugenol and G-eug dimer to SH-MSPNs through changes in surface properties. After eugenol and G-eug dimer attachment, the surface charge changed from -22.2 ± 0.5 mV (SH-MSPNs) to -12.8 ± 0.5 mV and -15.5 ± 0.5 mV respectively (**Table 5.1**).

Successful eugenol and G-eug dimer attachment were confirmed by exposing the nanoparticles in solution to FeCl_3 , which indicates the presence of phenolic groups through a color change [263]. The only phenolic groups present in the eugenol or dimer-grafted particles are in the eugenol or G-eug dimers themselves. **Appendix Figure B.2b-c** illustrates the color change after the G-eug dimer- and eugenol-grafted particles were exposed to FeCl_3 solution. Eugenol-MSNPs and G-eug dimer-MSNPs were pale yellow initially, but after exposure to FeCl_3 turned the suspension black or deep blue, respectively. Conversely, SH-MSNPs (control) showed no color change upon exposure to FeCl_3 solution (**Appendix Figure B.2a**), validating eugenol or G-eug dimer attachment to the particles.

Similar verification of functionalization is provided by the UV-vis spectra of eugenol-MSNPs and G-eug dimer-MSNPs relative to SH-MSNPs dispersed in isopropanol (**Appendix Figure B.3**). For eugenol- and G-eug dimer-functionalized particles, a sharp peak around 282 nm appears, which is also found in the spectra of eugenol or G-eug dimer in solution. The maximum at 282 nm for eugenol/dimer is in agreement with literature, arising from benzene aromaticity (270 nm) coupled with bathochromic shift of delocalized π -electrons conjugated with vinyl group [264, 265]. This peak is absent in SH-MSNPs.

TGA was used to quantify the attachment of eugenol and G-eug dimers from the weight loss profiles of four sets of particles (bare MSNPs, SH-MSNPs, eugenol-MSNPs, and G-eug dimer-MSNPs) as a function of temperature (**Figure 5.3**). A mass loss of 5.47, 3.87, 3.84, and 5.18% is observed from 25 °C to 200 °C for bare MSNPs, SH-MSNPs, eugenol-MSNPs, and G-eug dimer-MSNPs, respectively, which is attributed to evaporation of the water from the surface and the pores of the particles. The mass loss of bare MSNPs from 200 °C to 700 °C (3.49%) is attributed to organic impurities (such as

residual surfactant template) and further temperature-induced condensation of the silica framework. Additional mass loss by the organic functionalized particles (SH-MSNPs, eugenol-MSNPs and G-eug dimer-MSNPs) in the range of 200 °C to 700 °C relative to the bare MSNPs is used to quantify the amount of organic functional material. For SH-MSNPs, this additional mass loss (11.6%) corresponds to 0.77 mmol of thiol/g particle. In contrast, the amount of thiol groups on SH-MSNPs was quantified spectroscopically using Ellman's test as 0.37 mmol of thiol groups/g SH-MSNPs. While TGA quantifies all thiol groups, the Ellman's test measures accessible thiol groups. The inconsistency in these measurements suggests that regions of high density functionalization or pore blockage limit the accessibility of a portion of the thiol groups. Relative to SH-MSNPs, for eugenol-MSNPs and G-eug dimer-MSNPs, there are further mass losses of 3.6% (0.21 mmol eugenol/g particle) and 4.73% (0.13 mmol G-eug dimer/g particle), respectively. Evaluating the efficiency of dimer attachment based on accessible thiol groups (from Ellman's test), the attachment efficiency of the eugenol and G-eug dimer to the available thiol groups are 56.8% and 35.1% respectively.

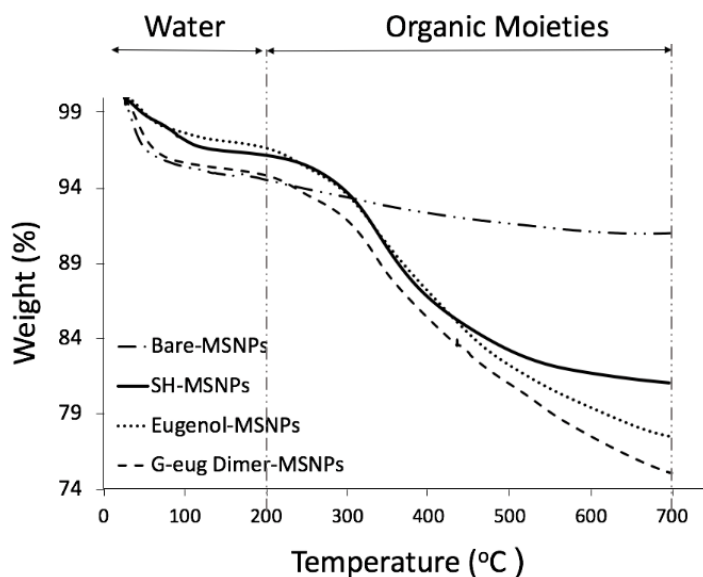


Figure 5.3 TGA of bare MSNPs, SH-MSNPs, eugenol-MSNPs, and G-eug dimer-MSNPs.

5.4.3 Interaction of Particles and Lipid Bilayers

Adhesion of nanoparticles to cell membranes has been identified as an important step in understanding the mechanisms of nanoparticle uptake and toxicity [95, 266]. Due to the complicated and dynamic nature of the actual biological membranes, model biological membranes comprised of synthetic lipid bilayers are frequently used as simpler substitutes for cell membranes [116]. QCM-D is a versatile technique to investigate the deposition and disruptive interactions of nanoparticles with lipid bilayers due to its simplicity of operation and availability of multiple types of model sensor surfaces [88, 95]. Previously, QCM-D has been used to study the deposition and adsorption of nanoparticles and nanotubes onto lipid membranes [255, 267], structural rearrangement of the nanoparticles upon adsorption to membranes [268], and the removal of lipid membranes by nanoparticles [118, 119].

The potential nanoparticle-cell interactions of eugenol and G-eug dimer covalently bound to a silica nanoparticle through an oriented attachment are inferred from the ability of the functionalized MSNPs to adhere to or disrupt supported lipid bilayer on gold QCM sensors. Oxidized gold is able to induce formation of lipid bilayers by liposome disruption [269], but the solvent-assisted bilayer deposition method has also been shown to be a viable strategy to form bilayers on unmodified gold sensors [86]. When a thin and rigid lipid layer is formed on the QCM sensor surface, the total mass of the film is proportional to the decrease in resonant frequency (Δf) of an oscillating crystal, as interpreted using the Sauerbrey equation [97, 213, 216]. In QCM-D, changes in dissipation (ΔD , the damping of oscillations after excitation) describe variations in the rigidity or viscoelasticity of the film formed on the surface [119]. The deformation of a soft film adhered to the sensor results in high dissipation; low dissipation is a characteristic of non-deformable rigid films. In the case of lipid bilayers supported on the QCM sensor surface, an increase in ΔD indicates that the lipid bilayer is loosening or thickening, overall becoming less rigid (more fluid) [101, 270]. When investigating particle interactions with supported lipid bilayers, an increase in dissipation is interpreted as a hydrodynamic effect caused by particle adsorption into the supported bilayer [226]. A maximum in dissipation can be observed on supported lipid bilayers if the concentration of the adsorbed particles becomes sufficient over time to create a more rigid film [271].

The effect of particle concentration on lipid bilayers has been previously investigated by Lesniak et al. [255] where the interaction of silica nanoparticles at concentrations of 0.025, 0.1, and 0.25 mg/mL with lipid bilayers on silica coated sensors was probed by QCM-D. They observed that for silica nanoparticles the kinetics of

adsorption to the membrane is strongly concentration dependent; the solution with the highest concentration demonstrated fast adsorption happening in less than 50 minutes, while the most dilute solution showed slower adsorption that took up to 250 minutes [255]. The concentration of the injected particle solution relative to the bilayer also contributes to the disruption of the bilayer. For instance, concentrations of 0.08 mg/mL and 0.1 mg/mL of 40 nm gold nanoparticles and 60 nm TiO₂ nanoparticles in solution have been demonstrated to remove some of the stable supported lipid membranes on QCM substrates, respectively [118, 119].

A typical QCM profile for Δf as a function of time for solvent-assisted lipid bilayer formation on the gold QCM sensor following the procedure of Tabaei et al. [86] is presented in **Figure 5.4**. First, PBS flowed through the QCM cell at a constant volumetric flowrate to establish a constant baseline. Next, pure isopropanol was flowed in the chamber to displace water and clear the sensor surface followed by a solution of DPPC lipids in isopropanol. Then PBS solution was pumped in the chamber again, which resulted in the formation of hydrated bilayers on the gold surface, corresponding to an increase in frequency (relative to the isopropanol solution of lipid) and a decrease in dissipation [86, 272]. After one hour of flowing PBS, the mass of the lipid bilayer formed on the sensor was determined from the change in frequency relative to the baseline established by PBS using the Sauerbrey equation (**Equation 2.4**). For all the lipid bilayers formed on the QCM sensor in this study, the mass of the lipid bilayer was equal or above 350 ng/cm², the reported value for rigid and strongly coupled supported lipid bilayer on the sensor [215, 223, 224].

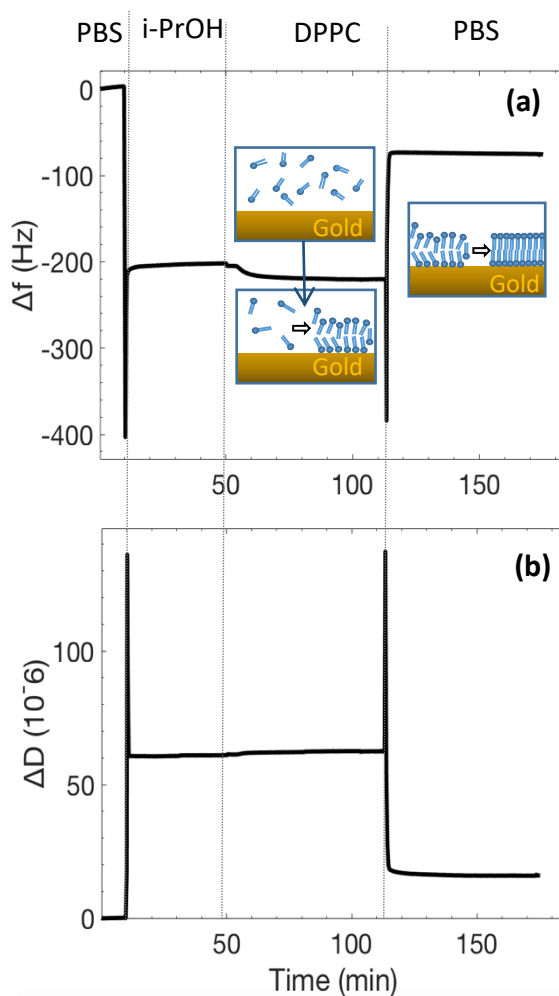


Figure 5.4 DPPC lipid bilayer formation on gold coated quartz crystal obtained by QCM-D in terms of frequency shifts at third overtone.

After formation of the bilayer on the sensor, G-eug dimer-MSNPs suspended in the PBS at three different concentrations (0.01, 0.2, 0.5 mg G-eug dimer-MSNPs/mL) were separately introduced to the QCM sensor containing the lipid bilayers. The resulting QCM results for Δf as a function of time are presented in **Figure 5.5**, in which the time of zero has been set as the beginning of the nanoparticle introduction into the QCM and a corresponding to Δf value of zero is set for the fully formed bilayer. The interaction of

nanoparticles with supported lipid bilayers normally begins with their deposition on the membranes [95]. As seen in **Figure 5.5**, for all concentrations of nanoparticles, Δf drops sharply as the nanoparticles flow into the QCM cell indicating the deposition of the particles. At concentrations of 0.01 and 0.2 mg/mL, the frequency continues to slowly decrease, indicating a mass increase of the bilayer due to particle adsorption. These particles are not removed from the bilayer when the solution is switched from nanoparticles to only PBS buffer, which was introduced after approximately one hour. At the highest studied concentration of G-eug dimer-MSNPs (0.5 mg/mL), the sharp decrease in Δf is followed by a constant increase in Δf , indicating mass is being removed from the sensor. The net mass loss was estimated as 58 ng/cm² (for an initial bilayer of 597 ng/cm²), where the actual loss of bilayer may be much greater due to the concurrent uptake of particles on the sensor surface.

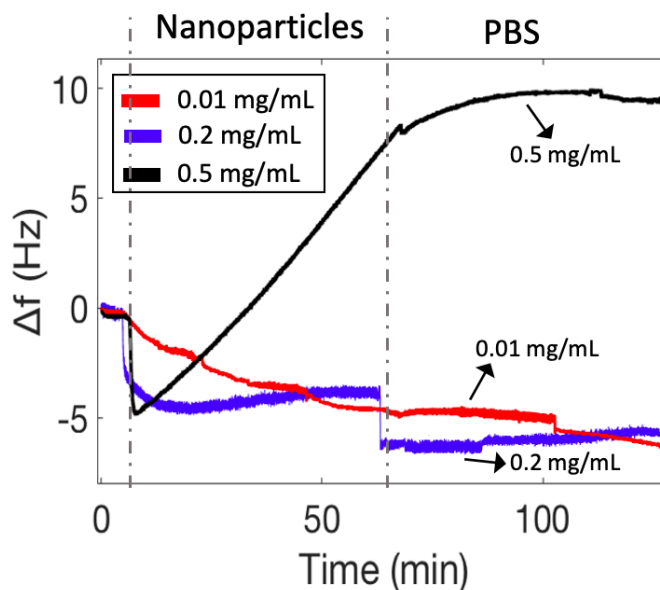


Figure 5.5 Change in frequency with the introduction of different concentrations of G-eug dimer-MSNPs on supported DPPC lipid bilayers on a gold QCM sensor. Time is measured from particle injection onto an existing bilayer ('Nanoparticles'), followed by the PBS buffer rinse ('PBS'). Δf is normalized to a value of 'zero' corresponding to the initial DPPC bilayer.

At a concentration of 0.5 mg/mL, G-eug dimer-MSNPs and eugenol-MSNPs have distinctly different interactions with fully formed bilayers, as interpreted from their frequency and dissipation shifts (**Figure 5.6**). For G-eug dimer-MSNPs, the time-dependent mass loss of the thin film (**Figure 5.6a**) and concomitant increase of the rigidity of the surface film (decreased dissipation (**Figure 5.6b**)) are interpreted as bilayer removal followed by particle accumulation on the semi-bare QCM sensor. Upon flowing pure PBS over the sensor, the step change in mass loss and dissipation increase suggest removal of some adhered nanoparticles, as described above. In contrast, the behavior of eugenol-MSNPs is consistent with adsorption of the particles on the bilayer without disruption. Following the introduction of eugenol-MSNPs (0.5 mg/mL) to the lipid bilayer, a significant decrease in Δf (increase in film mass) is followed by a more gradual increase in mass (**Figure 5.6a**). The net mass increase after eugenol-MSNPs introduction (~ 89 ng/cm²) is evidence for particles adsorbing to the lipid bilayer. The lack of regimes of positive changes in Δf while introducing eugenol-MSNPs indicates that these nanoparticles do not remove the supported lipid bilayer at this concentration, unlike G-eug dimer-MSNPs. The increase of dissipation with the introduction of eugenol-MSNPs (**Figure 5.6b**) is also consistent with nanoparticle incorporation in the bilayer, leading to hydrodynamic effects that increase dissipation loss with the surrounding medium [226]. In addition, minimal changes in thin film mass and rigidity are observed when flowing PBS over the QCM sensor, suggesting that the particles are not readily removed. In totality, the frequency and dissipation results for eugenol-MSNPs are consistent with the adsorption of the nanoparticles in the supported lipid bilayers. To further explore concentration-dependent behavior, at a concentration of 1 mg/mL, G-eug dimer-MSNPs continue to

disrupt and remove the supported bilayers while eugenol-MSNPs adsorb to the bilayer (see **Appendix Figure B.4**). However, these higher concentrations introduce more noise in the experiment and are outside the range of most concentrations reported for nanoparticle-bilayer interactions as interpreted using QCM.

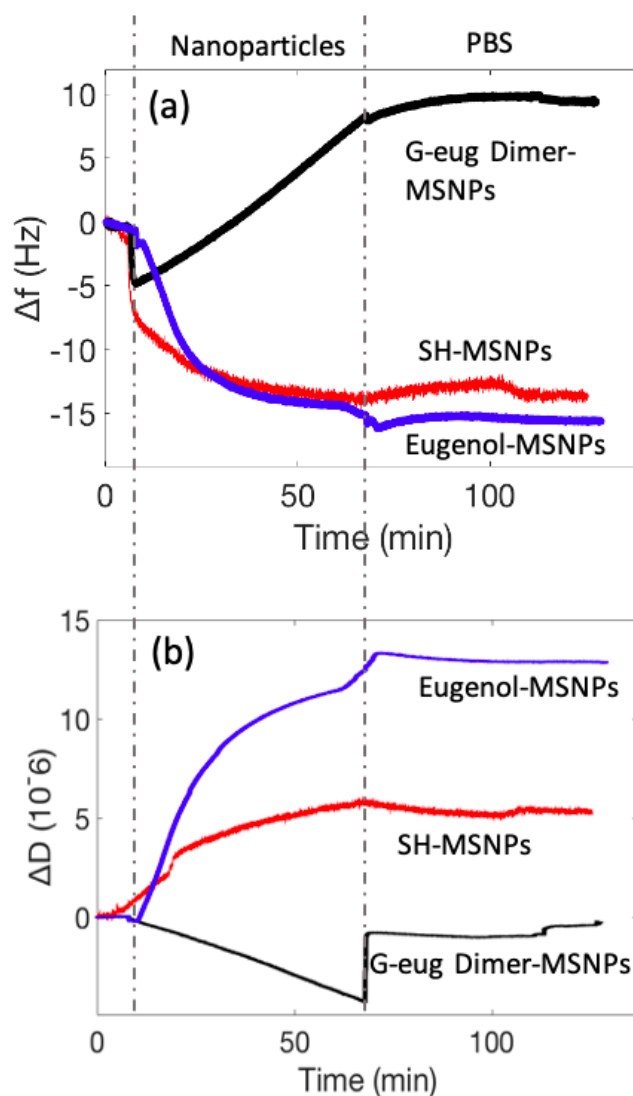


Figure 5.6 Change in (a) frequency and (b) dissipation with the introduction of SH-MSNPs, eugenol-MSNPs, G-eug dimer-MSNPs at 0.5 mg/mL on supported DPPC lipid bilayers on a gold QCM sensor. Time is measured from particle injection onto an existing bilayer ('Nanoparticles'), followed by the PBS buffer rinse ('PBS'). Δf and ΔD are normalized to a value of 'zero' corresponding to the initial DPPC bilayer.

SH-MSNPs (representing the nanoparticles prior to G-eug dimer or eugenol functionalization) at 0.5 mg/mL show similar trends in behavior as eugenol-MSNPs. While the lipid bilayer gain similar mass during introduction of the nanoparticles, the effect of SH-MSNPs on dissipation is reduced relative to eugenol-MSNPs. The adsorbed SH-MSNPs on the lipid bilayer appears to be stiffer due stronger adhesion to the bilayer, or a reduction in the degree of hydration of the particle/bilayer composite layer.

Destruction of supported bilayers by nanoparticles has been observed previously in QCM-D investigations. Bailey et al. [119] observed a notable mass loss (60 ng/cm² of net mass loss from a bilayer of 454 ng/cm²) using a 0.08 mg/mL solution of 40 nm gold nanoparticles in the presence of polymethacrylic acid (PMAA). Bilayer disruption was not observed in the absence of PMMA, where PMMA was a model organic suggested to adsorb to the particles and increase their adhesion to the bilayers. They concluded that this mass loss occurred due to the lipid bilayer engulfing the nanoparticles and being washed away from the surface of the substrate [119]. Moreover, Zhao et al. [118] tested the interaction of 60 nm TiO₂ nanoparticles in Tris buffer at concentration of 0.1 mg/mL, and observed bilayer removal (up to ~300 ng/cm² of a bilayer with mass of 406.2 ng/cm²). The suggested mechanism of bilayer removal was the weakening of the adhesion of the bilayer to the support due to the scavenging of Ca²⁺ by the TiO₂ nanoparticles. Ca²⁺ ions were initially added to the buffer when forming a negatively charged bilayer to overcome the electrostatic repulsion between the surface and the liposomes [118].

Here, lipid bilayer disruption by the G-eug dimer-MSNPs may be explained by the dimensions and lipophilicity of the dimer molecule, which are expected to be favorable for membrane insertion and subsequent removal of the bilayer. The antimicrobial activity of

lignin polymer is normally related to its chemical structure, more specifically the presence of phenolic compounds and various oxygen-containing functional groups[55]. Lignin-derived polyphenolic compounds (especially phenolic fragments) induce cell membrane damage and lysis in bacteria cell and result in loss of cell contents (mainly K^+) [273, 274]. While the lack of disruption of lipid bilayers by eugenol-MSNPs relative to G-eug dimer-MSNPs at the same concentration (0.5 mg/mL) is unexpected, eugenol is smaller and likely less lipophilic compared to the G-eug dimer. Increased hydrophobicity of lignin dimers compared to monomers which have nearly similar size as eugenol has been previously measured from the partitioning of lignin constituents into liposomes [105]. Thus, higher amount of accessible eugenol molecules might be needed to achieve the same disruptive effect as the G-eug dimer-MSNPs.

5.5 Conclusion

Herein we reported a successful method to attach eugenol and G-eug dimers molecules to thiol functionalized mesoporous silica nanoparticles (SH-MSNPs) by thiol-ene click chemistry. The method of attachment of eugenol and G-eug dimer to the SH-MSNPs using photo-activated reaction was proven to be successful using both qualitative and quantitative techniques and is suggested to be a versatile path to functionalizing surfaces with lignin-derived small molecules. The interactions of the functionalized particles with supported lipid and their ability to disrupt model lipid bilayers was examined using QCM. Although eugenol-MSNPs adsorbed to the supported lipid bilayer, they lacked the ability to disrupt a lipid bilayer at the concentrations tested (up to 1 mg/mL). The ability of G-eug dimer-MSNPs to penetrate and remove the supported lipid bilayers at concentrations as low as 0.5 mg/mL relative to eugenol-MSPNs is attributed to the

increased size of the oriented lipophilic functional group (from monomer sized eugenol to the G-eug dimer). The ability to design lignin-functionalized surfaces with either bilayer membrane adsorption or disruption properties can be considered a forerunner to applications of nanoparticles in drug delivery, therapeutic uses of lignans, and lignin-derived antimicrobial surfaces.

CHAPTER 6. THERMODYNAMIC INTERACTIONS OF LIGNIN DIMERS WITH β -CYCLODEXTRIN

6.1 Summary

Lignin-derived products have received growing attention due to the abundance of lignin in nature and the prevalence of lignin byproducts in industrial processes. Due to the complicated structure of lignin, a complex multi-component mixture of lignin derivatives is obtained when lignin is depolymerized. Developing methods to selectively separate, purify, and valorize lignin small derivatives is challenging. Cyclodextrins (CDs), particularly β -CD, are commonly used as selective adsorbents and are shaped like truncated cones with a hydrophilic surface and a hydrophobic core, which provide host-guest size and structure selectivity. The present work aims to study binding of β -CD to three types of lignin dimers of coniferyl alcohol using Isothermal Titration Calorimetry (ITC). These dimers include two dimers with β O4 linkages including a G- β O4'-G dimer with a hydroxypropenyl (HOC_3H_4-) group resembling natural lignin (GG dimer) and the commercially available G- β O4'-*trunc*G dimer without the HOC_3H_4- group. The binding of these β O4 dimers is compared to pinoresinol, a β c dimer of coniferyl alcohol (G- β β -G). The equilibrium binding constant (K) and the thermodynamic binding energies (ΔH , ΔS , and ΔG) for dimer- β -CD complexes are determined from fitting binding models to the ITC data. The results of this work show that in polar organic acetonitrile/water (10% v/v) medium, the less hydrophobic G- β O4'-G dimer binds to the β -CD through a different mechanism than more hydrophobic pinoresinol and G- β O4'-*trunc*G lignin dimers. The main driving forces in the complex formation of β -CD with pinoresinol and G- β O4'-*trunc*G dimers were hydrophobic interactions, which results in entropy-driven binding ($|\Delta S| > |\Delta H|$), while the driving forces of binding of β -CD with G- β O4'-G dimer

were predominantly van der Waals forces and hydrogen bonds, with enthalpy making a greater contribution to the Gibbs free energy ($|\Delta H| > |T\Delta S|$). Additional experiments were conducted in isopropanol/water (10% v/v) medium and the effect of isopropanol on the β -CD-dimer complex formation was investigated. Findings from this study were compared to those from MD simulation (performed by Dr. Moldovan's group, Louisiana State University) and the results from two methods were shown to be consistent [193]. The understanding of the interaction of lignin-derived small molecules with CDs in solution will support our efforts to create selective immobilized CD-grafted surfaces.

6.2 Introduction

The dependency of modern society on products obtained from non-renewable sources (e.g. petroleum-based chemicals) has become a growing concern. Lignocellulosic biomass, which is a form of carbon-based matter accessible on a renewable basis, is a potential organic feedstock for various molecules and chemicals [4]. Lignocellulosic biomass is made up of three major parts: cellulose, hemicellulose, and lignin. After cellulose, lignin (comprising 15-30% of biomass) is the second most abundant biopolymer on Earth [3]. Lignin is a promising potential source of sustainable and natural aromatics, and capitalizing on this valuable feedstock for producing chemicals that are currently produced from fossil fuel resources is of increasing interest [275, 276]. The deconstruction of lignin into aromatic and phenolic compounds is challenging and energy intensive, which is one of the reasons that lignin is usually underutilized by burning it as a fuel rather than using it as a feedstock for commodity chemicals [4]. Depending on the method used, harsh reaction conditions (temperatures as high as 1000 °C in flash pyrolysis and pressures as high as 30 MPa in gasification) are required to transform or depolymerize lignin, some of

which often result in production of undesired amounts of byproducts [1, 5, 26]. Thus, developing energetically-favorable and ecological methods to deconstruct lignin and separate resultant desired fragments from the lignin deconstruction mixture is of great importance [4].

A way to achieve the high level of molecular-level specificity needed to isolate specific lignin oligomers from a deconstruction mixture is by using host-guest binding chemistry, for example using cyclodextrins. Cyclodextrins (CDs) are cyclic oligosaccharides acquired from enzymatic deconstruction of starch [121]. The most common CDs are naturally occurring α -CD, β -CD, and γ -CD which contain six, seven, and eight 1,4-linked glycopyranose units respectively. The structure of CDs is similar to a truncated cone with a hydrophilic outside and a hydrophobic inside cavity [123, 125]. This unique structure enables the CDs to act as “host” molecules able to include hydrophobic “guest” molecules in their cavity. The structural features and encapsulation properties of the CDs result in “host–guest” interactions which can improve the physical, chemical, and/or biological properties of the guest molecules, enhance their water-solubility (especially in the case of hydrophobic pharmaceuticals), protect them from radicalization and polymerization, and retain volatile molecules in solution [124, 126, 127].

In directing polymeric lignin to smaller aromatic molecules, the dehydrogenation of lignin monomers is identified as an obstacle. Once activated, these monomers can be randomly and repeatedly coupled, which ultimately results in lignin repolymerization [277, 278]. Protecting smaller lignin fragments from dehydrogenation in a lignin deconstruction mixture facilitates the isolation and enrichment of those fragments and controls lignin’s further polymerization [277]. Host-guest complex formation between CDs and lignin

oligomers is shown to prevent the oxidation of lignin oligomers in the presence of oxidative enzymes [127, 277, 279]. For instance, Tarrago et al. showed that coniferyl alcohol, an aromatic phenolic monomer of lignin, and its derivative dimers form noncovalent host-guest inclusion complexes with CDs. They showed that among the CDs with different cavity sizes, β -CD interacts optimally with the coniferyl alcohol dimers (most specifically pinoresinol) and selectively inhibits the further oxidation of pinoresinol by the enzymes [127]. Moreover, the inclusion complex formed by α -CD with coniferyl alcohol was investigated and it was observed that α -CD interacts with an aromatic ring of coniferyl alcohol. The resulting inclusion complex forms with an 1.4 equivalent of α -CD for every coniferyl alcohol molecule [277]. Additionally, the complexation of β - and γ -CDs with α -guaiacoxycetoveratrone (GAV), a model compound containing key properties of lignin, was studied by Okano et al. [280]. It was observed that GAV is incorporated into both β -CD and γ -CD interiors to some extent. However, GAV is too large to entirely fit inside the β -CD cavity, thus for 1:1 complexes, some portion of the molecule is exposed to the bulk medium. At higher β -CD concentrations, small amounts of 1:2 (GAV: β -CD) complex form, which encompass the entire GAV molecule and protect it from the medium [280].

Investigating the nature of the binding between cyclodextrins and lignin small molecules with different chemical structures is a crucial initial step to evaluate the potential of cyclodextrins to protect and separate lignin small molecules, and to develop selective lignin small molecule separation techniques. Isothermal titration calorimetry (ITC) is a robust technique that can be used to measure enthalpies, entropies and equilibrium association/dissociation constants of complex formation, and has been widely employed to investigate the interaction of the CDs with the guest molecules [133-136, 138]. The

purpose of this study is to use ITC to advance our understanding of the selectivity of inclusion complexes of lignin dimers with β -CD with the goal of controlling and preventing the polymerization and oxidation of specific lignin derivatives in a lignin deconstruction mixture. A set of dimers based on guaiacyl (G) units (derivatives of coniferyl alcohol) are used to demonstrate structure-dependent binding to β -CD.

6.3 Materials and Methods

6.3.1 Chemicals and Reagents

Deionized water (ASTM type II), isopropanol (i-PrOH, 99%), and acetonitrile (ACN) were purchased from VWR International; β -cyclodextrin (β -CD, >97%) and guaiacylglycerol- β -guaiacyl ether (G- β O4'-*trunc*G, \geq 97%) dimer were purchased from TCI America; pinoresinol (G- $\beta\beta$ -G, \geq 95.0%) was purchased from Sigma Aldrich. All chemicals were used as received without further purification.

6.3.2 G- β O4'-G Lignin Dimer Synthesis

1-(4-hydroxy-3-methoxyphenyl)-2-[2-methoxy-4-(3-hydroxyprop-1-en-1-yl)phenoxy]propane-1,3-diol (referred to as G- β O4'-G in this dissertation) was synthesized by Dr. Lynn's group at University of Kentucky. The synthesis process of this dimer is described by Asare et al. [29]. G- β O4'-G lignin dimer has a 3-hydroxyprop-1-enyl tail but possesses the identical β O4 linked units as the guaiacylglycerol- β -guaiacyl ether, which is the commercially available G- β O4'-*trunc*G lignin dimer.

6.3.3 Isothermal Titration Calorimetry (ITC)

Isothermal titration calorimetry (ITC) measurements were conducted in a Low Volume Nano-ITC instrument (TA Instrument) including a gold sample cell. The lignin GG dimers have poor solubility in water. Therefore an organic solvent was used to solubilize the dimers. Solutions of β -CD and the three lignin dimers were made in a mixture of ACN/water (10% v/v) as well as a mixture of i-PrOH/water (10% v/v), separately. Both β -CD and lignin dimers solutions were degassed for 15 min before starting the ITC experiments to eliminate any gas bubble. The reference cell of the ITC device was filled with DI water. In a typical ITC experiment, 48.1 μ L of the β -CD solution (5 mM) was injected into the ITC cell containing 200 μ L of a lignin dimer solution (0.5 or 0.7 mM for G- β O4'-G and G- $\beta\beta$ -G, or G- β O4'-*trunc*G dimer respectively) with 13 distinct injections (3.7 μ L per injection) consecutively with a stirring rate of 350 rpm. The cell temperature was maintained at 298 K. Prior to starting the injections, adequate time was given for the baseline of the heat signal to stabilize and to diminish noise in the baseline level. Raw heat data (μ J/s) per injection were recorded with ITCRunTM software (TA Instruments) as a function of time. Dilution experiments were conducted by injecting β -CD solution (5 mM) in a cell containing 200 μ L of corresponding solvent (ACN/water or i-PrOH/water) without any dimers. Raw data (thermograms) are presented after correction for baseline drift in heat signal using NanoAnalyzeTM software (TA Instruments).

6.3.4 ITC Data Analysis and Fitting of Binding Models

The integrated heats (μ J) for each injection peak are calculated from the peak's starting point to its end (the return of the heat signal to the baseline) using NanoAnalyze

software. Integrated heat profiles, which are referred to as isotherms, were calculated by dividing the integrated heats (with dilution heat subtracted) at each injection point by the number of moles injectant per injection. As a conventional procedure, to avoid artifacts caused by mixing effects of syringe contents into the cell, the first injection point is removed [281]. Independent single thermodynamic binding models were fit to uniphasic binding curves of the isotherms using NanoAnalyze software. Thermodynamic parameters of binding (association constant (K_a), number of binding sites (n), and enthalpy change (ΔH)) are determined by non-linear least squares regression, where there are three fit parameters per binding site. Initially, n , ΔH and K_a are considered as floating variables during least squares fitting according to a Wiseman isotherm (single site binding model) [144, 282, 283]. The Wiseman isotherm describes a Langmuir-based equilibrium (**Equation 6.1**) between a ligand (X) and a receptor (M) with one set of identical binding sites [144, 145]. For the binding reaction demonstrated in **Equation 6.2**, the overall energy balance (**Equation 6.3**) and overall mass balance (**Equation 6.4**) are used to calculate the amount of heat generated by using **Equation 6.5**.

$$K_a = \frac{\theta}{(1-\theta)[X]} \quad (6.1)$$



$$Q = n\theta[M]_t\Delta HV_0 \quad (6.3)$$

$$[X]_t = [X] + n\theta[M]_t \quad (6.4)$$

$$Q = \frac{n[M]_t\Delta HV_0}{2} \left[1 + \frac{[X]_t}{n[M]_t} + \frac{1}{nK_a[M]_t} - \sqrt{\left(1 + \frac{[X]_t}{n[M]_t} + \frac{1}{nK_a[M]_t}\right)^2 - 4 \frac{[X]_t}{n[M]_t}} \right] \quad (6.5)$$

where $[X]_t$ and $[X]$ are the total and equilibrium ligand concentration, n is the number of binding sites, $[M]_t$ and $[M]$ are the total and equilibrium receptor concentration, Θ is the fraction of binding site occupied by ligand, and V_0 is the active cell volume [144, 284]. Based on the values of ΔH and K_a , the Gibbs energy of complex formation (ΔG) and the entropy of complex formation (ΔS) have been calculated using the thermodynamic relation presented in **Equations (6.6)** and **(6.7)**:

$$\Delta G = -RT \times \ln(K_a) \quad (6.6)$$

$$\Delta G = \Delta H - T\Delta S \quad (6.7)$$

where T is the isothermal temperature of the experiments and R is the gas constant (J/mol/K).

6.4 Results and Discussion

6.4.1 β -CD-Dimer Binding Thermodynamic Parameters

While for most binding studies, the receptor is usually in the cell and the ligand in the syringe, in the case of CD-guest interactions, cyclodextrin solution is placed in the syringe and the poorly water soluble guest is placed in the cell [136]. Moreover, to prevent self-aggregation of the cyclodextrins as well as production of high heat of dilution, use of highly concentrated cyclodextrin solutions is avoided. Bertaut et al. observed that heats of dilution were minimal for β -CD solution concentrations up to 5 mM and that the ratio between host and guest concentrations should be at least ten to achieve an acceptable binding isotherm [136]. Therefore, in this study, a concentration of 5 mM was selected for the β -CD solutions and a concentration range of 0.5-0.7 mM was selected for the dimer solutions placed in the

cell. Lignin dimers used in this study have poor water solubility, therefore co-solvents were used to dissolve the guest molecules [125]. Herein, a small amount of ACN or i-PrOH (10% v/v relative to water) were separately used as co-solvents to solubilize the lignin dimers in water. ACN was initially chosen as a polar organic solvent in an effort to minimize its impacts on CD-dimer interactions. However, there are concerns about its interactions with the gold cell, so i-PrOH was also used to confirm trends without interfering ACN-gold interactions.

ITC profiles for dilutions of β -CD (5 mM) in two different mixtures (ACN/water and i-PrOH/water) are presented in **Figure 6.1a** and **6.1b**, respectively. It should be noted that based on the chemical compatibility chart provided by TA Instruments (not shown), it is not recommended to use acetonitrile in the gold cell instruments, because use of acetonitrile will result in obtaining noisy data. Generally, use of Hastelloy as the cell material would resolve such compatibility issue. Because of the instrumental limits associated with use of ACN as the cosolvent, the ITC experiments could not be reproduced in ACN/water. Therefore, while the preliminary ITC data in ACN/water are still reported in this chapter, i-PrOH was selected as an alternative cosolvent and the measurements were performed in i-PrOH/water (10% v/v). Our preliminary results suggested that the dilution and binding interactions of β -CD in i-PrOH/water medium per every injection took longer to stabilize, therefore, the time between consecutive injections was increased to 300 s compared to 200 s for the ACN/water mixture. As observed in **Figure 6.1**, the heat of dilution of β -CD in i-PrOH/water (5 mM) into i-PrOH/water is significantly larger than that of β -CD into ACN/water. While solvent or buffer mismatch (i.e. the solvent used in the syringe being slightly different than the one in the cell) is a common reason for

observing large heats of dilution, herein, several trials yielded the similar results for the dilution of β -CD in i-PrOH/water into i-PrOH/water which potentially mean that the nature of the interaction between isopropanol and β -CD is different than that of ACN and β -CD.

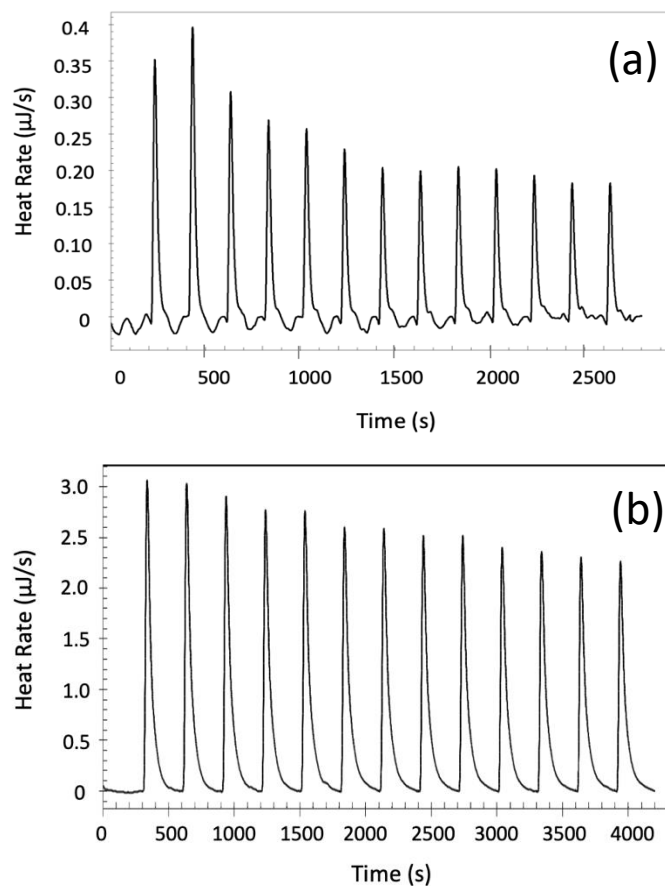


Figure 6.1 Heat of dilution of β -CD (5 mM) into (a) ACN/water (10% v/v), and (b) i-PrOH/water (10% v/v) at $T=298$ K.

ITC titration curves of the binding interaction between lignin dimers and β -CD are illustrated in **Figure 6.2a-c** (in ACN) and **Figure 6.3a-c** (in i-PrOH). Integrated heats for the corresponding dilution of β -CD (β -CD into corresponding solvent mixture, shown in **Figure 6.1**) was also calculated and subtracted from the heat of β -CD into dimers (**Figure 6.2a-c** and **Figure 6.3a-c** to find the heat of interaction at each injection point. As presented

in **Figure 6.2a-c** and **Figure 6.3a-c**, the heat profiles for all three dimers in both media are exothermic ($\Delta H < 0$), indicating that heat is released upon injections of aliquots of β -CD into lignin dimer solutions. The heat profiles also show that after each injection, the size of the peaks decreases indicating a reduction in the amount of the released heat per injection. As the concentration of available guest molecules in the solution decreases and the solution becomes saturated with the β -CDs, the heat signal plateaus progressively [125, 285]. The diminishing heat profiles shown in **Figure 6.2a-c** and **Figure 6.3a-c** suggest that as the injections proceed, fewer dimer molecules are available to interact with the newly injected β -CD molecules, and consequently, less heat is produced.

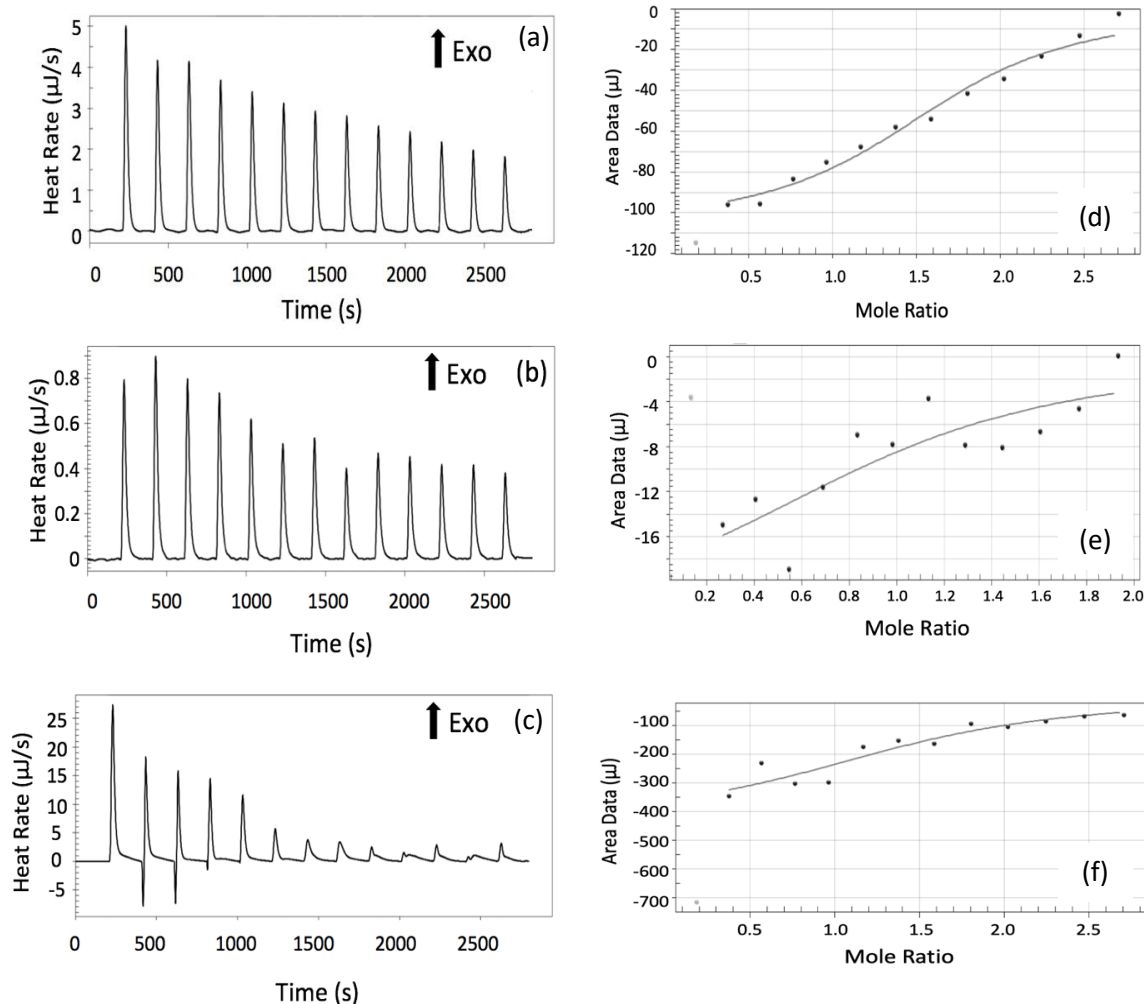


Figure 6.2 Raw heat rate with time for β -CD (5 mM) interaction with (a) G- $\beta\beta$ -G (0.5 mM), (b) G- $\beta\text{O}4'$ -*trunc*G (0.7 mM), and (c) G- $\beta\text{O}4'$ -G (0.5 mM) and integrated heat profiles after subtraction of dilution heat plotted against molar ratio of β -CD to the lignin dimers: (d) G- $\beta\beta$ -G, (e) G- $\beta\text{O}4'$ -*trunc*G, and (f) G- $\beta\text{O}4'$ -G in ACN/water mixture at $T=298$ K. First injection points were eliminated from thermodynamic analysis. Data points above integrated heat (μJ)= 0 (illustrated in pale gray) are automatically not included in the fitting model.

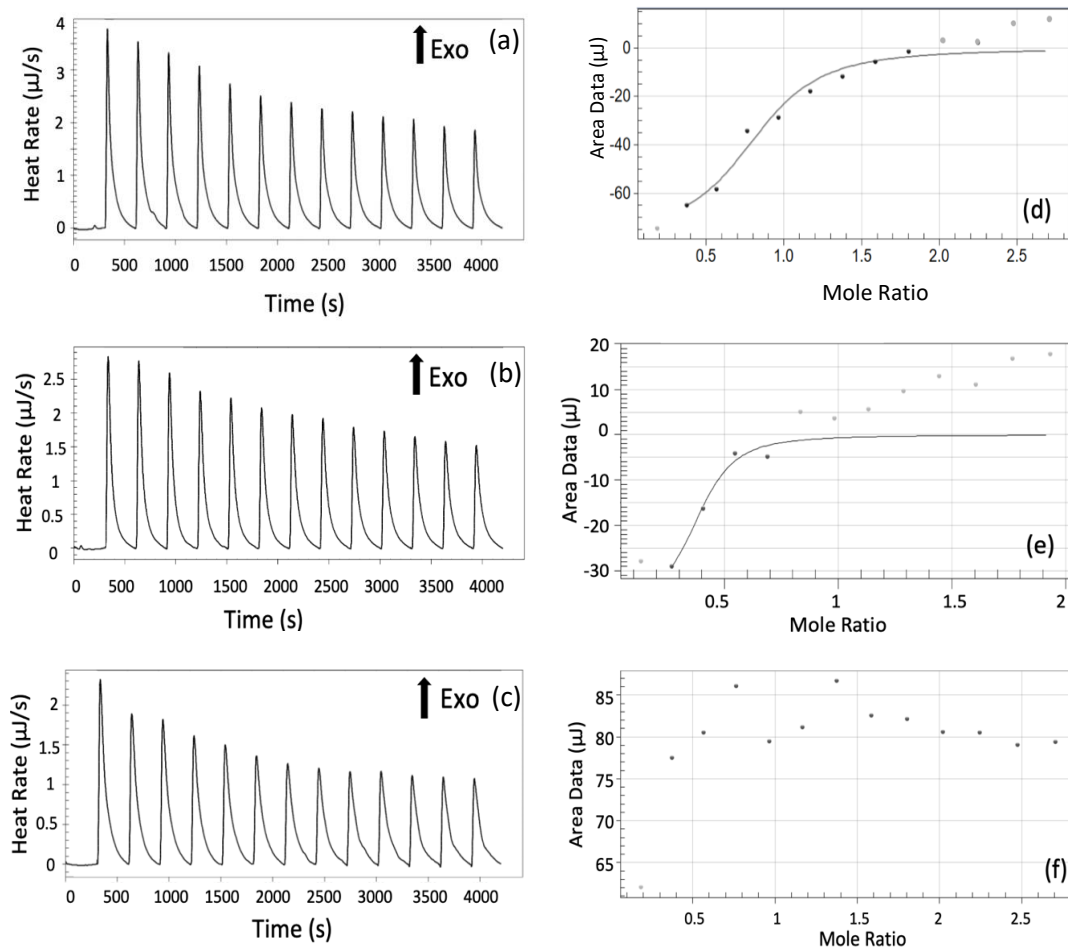


Figure 6.3 Raw heat rate with time for β -CD (5 mM) interaction with lignin GG dimers for (a) G- $\beta\beta$ -G (0.5 mM), (b) G- $\beta\text{O}4'$ -*trunc*G (0.7 mM), and (c) G- $\beta\text{O}4'$ -G (0.5 mM) and integrated heat profiles after subtraction of dilution heat plotted against molar ratio of β -CD to the lignin dimers: (d) G- $\beta\beta$ -G, (e) G- $\beta\text{O}4'$ -*trunc*G, and (f) G- $\beta\text{O}4'$ -G in i-PrOH/water mixture at $T=298$ K. First injection points were eliminated from thermodynamic analysis. Data points above integrated heat (μJ) = 0 (illustrated in pale gray) are automatically not included in the fitting model.

Figure 6.2d-f and **Figure 6.3d-f** demonstrates the curve fitting (isotherms) of the heat of complex formation for the studied systems. The areas under the peaks in **Figure 6.2a-c** and **Figure 6.3a-c** were integrated, corrected for the dilution effects (integrated heats for the dilution of β -CD into the corresponding solvent mixture were subtracted from the heat of dilution of β -CD into dimers), and presented as a function of the molar ratio of

β -CD to the dimers in **Figure 6.2d-f** and **Figure 6.3d-f**. The thermodynamic parameters of complex formation calculated by the model of a single set of identical sites (Wiseman isotherm) for all the investigated inclusion complexes are presented in **Table 6.1**. Generally, the parameter c governs the shape of the binding curve and geometrical features of the Wiseman binding isotherm which is calculated as shown in **Equation 6.8** [286]:

$$c = n \times K_a \times [M]_t \quad (6.8)$$

where n is the number of binding sites per receptor, K_a is the association constant, and $[M]_t$ is the total receptor concentration [286-288]. $c \leq 1$ yields a featureless binding isotherm with a shallow slope where the binding affinity can be determined with acceptable uncertainty, but the enthalpy cannot be precisely estimated unless the stoichiometry is already well known [286]. If $c \geq 10000$, a rectangular isotherm (step function) is acquired, from which the binding enthalpy can be estimated quite accurately, but the binding affinity cannot be reliably calculated [286, 287]. Ideal values for c fall within the [5-500] range, at which the receptor saturation can be fulfilled by injecting as little as 2 equivalents of ligand [144, 288]. Based on the data from **Table 6.1**, for G- $\beta\beta$ -G in ACN/water, c is greater than 5 ($c \sim 8$), therefore the shape of the binding curve (**Figure 6.2d**) is the appropriate sigmoidal shape for fitting the Wiseman isotherm. However, for G- β O4'-*trunc*G and G- β O4'-G in ACN/water (which are considered as low affinity systems ($\log K_a < 4$) [288]), the c values are small (~ 2.8 and ~ 3 , respectively), so fitting (**Figure 6.2e-f**) results in the large uncertainties for the enthalpy values presented in **Table 6.1** [287]. Variations in the shape of an ITC titration curve with c values are qualitatively shown in **Appendix Figure C.1** (reproduced from Ref. [288] with permission from American Chemical Society, copyright 2003).

A negative Gibbs free energy (ΔG) accounts for the spontaneity of the interaction, and the more negative the ΔG is, the greater the driving force for spontaneous binding [125]. Enthalpic and entropic contributions (which are frequently termed as driving factors) compromise the ΔG . Direct comparison of the absolute values of $|\Delta H|$ and $|T\Delta S|$ provides information about whether the complex formation is entropy-driven or enthalpy-driven. Determining the driving factor provides valuable information about the forces involved in the binding. In guest-CD complex formation, usually a combination of multiple forces and phenomena (including the hydrophobic interactions, electrostatic (Coulombic) interactions, van der Waals forces, hydrogen bonding, dispersive interactions, and charge–transfer interaction) happen simultaneously with some contributing more than the others [122, 132].

Table 6.1 Thermodynamic parameters for β -CD interaction with lignin GG dimers as determined using a one-binding site model through ITC at T=298 K. (confidence level=95%)

Dimer	Medium	n (mol β -CD/mol dimer)	K_a (M^{-1}) $\times 10^3$	ΔG (kJ/mol)	ΔH (kJ/mol)	$T\Delta S$ (kJ/mol)
G- $\beta\beta$ -G	ACN/water	1.6 ± 0.14	14.0 ± 9.0	-24.0 ± 2.0	-5.8 ± 0.5	19.0 ± 2.0
G- $\beta\beta$ -G	i-PrOH/water	0.7 ± 0.1	19.6 ± 19.6	-24.5 ± 2.5	-4.8 ± 2.1	19.7 ± 1.4
G- $\beta O4'$ - <i>trunc</i> G	ACN/water	1.0 ± 0.97	3.981 ± 1.3	-20.5 ± 0.8	-1.3 ± 14.9	19.0 ± 15.0
G- $\beta O4'$ - <i>trunc</i> G	i-PrOH/water	0.4 ± 0.2	63.1 ± 12.6	-27.4 ± 0.5	-2.1 ± 8.6	25.5 ± 8.6
G- $\beta O4'$ -G	ACN/water	1.4 ± 0.7	6.31 ± 2.0	-21.7 ± 0.8	-23.6 ± 44.8	-2 ± 45.0
G- $\beta O4'$ -G	i-PrOH/water

Based on the chemical structures, G- $\beta\beta$ -G is thought to be the most hydrophobic dimer investigated in this work. Our published work including Differential Scanning Calorimetry (DSC) and Molecular Dynamics (MD) simulations (performed by Dr. Moldovan's group at Louisiana State University) showed that the partition coefficient between DPPC lipids and aqueous solution is less for G- β O4'-G than for the G- β O4'-*trunc*G [11]. This corresponds to lower level of hydrophobicity for the former [11]. MD simulations (performed by Dr. Moldovan's group) at T=298 K and in water medium estimate the ΔG of β O4'-G dimer-CD binding to be -25 kJ/mol. The binding was enthalpy-driven, with ΔH =-37 kJ/mol, and $T\Delta S$ =-12 kJ/mol ($|\Delta H| > |T\Delta S|$) [193]. Similarly, Segura-Sanchez et al. studied the 1:1 complexation of (+)-usnic acid (UA) with β -CD and observed a large negative enthalpy (ΔH =-19.76 \pm 0.91 kJ/mol, $T\Delta S$ =-7.28 kJ/mol, $|\Delta H| > |T\Delta S|$) which is attributed to the presence of van der Waals forces dominating the interactions between (+)-usnic acid (UA) and CDs [138]. Moreover, Yamamura et al. studied the 1:1 complex formation of γ -CD with 2-carboxybenzoyl-d-glutamic-l-tyrosine and observed a large negative enthalpy value (-25.6 \pm 0.2 kJ/mol) resulting from strong van der Waals and π - π interactions between the guest's aromatic rings and the CD inside walls [139]. Inclusion complex formation of the CDs in aqueous solutions usually consist of the liberation of around 15-25 water molecules that initially filled the slightly apolar cavity of the CD into the bulk and replacement of those by the guest molecule [125, 131]. This liberation of the water molecules from the cavity to the bulk possibly contributes to an increase in entropy while the loss of degrees of freedom of the guest molecules due to binding may contribute to a decrease in entropy. Both Yamamura et al. and Segura-Sanchez et al. observed negative and unfavorable entropy values ($\Delta S < 0$) and concluded that this large negative

entropy arises from the significant translational and conformational restriction of the host and guest molecules upon complexation [138, 139].

In contrast, the interactions of the more hydrophobic G- β O4'-*trunc*G and G- $\beta\beta$ -G dimers with β -CD are entropy-driven ($|T\Delta S| > |\Delta H|$). (MD) simulation (performed by Dr. Moldovan's group) at T=298 K in water estimated the ΔG of the G- β O4'-*trunc*G and G- $\beta\beta$ -G binding to β -CD to be ~ -25 and ~ -30 kJ/mol respectively. They also confirmed that $|T\Delta S|$ is greater than $|\Delta H|$ for both of these dimers. This entropy-driven binding suggests that hydrophobic interactions play the major role in the complex formation [138]. Similarly, Sun et al. showed that the binding of paeonol and acetovanillone with β -CD is driven by entropy rather than enthalpy [135]. Their simultaneous ^1H NMR and ITC analysis suggested that the aromatic benzene rings of paeonol and acetovanillone penetrate deeply into the smaller opening of β -CD (where the primary hydroxyl groups are found) via hydrophobic interactions [135]. This occurrence leads to the liberation of energy-rich water molecules from the cavity, which results in a negative ΔH and a positive ΔS (with ΔS contributing more to the binding affinity) [135].

For some of the CD-guest systems, a correlation between enthalpy and entropy (known as enthalpy–entropy compensation) is suggested, in which an increase or decrease in ΔH is compensated by a matching concurrent increase or decrease in $T\Delta S$, such that the variation of ΔG is minimal [130, 139]. Solvent restructuring, rearrangement of solvent molecules near solute surfaces, and the dehydration of hydrophobic surface are some of the events that contribute to the enthalpy–entropy compensation phenomena [122, 130, 140, 141]. Enthalpy–entropy compensation is typically shown by a graph of $T\Delta S$ versus ΔH or *vice versa*. In either cases, the datapoints have to lie on straight lines [140]. In

Appendix Figure C.2a, $T\Delta S$ values for binding of all three lignin dimers to β -CD are plotted versus ΔH resulting in a linear fit ($R^2 = 0.98$). Further experiments are needed to reduce the uncertainty of the values and confirm these trends, but the slope ($\alpha = 0.99$) of ΔH - $T\Delta S$ plot in this figure represents the contribution of enthalpic gains to ΔG , occurring by variations in the guest molecules [289]. In **Appendix Figure C.2a**, the positive values of the intercept ($T\Delta S_0=21.78$) suggests that the inclusion complex is stabilized even if enthalpic stabilization is not present ($\Delta H=0$) [289]. In **Appendix Figure C.2b**, all $T\Delta S$ from **Table 2.1 (Chapter 2)** in addition to the $T\Delta S$ values for binding of the three lignin dimers are plotted versus ΔH for comparison.

6.4.2 Effect of i-PrOH on the Binding Thermodynamic Parameter

Because of the instrumental limits associated with use of ACN as the cosolvent (incompatibility of the gold sample cell with ACN), the ITC experiments could not be repeated in ACN/water to improve the high error values in **Table 6.1**. Thus, i-PrOH was selected as an alternative cosolvent and the measurements were performed in i-PrOH/water (10% v/v). The biggest issue associated with use of i-PrOH as a cosolvent in a system containing CD is the strong interaction of this alcohol with β -CD as inferred from the high dilution heat per injection of β -CD in blank i-PrOH/water mixture (**Figure 6.1b**). While the isotherm for G- $\beta\beta$ -G (which is the most hydrophobic dimer studied) fit to the single site binding model well (**Figure 6.3d**), the fit for data points for the G- $\beta O4'$ -*trunc*G (which is less hydrophobic compared to G- $\beta\beta$ -G) is not equally good, as observed in **Figure 6.3e** and **Table 6.1**. The heat released per injection is very small for this dimer, and subsequently, the heat calculated after subtraction of the dilution is also small and susceptible to the variability resulting from random noise. After correcting for the heat of

dilution, the last eight injection heats for G- β O4'-*trunc*G dimer in **Figure 6.3e** were positive heats and automatically were not included in the single site binding model, therefore the values reported for log K_a and ΔG for this dimer in i-PrOH/water medium (**Table 6.1**) are based on only four data point and suffer from high uncertainty values.

It appears from the values in **Table 6.1** that switching the solvent mixture from ACN/water to i-PrOH/water increases the affinity constant (log K) and $|\Delta G|$ for the hydrophobic G- $\beta\beta$ -G dimer, although further experiments will be required to reduce the uncertainty in the measured values. Liu et al. demonstrated that alcohols can impact CD-guest interactions and alter the complex stability [290]. They reported an experiment where a small amount of i-PrOH (4 vol%) increased the binding constant of a β -CD dimer toward the dye acridine red from log K_a =3.7 to 3.9. They hypothesized that i-PrOH displaces a large amount of water from the β -CD cavity and as a result improves the hydrophobic interaction between β -CD and the hydrophobic guest [290]. Similarly, a computational study on β -CD/guest complexes in aqueous alcohol solutions reported that the branched structure of i-PrOH effectively occupies much of the space in the cyclodextrin cavity and when a 20% i-PrOH solution is used, water molecules are almost entirely extruded from the cavity by alcohol [291].

When some water molecules are substituted by i-PrOH, due to the competition between i-PrOH and the guest molecules for binding to CD, some noncovalent forces between CD and guest (e.g. hydrogen bonding interactions) are altered [290]. Here, for G- β O4'-G in i-PrOH/water medium (**Figure 6.3f**), the integrated heat values after subtraction of dilution became positive, meaning that the heat released for dilution of β -CD in blank i-PrOH/water mixture was higher than the heat released for binding of β -CD to the G- β O4'-

G in the same medium. Therefore, the single site binding model could not be fit to these data and thermodynamic parameters could not be calculated. This finding, though unfavorable, supports our speculation that G- β O4'-G dimer binds to the β -CD through enthalpy-driven forces, such as van der Waals and hydrogen bonding, because the presence of i-PrOH in the solution undermined the enthalpic binding mechanisms of β -CD to G- β O4'-G.

6.5 Conclusion

Herein, the binding of β -CD to three lignin dimers of coniferyl alcohol is studied via ITC. The equilibrium binding constant (K) and the thermodynamic binding energies (ΔH , ΔS , and ΔG) for dimer- β -CD complexes, are calculated from fitting binding models to the ITC data. The analysis of ITC results along with MD simulation (performed by Dr. Moldovan's group) demonstrates that while β -CD forms inclusion complexes of stoichiometry 1:1 with all investigated lignin dimers, the difference in the chemical structure of the lignin dimers is reflecting in different driving forces of complex formation and binding modes. The short-term future work for this study involves reproducing the thermodynamic parameters reported in **Table 6.1** and attempting to achieve lower uncertainties for the reported values. Studying the interaction of β -CD with lignin small molecules with different structures allows for designing biocompatible separation techniques to selectively protect, separate, and enrich lignin fragments in a lignin deconstruction mixture while preventing lignin repolymerization. Hence, the long-term future work for this study includes design of β -CD conjugated surfaces and subjecting those surfaces to lignin mixtures.

CHAPTER 7. SYNTHESIS OF β -CYCLODEXTRIN-FUNCTIONALIZED MESOPOROUS SILICA NANOPARTICLES

7.1 Summary

Lignin polymers contain multiple functional groups and bond types, resulting in a heterogeneous mixture from which it is difficult to analyze and separate individual lignin oligomers. Cyclodextrins have been exploited frequently in separation applications because they selectively form inclusion complexes. Immobilizing cyclodextrin on solid surfaces is a potential biocompatible and facile approach for capturing, protecting and separating lignin small molecules from a lignin deconstruction mixture. Herein, mesoporous silica nanoparticles (MSNPs) were synthesized and treated with 3-aminopropyltrimethoxysilane (APTES) to acquire amine-functionalized silica nanoparticles (MSNPs). The resultant MSNPs were conjugated with β -cyclodextrin (β -CD) by reacting mono-2-O-(p-toluenesulfonyl)- β -CD (6-TsO- β -CD) molecules with MSNPs in N-methylpyrrolidone (NMP) solvent in presence of potassium iodide (KI). The presence of β -CD on the particles was confirmed by Fourier-transform infrared spectroscopy (FTIR), dynamic light scattering (DLS), and nitrogen adsorption. Thermogravimetric analysis (TGA) shows that attachment densities of approximately 0.87 mmol amine/g particle and 0.042 mmol β -CD/g particle were achieved. The ability of β -CD functionalized MSNPs to bind to pinoresinol (G- $\beta\beta$ -G lignin dimer) as well as a fluorescent probe (6-p-toluidinylnaphthalene-2-sulfonate (TNS)) in solution is compared to MSNPs without β -CD. Our results indicate that both of the guest molecules unexpectedly show higher affinity toward the amine groups on MSNPs rather than the β -CD moieties on CD-functionalized particles, possibly due to the non-specific electrostatic interactions with amines, hydrophobic interactions with the surface, and possibly limited

accessibility to the attached CDs. While further work will be needed demonstrate selective separation using immobilized β -CDs, this work introduces the initial steps to develop a platform to investigate interactions of lignin-based solutes and biomolecules with CD-functionalized surfaces.

7.2 Introduction

Lignin, a major component of lignocellulosic biomass, is a valuable potential resource for sustainable production of bulk chemicals and aromatic compounds traditionally derived from petroleum [278, 292]. Lignin is a complicated macromolecule made up of various smaller units and bonding motifs, the deconstruction of which is challenging and energy-intensive. In directing polymeric lignin to desired polyphenols, the capacity to selectively break lignin bonds, to characterize lignin products, and to separate these polyphenols have traditionally been a burdensome task and an obstacle to obtaining value-added products from lignin [278].

To overcome the obstacles found in isolating and purifying value-added lignin products, this chapter reports progress towards developing selective lignin oligomer separations using immobilized cyclodextrins. Cyclodextrins (CDs) are cyclic oligosaccharides composed of six (α -CD), seven (β -CD), or eight (γ -CD) connected glucose units. They are shaped like truncated cones with a hydrophilic exterior surface and a hydrophobic core, which provides host-guest size selectivity [293]. Cyclodextrins are promising media for separations because they selectively bind to certain compounds based on size and chemical functionality to form inclusion complexes. Use of CD-functionalized surfaces has been proposed as a more facile, biocompatible, and nontoxic option for

detection and separation of the hydrophobic guest molecules than some arduous and expensive methods such as high performance liquid chromatography (HPLC), liquid and gas chromatography, and capillary electrophoresis [149, 150]. Solid surfaces conjugated with CDs are attracting growing attention as separation platforms because they are easy to use, separate, regenerate and reuse. Unlike unsupported (free) CDs in solution, supported CD molecules can be extracted from the reaction solution (using centrifugation, filtration, or magnetic separation) and reutilized. Moreover, the compound captured inside the immobilized CD cavities is less likely to participate in side reactions (e.g. reaction with radical moieties in the reaction mixture) [146-148].

As supports, mesoporous silica nanoparticles (MSNPs) possess large surface areas ($> 600 \text{ m}^2/\text{g}$ [294]), adjustable particle size and pore structures, and tailorable surface properties [243]. Among various functionalized MSNPs, amine-functionalized MSNPs (MSNPsAs) are employed in a broad spectrum of applications including drug and gene delivery, RNA and DNA interference and transport, as well as loading and release of viruses and proteins [295]. More importantly, amine functional groups on silica provide binding sites for attachment of other molecules and facilitates the loading, delivery, protection, and release of those molecules [145]. A variety of functionalization methods have been proposed for grafting CDs to amine-functionalized nanoparticles. For instance, Cao et al. employed APTES, a routine aminosilane coupling agent, to prepare amine-functionalized magnetic Fe_3O_4 nanoparticles (APTES-MNP). They accomplished single-site attachment by using mono-2-O-(p-toluenesulfonyl)- β -cyclodextrin (6-TsO- β -CD) as the source of β -CD and added it to the as-synthesized APTES-MNPs in N,N-dimethylhexadecylamine (NMP). During the reaction, the -OTs group was substituted by

the -NH nucleophile to form a covalently linked β -CD [296]. Similarly, Santos et al. exploited the same molecule (6-TsO- β -CD) to graft β -CD to their APTES-modified superparamagnetic iron oxide nanoparticles using a different solvent and different reaction conditions. They dispersed APTES-functionalized particles in dry dimethylformamide (DMF) and added the 6-TsO- β -CD in the same solvent. The suspension was allowed to react at elevated temperature and the resultant CD-functionalized particles were separated and purified [297]. Zhang et al. applied Staudinger reactions under mild conditions to immobilize mono-(6-azido-6-deoxy)-perfunctionalized CDs onto the surface of amine-decorated silica gel [298]. Similarly, Silva et al. anchored a β -CD derivative (3,5-dimethylphenylcarbamoylated β -CD) on the surface of MSNPAs using a urea linkage through the Staudinger reaction [148].

Immobilized CDs have the potential to harness lignin as a source of aromatic compounds because unbound CDs have been shown to form inclusion complexes with hydrophobic solutes, such as phenolic compounds (e.g., monolignols and lignin dimers) [127, 277, 279]. Quantifying and predicting the interactions of CD to monolignols and the library of dimers and trimers of known monomer and bond chemistry, and model lignin decomposition products such as vanillin and syringaldehyde is of great importance. The host-guest interactions with these model compounds can be investigated in solution and with β -CD functionalized surfaces. Herein, the long-term objective is to develop CD-functionalized nanostructured ceramics as adsorbents for the recovery of lignin dimers from lignin deconstruction mixtures. However, the short-term objective and the focus of this chapter is to develop CD-functionalized high surface area silica nanoparticles using the chemistry shown in **Figure 7.1**, and examining the host-guest interactions of these

particles with a model lignin dimer (pinoresinol) which was previously shown to bind strongly to the hydrophobic cavity of β -CD in solution (**Chapter 6**). Along with pinoresinol, the fluorescent probe (6-p-toluidinylnaphthalene-2-sulfonate, TNS) was used to validate the functionality and efficiency of the CD-functionalized particles to entrap and capture guest molecules from solution.

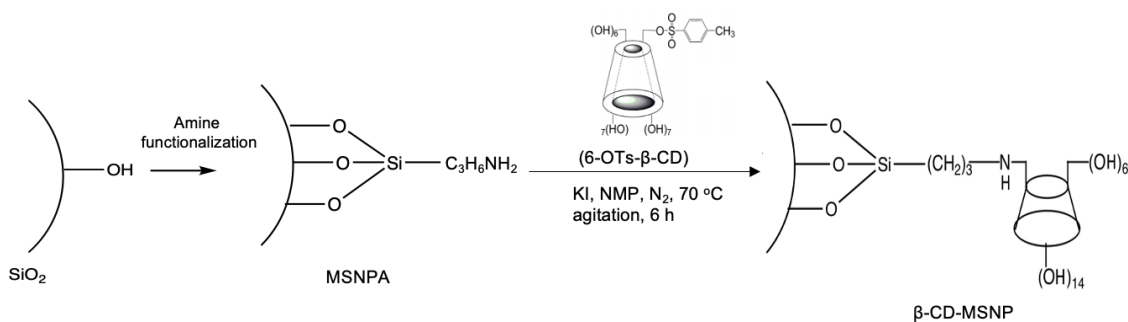


Figure 7.1 Schematics of the synthesis of β -CD-functionalized silica nanoparticles (CD-MSNPs).

7.3 Materials and Methods

7.3.1 Chemicals and Reagents

Hydrochloric acid (36.5-38%), 200 proof pure ethanol, deionized water (ASTM type II), N-methyl-2-pyrrolidone (NMP), mono-2-O-(p-toluenesulfonyl)- β -cyclodextrin hydrate ($\geq 97.0\%$), and (3-aminopropyl)trimethoxysilane (APTES, 95%) were purchased from VWR International; N,N-dimethylhexadecylamine (DMHA, $\geq 98\%$) from TCI America; tetraethyl orthosilicate (TEOS, 98%) from Fisher Scientific; octadecyltrimethylammonium bromide (OTAB) from Chem-Impex International; and Pluronic F-127, 6-(p-toluidino)-2-naphthalenesulfonic acid sodium salt (TNS), and pinoresinol ($\geq 95.0\%$) from MilliporeSigma. NaOH pellets ($\geq 97\%$) were purchased from

EMD Millipore. All of the acetate buffer solutions used in this study are 0.2 M and have a pH of 3.7.

7.3.2 Synthesis of Mesoporous Silica Nanoparticles (MSNPs)

The method of synthesis of MSNPs was previously explained in **Section 5.3.3**. MSNPs were synthesized by a surfactant templating sol-gel technique combined with pore swelling under basic conditions using a modified method established by Gu et al. [249]. Initially, 0.4 mL of DMHA, 1.02 g of OTAB and 0.3 g of Pluronic F127 were added to a solution containing 364 mL of DIUF water and 3.5 mL of 2 M NaOH at 80 °C under constant stirring. The solution was allowed to stir for an additional 30 minutes for complete dissolution of the constituents and then 5 mL of TEOS was added dropwise. A white suspension formed immediately, which was stirred for another 2 h to complete silica condensation and then the solution was cooled to room temperature rapidly. Particles were separated from the solution by high-speed centrifugation at 17,000 rpm for 5 minutes and washed with ethanol four times with repeated vortex mixing and centrifugation before being dried in an oven at 90 °C overnight. Surfactant templates were removed from the particle pores by washing with acidic ethanol according to the procedure of Khan et al. [243]. Dried as-synthesized particles were re-suspended in 200 mL of 1.5 M HCl in ethanol and allowed to stir for 48 h. Final particles were recovered by repeated high-speed centrifugation and washing with fresh ethanol and ultimately drying at 90 °C.

7.3.3 Amine Functionalization of Bare MSNPs

Amine functionalized MSNPs were acquired by condensing (3-aminopropyl)triethoxysilane (APTES) on the hydroxyl-terminated silica surface using

methods reported in the literature with slight modifications [299, 300]. Briefly, 200 mg of the MSNPs were sonicated in 25 mL of dry ethanol for 15 min until a uniformly dispersed solution was achieved. 0.5 mL of APTES was added dropwise while stirring under nitrogen environment and the solution was kept stirring overnight in a closed environment at room temperature. Particles were centrifuged at 17,000 rpm followed by repeated washing with dry ethanol, and then cured at 84 °C overnight. After curing, particles were stirred in excess ethanol for 24 h to remove any remaining loosely bound APTES and its hydrolysis products. The functionalized particles were again washed three times with dry ethanol and dried in an oven at 84 °C. Amine functionalized mesoporous particles were denoted as MSNPA.

7.3.4 Attachment of β -cyclodextrin to MSNPAs

To functionalized the silica surfaces with β -CD, a protocol proposed by Cao et al. (for grafting β -CD on APTES-coated superparamagnetic Fe_3O_4 nanoparticles) was followed with slight modifications (**Figure 7.1**) [296]. To attach β -CD to MSNPAs, mono-2-O-(p-toluenesulfonyl)- β -cyclodextrin (6-TsO- β -CD, 127.8 mg) and dried MSNPAs (81.6 mg) were placed in dry N-methylpyrrolidone (NMP) (4 mL) and the mixture was sonicated for 15 minutes before KI (3 mg) was added. Then, the suspension was heated to 70 °C and stirred. After 6 h, the reaction solution was cooled to room temperature and then particles were centrifuged out and washed with dry ethanol several times. The particles were dried in the oven at 50 °C overnight. All the procedures that NMP was involved in were carried out under N_2 protection to avoid possible oxidization during reaction. β -CD-functionalized mesoporous particles are denoted as CD-MSNPs.

7.3.5 Nanoparticle Characterization

Average pore diameter, pore size distribution, and surface area of MNSPs were estimated from nitrogen adsorption conducted at $-196\text{ }^{\circ}\text{C}$ using a Micromeritics TriStar 3000 instrument. Samples were degassed at $140\text{ }^{\circ}\text{C}$ for a minimum of 4 h under flowing dry N_2 gas before the adsorption experiment. The specific surface area was estimated using the Brunauer–Emmett–Teller (BET) isotherm, and average pore diameter and pore size distribution were estimated by the method of Barrett–Joyner–Halenda (BJH) using the adsorption branch of the isotherm. To confirm the successful attachment of β -CD, Fourier transform infrared (FTIR) spectroscopy was conducted on MSNPs, MSNPAs, CD-MSNPs, and β -CD using a Nexus 470 instrument (ThermoNicolet) with a deuterated triglycine sulfate (DTGS) detector. For the analysis, 0.5 g of KBr was mixed with the particles (0.5–1.0 wt %) and the mixture was compressed until it formed a transparent, rigid pellet. The pellet was then placed in FTIR chamber under a constant flow of dry, CO_2 -free air, and FTIR spectra were recorded using Thermo OMNIC software. Dynamic light scattering (DLS) was used for zeta potential measurement using an Anton-Paar Lightsizer 500 equipment. Around 0.1 mg of the particles were sonicated in 1 mL of acetate buffer or DI water separately (pH=3.7 and 5.8 respectively) to produce homogeneous suspensions that were analyzed in an Omega cuvette consisting of inverted Ω -shaped capillary. To quantify the amount of APTES and β -CD attached to the particles, thermogravimetric analysis (TGA) was conducted using a Universal.7A instrument (TA Instruments) using a temperature ramp of $10\text{ }^{\circ}\text{C}/\text{min}$ from 25 to $700\text{ }^{\circ}\text{C}$. Thermal decomposition of bare, amine-functionalized, and β -CD-functionalized, and was determined under N_2 .

7.3.6 UV-vis and Solution Depletion Studies with Pinoresinol

Adsorption of pinoresinol on CD-MSNPs and MSNPAs (control) was measured by following a procedure similar to that of Khan et al. [243]. The UV-vis absorbance of pinoresinol (279 nm) was used to quantify the concentration of pinoresinol in solution. The two media of ACN/water (10% v/v) and ACN/acetate buffer (pH=3.7, 10% v/v) were used for these studies. For adsorption experiments, 15 mg of particles was prewetted under vortex mixing in a series of 2 mL centrifuge tubes with 1 mL of the appropriate solvent for 24 h, and centrifuged for 3 min at 17000×g using an AccuSpin Micro 17 centrifuge (Fisher Scientific), and supernatants were discarded. Then, 1 mL of pinoresinol solutions ($C_i = 0.025, 0.05, \text{ and } 0.13 \text{ mg/mL}$) in ACN/water or ACN/acetate buffer (10% v/v) was added to the prewetted particles (both CD-MSNPs and MSNPAs as control). After vortex mixing for 24 h in the dark, the particles were centrifuged again, and 200 μL of supernatant was analyzed using a BioTek plate reader (Winooski, VT). The initial pinoresinol solution was also analyzed in the same way, and two calibration curves (in both ACN/water and ACN/acetate buffer (10% v/v), **Appendix Figure D.1**), were used to determine the amount of pinoresinol adsorbed on to the particle surface $q_{e(ads)}$ (mg pinoresinol/g particles) by solution depletion using **Equation 7.1** as shown below:

$$q_{e(ads)} = \frac{C_i - C_{e(ads)}}{m_p} V \times 1000 \quad (7.1)$$

where C_i is the initial concentration (mg/ml); $C_{e(ads)}$ is the equilibrium concentration (mg/ml) after adsorption; and m_p and V are the mass of particle (mg) and volume of the pinoresinol solution (mL) used for adsorption experiment, respectively.

7.3.7 Fluorescence and Solution Depletion Studies Using TNS

Entrapment of TNS by CD-MSNPs was qualitatively determined by taking advantage of the pronounced fluorescence enhancement of TNS when it is added to β -CD [301, 302]. Initially, 4 mg of CD-MSNPs and MSNPAs (control) were prewetted separately in acetate buffer (0.2 M, pH=3.7) for 24 hours. Use of acetate buffer for CD-TNS studies has been previously reported [301]. Next, the prewetted particles were centrifuged out and added to 4 mL of a solution of TNS in acetate buffer (10^{-5} M) in each vial. The mixtures were allowed to stir in the dark for 24 hours. After 24 hours, the fluorescence emission spectra of particles in the TNS solutions were obtained using a Cary Eclipse fluorescence spectrophotometer (Varian, Inc.) at excitation=366 nm, and were compared to the fluorescence emission spectra of particles in the blank acetate buffer (no TNS) with the same concentration (1 mg/mL). The excitation wavelength of the TNS- β -CD system is reported to be 365-366 nm [301, 302].

7.4 Results and Discussion

7.4.1 Characterization of The Particles

Mesoporous silica nanoparticles (MSNPs) were synthesized by a surfactant templated sol-gel route using TEOS as silica source with cationic surfactant OTAB as structure directing agent, DMHA as pore expander and Pluronic F127 to control particle size [249]. Templates were removed after synthesis by acidic ethanol wash. After synthesis, MSNPs were functionalized with amine groups through the reaction of APTES with surface silanol groups. The effect of functionalization on the surface properties of MSNP

was studied using nitrogen sorption isotherms and BJH pore size distribution as shown in **Appendix Figure D.2** and **Table 7.1**.

The decrease of surface area, pore volume and average pore diameter after APTES treatment are consistent with successful functionalization (**Table 7.1**). The pore size distribution of MSNPAs relative to bare MSNPs, obtained by the Barrett, Joyner and Halenda (BJH) method, indicates that pore sizes were reduced uniformly as a result of functionalization of silica pore walls without significant pore blockage. Additionally, a high specific surface area ($853.7 \text{ m}^2/\text{g}$) and pore volume ($1.51 \text{ cm}^3/\text{g}$), and large pore diameter (4-5 nm) determined by nitrogen adsorption, as well as clear capillary condensation in adsorption isotherm (type IV) suggests, uniform mesoporosity and the applicability of the nanoparticles for amine functionalization and subsequent CD grafting. Zeta potential measurements provided indirect verification of successful attachment. In acetate buffer, at a pH of 3.7, the zeta potential of the particles after amine functionalization changed from $1.8 \pm 0.3 \text{ mV}$ for bare MSNPs to $34.5 \pm 0.5 \text{ mV}$ for MSNPAs. These values are consistent with values reported by Khan et al. for similar bare MSNPs and MSNPAs at pH=4 (-2.8 and 39.3 mV respectively) [248]. The zeta potential of MSNPA is more positive than MSNPs at this pH due to the protonation of the amine groups [297]. After functionalizing the particles with β -CD, the zeta potential value increased further to $37 \pm 0.3 \text{ mV}$. The increase of the zeta potential after functionalizing with CDs suggests that the CDs' hydroxyl groups on CD-MSNPs become protonated at acidic pH, and result in more positive zeta potential values [303]. In DI water (pH=5.8), the zeta potential of the MSNPs, MSNPAs, and CD-MSNPs were measured to be -38.1 ± 1.2 , -14.0 ± 0.7 , and 13.5 ± 0.5

mV, respectively. Similar to the trend observed for pH=3.7, the zeta potential increases after functionalization with amines and CDs at pH=5.8 as well.

Table 7.1 BET surface area, BJH average pore diameter and pore size distribution obtained from nitrogen adsorption

Particle type	Pore diameter peak ^a (nm)	BJH average pore diameter (nm)	BJH pore volume (cm ³ /g)	BET surface area (m ² /g)
Bare MSNP	4.7 ± 1.1	4.16	1.51	853.7
MSNPA	4.1 ± 0.9	3.8	0.94	547.5
CD-MSNP	4.0 ± 1.05	4.16	0.88	464.7

^a The ranges are determined from the full width at half maximum (FWHM) of the BJH pore size distribution

To show successful grafting of β -CD, FTIR spectra of the particles before and after amine functionalization and β -CD attachment were measured and recorded (**Appendix Figure D.3**). The expanded FTIR spectra of MSNPAs, and CD-MSNPs are compared in **Figure 7.2**, together with the spectra of β -CD itself. As observed in **Appendix Figure D.3**, the FTIR spectra of the bare MPSNs does not contain a peak due to $-\text{CH}_2$ stretching (2800-3000 cm^{-1}), suggesting complete removal of the organic template following particle synthesis. For bare MSNPs and MSNPAs, the most prominent peaks were bands corresponding to Si-O-Si and Si-OH vibration, located at 1080 and 960 cm^{-1} , respectively [46]. Primary amine peaks are not clearly visible, but amine functionalization was quantified by chemical analysis as described previously. As shown in **Figure 7.2**, for CD-MSNPs there are peaks at 703, 860 and 944 cm^{-1} which are also observed in the spectra of β -CD and correspond to cis-RCH=CHR, C-H bending, and the α -1,4 linkage in the skeletal

mode of β -CD respectively [304, 305]. These peaks were not observed in the spectra of MSNPA (as control).

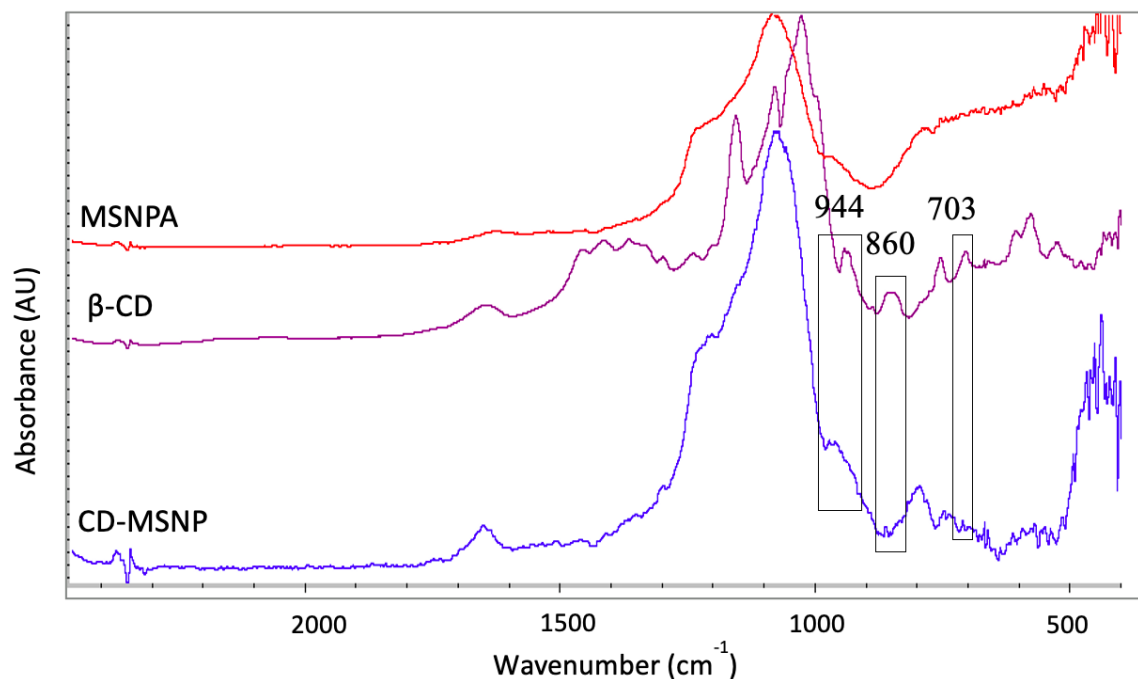


Figure 7.2 Expanded FTIR spectra of MSNPAs, CD-MSNPs, and β -CD in the range of 500-2500 cm^{-1} .

TGA was used to quantify the attachment of APTES and β -CD from the weight loss profiles of three sets of particles (bare MSNPs, MSNPAs, CD-MSNPs) as a function of temperature (**Figure 7.3**). A mass loss of 3.23, 2.63, 8.81% is observed from 25 °C to 200 °C for bare MSNPs, MSNPAs, CD-MSNPs respectively, which is attributed to evaporation of the water from the surface and the pores of the particles. The mass loss of bare MSNPs from 200 °C to 700 °C (1.54 %) is attributed to impurities such as residual template and further temperature-induced condensation of silica and is subtracted before calculating the organic content of the other particles based on mass loss in this temperature range. Additional mass loss by the organic functionalized particles (MSNPA and CD-MSNPs) in the range of 200 °C to 700 °C relative to the bare MSNPs is used to quantify

the amount of organic functional material. For MSNPAs, this additional mass loss (7.47 %) corresponds to 0.87 mmol of amine/g particle. Relative to MSNPAs, for CD-MSNPs, there is further mass losses of 4.73 % (47.3 mg β -CD/g particle or 0.042 mmol β -CD/g particle). This value is consistent with the value reported by Wang et al. (46.32 mg/g particle) where the same CD-functionalization strategy was used on magnetic Fe_3O_4 nanoparticles [306]

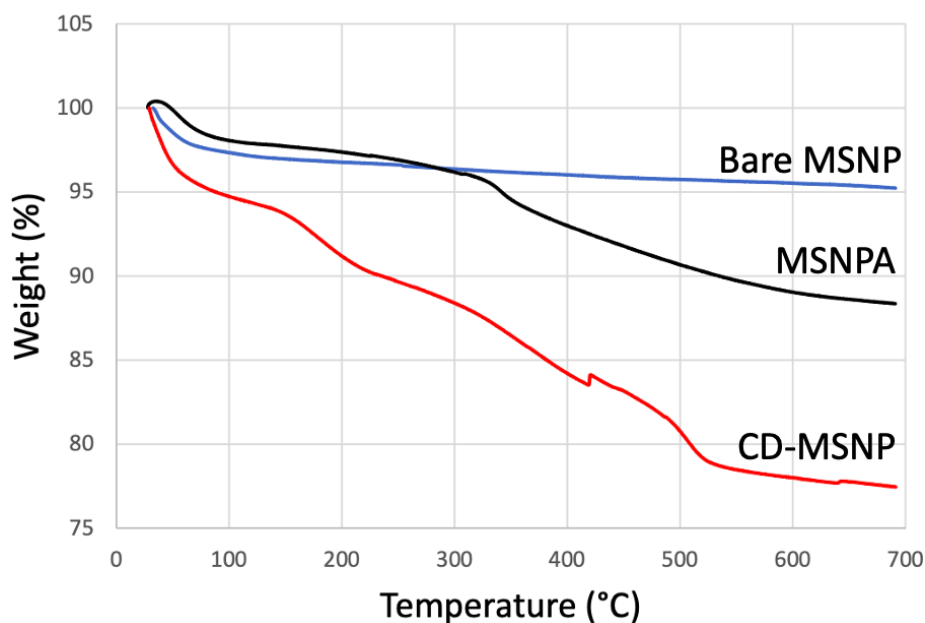


Figure 7.3 TGA of bare MSNPs, MSNPAs, and CD-MSNPs.

7.4.2 UV-vis and Solution Depletion Studies Using Pinorensinol

Using the same CD functionalization method that we used, the maximum adsorption capacities for stereoisomeric doxorubicin (DOX) and epirubicin (EPI) by β -CD functionalized Fe_3O_4 nanoparticles have been reported to be 72.48 and 39.46 mg per gram particle respectively [306]. In another study where a similar approach was utilized for CD functionalization (described in section **Section 7.2**) it is reported that loaded amount of DOX is 0.81 mg per every gram of the CD-MNP [297]. Herein, to quantify the binding

of pinoresinol into the CD cavities on the particles, both CD-MSNPs and MSNPAs (as control) were placed with pinoresinol under vortex mixing for 24 hours in the dark. **Figure 7.4** illustrates the changes in the amount of pinoresinol adsorbed on the particles ($q_{e(ads)}$) versus the equilibrium concentration ($C_{e(ads)}$) of pinoresinol in the supernatant solutions. Details of these measurements are thoroughly included in **Appendix Table D.1-4**. As shown in **Figure 7.4** both MSNPAs and CD-MSNPs can adsorb pinoresinol, with MSNPA exhibiting a larger binding affinity for pinoresinol than CD-MSNPs. Numerous studies observed an event where the hydrophobic guest molecules showed an affinity towards both APTES functionalized and β -CD functionalized nanoparticles with higher affinity towards the latter because of the inclusion complex formation with β -CD [297, 306, 307]. However, results at pH=5.8 indicate that the adsorption of pinoresinol by MSNPA is higher than CD-MSNPs. This unexpected observation can possibly suggest that there are charge interactions between positively charged amines and oxygen lone pairs or deprotonated pinoresinol. The non-specific binding and adsorption of pinoresinol to the MSNPAs can also be attributed to the hydrophobic interactions between pinoresinol and aminopropyl groups as well as the tendency of hydrophobic pinoresinol to bind to the particles' surfaces just to avoid remaining in water [306, 307].

As illustrated in **Figure 7.4**, at low pH of 3.7, the loading of pinoresinol by MSNPAs dramatically decreased. Electrostatic interactions of small molecules and amines are pH dependent. At pH=3.7, the surface of MSNPAs bares a markedly high positive charge that results in the reduction of proton activity at the surface [308]. Additionally, we can speculate that at pH=3.7, the numbers of deprotonated pinoresinol molecules or oxygen

lone pairs of pinoresinol decreases significantly, and hence the electrostatic interactions between pinoresinol and amines decreases dramatically as observed in **Figure 7.4**.

Figure 7.4 also shows that at pH=3.7, the loading of pinoresinol by CD-MSNPs significantly diminished as well. There are several studies in which the effect of pH on the loading of the solutes by free β -CD in solution as well as immobilized β -CDs has been investigated [306, 309, 310]. Changing the pH can potentially impact loading of the solutes by CDs [310]. This impact depends on the functional groups and charge properties of the solute, and changes in polarity and conformation of the solutes at different pHs. For instance, Wang et al. studied the effect of pH on the loading of stereoisomeric doxorubicin (DOX) and epirubicin (EPI) on β -CD functionalized Fe_3O_4 nanoparticles and showed that the drugs loading capacity decreases significantly from pH 7.0 to 3.0, and the highest loading is attained at pH=7 [306]. Similarly, Zhu et al. showed that salicylfluorone easily includes into the CD cavity at pH=6 via hydrophobic interactions [309]. However, in acidic and basic environments (pH=3.2 and 9 respectively), salicylfluorone becomes charged [309]. This change ultimately weakens the salicylfluorone's binding to the hydrophobic interior of the CDs which was driven by hydrophobic interactions [309]. Here also, it seem like lowering pH decreases the surface hydrophobicity of pinoresinol and weakens the hydrophobic interactions between pinoresinol and the CD cavity. This could be responsible for part of the dramatic decrease observed in **Figure 7.4** for CD-MSNPs.

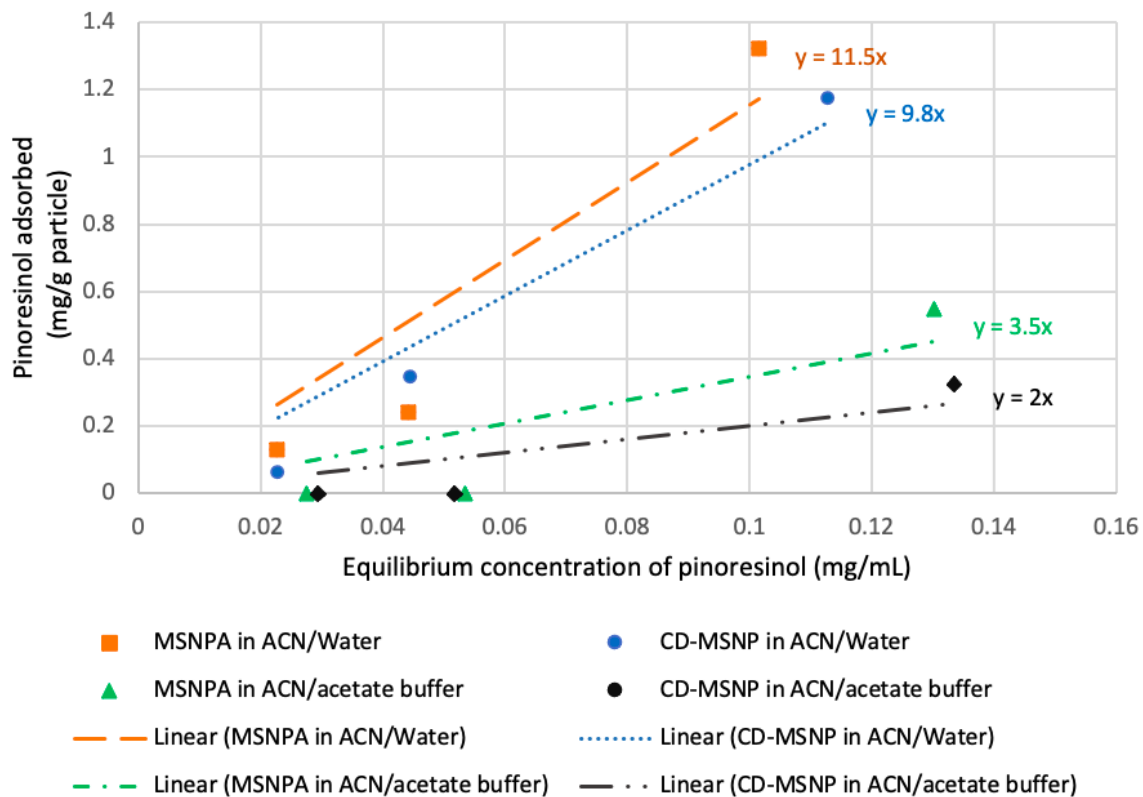
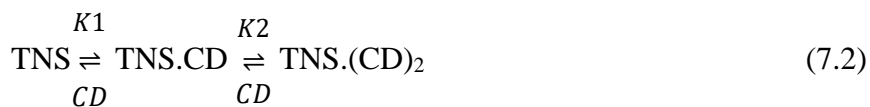


Figure 7.4 Comparison between MSNPAs and CD-MSNPs in terms of pinosresinol adsorption in two different media, ACN/water (pH=5.8) and ACN/acetate buffer (pH=3.7). Data points and lines represent experimental values and corresponding Langmuir linear fit, respectively.

7.4.3 Fluorescence and Solution Depletion Studies Using TNS

β -CD forms 1:1 as well as 2:1 complexes with TNS; in the latter one TNS molecule binds to two β -CD molecules [301] as shown in **Equation 7.2** below:



Formation constants K_1 and K_2 for 1:1 and 2:1 complexes, respectively were measured to be 3240 and 11.9 M^{-1} in phosphate buffer (pH=7.4, $T=25^\circ\text{C}$) [302]. TNS fluorescence increases significantly when β -CD is added to the aqueous solution [302]. The

remarkable enhancement of TNS fluorescence upon inclusion might be because of an alteration in the environment from hydrophilic in aqueous medium to hydrophobic (in the CD cavity) or to a change in the freedom of intramolecular rotation of TNS [301]. The excitation and emission wavelengths of the TNS- β -CD system are 366 nm and 460 nm respectively [301]. Comparing the fluorescence emission spectra of particles suspension with and without TNS can potentially help with qualitative confirmation of formation of CD-TNS complex on the particles and the presence of accessible β -CD on the CD-MSNPs. Based on the TGA data, for every 1 mg of the CD-MSNPs, there are 4.2×10^{-5} mmol β -CD present on the particles, hence the concentration of immobilized β -CD in the particle suspensions is 4.2×10^{-5} M. The fluorescence spectra of both CD-MSNPs and MSNPAs suspensions in acetate buffer (1 mg/mL) with and without TNS (10^{-5} M) were obtained and are illustrated in **Figure 7.5**. The reason that the particle concentration of 1 mg/mL was selected for this study is that at higher concentrations (e.g. 10 mg/mL), the background noise from the presence of the particles in the suspension interferes with the fluorescence intensities and results in noisy and inaccurate readings. At lower concentrations (0.1 and 0.01 mg/mL), there is not enough CDs present on the CD-MSNPs to provide a significant and noticeable signal once bound to TNS. The spectra of various blank particles suspensions at different particle concentrations in acetate buffer are shown in **Appendix Figure D.4**).

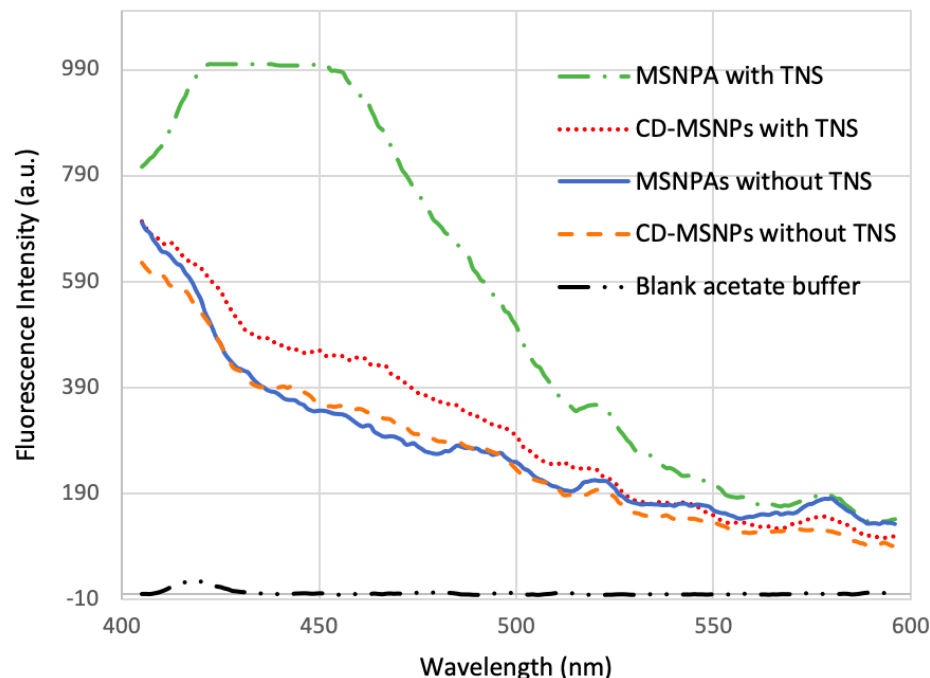


Figure 7.5 The emission fluorescence spectra of MSNPA and CD-MSNPs in acetate buffer (1 mg/mL, pH=3.7) before and after adding TNS (10^{-5} M) to the suspensions. $\lambda_{\text{excitation}}=366$ nm. For “MSNPA with TNS” in the $\sim 421\text{--}456$ nm range, the fluorescence intensity readings were outside of the dynamic range (overflow), hence the datapoints in that range are shown as a flat horizontal line.

As observed in **Figure 7.5**, the spectra of CD-MSNPs with and without TNS are similar, suggesting that the TNS did not adequately bind to the immobilized CDs on the particles to demonstrate a noticeable fluorescence peak at 460 nm. However, the pronounced spectra of MSNPAs after addition of TNS shows that there has been some non-specific binding of TNS to the APTES moieties.

Collectively, our results indicate that there is not clear evidence that the β -CD on CD-MSNPs is accessible to pinoresinol or TNS, and it also appears that the affinity of pinoresinol and TNS to the particles is caused by interactions with the amine functional groups. We would not have expected all amines to completely bind to β -CD after β -CD functionalization (maximum $\sim 4\text{--}5\%$ of amines are expected to have reacted with

cyclodextrins based on TGA), so it raises concerns that the functionalization procedure may be masking or cleaving off some of the rest of amines without actually attaching adequate and accessible β -CDs. It is also possible that the β -CDs are there but are not oriented in a direction that provides access to the hydrophobic cavity.

There are a number of ways the findings in this chapter can lead to new avenues to explore in future studies. Trying a different CD functionalization with less intensive reaction conditions and higher CD attachment efficiency is one way to achieve this (e.g. the method of CD functionalization by Santos et al. [297] as explained in **Section 7.2**). Another way of improving future studies would be to select a fluorescence-responsive or UV-vis-responsive CD probe that does not respond to adsorbing to charged surfaces (like TNS does). For instance, when using N,N-dimethylaminonaphthyl-(acrylo)-nitrile (DMANAN) as a guest with β -CD, a new fluorescence emission band grows near 420 nm due to complexation [311]. That band is totally absent if no β -CD is present. More importantly, although DMANAN binds to CTAB micelles in solution (most similar to our amine-decorated particles), the presence of the band near 420 nm depends on pH. The band is there at low pH, but not at high pH. Thus, performing fluorescence studies near neutral pH using DMANAN allows the use of the 420 nm band as evidence of CD binding [312]. Moreover, negative calorimetric detection techniques using phenolphthalein can also be employed to detect β -CD on the particles. Once phenolphthalein under alkaline

solution is incorporated into the cavity of β -CD ($K_a=21600 \text{ M}^{-1}$), its UV-vis absorption at 546-550 nm decreases, hence β -CD can be detected with high detection limit of $1 \text{ }\mu\text{g/ml}$ (0.77 nmol/ml) [313]. More importantly, it is shown that polyethylenimine (PEI) functionalized nanoparticles (containing $(\text{NH}_2)_n$ groups on the surface) do not adsorb a significant amount of phenolphthalein [314], thus in our case, the non-specific binding to MSNPs is expected to not be an issue using this technique.

7.5 Conclusion

In summary, a strategy was proposed to functionalize mesoporous silica nanoparticles (MSNPs) with β -cyclodextrins (β -CD) as host molecules with inclusion complex formation properties. The attachment strategy was based on initial decoration of the surface of silica with amine groups using 3-aminopropyltrimethoxysilane (APTES), and subsequent covalent attachment of β -CD to the grafted amine groups. The functionality of the as-synthesized particles was examined in the presence of pinosresinol, a hydrophobic model lignin dimer, as well as TNS, a fluorescence probe known to exhibit a fluorescence intensity increase upon formation of CD-TNS inclusion complexes. Our findings suggest that both of the guest molecules demonstrate greater affinity toward the amine groups on MSNPs instead of the β -CD molecules on CD-MSNPs. This phenomenon is attributed to the non-specific hydrophobic interactions with amines as well as the possible wrong orientation of attached β -CD moieties which limits the access of the guest molecules to the hydrophobic interior.

Developing efficient CD-functionalized particles with accessible grafted CD molecules and finding a way to limit the non-specific binding of guest molecules to the particles is very much the key components in future attempts to overcome. Once such CD-functionalized particles are developed, they could potentially serve as an environmentally benign platform for selective separation, loading, and delivery of lignin oligomers.

CHAPTER 8. CONCLUSIONS AND FUTURE DIRECTIONS

The overall objective of this dissertation is to find ways of capitalizing on the underutilized lignin and its derivatives by learning more about lignin oligomers (more specifically lignin dimers) and establishing structure–function relationships for well-defined lignin derivatives. Understanding the characteristics and behavior of lignin oligomers of different structures at biologically relevant surfaces is the initial step for designing value-added lignin-based pharmacological and therapeutical products and has been investigated in this dissertation. Moreover, developing versatile biocompatible approaches to purify and valorize desired lignin oligomers from lignin deconstruction mixture also falls within the locus of attention of this dissertation.

Chapter 3 describes the interactions between fully hydrated DPPC liposomes and coniferyl alcohol-derived lignin G-G dimers and their chemically modified derivatives at low concentrations using DSC. In **Chapter 4**, the interactions of the concentrated amounts of these dimers with supported DPPC lipid bilayers were probed using QCM-D. Findings presented in **Chapter 3 and 4** strengthen our understanding of characteristic needed for lignin oligomers to be utilized as potential biologically-active compounds. It was revealed that the more hydrophobic G- β O4'-*trunc*G and *benz*G- β O4'-G dimers penetrated more deeply into the bilayer interior and have a greater affinity for the bilayer interior. This conclusion is drawn from the higher liposome-water partition coefficients as well as greater mass of dimer diffused into the supported lipid bilayer and the dissipation (viscoelasticity) of the bilayer for these two dimers. In contrast, the G- β O4'-G dimer exhibited weaker affinity towards the interior of the lipid bilayer as deduced from the minimal shifts in the gel-fluid transition temperature. In addition, G- β O4'-G dimer had the smallest partition

coefficient, consistent with the least mass uptake and impact on dissipation of the bilayer as measured by QCM. As suggested by other studies [110], possessing more than three free hydroxyl groups in the chemical structure of a small molecule acts as a barrier against the deep transport of the molecule into the lipid bilayer interior. G- β O4'-G has four free hydroxyl groups, one of which is part of the hydroxypropenyl (HOC_3H_4-) tail. These free hydroxyl groups increase the hydrophilicity of the dimer and result in residence of most of this dimer on the surface of the bilayer rather than its interior. The results from **Chapters 3 and 4** suggest that the hydrophobicity of the lignin oligomers correlates with their affinity towards the lipid bilayers and appears to be of great importance for their interaction at biologically-relevant surfaces. Functional groups that contribute to the hydrophilicity of lignin oligomers (e.g. -OH groups) may present a hindrance to the penetration of the oligomers into the cell, and thus may obstruct their bioavailability. This inhibition can be bypassed by discarding those functional groups or introducing additional hydrophobic groups to the oligomers' chemical structures. Combined with the Molecular Dynamics simulation results (conducted by Dr. Moldovan's group at Louisiana State University), **Chapters 3 and 4** provide a detailed picture of the studied dimers' activity at a model of the biological cell membrane. To further the goal of this study, lignin dimers can be chemically modified to become more hydrophobic and can be examined with actual bacteria and/or bacteria-membrane mimetic model systems to test for their potential antimicrobial properties with respect to microorganisms. The work done in **Chapter 3 and 4** shows that the combination of experiments with MD simulations can be effectively utilized to systematically investigate and screen the interactions of lignin oligomers and their derivatives with lipid bilayers.

In **Chapter 5**, mesoporous silica nanoparticles (MSNPs) were successfully grafted with eugenol and allyl-modified G- β O4'-*trunc*G lignin dimer (G-eug dimer) via thiol-ene click chemistry. The proposed step-by-step attachment strategy involved functionalizing bare MSNPs with thiol groups, followed by covalent binding of eugenol and G-eug dimers molecules to thiol functional groups on the particles using UV-activated reactions. QCM-D was employed to probe the cell penetration/disruption properties of the functionalized particles using model DPPC bilayer as synthetic cell membrane on gold surface. Results showed that although eugenol-MSNPs were incorporated into the lipid bilayer, they did not possess the ability to destruct the bilayer at the examined concentrations (up to 1 mg/mL). However, G-eug dimer-MSNPs were able to penetrate and remove the supported lipid bilayers at concentrations as low as 0.5 mg/mL compared to eugenol-MSPNs. This ability is thought to be due to the larger size of the oriented lipophilic functional group (from monomer sized eugenol to the G-eug dimer). **Chapter 5** proposed a novel pathway to design functional advanced materials and interfaces based on lignin-derived compounds, which should pave the way for utilizing a vast bio-based resource in various applications. The efficacy of the functionalized particles in interacting with the bilayer (in form of adhering to or destructing the bilayer) can be considered as harbinger of more pragmatic applications such as delivery to actual microbial cell membranes or relieving pathogenic infection in the human body. Moreover, the strategy proposed in this chapter using thiol-ene “click” chemistry reactions can be utilized for manufacturing lignin-containing polymer networks, membranes, adhesives and composite materials with antibacterial properties from lignin derivatives as was previously done using eugenol as the antimicrobial agent [231, 259-261]. Some preliminary work was conducted to

functionalize silicon wafers as well as QCM silica coated sensors with thiol using the same thiol-ene click chemistry strategy (characterization data included in **Appendix Figures F.2-4** and **Tables F.1-4**).

In **Chapter 6**, ITC was employed to characterize inclusion complex formation of β -cyclodextrins (β -CD) with three lignin dimers of coniferyl alcohol (pinoresinol, G- β O4'-*trunc*G, and G- β O4'-G) dissolved in acetonitrile/water (10% v/v). β -CD forms inclusion host-guest complexes of stoichiometry 1:1 with these dimers. However, the mechanism of the interactions varies depending on the chemical structure and hydrophobicity of the dimers. The major driving forces for the complexation of β -CD with pinoresinol and G- β O4'-*trunc*G were hydrophobic interactions, which results in the binding to be entropy-driven ($|T\Delta S| > |\Delta H|$), whereas the driving forces of the complexation of β -CD with the less hydrophobic G- β O4'-G dimer were mostly Van der Waals forces, hydrogen bonds, and possibly electrostatic forces with enthalpy making a larger contribution to the Gibbs free energy ($|T\Delta S| < |\Delta H|$). Findings from this study were in accordance with MD simulation (performed by Dr. Moldovan's group) on the same systems [193]. Due to the instrumental limits raised from use of acetonitrile as the cosolvent to help solubilizing the lignin dimers in water, the ITC experiments could not be reproduced in acetonitrile/water (10% v/v). Thus, the measurements were performed in i-PrOH/water (10% v/v). Use of different organic cosolvents with different properties in study of the dimer-CD systems provides indirect information about the nature of the interaction between guest molecules and CDs and allows to test hypotheses. For instance, smaller alcohols (e.g. methanol) show completely different behavior in presence of CDs than bulky alcohols (e.g. i-PrOH). By introducing methanol to the CD/guest system, the weakening of electrostatic and hydrogen

bonding interactions significantly overshadows the increase of hydrophobic interactions, and notably undermines the host-guest binding. On the contrary, as explained in **Chapter 6**, the presences of i-PrOH in the system increases the value of the binding affinity of hydrophobic guests to CD. Ethanol shows a more moderate behavior compared to these two extremes and has a more equitable effect on the binding ability [290]. Ethanol/water mixtures (50% and 10% v/v) were previously utilized to investigate the interactions of docetaxel with methyl- β -CD and hydroxypropyl- β -CD (HP- β -CD) with capsaicin, respectively [315, 316]. Efforts to perform complementary binding studies using the fluorescent probe, TNS, are described in **Appendix Figure D.5**. The interaction of TNS with β -CD in solution was investigated in PBS (pH=7.4) and acetate buffer (pH=3.7) using UV-vis and fluorescence spectroscopy respectively, and results that confirm the formation of CD-TNS inclusion complexes were observed. Additionally, the interactions of ibuprofen as a water-soluble model guest with β -CD were studied using ITC and the heat signals were recorded and illustrated in **Chapter 2, Figure 2.13a**. The ibuprofen/CD thermodynamic values obtained from ITC are in agreement with those reported by Bertaut et al. [136] (shown in **Appendix Table C.1**). In sum, while we showed that ITC is a valuable technique for studying CD/guest system, it is recommended that along with ITC, complementary techniques such as NMR, Mass Spectrometry and MD simulation be employed to validate the conclusions drawn from ITC in different media.

As a follow-up to the characterization of inclusion complexes of β -CD with lignin dimers (**Chapter 6**), a surface modification strategy was proposed in **Chapter 7** to covalently attach β -CD on solid silica surfaces. The goal of this chapter was to develop a platform to selectively separate and protect lignin-derived small molecules. To this end,

the bare MSNPs were synthesized and initially functionalized with amine groups ($-\text{NH}_2$) to yield MSNPAs. In the next step, the commercially available 6-TsO- β -CD was stirred with the MSNPAs in N-methylpyrrolidone (NMP) in presence of Potassium Iodide (KI). The resultant β -CD functionalized particles (CD-MSNPs) were characterized via various analytical techniques and were shown to possess a loading capacity of 0.042 mmol β -CD/g particle. The ability of CD-MSNPs to capture pinoresinol and a fluorescence probe (TNS) out of the solution through forming host-guest inclusion complexes was examined and compared to that of MSNPAs. The results showed that the MSNPAs captured more TNS and pinoresinol (through weak hydrophobic interactions of APTES) compared to CD-MSNPs. This is potentially because the grafted β -CD moieties on the particles were not oriented in a favorable direction and their hydrophobic cavities were not effectively facing the target guest molecules in the solution, therefore they lacked the efficacy to capture adequate guest molecules. Finding ways to modify surfaces with favorably-oriented CDs is the key struggle in future attempts to overcome. In addition to the measurements performed in **Chapter 7** with CD-MSNPs, solution depletion with eugenol-MSNPs as well as G-eug dimer-MSNPs and free β -CD (using TNS as the probe) was done (**Appendix Tables D.5-6**). While some satisfactory results were obtained for eugenol-MSNPs (binding of free CDs to eugenol-MSNPs), the solution depletion measurements with dimer-MSNPs and free β -CD did not yield desired results, possibly due to the lower amount of dimers on the particles relative to eugenol, meaning that less lignin dimers were available on the particles to interact with CDs.

Previous efforts to test another CD binding approach using MSNPs and thiol-ene click chemistry are included in **Appendix E** (grafting chemistry is shown in **Appendix**

Figure E.1). Currently, a different CD functionalization method with less intensive reaction conditions and lower possibility of removing the existing amine bonds is being investigated by our group (the method of CD functionalization by Santos et al. [297] as explained in **Section 7.2**). In this method, MSNPs are dispersed in dry dimethylformamide (DMF) and added the 6-TsO- β -CD in the same solvent. The suspension is allowed to react at elevated temperature and the resultant CD-MSNPs will be separated and purified [297]. Another way of improving future studies would be to select a fluorescence-responsive CD probe that does not respond to adsorbing to charged surfaces (like TNS does). For instance, when using N,N-dimethylaminonaphthyl-(acrylo)-nitrile (DMANAN) as a guest with β -CD, a new fluorescence emission band near 420 nm grows due to complexation [311]. That band is totally absent if no β -CD is present. More importantly, although DMANAN binds to CTAB micelles in solution (most similar to our amine-decorated particles), the presence of the band near 420 nm depends on pH. The band is there at low pH, but not at high pH. Thus, performing fluorescence studies near neutral pH using DMANAN allows the use of the 420 nm band as evidence of CD binding [312]. In sum, once proper CD-functionalized nanoparticles are obtained, methods such as solution depletion, spectroscopy, and ITC can be employed to test the efficacy and versatility of the particles in capturing small guest molecules. However, future research should be eventually conducted in more realistic settings (e.g. functionalized surfaces being subjected to actual lignin deconstruction mixtures) to test the CD-functionalized surfaces for their efficiency and selectivity towards lignin oligomers of different structures.

APPENDICES

APPENDIX A. SUPPLEMENTARY MATERIALS FOR CHAPTER 4

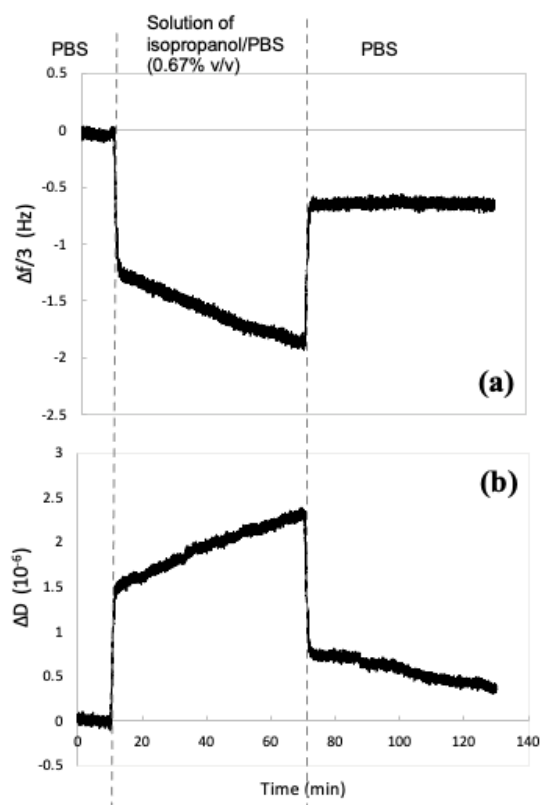


Figure A.1 QCM-D monitoring of changes in frequency with time as an isopropanol/PBS solution (0.67% v/v) flowed over a supported DPPC lipid bilayer: (a) change in frequency divided by the overtone number ($n=3$), and (b) change in dissipation. Time is measured from when isopropanol in PBS solution was injected, followed by the final PBS rinse and to the end of the experiment. Data are presented for the third overtone ($n=3$).

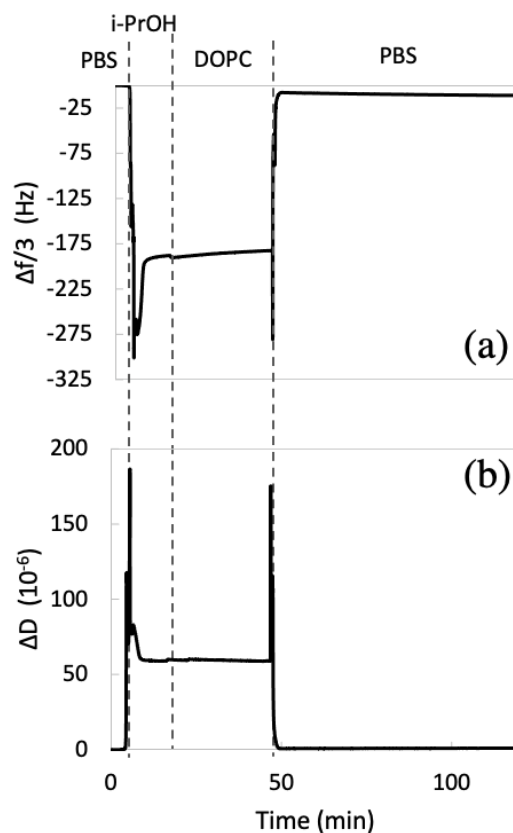


Figure A.2 Representative QCM-D results for solvent-assisted DOPC lipid bilayer formation on a gold sensor. (a) Frequency shifts divided by the overtone number ($n=3$) and (b) dissipation shifts presented for the third overtone ($n=3$). The frequency data are divided by the overtone number ($n=3$). The parts of the graphs separated by the vertical dashed lines denote the introduction of flowing PBS, isopropanol ('i-PrOH'), 0.5 mg/mL DOPC lipid in isopropanol ('DOPC'), and finally PBS.

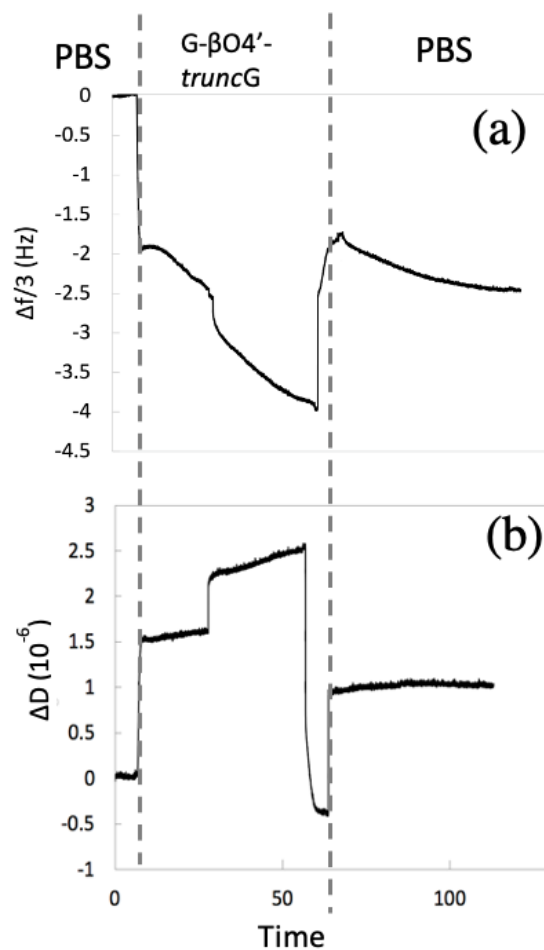


Figure A.3 Interactions of G-βO4'-truncG dimers with supported DOPC lipid bilayers supported on gold coated quartz crystal sensors obtained by QCM-D: (a) change in frequency divided by the overtone number ($n=3$) and (b) change in dissipation presented for the third overtone ($n=3$). Times are indicated for dimer solution injection onto an existing bilayer, followed by the PBS buffer rinse ('PBS'). Δf and ΔD are normalized to a value of 'zero' corresponding to the initial DOPC bilayer.

Table A.1 Quantitative QCM-D results of the uptake of G- β O4'-*trunc*G dimers with the synthetic DOPC lipid bilayers after 1 hr of exposure at a concentration of 0.1 mg/mL of dimer solutions. Three replicates were performed to determine this value.

Dimer	G- β O4'- <i>trunc</i> G
Average ratio of mass of the bound dimer to the mass of the pure DOPC bilayer	0.20 \pm 0.09

APPENDIX B. SUPPLEMENTARY MATERIALS FOR CHAPTER 5

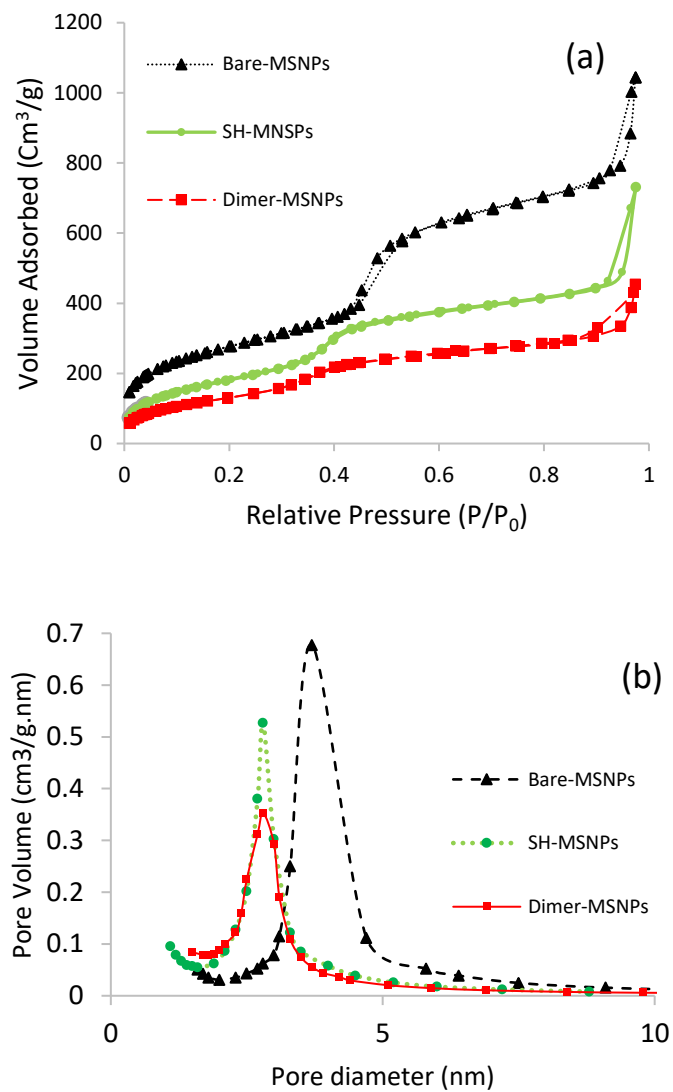


Figure B.1 Nitrogen sorption isotherms of the bare MSNPs, SH-MSNPs, and G-eug dimer-MSNPs.

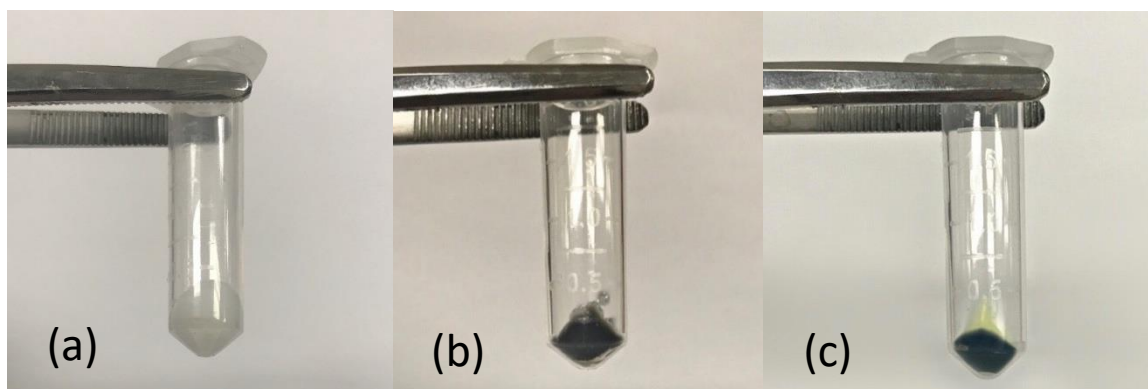


Figure B.2 Photograph of (a) SH-MSNPs, (b) eugenol-MSNPs and (c) G-eug dimer-MSNPs after exposure to 1% ferric chloride solution in ethanol, centrifugation and washing indicating successful eugenol and dimer attachment.

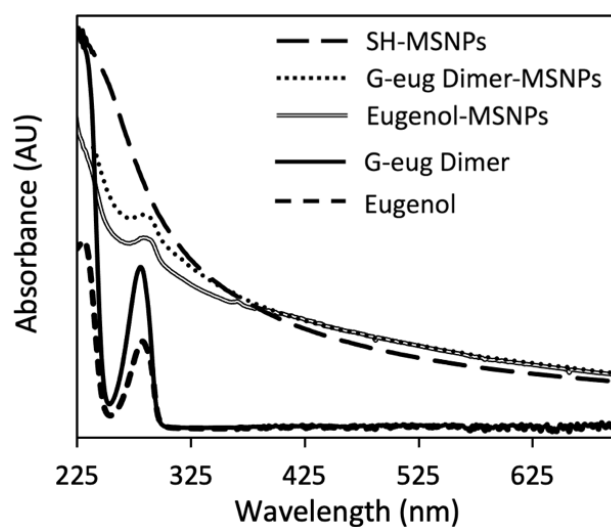


Figure B.3 UV-vis absorption spectra of the SH-MSNPs, eugenol-MSNPs, and G-eug dimer-MSNPs particles dispersed in isopropanol compared to that of eugenol and G-eug dimer dissolved in isopropanol.

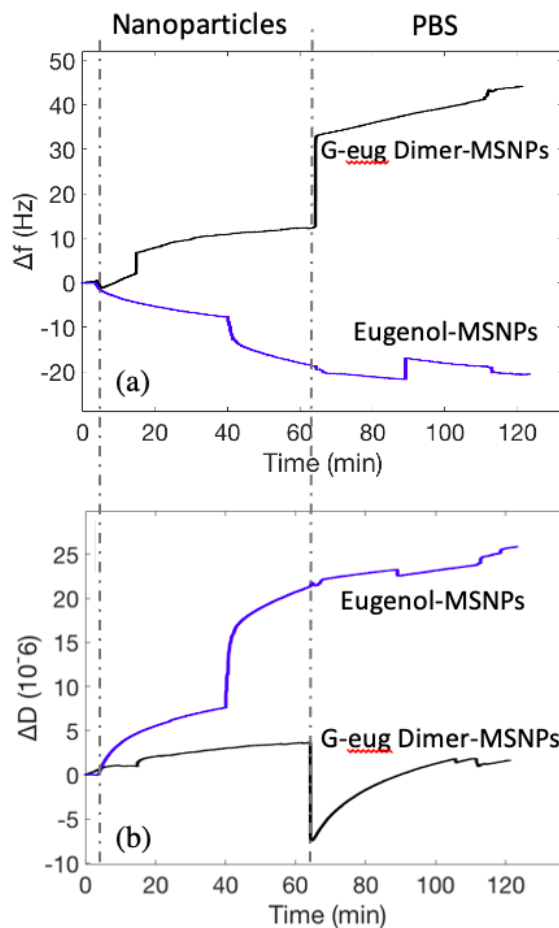


Figure B.4 Change in (a) frequency and (b) dissipation with the introduction of eugenol-MSNPs and G-eug dimer-MSNPs at 1 mg/mL on supported DPPC lipid bilayers on a gold QCM sensor. Time is measured from particle injection onto an existing bilayer ('Nanoparticles'), followed by the PBS buffer rinse ('PBS'). Δf and ΔD are normalized to a value of 'zero' corresponding to the initial DPPC bilayer.

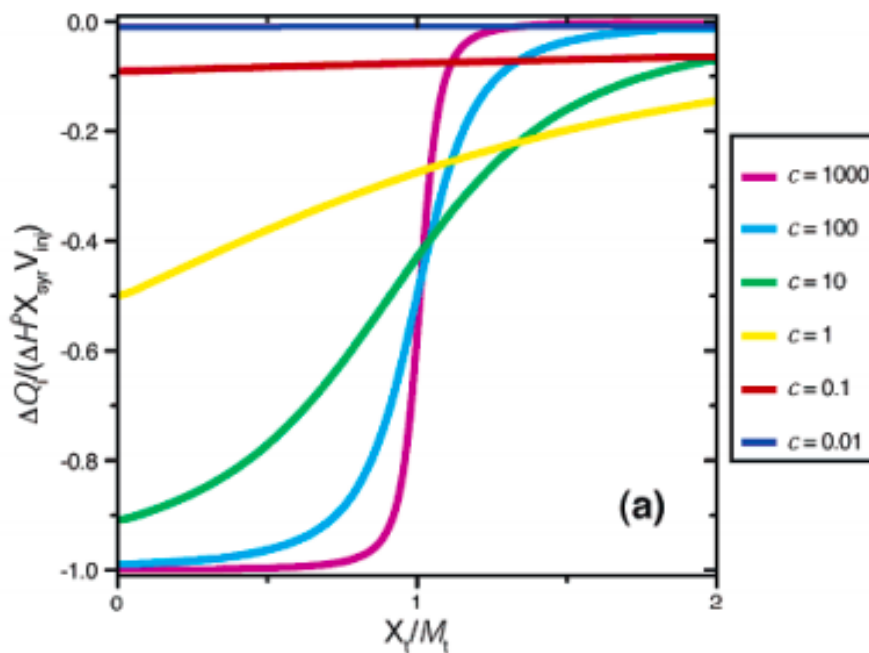


Figure C.1 The shape of an ITC titration curve varies with c , that is, the product of the receptor concentration (M_t) and the association constant (K_a). The ligand concentration is abbreviated as X_t . Reproduced from Ref. [288] (Turnbull et al., *Journal of the American Chemical Society* 125, no. 48 (2003)), with permission from American Chemical Society, copyright 2003.

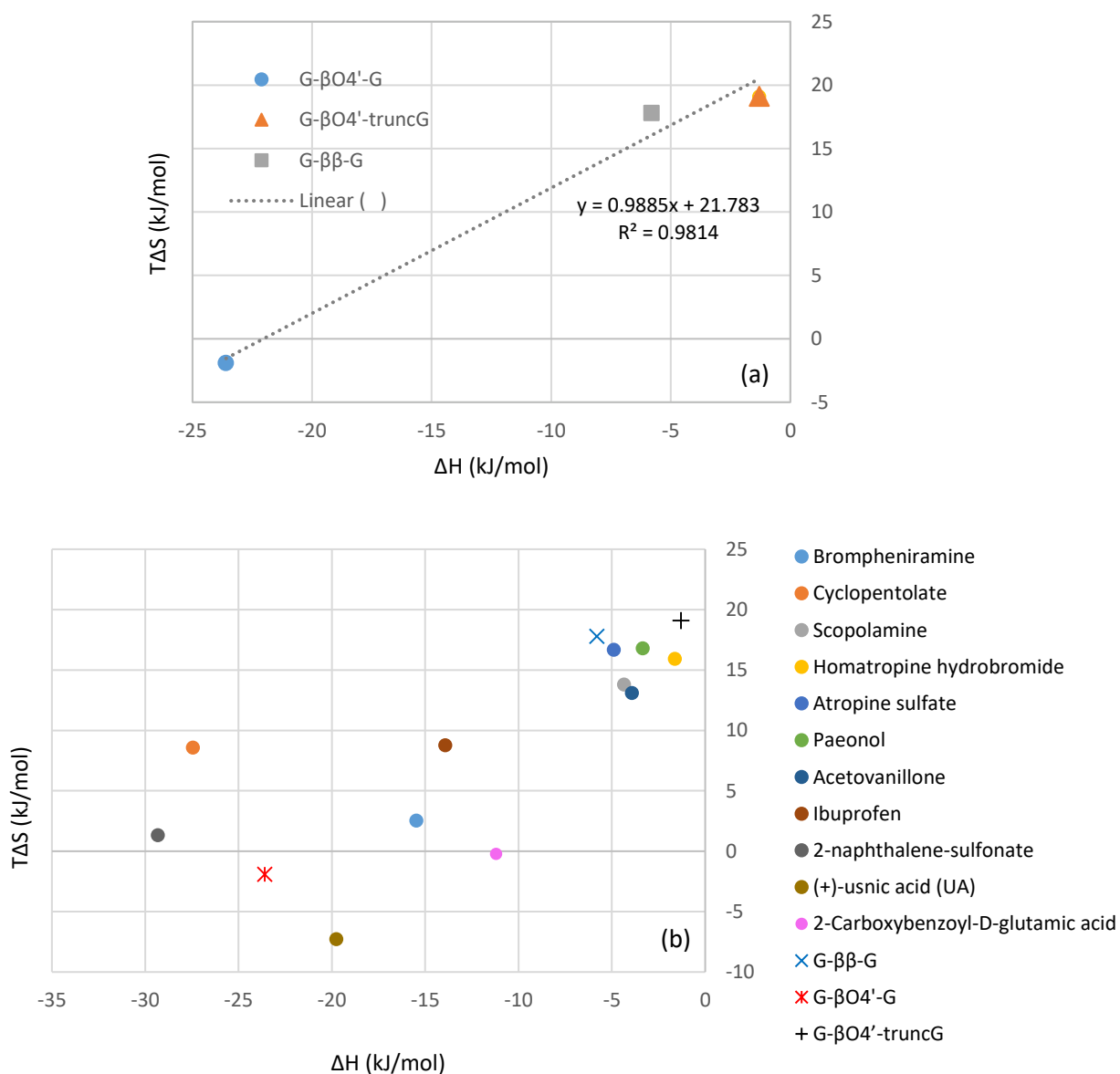


Figure C.2 Enthalpy–entropy compensation diagram (plot of $T\Delta S$ vs ΔH) for (a) lignin dimers- β -CD interaction in ACN/water (10 % v/v), and (b) for the interaction of β -CD with the small molecules listed in Table 2.1 (Chapter 2) (circles) and the lignin dimers investigated in this study (X's)

The interaction of ibuprofen and β -CD has been investigated previously. In order to validate our ITC experiments, the interaction of ibuprofen and β -CD was examined in two different media and compared to literature. The experiments consisted of four ITC

measurements (two actual experiments and their two corresponding blank experiments) in which β -CD was injected into ibuprofen in PBS (phosphate buffered saline) and phosphate buffer, separately. The results are summarized in the table below and compared to those of Bertaut et al. for the similar system [136].

Table C.1 Thermodynamic parameters for β -CD interaction with ibuprofen in PBS and phosphate buffer as determined using a one-binding site model through ITC at T=298 K.

Medium	T K	Equilibrium constants (K) M^{-1}	ΔH kJ/mol	ΔG kJ/mol	$T\Delta S$ kJ/mol	ΔS J/K.mol	ref
Phosphate buffer	298	9558*	-13.92 ± 0.05	-22.71	8.79	29.50	[136]
Phosphate buffer	298	16610*	-11.45 ± 0.834	-24.09	12.64	42.39	Our work
PBS	298	8937*	-11.89 ± 1.24	-22.55	10.66	35.77	Our work

*For ibuprofen/CD, the range of affinity (7000–14000 M^{-1}) was found in most published studies, although some extreme values have also been observed [136].

APPENDIX D. SUPPLEMENTARY MATERIALS FOR CHAPTER 7

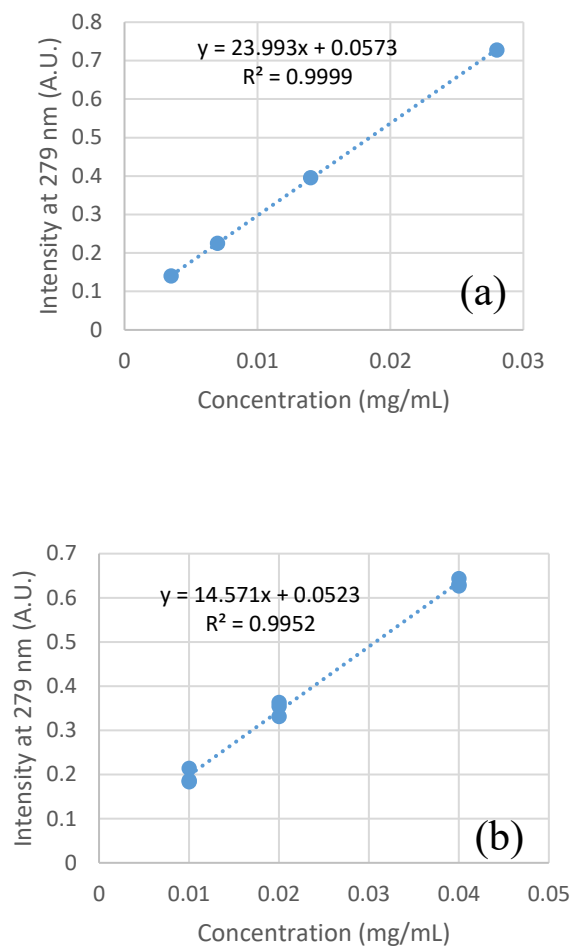


Figure D.1 Calibration curve of UV-vis intensity of pinoresinol at 279 nm, for determination of nanoparticles uptake. (a) in ACN/water (10% v/v) (b) ACN/acetate buffer (10% v/v).

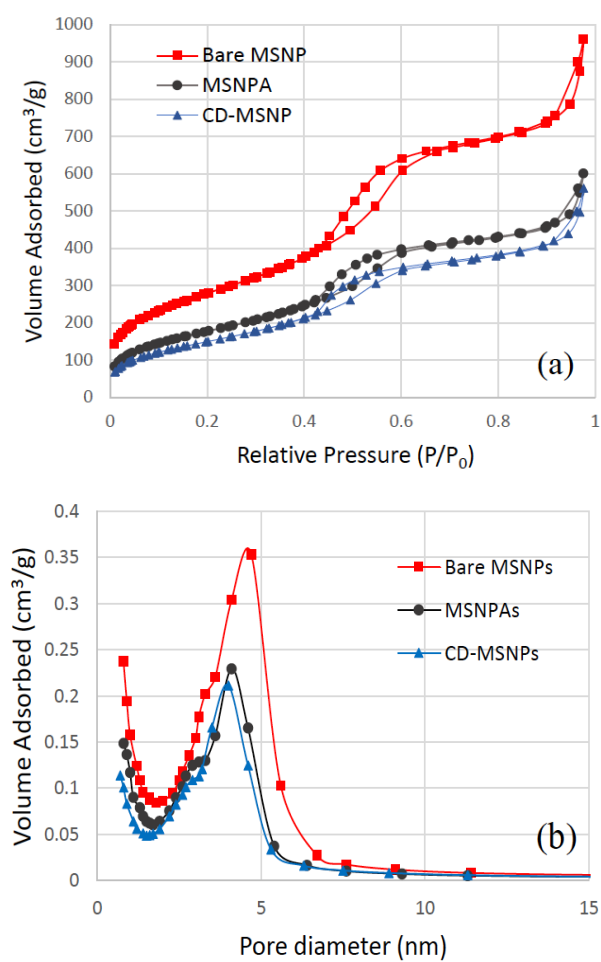


Figure D.2 Surface properties characterization of non-functionalized and functionalized MSNPs (a) Nitrogen sorption isotherms, (b) Pore size distribution.

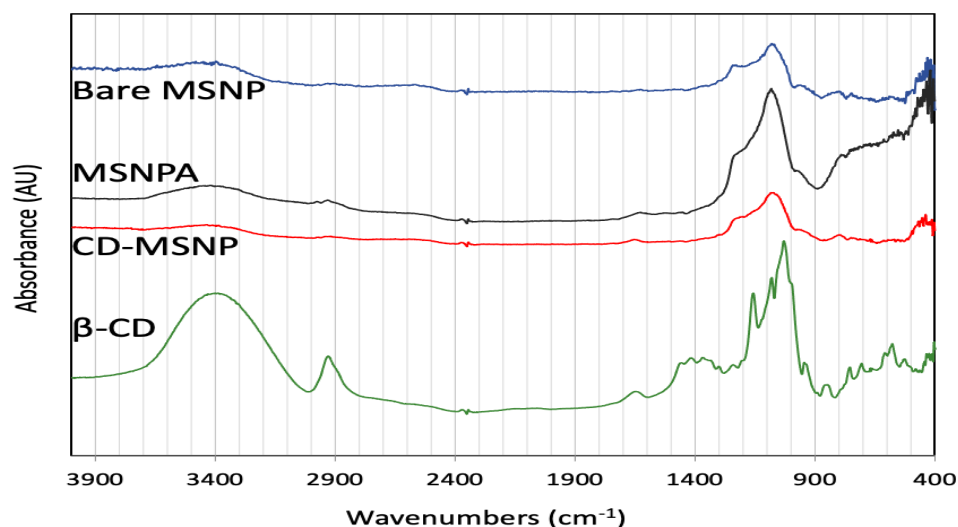


Figure D.3 FTIR spectra of β -CD-functionalized particles relative to bare MSNPs and MSNPAs, as well as β -CD.

Table D.1 Details of the solution depletion and UV-Vis spectroscopy measurements with pinoresinol and MSNPAs in ACN/water (10%). Each sample included 15 mg of the MSNPAs in 1 mL of pinoresinol solution.

Amount CD in 15 mg NPs (mmol)	Desired conc. of pinoresinol (mg/mL)	Actual conc. of pinoresinol before putting with MSNPAs Ci (mg/mL)	Pinoresinol conc. (mmol/mL)	UV intensity of the pinoresinol solutions before putting with MSNPAs	UV intensity of the pinoresinol solutions after 24 h putting with MSNPAs	Conc. of pinoresinol supernatant after taking out the MSNPAs Ce (mg/mL)	Amount adsorbed qe (mg/ g particle)
0	0.015	0.01537 ± 0.0013	0.000043	0.426 ± 0.03	0.368 ± 0.006	0.0129 ± 0.0002	0.165
0	0.025	0.02462 ± 0.0009	0.000069	0.648 ± 0.02	0.601 ± 0.009	0.0227 ± 0.0004	0.128
0	0.05	0.04783 ± 0.0015	0.000133	1.205 ± 0.04	1.118 ± 0.012	0.0442 ± 0.0005	0.242
0	0.13	0.1214 ± 0.0151	0.00034	$0.349 \pm 0.036^*$	$0.301 \pm 0.004^*$	0.1016 ± 0.0017	1.32

*this UV intensity is taken after 10X dilution.

Table D.2 Details of the solution depletion and UV-Vis spectroscopy measurements with pinoresinol and CD-MSNPs in ACN/water (10%). Each sample included 15 mg of the CD-MSNPs in 1 mL of pinoresinol solution.

Amount CD in 15 mg NPs (mmol)	Desired conc. of pinoresinol (mg/mL)	Conc. of pinoresinol before putting with CD-MSNPs C_i (mg/mL)	Pinoresinol conc. (mmol/mL)	UV intensity of the dimer solutions before putting with CD-MSNPs	UV intensity of the dimer solutions after 24 h putting with CD-MSNPs	Conc. of pinoresinol supernatant after taking out the CD-MSNPs C_e (mg/mL)	Amount adsorbed (mg/g particles) q_e
0.00063	0.015	0.0159 ± 0.0003	0.000044	0.438 ± 0.007	0.428 ± 0.008	0.0155 ± 0.0003	0.023
0.00063	0.025	0.0238 ± 0.0002	0.000069	0.629 ± 0.005	0.607 ± 0.005	0.0229 ± 0.0002	0.060
0.00063	0.05	0.0497 ± 0.0006	0.000133	1.251 ± 0.015	1.124 ± 0.013	0.0445 ± 0.0006	0.347
0.00063	0.13	0.1305 ± 0.0002	0.00034	$0.37 \pm 0.0006^*$	$0.599 \pm 0.0065^{**}$	0.1129 ± 0.0014	1.173

*this UV intensity is taken after 10X dilution.

** this UV intensity is taken after 5X dilution

Table D.3 Details of the solution depletion and UV-Vis spectroscopy measurements with pinoresinol and MSNPAs in ACN/acetate buffer (10%)

Amount CD in 15 mg NPs (mmol)	Desired conc. of pinoresinol (mg/mL)	Actual conc. of pinoresinol before putting with MSNPAs C_i (mg/mL)	Pinoresinol conc. (mmol/mL)	UV intensity of the pinoresinol solutions before putting with MSNPAs	UV intensity of the pinoresinol solutions after 24 h putting with MSNPAs	Conc. of pinoresinol supernatant after taking out the MSNPAs C_e (mg/mL)	Amount adsorbed in acetate buffer medium q_e (mg/ g particle)
0	0.025	0.02448 ± 0.0006	0.000007	0.409 ± 0.0089	0.4533 ± 0.0145	0.027523 ± 0.00099	0
0	0.05	0.05067 ± 0.0013	0.00014	0.7907 ± 0.0196	0.8323 ± 0.0119	0.053533 ± 0.00082	0
0	0.13	0.13843 ± 0.0031	0.00036	$0.254 \pm 0.0046^*$	$0.242 \pm 0.0056^*$	0.13019 ± 0.0038	0.5493

*this UV intensity is taken after 10X dilution.

Table D.4 Details of the solution depletion and UV-Vis spectroscopy measurements with pinoresinol and CD-MSNPs in ACN/acetate buffer (10%)

Amount CD in 15 mg NPs (mmol)	Desired conc. of pinoresinol (mg/mL)	Actual conc. of pinoresinol before putting with MSNPAs C_i (mg/mL)	Pinoresinol concentration (mmol/mL)	UV intensity of the pinoresinol solutions before putting with MSNPAs	UV intensity of the pinoresinol solutions after 24 h putting with MSNPAs	Concentration of pinoresinol supernatant after taking out the MSNPAs C_e (mg/mL)	Amount adsorbed in acetate buffer medium q_e (mg/ g particle)
0.00063	0.025	0.02448 ± 0.0006	0.000007	0.409 ± 0.0089	0.4817 ± 0.01331	0.02947 ± 0.00091	0
0.00063	0.05	0.05067 ± 0.0013	0.00014	0.7907 ± 0.0196	0.8077 ± 0.02350	0.05184 ± 0.00161	0
0.00063	0.13	0.13843 ± 0.0031	0.00036	0.254 ± 0.0046 *	0.247 ± 0.00173 *	0.1336 ± 0.0012	0.322

*this UV intensity is taken after 10X dilution.

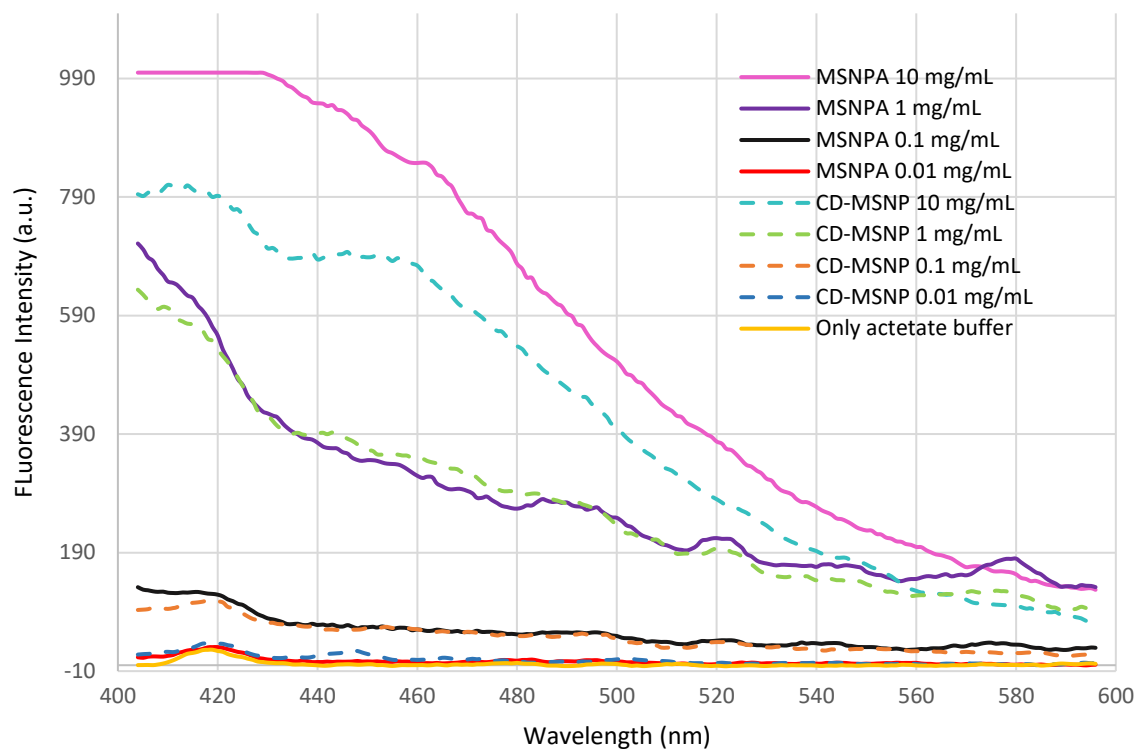


Figure D.4 The emission fluorescence spectra of suspensions of MSNPA and CD-MSNPs with various concentrations in acetate buffer (pH=3.7).

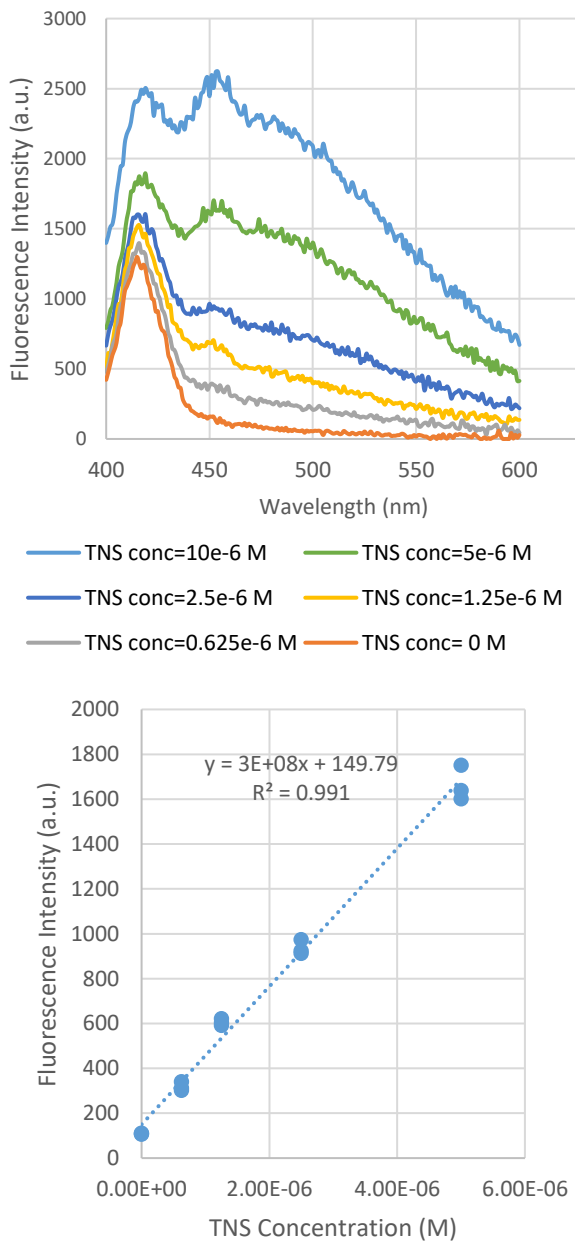


Figure D.5 β -CD/guest binding studies using the fluorescent probe, TNS in acetate buffer (pH 3.7, 25 °C). (a) fluorescence spectra of TNS in the presence of free β -CD with concentration set constant at 4.5×10^{-5} M. TNS concentration varied as follows: (10, 5, 2.5, 1.25, 0.625) $\times 10^{-6}$ M (b) Calibration curve of fluorescence intensity of TNS-CD at $\lambda_{\text{excitation}}=366$ nm and $\lambda_{\text{emmission}}=460$ nm, in acetate buffer (pH=3.7) at constant β -CD concentration of 4.5×10^{-5} M and various concentrations of TNS.

Solution Depletion with Eugenol-MSNPs and G-Eug Dimer-MSNPs Synthesized in Chapter 5 and Free β -CD in PBS

Solution depletion with eugenol-MSNPs as well as G-eug dimer-MSNPs and free β -CD (using TNS as the probe) was done. Constant amount of the particles (5 mg) and various amount of β -CD was used and put together in each vial. Solutions of β -CD in PBS with different concentrations (10^{-4} M, 2×10^{-4} M, 4×10^{-4} M, 16×10^{-4} M, 32×10^{-4} M, 64×10^{-4} M) were prepared. Next, 5 mg of the eugenol-MSNPs and G-eug dimer-MSNPs were separately added to those solutions, and the solutions were allowed to stir overnight. Next, the particles were centrifuged out, and TNS was added to the supernatant solutions, and allowed to stir for 1 hour before the fluorescence intensities of the supernatant solutions were measured. Next, the concentration of the residual β -CD in the supernatant solutions was read from the calibration curve and the number of bound β -CD molecules to the particles was calculated. While some satisfactory results were obtained for eugenol-MSNPs, the solution depletion measurements with dimer-MSNPs and free β -CD did not give satisfactory results. One possible reason for the failure could be the lower amount of dimers on the particles relative to eugenol, meaning that less lignin dimers were available on the particles to interact with CDs.

Table D.5 Details of the solution depletion and fluorescence spectroscopy measurements with eugenol-MSNPs and free β -CD in PBS using TNS as the probe.

Initial β -CD mmoles Ci	10^{-4}	2×10^{-4}	4×10^{-4}	16×10^{-4}	32×10^{-4}	64×10^{-4}
Eugenol mmoles (from TGA)	0.0011	0.0011	0.0011	0.0011	0.0011	0.0011
mmols of the added TNS	10^{-4}	10^{-4}	10^{-4}	4×10^{-4}	8×10^{-4}	16×10^{-4}
Fluorescence intensity of the supernatant after adding TNS	777.67 ± 41.6	1232.67 ± 9.5	3164.33 ± 76.2	32203 ± 53.7	57998 ± 138.3	87695 ± 321.0
Final β -CD mmoles in the supernatant Cf	3.55×10^{-6}	1.87×10^{-5}	8.31×10^{-5}	1.78×10^{-4}	1.12×10^{-3}	3.51×10^{-3}
Bound β -CD mmoles: Ci-Cf	9.64×10^{-5}	1.81×10^{-4}	3.17×10^{-4}	1.42×10^{-3}	2.08×10^{-3}	2.89×10^{-3}
Bound β -CD (Ci-Cf) / eugenol mmoles on the NPs	0.09	0.16	0.29	1.29	1.89	2.63

Table D.6 Details of the solution depletion and fluorescence spectroscopy measurements with G-eug-dimer-MSNPs and free β -CD in PBS using TNS as the probe.

Initial β -CD mmoles (Ci)	10^{-4}	2×10^{-4}	4×10^{-4}	8×10^{-4}	16×10^{-4}	32×10^{-4}	64×10^{-4}
Dimer mmoles (from TGA)	6.5×10^{-4}	6.5×10^{-4}	6.5×10^{-4}	6.5×10^{-4}	6.5×10^{-4}	6.5×10^{-4}	6.5×10^{-4}
mmols of the added TNS	10^{-4}	10^{-4}	10^{-4}	2×10^{-4}	4×10^{-4}	8×10^{-4}	16×10^{-4}
Fluorescence intensity of the supernatant after adding TNS	1531.7 ± 293.1	9889 ± 521.6	11491 ± 43.7	14809 ± 203.8	14439 ± 419.2	88552 ± 24.4	overflow
Final β -CD mmoles in the supernatant (Cf)	2.87×10^{-5}	2.09×10^{-4}	2.1×10^{-4}	3.52×10^{-4}	3.66×10^{-4}	1.57×10^{-3}	4.74×10^{-3}
Bound β -CD mmoles Ci-Cf	7.13×10^{-5}	----	1.9×10^{-4}	4.48×10^{-4}	12.34×10^{-4}	---	---
Bound β -CD (Ci-Cf)/dimer mmoles on the NPs	0.11	----	0.29	0.69	1.9	----	---

APPENDIX E. Alternative β -CD Functionalization Technique Based on Thiol-ene Click Chemistry

Chapter 7 reports the results of functionalizing MSNPA particles with β -CD using the a nucleophilic displacement reaction with the amine groups grafted to the MSNP surface. Here, an alternative approach was taken based on the thiol-ene click reaction between mercaptopropyl groups grafted to the MSNP surface and allyl groups grafted to β -CD. The materials synthesis is described along with the physical and chemical characterization of the properties of the materials.

500 mg 6-OTs- β -CD and 6.5 mL allylamine were placed into a 250 mL round bottom flask. The flask with a reflux device then will be placed in 60 °C water bath. The mixture was stirred for 4 h. After the completion of the reaction, the mixture was cooled to room temperature. 5 mL methanol was added into the mixture. The solution was mixed. Then 40 mL acetonitrile was added. The white precipitate was centrifuged and the white solid was collected and purified by methanol and acetonitrile. The obtained product was dried under vacuum at 35°C for 24 h. This method was not successful due to problems associated with synthesis of mono-(6-N-allylamino-6-deoxy)- β -CD.

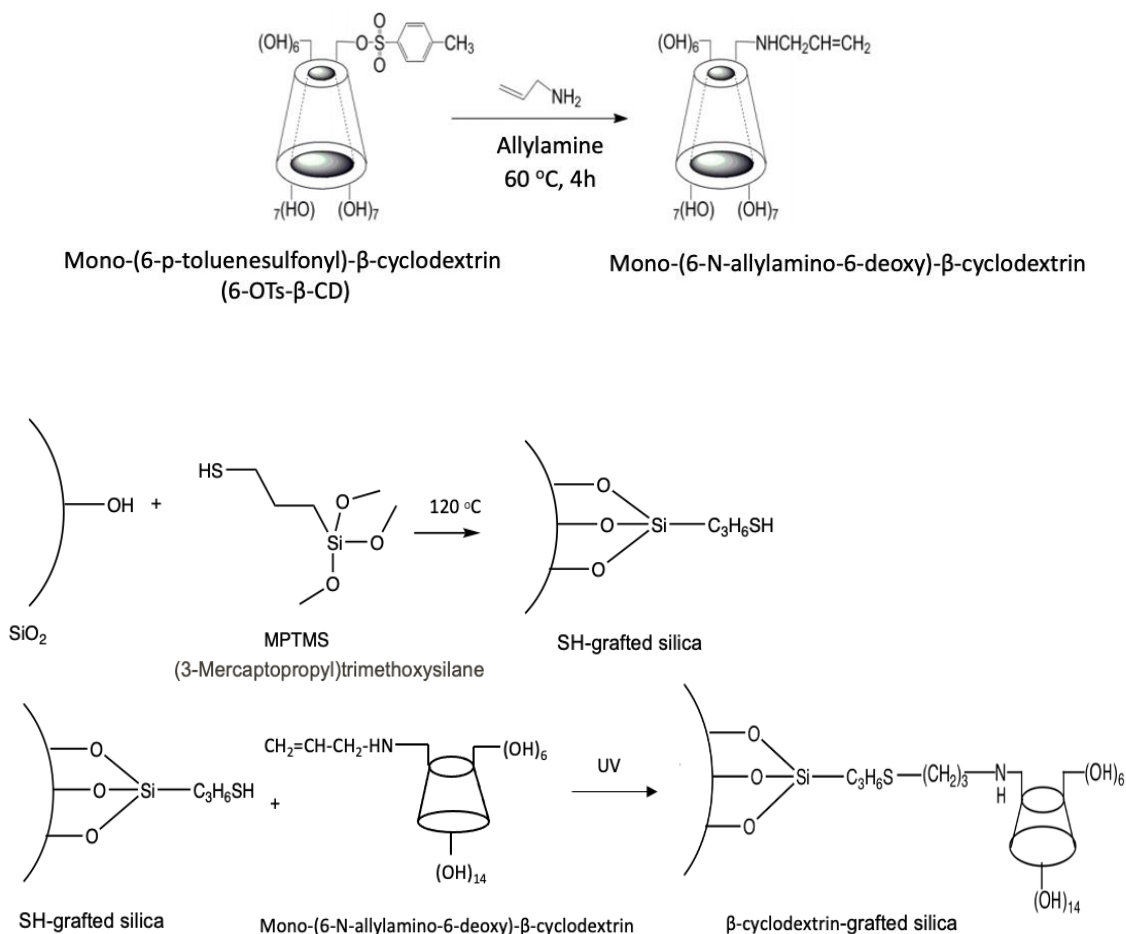


Figure E.1 Synthesis of MSNPs functionalized with β -CD using mono-(6-N-allylamino-6-deoxy)- β -cyclodextrin as the β -CD source and thiol-ene click chemistry as the binding approach.

To quantify the amount of thiol and β -CD attached to the particles, thermogravimetric analysis (TGA) was conducted on the Universal.7A TA Instruments using a temperature ramp of 10 $^\circ\text{C}/\text{min}$ from 25 to 700 $^\circ\text{C}$. Thermal decomposition of bare, thiol-functionalized, and β -CD-functionalized MSNPs was determined under nitrogen. The weight loss profiles of three sets of particles (bare MSNPs, SH-MSNPs, and CD-MSNPs) are plotted as a function of temperature (**Figure E.2**). As seen in **Table E.1**, a mass loss of 4.4, 2.2, and 2.5% is observed from 25 $^\circ\text{C}$ to 200 $^\circ\text{C}$ for bare MSNPs, SH-MSNPs, and CD-

MSNPs respectively, which is attributed to evaporation of the water from the surface and the pores of the particles. The mass loss of bare MSNPs from 200 °C to 700 °C (4.24%) is attributed to organic impurities (such as residual surfactant template) and further temperature-induced condensation of the silica framework. Additional mass loss by the organic functionalized particles (SH-MSNPs and CD-MSNPs) in the range of 200 °C to 700 °C relative to the bare MSNPs is used to quantify the amount of organic functional material. For SH-MSNPs, this additional mass loss (8.52%) corresponds to 0.53 mmol of thiol/g particle. Relative to SH-MSNPs, for CD-MSNPs, there is a further mass loss of 4.92% (0.042 mmol mono-(6-N-allylamino-6-deoxy)- β -CD /g particle). Evaluating the efficiency of CD attachment based on thiol groups, the attachment efficiency of the CD to the thiol groups is 7.92%.

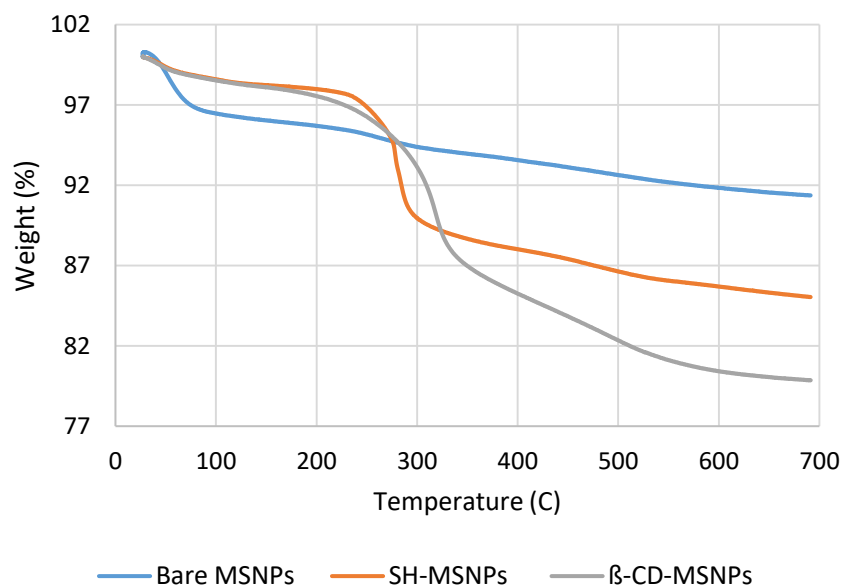


Figure E.2 TGA of bare MSNPs, SH-MSNPs, and β -CD-MSNPs.

Table E.1 TGA of bare MSNPs, SH-MSNPs, and β -CD-MSNPs.

	Water loss (weight %) (up to 200 °C)	MPTMS loss (weight %)	Unknown organic moieties loss (weight %)	mono-(6-N- allylamino- 6pdeoxy)- β -CD loss (weight%)	Total loss (weight %)
Bare-MSNPs	4.4	0	4.24	---	8.64
SH-MSNPs	2.2	8.52	4.24	---	14.96
β -CD-MSNPs	2.5	8.52	4.24	4.92	20.14

The click chemistry reaction with SH-MSNPs and mono-(6-N-allylamino-6-deoxy)- β -CD dissolved in methanol under UV was redone to get higher efficiency of attachment. 50 mg of SH-MSNPs (0.027 mmol SH), 25 mg of mono-(6-N-allylamino-6-deoxy)- β -CD (would be 0.021 mmol if the molecule synthesized was pure), and 8 mg of the photo-initiator (0.03 mmol) were put in a quartz cuvette in 3.5 mL of methanol under UV for 48 hours, and then the particles were centrifuged out and the amount of CD attached to them was measured through TGA again as shown below:

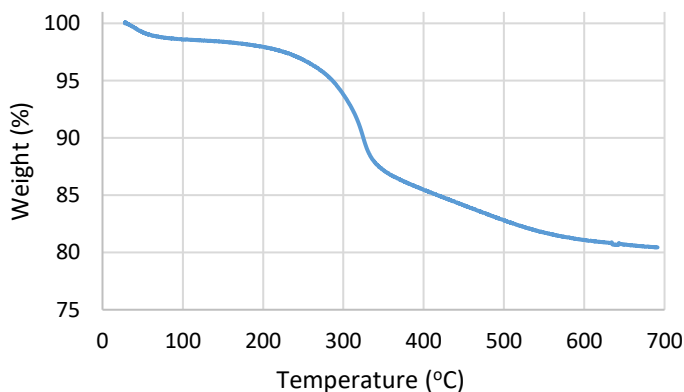


Figure E.3 TGA of β -CD-MSNPs after repeating the attachment procedure

As seen in **Figure E.3**, the results were still not satisfactory (~80%), so the β -CD-MSNPs were put back in the reaction with 30 mg of the mono-(6-N-allylamino-6-deoxy)- β -CD and 8 mg of the photo-initiator under UV for 24 hours, and then the particles were centrifuged out and the amount of CD attached to the was measured again through TGA. As seen in **Figure E.4** and **Table E.2**, the weight loss for the CD-MSNPs slightly increased (0.045 mmol of mono-(6-N-allylamino-6pdeoxy)- β -CD per every gram of the particles which corresponds to an efficiency of attachment of 8.44%).

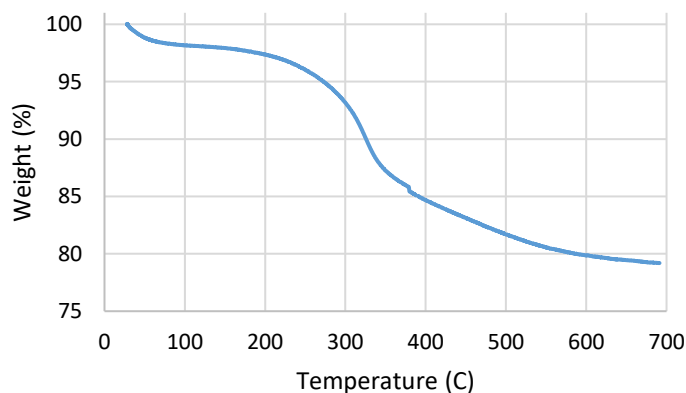


Figure E.4 TGA of β -CD-MSNPs after being placed back in the reaction flask

Table E.2 TGA of β -CD-MSNPs after being placed back in the reaction flask

	Water loss (weight %) (up to 200 °C)	MPTMS loss (weight %)	Unknown organic moieties loss (weight %)	mono-(6-N- allylamino- 6pdeoxy)- β -CD loss (weight%)	Total loss (weight %)
Bare-MSNPs	4.4	0	4.24	---	8.64
SH-MSNPs	2.2	8.52	4.24	---	14.96
β -CD-MSNPs	2.8	8.52	4.24	5.25	20.81

Additionally, the particles were characterized using BET as observed in **Figure E.5** and **Table E.3**. The pore size distribution of SH-MSNPs relative to bare MSNPs, obtained by the Barrett, Joyner and Halenda (BJH) method, indicates that pore sizes were reduced

uniformly as a result of functionalization of silica pore walls without significant pore blockage. Additionally, high specific surface area ($936.7 \text{ m}^2/\text{g}$) and pore volume ($2.42 \text{ cm}^3/\text{g}$), and large average pore diameter ($\sim 7.5 \text{ nm}$) of synthesized MSNPs determined by nitrogen adsorption at 77 K as provided in **Table E.3**, as well as clear capillary condensation at relative pressure 0.5 in adsorption isotherm (type IV) point to uniform mesoporosity and the applicability of the nanoparticles for antimicrobial loading and as delivery vehicle (**Figure E.5**).

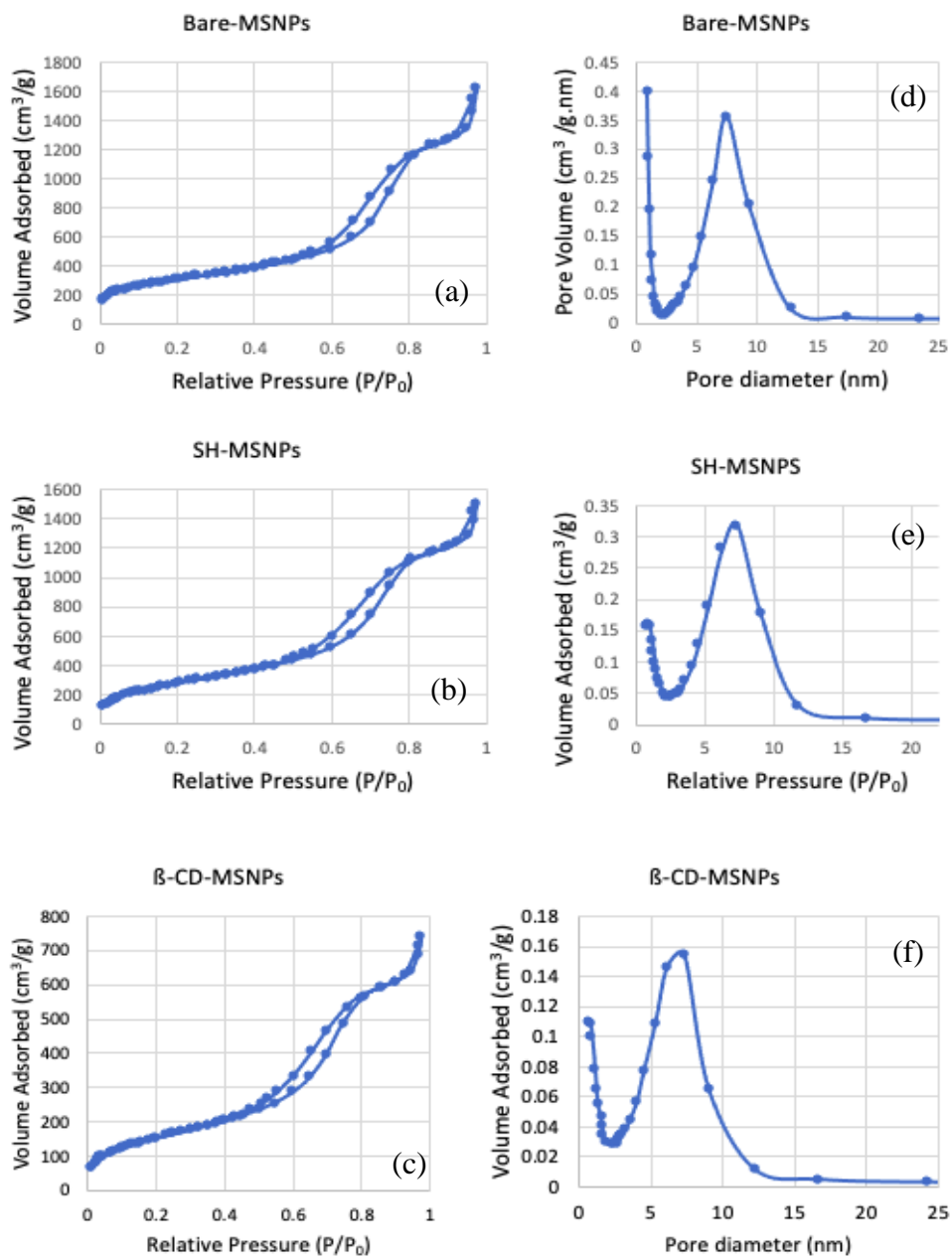


Figure E.5 Surface properties characterization of bare-MNSPs, SH-MSNPs, and CD-MSNPs using the attachment process including mono-(6-N-allylamino-6-deoxy)- β -cyclodextrin. (a,b,c) Nitrogen sorption isotherms, (d,e,f) Pore size distribution.

Table E.3 BET surface area, BJH average pore diameter and pore size distribution obtained from nitrogen adsorption

Particle type	Pore diameter peak ^a (nm)	BJH average pore diameter (nm)	BJH pore volume (cm ³ /g)	BET surface area (m ² /g)
Bare MSNPs	7.5 ± 1.9	7.36	2.42	936.7
SH-MSNPs	7.3 ± 1.8	6.21	2.27	888.9
β-CD-MSNPs	7.3 ± 1.4	5.82	1.12	478.7

^a The ranges are determined from the full width at half maximum (FWHM) of the BJH pore size distribution.

Although the pore diameter does not show a significant change after functionalizing the particles with β-CD, the other parameters including the surface area show relatively higher changes. The surface occupied by 0.045 moles of mono-(6-N-allylamino-6pdeoxy)-β-CD is 410.2 m², which indicates that every molecule takes up about 0.015 nm² of the surface.

In sum, this attachment method was not successful due to problems associated with synthesis of mono-(6-N-allylamino-6-deoxy)-β-CD (low yield of the product and high amount of byproducts and impurities produced during the synthesis based on NMR and mass spec analysis (data not shown)).

APPENDIX F. Functionalizing Silica Coated QCM Substrates with Thiol Functional Groups Through Hydroxylation of MPTMS

Herein, two methods (A and B) are provided for functionalization silica films with MPTMS (thiol groups). The ultimate goal of this work was to provide a platform for attachment of other molecules such as cyclodextrins and lignin dimers via thiol-ene click reactions. Method A includes the immersing of the films in a dilute solution of MPTMS in ethanol at elevated temperatures, while method B involves the drop casting of pure MPTMS on the films and curing the films at high temperatures. Method A provided acceptable QCM-D data (consistent with formation of a monolayer of thiol) and allowed for the sensors to be tested with BSA using QCM-D. On the contrary, method B provided promising XPS data but because of the large thickness of the adjacent grafted MPTMS multilayers on the surface, QCM-D was not applicable. Below, the two methods are described in detail.

METHOD A: Immersing the silica films in a dilute solution of MPTMS in ethanol at elevated temperatures

Chemicals and reagents

Isopropanol (99%), 200 proof pure ethanol, Bovine Serum Albumin (BSA) crystalline, Sodium Dodecyl Sulfate (SDS) 20% solution, Ammonium Hydroxide (28-30%) and deionized water (ASTM type II), were purchased from VWR International. (3-Mercaptopropyl)trimethoxysilane (MPTMS, 95%) was purchased from Alfa Aesar.

Phosphate buffered saline (PBS) was purchased from Sigma Aldrich. Hydrogen Peroxide was purchased from Fisher Scientific.

Cleaning the substrates

Commercially available silica coated QCM sensors with a fundamental oscillating frequency of 4.95 MHz were used as the substrates. Prior to any attachment, the substrates were cleaned by thoroughly washing with 20% SDS detergent and absolute ethanol, and then, dried in a stream of nitrogen. Next, to remove any remaining organic contaminants, the substrates were cleaned by immersing in a 5:1:1 mixture of DI water, ammonia, and hydrogen peroxide at 75 °C for 15 minutes followed by rinsing with water and drying in a stream of nitrogen. Then, the mass of the bare substrates was measured through QCM-D. This mass has been set as a baseline to enable the mass measurement of the functional groups that have later been adhered to the substrate. Frequency value of the resonating sensor was recorded with time using Qtools software, and then converted to mass using Sauerbrey equation (**Equation 2.4**).

Functionalization of the substrates with thiols

To functionalize the surface with thiol groups, the silica substrate was placed in a Teflon autoclave at 90 °C for 48 hr together with 36 mL of ethanol and 5 mL of MPTMS. Next, the substrate was thoroughly rinsed by ethanol and SDS 20% several times to remove any unattached MPTMS molecules from the surface. The hydrophobicity of the surface after thiol functionalization was determined by water contact angle measurements. Water contact angle measurements were performed using a Drop Shape Analyzer (KRÜSS

DSA100S), at 20 °C with 12 μ L water droplets. The mass of the thiol layer formed on the substrate was measured using QCM.

Protein adsorption on the substrate

To monitor the adsorption of proteins on the functionalized surfaces, QCM-D was employed. First, the sensor were mounted in the QCM chamber at 20 °C, then to stablish the baseline, and eliminate the effect of the solvent on frequency and mass changes, PBS was flowed through the chamber for 10 minutes. Next, solutions of BSA in PBS (1 mg/mL) were prepared and run through the QCM chamber for 20-30 minutes followed by a final PBS rinse for 10 minutes. Changes in the frequency and dissipation upon addition of BSA to the surface was recorded.

Results and Discussion

Characterization of the substrates functionalized with thiols

The thiol-coated substrates were tested by two methods: water contact angle measurements and QCM-D. Contact angle (CA) measurements was employed to measure the hydrophobicity of the surface after functionalization with thiol. The CA measurement results are shown in **Table F.1**. These results show that after functionalization with the MPTMS groups, the water contact angle increases from $59.75 \pm 0.42^\circ$ for bare sensor to $68.97 \pm 1.7^\circ$ for thiol-coated sensor suggesting improved hydrophobicity post attachement.

Table F.1 Water contact angle measurements for bare and MPTMS-functionalized silica substrates

silicon wafer	Average angle °
Bare	59.75 ± 0.42
Thiol functionalized	68.97 ± 1.7

The mass of the covalently attached MPTMS layer on the sensor was measured via QCM by measuring the frequency of the resonating sensor after functionalization and comparing it to the resonating frequency of the same sensor prior to functionalization (**Figure F.1**). The sensor was placed in the QCM cell and was allowed to resonate for ~13 minutes before and after functionalization. At the third overtone, after functionalization of the sensor, the sensor resonates at frequency of -8.38 ± 0.83 Hz which corresponds to the mass of 49.43 ± 3.44 ng/cm² or 0.48 nmol/ cm². This value is an average of two separate measurements \pm S.D .

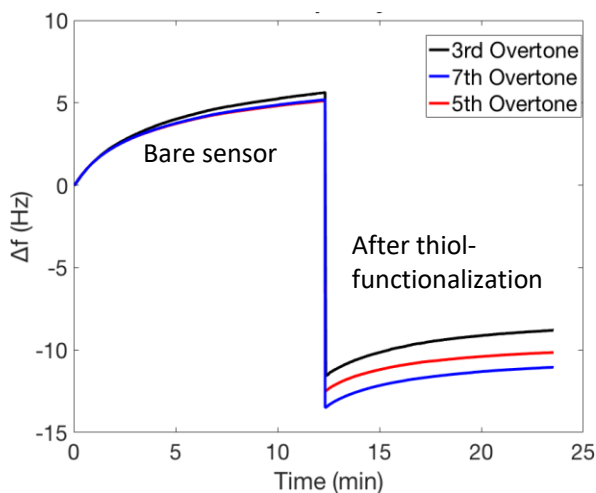


Figure F.1 Changes in the resonating frequency of the QCM silica coated sensor before and after thiol-treatment.

BSA adsorption on the thiol-functionalized substrates

The QCM-D sensor was utilized to quantify the protein adsorption on thiol SAMs in order to test the effect of thiol coating in terms of antifouling property. The QCM-D is a real-time screening tool for protein adsorption on silicon sensor chips. An alternating voltage is applied to drive the oscillation of the quartz sensor at its resonance frequency. The mass change at the sensor surface will be proportional to a change in frequency (Δf). When the adsorbed mass is sufficiently soft that it does not follow the sensor oscillation perfectly, this attributes to internal friction in the adlayer and thus to dissipation of oscillation energy. The more flexible the adlayers, the more the oscillation will induce. Therefore, monitoring protein adsorption requires using the dissipation parameter to fully characterize the adsorption of a viscoelastic structure [317]. In this study, the experiments

were designed according to the method described by Huang et al [318]. The bare chips as well as the chips covered with MPTMS groups were exposed to BSA solutions for 20-30 minutes, followed by washing with PBS as shown in **Figure F.2**. For the bare substrates, the frequency at $n=3$ before introduction of the BSA to the surface was ~ 5 Hz. After BSA, the frequency drops to ~ -15 Hz, indicating the adsorption of the proteins to the surface. After ~ 15 minutes of BSA running on the substrate, the buffer was introduced to the surface which removed some of the proteins off the sensor and increased the frequency from ~ -15 to ~ -10 Hz (**Figure F.2a**). The net decrease in frequency corresponds to the net mass change of ~ 60 ng/cm² associated with the adsorbed BSA on the surface. The dissipation changes from initial value of $\sim -0.25 \times 10^{-6}$ to $\sim 1 \times 10^{-6}$ due to introduction of BSA to the sensor; however, after ~ 10 min of buffer rinse in the end, it goes back to ~ 0 (**Figure F.2b**). As for the thiol-functionalized sensor, the frequency prior to introduction of the BSA to the surface was ~ 2 Hz. After BSA, the frequency decreases to ~ -20 Hz. After ~ 25 minutes of BSA running on the substrate, the buffer was flowed on the surface to remove the unattached proteins off the sensor, which ultimately increased the frequency from ~ -20 to ~ -16.5 Hz (**Figure F.2c**). This change in frequency corresponds to the net mass change of ~ 97 ng/cm² associated with the adsorbed BSA on the thiol-coated surface. The dissipation increases from initial value of ~ 0 to $\sim 0.8 \times 10^{-6}$ due to introduction of BSA to the sensor; however, after ~ 10 min of buffer rinse in the end, it decreases to $\sim 0.3 \times 10^{-6}$ (**Figure F.2d**). The increase in the dissipation happening on both bare and thiol-functionalized sensors following the addition of the BSA to the sensor is an indicator of the material adsorption to the surface. The comparison of bare and thiol-functionalized substrates frequency data clearly suggests that the covalently attached MPTMS molecules did not exhibit any

resistance to protein adsorption. Since the mass of the BSA remained on the sensor after buffer wash is higher for the thiol-coated sensor, it could be concluded that the presence of MPTMS molecules on the sensors reinforces the attachment of the BSA, rather than repelling it.

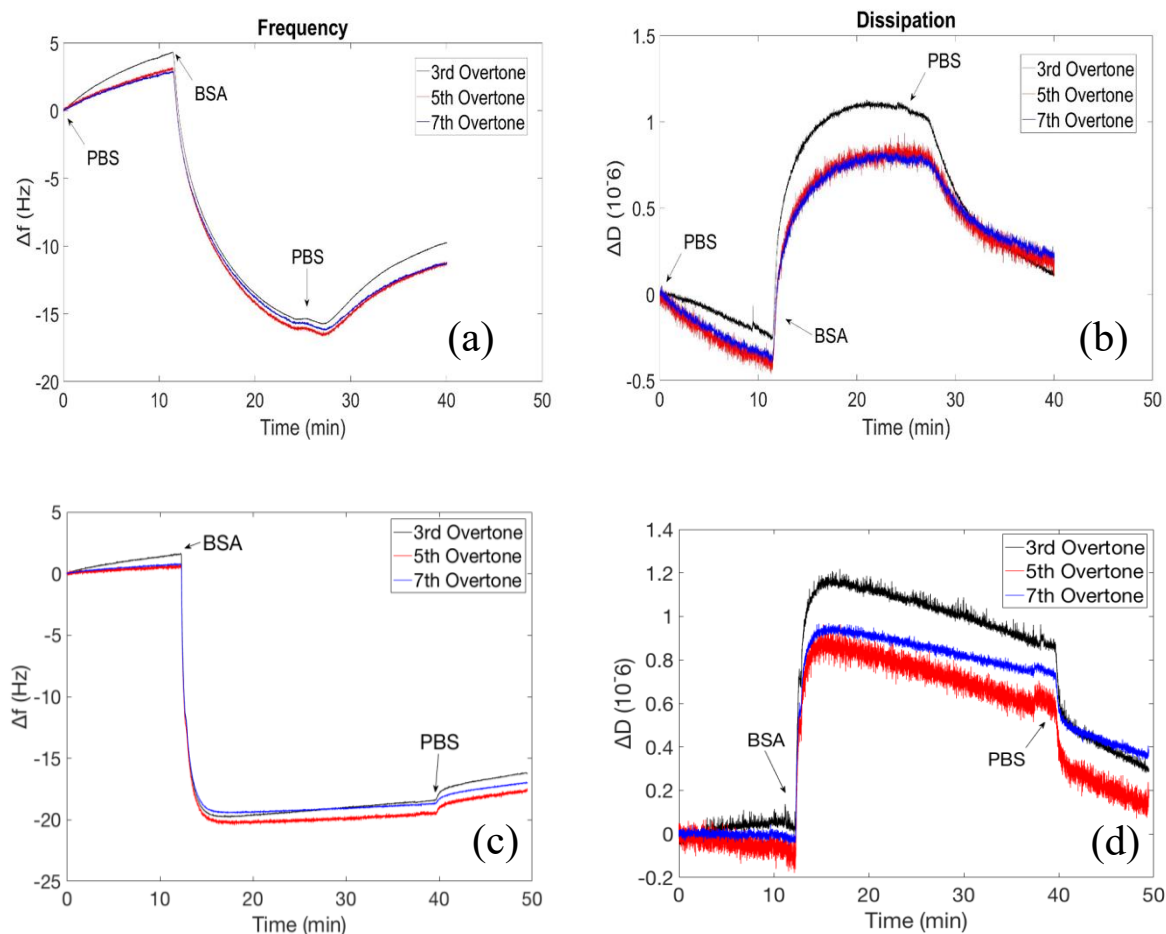


Figure F.2 QCM-D studies of BSA adsorption from PBS at pH 7.4 on surfaces of bare silicon and thiol-coated silicon sensors. (a) changes in frequency of the bare sensor vs. time (b) change in dissipation of the bare sensor vs. time (c) changes in frequency of the thiol-coated sensor vs. time (d) change in dissipation of the thiol-coated sensor vs. time.

METHOD B: MPTMS-functionalization and characterization of silica via drop casting method

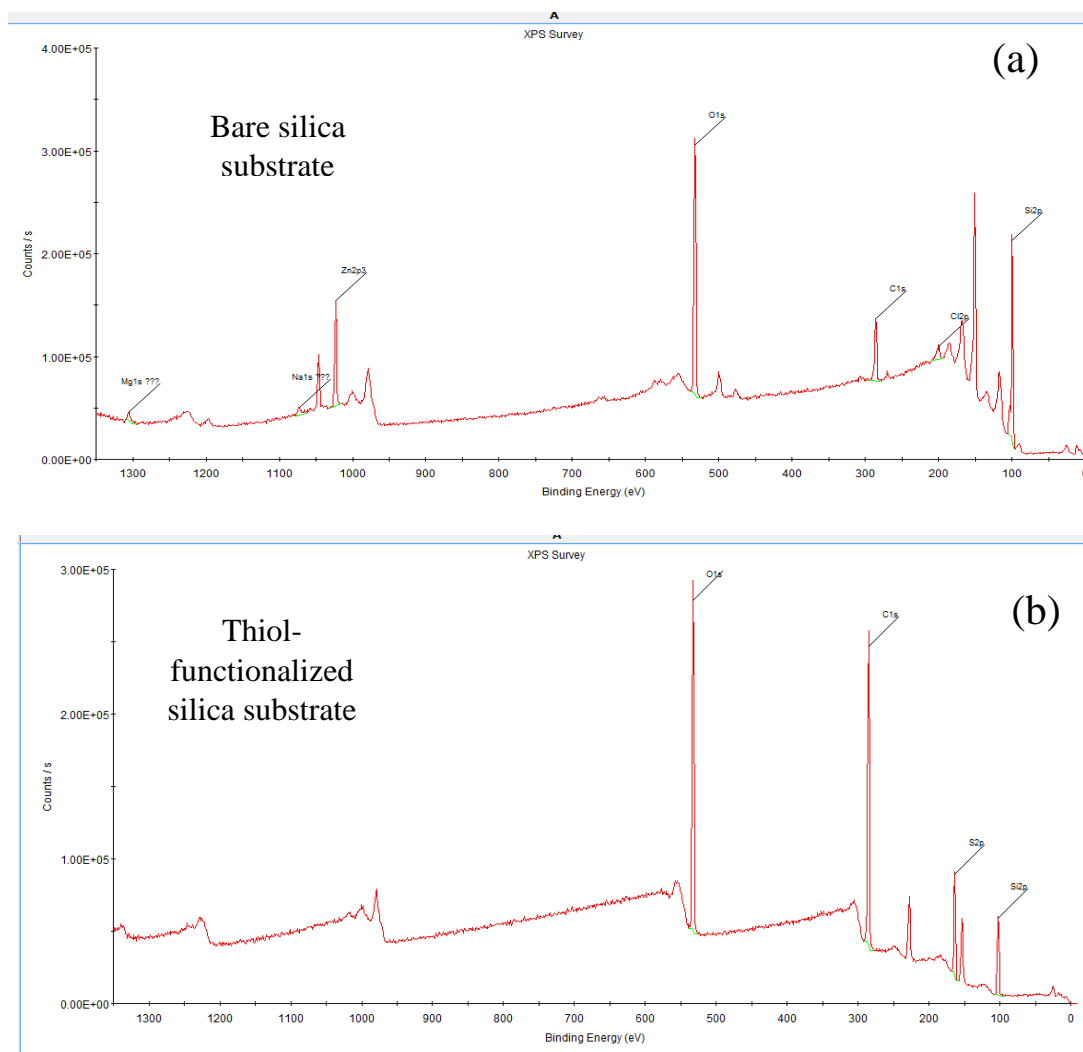
Regular silica wafers (not QCM sensors):

The bare silicon wafer “control” was cleaned with only a 5:1:1 mixture of DI water, ammonia, and H₂O₂ at 75 °C for 10 mins (no exposure to any thiol-containing chemical e.g. sulfuric acid). The silicon wafers which were supposed to be treated with thiol were initially cleaned with a mixture of Nochromix and sulfuric acid, and then were coated with droplets of pure MPTMS and cured at 110 °C overnight. The wafers were analyzed by X-ray Photoelectron Spectroscopy (XPS) and water contact angle measurements.

A K α XPS instrument (Thermo Scientific) was employed to measure compositions of the elements of C, N, Si, S and O of the adlayer under ultra-high vacuum. For XPS measurements, one bare silicon wafer and two thiol functionalized silicon wafers (functionalized through the same method) were tested. For each wafer, two different spots were analyzed.

Table F.2 Atomic percentages derived from XPS for bare silica and MPTMS-functionalized silica wafers (not QCM sensors) from method B

Atomic percent	O	C	Si	S	Mg	Cl	Zn	Na	Cd	Ca
Bare silicon wafer	27.88	19.61	46.73	---	---	2.45	3.33	---	---	---
Bare silicon wafer (repeat at a different spot)	27.27	19.95	46.37	---	1.09	2.13	2.35	0.83	--	---
Thiol functionalized wafer	21.48	58.4	12.25	6.96	---	---	---	---	---	0.9
Thiol functionalized wafer (repeat at a different spot)	22.31	57	12.56	8.07	---	---	---	---	0.05	---
Another thiol functionalized wafer	22.61	54.54	13.3	9.55	---	---	---	---	---	---
Another thiol functionalized wafer (repeat at a different spot)	23.16	55.43	13.09	8.32	---	---	---	---	---	---



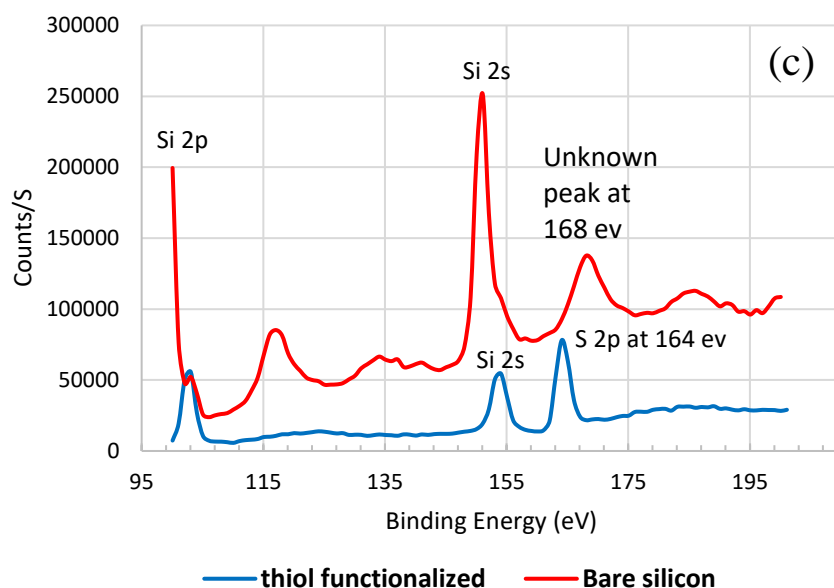


Figure F.3 XPS spectra for (a) bare silica substrate, (b) MPTMS-functionalized silica substrate, and (c) expanded spectra of the bare and thiol functionalized silica substrates for comparison.

Table F.3 Water contact angle measurements for bare and MPTMS-functionalized silica substrates from method B

Silica Substrate	Average angle °
Bare	40.83 ± 6.89
Thiol functionalized	81.83 ± 4.57

Thiol functionalization and characterization of QCM silica sensors:

The bare QCM silica sensor was cleaned with only a 5:1:1 mixture of DI water, ammonia, and H₂O₂ at 75 °C for 10 mins (no exposure to any sulfur-containing chemical

e.g. sulfuric acid). The QCM silica sensor which was supposed to be functionalized with thiol were coated with droplets of pure MPTMS and cured at 110 °C overnight. The sensors were analyzed by XPS.

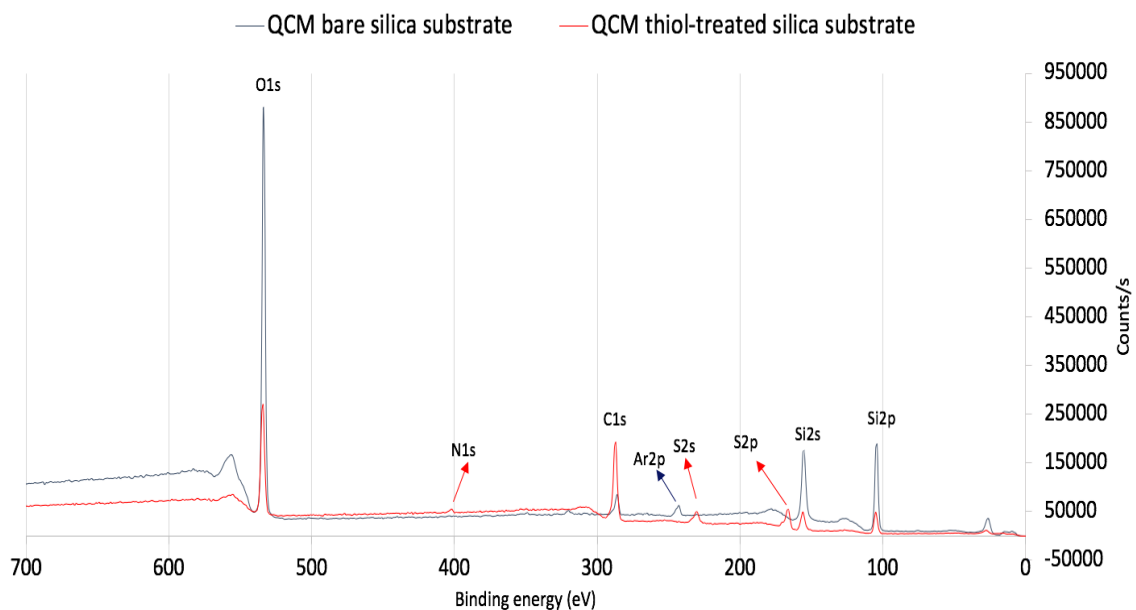


Figure F.4 XPS spectra for (a) bare silica and (b) MPTMS-functionalized silica QCM sensors from method B.

Table F.4 Atomic percentages derived from XPS for bare silica and MPTMS-functionalized silica QCM sensors from method B

Atomic percent	O	C	Si2p	Si2s	S2p	S2s	Ar	N
QCM bare silica sensor	44.57	6.75	23.51	24.06	----	----	1.11	----
QCM MPTMS-treated silica sensor	25.41	45.27	10.78	10.21	5.98	0.61	---	1.74

In sum, it was shown that method A provided acceptable QCM-D data (consistent with formation of a monolayer of thiol) and allowed for the sensors to be tested with BSA using QCM-D. On the contrary, method B provided promising XPS data, but because of

the large thickness of the adjacent grafted MPTMS multilayers on the surface, QCM-D was not applicable. Since the goal of this study was to achieve a monolayer of thiol on silica (detectable by QCM) and later functionalizing the thiol groups with other molecules (e.g. lignin dimers or double-bond modified CDs through thiol-ene click chemistry) use of method A is preferred over method B.

REFERENCES

1. Figueiredo, P., et al., *Properties and chemical modifications of lignin: Towards lignin-based nanomaterials for biomedical applications*. Progress in Materials Science, 2018. **93**: p. 233-269.
2. Kai, D., et al., *Engineering highly stretchable lignin-based electrospun nanofibers for potential biomedical applications*. Journal of Materials Chemistry B, 2015. **3**(30): p. 6194-6204.
3. Pt, M., et al., *Discovery of Lignin in Seaweed Reveals Convergent Evolution of Cell-Wall Architecture*. Cur. bio, 2009. **19**(2): p. 169-75.
4. Upton, B.M. and A.M. Kasko, *Strategies for the conversion of lignin to high-value polymeric materials: review and perspective*. Chemical reviews, 2015. **116**(4): p. 2275-2306.
5. Kleinert, M. and T. Barth, *Phenols from lignin*. Chemical Engineering & Technology: Industrial Chemistry-Plant Equipment-Process Engineering-Biotechnology, 2008. **31**(5): p. 736-745.
6. Awungacha Lekelefac, C., et al., *Photocatalytic based degradation processes of lignin derivatives*. 2015. **2015**.
7. Demuner, I.F., et al., *Biorefinery review: Wide-reaching products through kraft lignin*. BioResources, 2019. **14**(3): p. 7543-7581.
8. Li, C., et al., *Catalytic Transformation of Lignin for the Production of Chemicals and Fuels*. Chem Rev, 2015. **115**(21): p. 11559-624.
9. Carey, F.A. and R.J. Sundberg, *Aromatic substitution*, in *Advanced Organic Chemistry*. 2007, Springer. p. 771-831.
10. Kumar, Y., et al., *AromaDb: A Database of Medicinal and Aromatic Plant's Aroma Molecules With Phytochemistry and Therapeutic Potentials*. Frontiers in plant science, 2018. **9**.
11. Tong, X., et al., *Experimental and Molecular Dynamics Simulation Study of the Effects of Lignin Dimers on the Gel-to-Fluid Phase Transition in DPPC Bilayers*. Journal of Physical Chemistry B, 2019. **129**(39): p. 8247-8260.
12. Moradipour, M., et al., *Interaction of lignin dimers with model cell membranes: A quartz crystal microbalance and molecular dynamics simulation study*. Biointerphases, 2021. **16**(4).
13. Moradipour, M., et al., *Interaction of lignin-derived dimer and eugenol-functionalized silica nanoparticles with supported lipid bilayers*. Colloids and Surfaces B: Biointerfaces, 2020. **191**: p. 111028.
14. Rajan, K., et al., *Sustainable hydrogels based on lignin-methacrylate copolymers with enhanced water retention and tunable material properties*. Biomacromolecules, 2018.
15. Beisl, S., A. Miltner, and A. Friedl, *Lignin from micro-to nanosize: production methods*. International journal of molecular sciences, 2017. **18**(6): p. 1244.

16. Du, L., et al., *A comparison of monomeric phenols produced from lignin by fast pyrolysis and hydrothermal conversions*. International Journal of Chemical Reactor Engineering, 2013. **11**(1): p. 135-145.
17. Laurichesse, S. and L. Avérous, *Chemical modification of lignins: Towards biobased polymers*. Progress in polymer science, 2014. **39**(7): p. 1266-1290.
18. Gall, D.L., et al., *A group of sequence-related sphingomonad enzymes catalyzes cleavage of β -aryl ether linkages in lignin β -guaiacyl and β -syringyl ether dimers*. Environmental science & technology, 2014. **48**(20): p. 12454-12463.
19. Ardalani, H., A. Avan, and M. Ghayour-Mobarhan, *Podophyllotoxin: a novel potential natural anticancer agent*. Avicenna journal of phytomedicine, 2017. **7**(4): p. 285.
20. MacRae, W.D. and G.N. Towers, *Biological activities of lignans*. Phytochemistry, 1984. **23**(6): p. 1207-1220.
21. Zhou, H., J. Ren, and Z. Li, *Antibacterial activity and mechanism of pinoresinol from Cinnamomum Camphora leaves against food-related bacteria*. Food Control, 2017. **79**: p. 192-199.
22. Brenes, M., et al., *Pinoresinol and 1-acetoxypinoresinol, two new phenolic compounds identified in olive oil*. Journal of the American Oil Chemists' Society, 2000. **77**(7): p. 715-720.
23. Yue, F., et al., *Lignin-derived thioacidolysis dimers: reevaluation, new products, authentication, and quantification*. ChemSusChem, 2017. **10**(5): p. 830-835.
24. Schroeder, F.C., et al., *Pinoresinol: a lignol of plant origin serving for defense in a caterpillar*. Proceedings of the National Academy of Sciences, 2006. **103**(42): p. 15497-15501.
25. Vanholme, R., et al., *Lignin biosynthesis and structure*. Plant physiology, 2010. **153**(3): p. 895-905.
26. Zhang, J.-j., et al., *Pyrolysis mechanism of a β -O-4 type lignin dimer model compound*. Journal of Thermal Analysis and Calorimetry, 2016. **123**(1): p. 501-510.
27. Goñi, M.A. and J.I. Hedges, *Lignin dimers: Structures, distribution, and potential geochemical applications*. Geochimica et Cosmochimica Acta, 1992. **56**(11): p. 4025-4043.
28. Njiojob, C.N., et al., *Synthesis of enantiomerically pure lignin dimer models for catalytic selectivity studies*. The Journal of organic chemistry, 2015. **80**(3): p. 1771-1780.
29. Asare, S.O., et al., *Application of Chloride Adduct Ionization Tandem Mass Spectrometry for Characterizing and Sequencing Synthetic Lignin Model Compounds*. Energy & Fuels, 2018. **32**(5): p. 5990-5998.
30. Duval, A. and M. Lawoko, *A review on lignin-based polymeric, micro-and nano-structured materials*. Reactive and Functional Polymers, 2014. **85**: p. 78-96.
31. Joffres, B., et al., *Thermochemical conversion of lignin for fuels and chemicals: A review*. Oil & Gas Science and Technology—Revue d'IFP Energies nouvelles, 2013. **68**(4): p. 753-763.
32. Ponnusamy, V.K., et al., *A review on lignin structure, pretreatments, fermentation reactions and biorefinery potential*. Bioresource technology, 2019. **271**: p. 462-472.

33. Martínez, Á.T., et al., *Biodegradation of lignocellulosics: microbial, chemical, and enzymatic aspects of the fungal attack of lignin*. 2005.
34. Beisl, S., et al., *Production of Micro- and Nanoscale Lignin from Wheat Straw Using Different Precipitation Setups*. *Molecules*, 2018. **23**(3): p. 633.
35. Barakat, A., et al., *Supramolecular organization of heteroxylan-dehydrogenation polymers (synthetic lignin) nanoparticles*. *Biomacromolecules*, 2008. **9**(2): p. 487-93.
36. Dai, L., et al., *Lignin-Containing Self-Nanoemulsifying Drug Delivery System for Enhance Stability and Oral Absorption of trans-Resveratrol*. *Particle & Particle Systems Characterization*, 2018. **35**(4): p. 1700447.
37. Lievonen, M., et al., *A simple process for lignin nanoparticle preparation*. *Green Chemistry*, 2016. **18**(5): p. 1416-1422.
38. Byrne, C.E., et al., *Lignin-graft-PLGA drug-delivery system improves efficacy of MEK1/2 inhibitors in triple-negative breast cancer cell line*. *Nanomedicine*, 2020. **15**(10): p. 981-1000.
39. Figueiredo, P., et al., *In vitro evaluation of biodegradable lignin-based nanoparticles for drug delivery and enhanced antiproliferation effect in cancer cells*. *Biomaterials*, 2017. **121**: p. 97-108.
40. Lintinen, K., et al., *Closed cycle production of concentrated and dry redispersible colloidal lignin particles with a three solvent polarity exchange method*. *Green Chemistry*, 2018. **20**(4): p. 843-850.
41. Nair, S.S., et al., *Investigating the effect of lignin on the mechanical, thermal, and barrier properties of cellulose nanofibril reinforced epoxy composite*. *Industrial Crops and Products*, 2017. **100**: p. 208-217.
42. Piccinino, D., et al., *Layer-by-Layer Preparation of Microcapsules and Nanocapsules of Mixed Polyphenols with High Antioxidant and UV-Shielding Properties*. *Biomacromolecules*, 2018. **19**(9): p. 3883-3893.
43. Chen, N., L.A. Dempere, and Z. Tong, *Synthesis of pH-Responsive Lignin-Based Nanocapsules for Controlled Release of Hydrophobic Molecules*. *ACS Sustainable Chemistry & Engineering*, 2016. **4**(10): p. 5204-5211.
44. Klapiszewski, L., et al., *Kraft lignin/silica-AgNPs as a functional material with antibacterial activity*. *Colloids and Surfaces B: Biointerfaces*, 2015. **134**: p. 220-228.
45. Asnis, J., *Production, characterization, and biodistribution of lignin-capped silver nanoparticles to combat multidrug resistant bacteria in vitro and in vivo*. 2018, University of British Columbia: Vancouver, Canada.
46. Hu, S. and Y.-L. Hsieh, *Silver nanoparticle synthesis using lignin as reducing and capping agents: A kinetic and mechanistic study*. *International Journal of Biological Macromolecules*, 2016. **82**: p. 856-862.
47. Azimvand, J., K. Didehban, and S. Mirshokraie, *Preparation and Characterization of Nano-lignin Biomaterial to Remove Basic Red 2 dye from aqueous solutions*. *Pollution*, 2018. **4**(3): p. 395-415.
48. Li, Z., Y. Ge, and L. Wan, *Fabrication of a green porous lignin-based sphere for the removal of lead ions from aqueous media*. *Journal of Hazardous Materials*, 2015. **285**: p. 77-83.

49. Myint, A.A., et al., *One pot synthesis of environmentally friendly lignin nanoparticles with compressed liquid carbon dioxide as an antisolvent*. Green Chemistry, 2016. **18**(7): p. 2129-2146.
50. Chen, F., et al., *Sheet-Like Lignin Particles as Multifunctional Fillers in Polypropylene*. ACS Sustainable Chemistry & Engineering, 2016. **4**(9): p. 4997-5004.
51. Frangville, C., et al., *Fabrication of Environmentally Biodegradable Lignin Nanoparticles*. ChemPhysChem, 2012. **13**(18): p. 4235-4243.
52. Iravani, S., *Biomedical applications of lignin-based nanoparticles*, in *Nanoparticles and their Biomedical Applications*. 2020, Springer. p. 217-224.
53. Alzagameem, A., et al., *Antimicrobial activity of lignin and lignin-derived cellulose and chitosan composites against selected pathogenic and spoilage microorganisms*. Polymers, 2019. **11**(4): p. 670.
54. Xiong, F., et al., *Transparent Nanocomposite Films of Lignin Nanospheres and Poly(vinyl alcohol) for UV-Absorbing*. Industrial & Engineering Chemistry Research, 2018. **57**(4): p. 1207-1212.
55. Yang, W., et al., *Synergic effect of cellulose and lignin nanostructures in PLA based systems for food antibacterial packaging*. European Polymer Journal, 2016. **79**: p. 1-12.
56. Zadeh, E.M., S.F. O'Keefe, and Y.-T. Kim, *Utilization of lignin in biopolymeric packaging films*. ACS omega, 2018. **3**(7): p. 7388-7398.
57. Yang, W., et al., *Valorization of Acid Isolated High Yield Lignin Nanoparticles as Innovative Antioxidant/Antimicrobial Organic Materials*. ACS Sustainable Chemistry & Engineering, 2018. **6**(3): p. 3502-3514.
58. Pang, Y., et al., *Preparation of Lignin/Sodium Dodecyl Sulfate Composite Nanoparticles and Their Application in Pickering Emulsion Template-Based Microencapsulation*. Journal of Agricultural and Food Chemistry, 2017. **65**(50): p. 11011-11019.
59. Tian, D., et al., *Lignin valorization: lignin nanoparticles as high-value bio-additive for multifunctional nanocomposites*. Biotechnology for biofuels, 2017. **10**(1): p. 192.
60. Kai, D., et al., *Sustainable and Antioxidant Lignin–Polyester Copolymers and Nanofibers for Potential Healthcare Applications*. ACS Sustainable Chemistry & Engineering, 2017. **5**(7): p. 6016-6025.
61. Kai, D., et al., *Engineering poly (lactide)–lignin nanofibers with antioxidant activity for biomedical application*. ACS Sustainable Chemistry & Engineering, 2016. **4**(10): p. 5268-5276.
62. Yang, W., et al., *Role of lignin nanoparticles in UV resistance, thermal and mechanical performance of PMMA nanocomposites prepared by a combined free-radical graft polymerization/masterbatch procedure*. Composites Part A: Applied Science and Manufacturing, 2018. **107**: p. 61-69.
63. de Assis, C.A., et al., *Techno-Economic Assessment, Scalability, and Applications of Aerosol Lignin Micro- and Nanoparticles*. ACS Sustainable Chemistry & Engineering, 2018. **6**(9): p. 11853-11868.
64. Parit, M., et al., *Transparent and Homogenous Cellulose Nanocrystal/Lignin UV-Protection Films*. ACS Omega, 2018. **3**(9): p. 10679-10691.

65. Rak, M.J., T. Friščić, and A. Moores, *One-step, solvent-free mechanosynthesis of silver nanoparticle-infused lignin composites for use as highly active multidrug resistant antibacterial filters*. RSC advances, 2016. **6**(63): p. 58365-58370.
66. Lee, E.-S., et al., *Antimicrobial properties of lignin-decorated thin multi-walled carbon nanotubes in poly (vinyl alcohol) nanocomposites*. European Polymer Journal, 2018. **105**: p. 79-84.
67. Yang, W., et al., *Antioxidant and antibacterial lignin nanoparticles in polyvinyl alcohol/chitosan films for active packaging*. Industrial Crops and Products, 2016. **94**: p. 800-811.
68. Bian, H., et al., *Lignin nanoparticles as nano-spacers for tuning the viscoelasticity of cellulose nanofibril reinforced polyvinyl alcohol-borax hydrogel*. European Polymer Journal, 2018. **107**: p. 267-274.
69. Wang, X., et al., *Thermal, mechanical, and degradation properties of nanocomposites prepared using lignin-cellulose nanofibers and poly (lactic acid)*. BioResources, 2014. **9**(2): p. 3211-3224.
70. Wang, X., et al., *Influence of the lignin content on the properties of poly (lactic acid)/lignin-containing cellulose nanofibrils composite films*. Polymers, 2018. **10**(9): p. 1013.
71. Gupta, A.K., S. Mohanty, and S. Nayak, *Influence of addition of vapor grown carbon fibers on mechanical, thermal and biodegradation properties of lignin nanoparticle filled bio-poly (trimethylene terephthalate) hybrid nanocomposites*. RSC Advances, 2015. **5**(69): p. 56028-56036.
72. Mhd Haniffa, M.A.C., et al., *Review of bionanocomposite coating films and their applications*. Polymers, 2016. **8**(7): p. 246.
73. Peetla, C., A. Stine, and V. Labhasetwar, *Biophysical interactions with model lipid membranes: applications in drug discovery and drug delivery*. Molecular pharmaceutics, 2009. **6**(5): p. 1264-1276.
74. Alberts, B., *Molecular biology of cell*, Bruce Alberts, Dennis Bray, Julian Lewis, Martin Raff, Keith Roberts, James D. Watson. 1989.
75. Rahmaninejad, H. and D.D. Vaughan, *Effect of membrane cholesterol on dynamical properties of solvent molecules*. bioRxiv, 2021.
76. Alberts, B., et al., *The cell cycle*. Molecular biology of the cell, 2008. **5**: p. 1053-1114.
77. Cooper, G.M. and D. Ganem, *The cell: a molecular approach*. Nature Medicine, 1997. **3**(9): p. 1042-1042.
78. Lasic, D. and D. Papahadjopoulos, *Liposomes revisited*. Science, 1995. **267**(5202): p. 1275-1277.
79. Chan, Y.-H.M. and S.G. Boxer, *Model membrane systems and their applications*. Current opinion in chemical biology, 2007. **11**(6): p. 581-587.
80. Demetzos, C., *Differential scanning calorimetry (DSC): a tool to study the thermal behavior of lipid bilayers and liposomal stability*. Journal of liposome research, 2008. **18**(3): p. 159-173.
81. Faraji, A.H. and P. Wipf, *Nanoparticles in cellular drug delivery*. Bioorganic & medicinal chemistry, 2009. **17**(8): p. 2950-2962.
82. Ferhan, A.R., et al., *Solvent-assisted preparation of supported lipid bilayers*. Nat. Protoc., 2019. **14**: p. 2091-2118.

83. Hardy, G.J., R. Nayak, and S. Zauscher, *Model cell membranes: Techniques to form complex biomimetic supported lipid bilayers via vesicle fusion*. Current opinion in colloid & interface science, 2013. **18**(5): p. 448-458.
84. Tamm, L.K. and H.M. McConnell, *Supported phospholipid bilayers*. Biophysical journal, 1985. **47**(1): p. 105.
85. Loose, M. and P. Schwille, *Biomimetic membrane systems to study cellular organization*. Journal of structural biology, 2009. **168**(1): p. 143-151.
86. Tabaei, S.R., et al., *Solvent-assisted lipid bilayer formation on silicon dioxide and gold*. Langmuir, 2014. **30**(34): p. 10363-73.
87. Anderson, T.H., et al., *Formation of supported bilayers on silica substrates*. Langmuir, 2009. **25**(12): p. 6997-7005.
88. Farnoud, A.M. and S. Nazemidashtarjandi, *Emerging investigator series: interactions of engineered nanomaterials with the cell plasma membrane; what have we learned from membrane models?* Environ. Sci. Nano, 2019. **6**(1): p. 13-40.
89. Blume, A., *A comparative study of the phase transitions of phospholipid bilayers and monolayers*. Biochimica et Biophysica Acta (BBA)-Biomembranes, 1979. **557**(1): p. 32-44.
90. Spink, C.H., *Differential scanning calorimetry*. Methods in cell biology, 2008. **84**: p. 115-141.
91. Riske, K.A., et al., *Lipid bilayer pre-transition as the beginning of the melting process*. Biochimica et Biophysica Acta (BBA)-Biomembranes, 2009. **1788**(5): p. 954-963.
92. Fujisawa, S., Y. Kadoma, and E. Masuhara, *A calorimetric study of the interaction of synthetic phospholipid liposomes with vinyl monomers, acrylates and methacrylates*. Journal of biomedical materials research, 1984. **18**(9): p. 1105-1114.
93. Ojogun, V., et al., *Partitioning of homologous nicotinic acid ester prodrugs (nicotinates) into dipalmitoylphosphatidylcholine (DPPC) membrane bilayers*. Colloids Surf B Biointerfaces, 2010. **78**(1): p. 75-84.
94. Inoue, T., K. Miyakawa, and R. Shimozaawa, *Interaction of surfactants with vesicle membrane of dipalmitoylphosphatidylcholine. Effect on gel-to-liquid-crystalline phase transition of lipid bilayer*. Chemistry and physics of lipids, 1986. **42**(4): p. 261-270.
95. Yousefi, N. and N. Tufenkji, *Probing the interaction between nanoparticles and lipid membranes by quartz crystal microbalance with dissipation monitoring*. Frontiers in chemistry, 2016. **4**: p. 46.
96. Dixon, M.C., *Quartz crystal microbalance with dissipation monitoring: enabling real-time characterization of biological materials and their interactions*. Journal of biomolecular techniques: JBT, 2008. **19**(3): p. 151.
97. Andersson, M., et al., *Acoustics of blood plasma on solid surfaces*. Journal of Biomaterials Science, Polymer Edition, 2002. **13**(8): p. 907-917.
98. Rodahl, M. and B. Kasemo, *A simple setup to simultaneously measure the resonant frequency and the absolute dissipation factor of a quartz crystal microbalance*. Review of Scientific Instruments, 1996. **67**(9): p. 3238-3241.

99. Sadman, K., et al., *Quantitative rheometry of thin soft materials using the quartz crystal microbalance with dissipation*. Analytical chemistry, 2018. **90**(6): p. 4079-4088.
100. Mechler, A., et al., *Specific and selective peptide-membrane interactions revealed using quartz crystal microbalance*. Biophysical journal, 2007. **93**(11): p. 3907-3916.
101. Joshi, T., et al., *Real-time examination of aminoglycoside activity towards bacterial mimetic membranes using Quartz Crystal Microbalance with Dissipation monitoring (QCM-D)*. Biochimica et Biophysica Acta, 2015. **1848**(2): p. 385-91.
102. Strauss, J., Y. Liu, and T.A. Camesano, *Bacterial adhesion to protein-coated surfaces: An AFM and QCM-D study*. Jom, 2009. **61**(9): p. 71-74.
103. Richter, R.P., R. Bérat, and A.R. Brisson, *Formation of solid-supported lipid bilayers: an integrated view*. Langmuir, 2006. **22**(8): p. 3497-3505.
104. Boija, E. and G. Johansson, *Interactions between model membranes and lignin-related compounds studied by immobilized liposome chromatography*. Biochimica et Biophysica Acta (BBA)-Biomembranes, 2006. **1758**(5): p. 620-626.
105. Fujisawa, S., Y. Kadoma, and E. Masuhara, *A calorimetric study of the interaction of synthetic phospholipid liposomes with lipid-soluble small molecules used as dental materials and devices*. Journal of biomedical materials research, 1987. **21**(1): p. 89-98.
106. Jain, M.K. and N.M. Wu, *Effect of small molecules on the dipalmitoyl lecithin liposomal bilayer: III. Phase transition in lipid bilayer*. The Journal of Membrane Biology, 1977. **34**(1): p. 157-201.
107. MacCallum, J.L. and D.P. Tieleman, *Interactions between small molecules and lipid bilayers*. Current Topics in Membranes, 2008. **60**: p. 227-256.
108. Kannisto, K., L. Murtomäki, and T. Viitala, *An impedance QCM study on the partitioning of bioactive compounds in supported phospholipid bilayers*. Colloids and Surfaces B: Biointerfaces, 2011. **86**(2): p. 298-304.
109. Wargenau, A., et al., *Evaluating the Cell Membrane Penetration Potential of Lipid-Soluble Compounds Using Supported Phospholipid Bilayers*. Journal of Analytical Chemistry, 2018. **90**(19): p. 11174-11178.
110. Tammela, P., et al., *Permeability characteristics and membrane affinity of flavonoids and alkyl gallates in Caco-2 cells and in phospholipid vesicles*. Archives of biochemistry and biophysics, 2004. **425**(2): p. 193-199.
111. Narayan, R., et al., *Mesoporous silica nanoparticles: A comprehensive review on synthesis and recent advances*. Pharmaceutics, 2018. **10**(3): p. 118.
112. Rosenholm, J.M., et al., *Mesoporous silica nanoparticles in tissue engineering—a perspective*. Nanomedicine, 2016. **11**(4): p. 391-402.
113. Korzeniowska, B., et al., *Silica nanoparticles for cell imaging and intracellular sensing*. Nanotechnology, 2013. **24**(44): p. 442002.
114. Sheet, I., A. Kabbani, and H. Holail, *Removal of heavy metals using nanostructured graphite oxide, silica nanoparticles and silica/graphite oxide composite*. Energy Procedia, 2014. **50**: p. 130-138.

115. Ding, H.m. and Y.q. Ma, *Theoretical and computational investigations of nanoparticle–biomembrane interactions in cellular delivery*. Small, 2015. **11**(9-10): p. 1055-1071.
116. Chen, Q., et al., *QCM-D study of nanoparticle interactions*. Advances in colloid and interface science, 2016. **233**: p. 94-114.
117. Michel, R. and M. Gradzielski, *Experimental aspects of colloidal interactions in mixed systems of liposome and inorganic nanoparticle and their applications*. International journal of molecular sciences, 2012. **13**(9): p. 11610-11642.
118. Zhao, F., et al., *TiO₂ nanoparticle interactions with supported lipid membranes—an example of removal of membrane patches*. RSC Advances, 2016. **6**(94): p. 91102-91110.
119. Bailey, C.M., et al., *Size dependence of gold nanoparticle interactions with a supported lipid bilayer: A QCM-D study*. Biophys Chem, 2015. **203-204**: p. 51-61.
120. Liu, X. and K.L. Chen, *Aggregation and interactions of chemical mechanical planarization nanoparticles with model biological membranes: role of phosphate adsorption*. Environmental Science: Nano, 2016. **3**(1): p. 146-156.
121. Loftsson, T. and D. Duchêne, *Cyclodextrins and their pharmaceutical applications*. International journal of pharmaceutics, 2007. **329**(1-2): p. 1-11.
122. Brewster, M.E. and T. Loftsson, *Cyclodextrins as pharmaceutical solubilizers*. Advanced drug delivery reviews, 2007. **59**(7): p. 645-666.
123. Kurkov, S.V. and T. Loftsson, *Cyclodextrins*. International journal of pharmaceutics, 2013. **453**(1): p. 167-180.
124. Crini, G., *A history of cyclodextrins*. Chemical reviews, 2014. **114**(21): p. 10940-10975.
125. Bouchemal, K. and S. Mazzaferro, *How to conduct and interpret ITC experiments accurately for cyclodextrin–guest interactions*. Drug Discovery Today, 2012. **17**(11-12): p. 623-629.
126. Kfoury, M., D. Landy, and S. Fourmentin, *Characterization of cyclodextrin/volatile inclusion complexes: a review*. Molecules, 2018. **23**(5): p. 1204.
127. Tarrago, L., et al., *Controlling the polymerization of coniferyl alcohol with cyclodextrins*. New Journal of Chemistry, 2018. **42**(14): p. 11770-11775.
128. Shelley, H. and R.J. Babu, *Role of cyclodextrins in nanoparticle-based drug delivery systems*. Journal of pharmaceutical sciences, 2018. **107**(7): p. 1741-1753.
129. Loftsson, T., et al., *Cyclodextrins in drug delivery*. Expert opinion on drug delivery, 2005. **2**(2): p. 335-351.
130. Schönbeck, C. and R. Holm, *Exploring the Origins of Enthalpy–Entropy Compensation by Calorimetric Studies of Cyclodextrin Complexes*. The Journal of Physical Chemistry B, 2019. **123**(31): p. 6686-6693.
131. Cameron, D.L., et al., *Pressure perturbation calorimetry and the thermodynamics of noncovalent interactions in water: comparison of protein–protein, protein–ligand, and cyclodextrin–adamantane complexes*. The Journal of Physical Chemistry B, 2010. **114**(49): p. 16228-16235.
132. Biedermann, F., W.M. Nau, and H.J. Schneider, *The Hydrophobic Effect Revisited—Studies with Supramolecular Complexes Imply High-Energy Water as*

- a Noncovalent Driving Force*. Angewandte Chemie International Edition, 2014. **53**(42): p. 11158-11171.
133. Wszelaka-Rylik, M. and P. Gierycz, *Isothermal titration calorimetry (ITC) study of natural cyclodextrins inclusion complexes with drugs*. Journal of thermal analysis and calorimetry, 2013. **111**(3): p. 2029-2035.
 134. Wszelaka-Rylik, M. and P. Gierycz, *Isothermal titration calorimetry (ITC) study of natural cyclodextrins inclusion complexes with tropane alkaloids*. Journal of Thermal Analysis and Calorimetry, 2015. **121**(3): p. 1359-1364.
 135. Sun, D.-Z., et al., *Isothermal titration calorimetry and ¹H NMR studies on host-guest interaction of paeonol and two of its isomers with β -cyclodextrin*. International journal of pharmaceutics, 2006. **316**(1-2): p. 7-13.
 136. Bertaut, E. and D. Landy, *Improving ITC studies of cyclodextrin inclusion compounds by global analysis of conventional and non-conventional experiments*. Beilstein journal of organic chemistry, 2014. **10**(1): p. 2630-2641.
 137. Inoue, Y., et al., *Calorimetric titration of inclusion complexation with modified. beta.-cyclodextrins. Enthalpy-entropy compensation in host-guest complexation: from ionophore to cyclodextrin and cyclophane*. Journal of the American Chemical Society, 1993. **115**(23): p. 10637-10644.
 138. Segura-Sanchez, F., et al., *Elucidation of the complexation mechanism between (+)-usnic acid and cyclodextrins studied by isothermal titration calorimetry and phase-solubility diagram experiments*. Journal of Molecular Recognition: An Interdisciplinary Journal, 2009. **22**(3): p. 232-241.
 139. Yamamura, H., et al., *Factors controlling the complex architecture of native and modified cyclodextrins with dipeptide (Z-Glu-Tyr) studied by microcalorimetry and NMR spectroscopy: critical effects of peripheral bis-trimethylamination and cavity size*. Journal of the American Chemical Society, 2004. **126**(43): p. 14224-14233.
 140. Schönbeck, C., P. Westh, and R. Holm, *Complexation thermodynamics of modified cyclodextrins: extended cavities and distorted structures*. The Journal of Physical Chemistry B, 2014. **118**(34): p. 10120-10129.
 141. Grunwald, E. and C. Steel, *Solvent reorganization and thermodynamic enthalpy-entropy compensation*. Journal of the American Chemical Society, 1995. **117**(21): p. 5687-5692.
 142. Breiten, B., et al., *Water networks contribute to enthalpy/entropy compensation in protein-ligand binding*. Journal of the American Chemical Society, 2013. **135**(41): p. 15579-15584.
 143. Velázquez-Campoy, A., et al., *Isothermal titration calorimetry*. Current protocols in cell biology, 2004. **23**(1): p. 17.8. 1-17.8. 24.
 144. Wiseman, T., et al., *Rapid measurement of binding constants and heats of binding using a new titration calorimeter*. Analytical biochemistry, 1989. **179**(1): p. 131-137.
 145. Khan, M.A., *Nanoharvesting and Delivery of Bioactive Materials Using Engineered Silica Nanoparticles*. 2019.
 146. Lee, J., et al., *Mesoporous nanocarriers with a stimulus-responsive cyclodextrin gatekeeper for targeting tumor hypoxia*. Nanoscale, 2017. **9**(20): p. 6901-6909.

147. Roik, N.V., et al., *Mesoporous silicas with covalently immobilized β -cyclodextrin moieties: synthesis, structure, and sorption properties*. Journal of Nanoparticle Research, 2017. **19**(9): p. 317.
148. Silva, M., et al., *Ordered mesoporous silica functionalized with β -cyclodextrin derivative for stereoisomer separation of flavanones and flavanone glycosides by nano-liquid chromatography and capillary electrochromatography*. Journal of Chromatography A, 2017. **1490**: p. 166-176.
149. Chen, X., et al., *β -Cyclodextrin-functionalized silver nanoparticles for the naked eye detection of aromatic isomers*. ACS nano, 2010. **4**(11): p. 6387-6394.
150. Xavier, S.S.J., et al., *Colorimetric detection of melamine using β -cyclodextrin-functionalized silver nanoparticles*. Analytical Methods, 2014. **6**(20): p. 8165-8172.
151. Kang, Y., et al., *β -Cyclodextrin-modified hybrid magnetic nanoparticles for catalysis and adsorption*. Journal of Materials Chemistry, 2011. **21**(11): p. 3704-3710.
152. Bibby, A. and L. Mercier, *Adsorption and separation of water-soluble aromatic molecules by cyclodextrin-functionalized mesoporous silica*. Green Chemistry, 2003. **5**(1): p. 15-19.
153. Raoov, M., S. Mohamad, and M.R. Abas, *Synthesis and characterization of β -cyclodextrin functionalized ionic liquid polymer as a macroporous material for the removal of phenols and As (V)*. International journal of molecular sciences, 2014. **15**(1): p. 100-119.
154. Hu, Q.-D., G.-P. Tang, and P.K. Chu, *Cyclodextrin-based host-guest supramolecular nanoparticles for delivery: from design to applications*. Accounts of chemical research, 2014. **47**(7): p. 2017-2025.
155. Olteanu, A.A., et al., *Effect of β -cyclodextrins based nanosponges on the solubility of lipophilic pharmacological active substances (repaglinide)*. Journal of inclusion phenomena and macrocyclic chemistry, 2014. **80**(1-2): p. 17-24.
156. Gholibegloo, E., et al., *Improved curcumin loading, release, solubility and toxicity by tuning the molar ratio of cross-linker to β -cyclodextrin*. Carbohydrate polymers, 2019. **213**: p. 70-78.
157. Shende, P.K., et al., *Effect of inclusion complexation of meloxicam with β -cyclodextrin-and β -cyclodextrin-based nanosponges on solubility, in vitro release and stability studies*. Colloids and surfaces B: biointerfaces, 2015. **136**: p. 105-110.
158. Pinho, E., et al., *Cyclodextrin-based hydrogels toward improved wound dressings*. Critical reviews in biotechnology, 2014. **34**(4): p. 328-337.
159. Lu, Q., D. Chen, and X. Jiao, *Fabrication of mesoporous silica microtubules through the self-assembly behavior of β -cyclodextrin and triton X-100 in aqueous solution*. Chemistry of materials, 2005. **17**(16): p. 4168-4173.
160. Huq, R., L. Mercier, and P. Kooyman, *Incorporation of cyclodextrin into mesostructured silica*. Chemistry of materials, 2001. **13**(12): p. 4512-4519.
161. Palaniappan, A., et al., *Cyclodextrin functionalized mesoporous silica films on quartz crystal microbalance for enhanced gas sensing*. Sensors and Actuators B: Chemical, 2006. **119**(1): p. 220-226.

162. Wan, Y. and D. Zhao, *On the controllable soft-templating approach to mesoporous silicates*. Chemical reviews, 2007. **107**(7): p. 2821-2860.
163. Ortiz-Bustos, J., et al., *Surface-functionalization of mesoporous SBA-15 silica materials for controlled release of methylprednisolone sodium hemisuccinate: influence of functionality type and strategies of incorporation*. Microporous and Mesoporous Materials, 2017. **240**: p. 236-245.
164. Lebeau, B., et al., *Organically modified ordered mesoporous siliceous solids*, in *Ordered porous solids*. 2009, Elsevier. p. 283-308.
165. Morin-Crini, N., et al., *Synthesis of silica materials containing cyclodextrin and their applications in wastewater treatment*. Environmental Chemistry Letters, 2019. **17**(2): p. 683-696.
166. Vinardell, M.P. and M. Mitjans, *Lignins and their derivatives with beneficial effects on human health*. International journal of molecular sciences, 2017. **18**(6): p. 1219.
167. Sato, S., et al., *Effect of lignin-derived lignophenols on hepatic lipid metabolism in rats fed a high-fat diet*. Environmental Toxicology and Pharmacology, 2012. **34**(2): p. 228-234.
168. Witzler, M., et al., *Lignin-Derived Biomaterials for Drug Release and Tissue Engineering*. Molecules, 2018. **23**(8): p. 1885.
169. Baurhoo, B., C. Ruiz-Feria, and X. Zhao, *Purified lignin: Nutritional and health impacts on farm animals—A review*. Animal Feed Science and Technology, 2008. **144**(3-4): p. 175-184.
170. Pan, X., et al., *Organosolv ethanol lignin from hybrid poplar as a radical scavenger: relationship between lignin structure, extraction conditions, and antioxidant activity*. Journal of agricultural and food chemistry, 2006. **54**(16): p. 5806-5813.
171. Azadfar, M., et al., *Structural characterization of lignin: A potential source of antioxidants guaiacol and 4-vinylguaiacol*. International journal of biological macromolecules, 2015. **75**: p. 58-66.
172. Xü, Y., et al., *Protein-mediated lipid transfer. The effects of lipid-phase transition and of charged lipids*. Biochemical Journal, 1983. **213**(1): p. 21-24.
173. Saija, A., et al., *Flavonoids as antioxidant agents: importance of their interaction with biomembranes*. Free Radical Biology and Medicine, 1995. **19**(4): p. 481-486.
174. Hendrich, A.B., et al., *Differential interaction of Sophora isoflavonoids with lipid bilayers*. European journal of pharmaceutical sciences, 2002. **16**(3): p. 201-208.
175. Zhao, L., et al., *DSC and EPR investigations on effects of cholesterol component on molecular interactions between paclitaxel and phospholipid within lipid bilayer membrane*. 2007. **338**(1-2): p. 258-266.
176. Liu, C.-J., Y.-C. Miao, and K.-W. Zhang, *Sequestration and Transport of Lignin Monomeric Precursors*. Molecules, 2011. **16**(1): p. 710-727.
177. Miao, Y.-C. and C.-J. Liu, *ATP-binding cassette-like transporters are involved in the transport of lignin precursors across plasma and vacuolar membranes*. Proceedings of the National Academy of Sciences, 2010. **107**(52): p. 22728-22733.

178. Perkins, M., R.A. Smith, and L. Samuels, *The transport of monomers during lignification in plants: anything goes but how?* Current Opinion in Biotechnology, 2019. **56**: p. 69-74.
179. Sibout, R. and H. Höfte, *Plant Cell Biology: The ABC of Monolignol Transport*. Current Biology, 2012. **22**(13): p. R533-R535.
180. Szoka Jr, F., D.J.A.r.o.b. Papahadjopoulos, and bioengineering, *Comparative properties and methods of preparation of lipid vesicles (liposomes)*. 1980. **9**(1): p. 467-508.
181. Olson, F., et al., *Preparation of liposomes of defined size distribution by extrusion through polycarbonate membranes*. 1979. **557**(1): p. 9-23.
182. RN, M., *The use of differential scanning calorimetry and differential thermal analysis in studies of model and biological membranes*. Chem Phys Lipids, 1982. **30**: p. 229–59.
183. Chiu, M.H. and E.J. Prenner, *Differential scanning calorimetry: An invaluable tool for a detailed thermodynamic characterization of macromolecules and their interactions*. J Pharm Bioallied Sci, 2011. **3**(1): p. 39-59.
184. Maeda, Y., K. Nunomura, and E. Ohtsubo, *Differential scanning calorimetric study of the effect of intercalators and other kinds of DNA-binding drugs on the stepwise melting of plasmid DNA*. J Mol Biol, 1990. **215**(2): p. 321-9.
185. Heerklotz, H.J.Q.r.o.b., *Interactions of surfactants with lipid membranes*. 2008. **41**(3-4): p. 205-264.
186. De Young, L.R. and K.A.J.B. Dill, *Solute partitioning into lipid bilayer membranes*. 1988. **27**(14): p. 5281-5289.
187. Reiner, G.N., et al., *Lipophilicity of some GABAergic phenols and related compounds determined by HPLC and partition coefficients in different systems*. 2009. **49**(3): p. 686-691.
188. Marchese, A., et al., *Antibacterial and antifungal activities of thymol: A brief review of the literature*. 2016. **210**: p. 402-414.
189. Marinelli, L., A. Di Stefano, and I.J.P.R. Cacciatore, *Carvacrol and its derivatives as antibacterial agents*. 2018. **17**(4): p. 903-921.
190. Barber, M.S., V.S. McConnell, and B.S.J.P. DeCaux, *Antimicrobial intermediates of the general phenylpropanoid and lignin specific pathways*. 2000. **54**(1): p. 53-56.
191. Kuentz, M.T. and Y. Arnold, *Influence of molecular properties on oral bioavailability of lipophilic drugs – Mapping of bulkiness and different measures of polarity*. Pharmaceutical Development and Technology, 2009. **14**(3): p. 312-320.
192. Koynova, R. and M. Caffrey, *Phases and phase transitions of the phosphatidylcholines*. Biochim Biophys Acta, 1998. **1376**(1): p. 91-145.
193. Tong, X., *Molecular Dynamics Simulations of Interaction of DNA Nucleotides and Lignin Oligomers With Small Molecules and Interfaces*. LSU Doctoral Dissertations, 2019. **5114**.
194. Kai, D., et al., *Towards lignin-based functional materials in a sustainable world*. Green Chemistry, 2016. **18**(5): p. 1175-1200.
195. Belgodere, J.A., et al., *Modulating Mechanical Properties of Collagen–Lignin Composites*. ACS Applied Bio Materials, 2019. **2**(8): p. 3562-3572.

196. Chen, J., et al., *Production of flocculants, adsorbents, and dispersants from lignin*. *Molecules*, 2018. **23**(4): p. 868.
197. Sun, Z., et al., *Bright Side of Lignin Depolymerization: Toward New Platform Chemicals*. *Chemical Reviews*, 2018. **118**(2): p. 614-678.
198. Bugg, T.D.H., et al., *Pathways for degradation of lignin in bacteria and fungi*. *Natural Product Reports*, 2011. **28**(12): p. 1883-1896.
199. Choi, Y.S., et al., *Pyrolysis reaction networks for lignin model compounds: unraveling thermal deconstruction of β -O-4 and α -O-4 compounds*. *Green Chemistry*, 2016. **18**: p. 1762–1773.
200. Kazzaz, A.E., Z.H. Feizi, and P. Fatehi, *Grafting strategies for hydroxy groups of lignin for producing materials*. *Green Chem.*, 2019. **21**(21): p. 5714-5752.
201. Arroo, R.R.J., et al., *Plant cell factories as a source for anti-cancer lignans*. *Phytochemistry Reviews*, 2002. **1**(1): p. 27-35.
202. Kiyama, R., *Biological effects induced by estrogenic activity of lignans*. *Trends in Food Science & Technology*, 2016. **54**: p. 186-196.
203. Landete, J., *Plant and mammalian lignans: a review of source, intake, metabolism, intestinal bacteria and health*. *Food Res. Int.*, 2012. **46**(1): p. 410-424.
204. Zhang, J., et al., *New lignans and their biological activities*. *Chem Biodivers*, 2014. **11**(1): p. 1-54.
205. Cragg, S.M., et al., *Lignocellulose degradation mechanisms across the Tree of Life*. *Curr Opin Chem Biol*, 2015. **29**: p. 108-19.
206. Lange, H., S. Decina, and C. Crestini, *Oxidative upgrade of lignin – Recent routes reviewed*. *European Polymer Journal*, 2013. **49**(6): p. 1151-1173.
207. Neville, F., et al., *Lipid headgroup discrimination by antimicrobial peptide LL-37: insight into mechanism of action*. *Biophysical journal*, 2006. **90**(4): p. 1275-1287.
208. Vahedi, A., P. Bigdelou, and A.M. Farnoud, *Quantitative analysis of red blood cell membrane phospholipids and modulation of cell-macrophage interactions using cyclodextrins*. *Sci. Rep*, 2020. **10**(1): p. 1-13.
209. Nouri-Sorkhabi, M.H., et al., *Quantitative ^{31}P nuclear magnetic resonance analysis of the phospholipids of erythrocyte membranes using detergent*. *Lipids*, 1996. **31**(7): p. 765-770.
210. Keller, S., et al., *Red blood cell lipids form immiscible liquids*. *Phys. Rev. Lett.*, 1998. **81**(22): p. 5019.
211. Veldhuizen, E.J. and H.P. Haagsman, *Role of pulmonary surfactant components in surface film formation and dynamics*. *Biochim. Biophys. Acta, Biomembr.*, 2000. **1467**(2): p. 255-270.
212. Bigdelou, P., et al., *Loss of membrane asymmetry alters the interactions of erythrocytes with engineered silica nanoparticles*. *Biointerphases*, 2020. **15**(4): p. 041001.
213. Patel, A.R. and C.W. Frank, *Quantitative Analysis of Tethered Vesicle Assemblies by Quartz Crystal Microbalance with Dissipation Monitoring: Binding Dynamics and Bound Water Content*. *Langmuir*, 2006. **22**(18): p. 7587-7599.
214. Cho, N.-J., et al., *Quartz crystal microbalance with dissipation monitoring of supported lipid bilayers on various substrates*. *Nature Protocols*, 2010. **5**: p. 1096.

215. Evans, K.O., *Supported phospholipid bilayer interaction with components found in typical room-temperature ionic liquids—a QCM-D and AFM study*. International journal of molecular sciences, 2008. **9**(4): p. 498-511.
216. Santos-Martinez, M.J., et al., *The use of quartz crystal microbalance with dissipation (QCM-D) for studying nanoparticle-induced platelet aggregation*. Int J Nanomed, 2012. **7**: p. 243–255.
217. Lind, T.K. and M. Cardenas, *Understanding the formation of supported lipid bilayers via vesicle fusion-A case that exemplifies the need for the complementary method approach (Review)*. Biointerphases, 2016. **11**(2).
218. Shpigel, N., et al., *In situ real-time mechanical and morphological characterization of electrodes for electrochemical energy storage and conversion by electrochemical quartz crystal microbalance with dissipation monitoring*. Accounts of chemical research, 2018. **51**(1): p. 69-79.
219. Adib, A.A., et al., *Engineered silica nanoparticles interact differently with lipid monolayers compared to lipid bilayers*. Environ. Sci. Nano, 2018. **5**(2): p. 289-303.
220. Keller, C. and B. Kasemo, *Surface specific kinetics of lipid vesicle adsorption measured with a quartz crystal microbalance*. Biophys. J., 1998. **75**(3): p. 1397-1402.
221. Richter, R., A. Mukhopadhyay, and A. Brisson, *Pathways of lipid vesicle deposition on solid surfaces: a combined QCM-D and AFM study*. Biophys. J., 2003. **85**(5): p. 3035-3047.
222. Lind, T.K., M. Cárdenas, and H.P. Wacklin, *Formation of supported lipid bilayers by vesicle fusion: effect of deposition temperature*. Langmuir, 2014. **30**(25): p. 7259-7263.
223. Zwang, T.J., et al., *Quantification of the layer of hydration of a supported lipid bilayer*. Langmuir, 2010. **26**(7): p. 4598-4601.
224. Marquês, J.T., A.S. Viana, and R.F. de Almeida, *A biomimetic platform to study the interactions of bioelectroactive molecules with lipid nanodomains*. Langmuir, 2014. **30**(42): p. 12627-12637.
225. Shen, H.-H., et al., *The interaction of cubosomes with supported phospholipid bilayers using neutron reflectometry and QCM-D*. Soft Matter, 2011. **7**(18): p. 8041-8049.
226. Tellechea, E., et al., *Model-independent analysis of QCM data on colloidal particle adsorption*. Langmuir, 2009. **25**(9): p. 5177-5184.
227. Kamm, B. and M. Kamm, *Biorefineries--multi product processes*. Adv Biochem Eng Biotechnol, 2007. **105**: p. 175-204.
228. Nada, A.M.A., A.I. El-Diwany, and A.M. Elshafei, *Infrared and antimicrobial studies on different lignins*. Acta Biotechnol, 1989. **9**(3): p. 295–298.
229. Larraneta, E., et al., *Synthesis and Characterization of Lignin Hydrogels for Potential Applications as Drug Eluting Antimicrobial Coatings for Medical Materials*. ACS Sustain Chem Eng, 2018. **6**(7): p. 9037-9046.
230. Kamatou, G.P., I. Vermaak, and A.M. Viljoen, *Eugenol--from the remote Maluku Islands to the international market place: a review of a remarkable and versatile molecule*. Molecules, 2012. **17**(6): p. 6953-81.

231. Modjinou, T., et al., *Antibacterial and antioxidant bio-based networks derived from eugenol using photo-activated thiol-ene reaction*. Reactive and Functional Polymers, 2016. **101**: p. 47-53.
232. Chowdhry, B.Z., et al., *Infrared and Raman Spectroscopy of Eugenol, Isoeugenol, and Methyl Eugenol: Conformational Analysis and Vibrational Assignments from Density Functional Theory Calculations of the Anharmonic Fundamentals*. J Phys Chem A, 2015. **119**(46): p. 11280-92.
233. Bennis, S., et al., *Eugenol induces damage of bacterial and fungal envelope*. Moroccan J. Biol, 2001. **1**: p. 33-39.
234. Devi, K.P., et al., *Eugenol (an essential oil of clove) acts as an antibacterial agent against Salmonella typhi by disrupting the cellular membrane*. Journal of Ethnopharmacology, 2010. **130**(1): p. 107-115.
235. Di Pasqua, R., et al., *Membrane Toxicity of Antimicrobial Compounds from Essential Oils*. Journal of Agricultural and Food Chemistry, 2007. **55**(12): p. 4863-4870.
236. Marchese, A., et al., *Antimicrobial activity of eugenol and essential oils containing eugenol: A mechanistic viewpoint*. Critical Reviews in Microbiology, 2017. **43**(6): p. 668-689.
237. da Silva, F.F.M., et al., *Eugenol derivatives: synthesis, characterization, and evaluation of antibacterial and antioxidant activities*. Chemistry Central Journal, 2018. **12**(1): p. 34.
238. Ultee, A., M.H.J. Bennik, and R. Moezelaar, *The Phenolic Hydroxyl Group of Carvacrol Is Essential for Action against the Food-Borne Pathogen Bacillus cereus*. Applied and Environmental Microbiology, 2002. **68**(4): p. 1561-1568.
239. Grumezescu, A.M., B.S. Vasile, and A.M. Holban, *Eugenol functionalized magnetite nanostructures used in anti-infectious therapy*. Letters in Applied NanoBioScience, 2013. **2**: p. 120-123.
240. Chen, F., et al., *Antioxidant and antibacterial activities of eugenol and carvacrol-grafted chitosan nanoparticles*. Biotechnology and Bioengineering, 2009. **104**(1): p. 30-39.
241. Jung, B.O., S.J. Chung, and S.B. Lee, *Preparation and characterization of eugenol-grafted chitosan hydrogels and their antioxidant activities*. Journal of Applied Polymer Science, 2006. **99**(6): p. 3500-3506.
242. Schlipf, D.M., et al., *Effects of Pore Size and Tethering on the Diffusivity of Lipids Confined in Mesoporous Silica*. Advanced Materials Interfaces, 2017. **4**(9): p. 1601103.
243. Khan, M.A., et al., *Adsorption and Recovery of Polyphenolic Flavonoids Using TiO₂-Functionalized Mesoporous Silica Nanoparticles*. ACS Applied Materials & Interfaces, 2017. **9**(37): p. 32114-32125.
244. Li, Z., et al., *Mesoporous silica nanoparticles in biomedical applications*. Chemical Society Reviews, 2012. **41**(7): p. 2590-2605.
245. Mangos, D.N., T. Nakanishi, and D.A. Lewis, *A simple method for the quantification of molecular decorations on silica particles*. Sci Technol Adv Mater, 2014. **15**(1): p. 015002.

246. Cao, Y., et al., *Evidence of single-nanoparticle translocation through a solid-state nanopore by plasmon resonance energy transfer*. Chemical Communications, 2016. **52**(30): p. 5230-3.
247. Slowing, I.I., et al., *Mesoporous Silica Nanoparticles for Drug Delivery and Biosensing Applications*. Advanced Functional Materials, 2007. **17**: p. 1225–1236.
248. Khan, M.A., et al., *Nanoharvesting of bioactive materials from living plant cultures using engineered silica nanoparticles*. Materials Science and Engineering: C, 2020. **106**: p. 110190.
249. Gu, J., et al., *Sub-150 nm mesoporous silica nanoparticles with tunable pore sizes and well-ordered mesostructure for protein encapsulation*. Journal of Colloid and Interface Science, 2013. **407**: p. 236-242.
250. Chen, F., et al., *In vivo tumor targeting and image-guided drug delivery with antibody-conjugated, radiolabeled mesoporous silica nanoparticles*. ACS Nano, 2013. **7**(10): p. 9027-39.
251. Ricci, F., et al., *Glutathione amperometric detection based on a thiol–disulfide exchange reaction*. Analytica Chimica Acta, 2006. **558**(1): p. 164-170.
252. Leubner, S., et al., *Experimental and theoretical investigations of the ligand structure of water-soluble CdTe nanocrystals*. Dalton Trans, 2013. **42**(35): p. 12733-40.
253. Wesp, E.F. and W.R. Brode, *The Absorption Spectra of Ferric Compounds. I. The Ferric Chloride—Phenol Reaction*. Journal of the American Chemical Society, 1934. **56**(5): p. 1037-1042.
254. Khattab, T.A., S.A. Aly, and T.M. Klapötke, *Naked-eye facile colorimetric detection of alkylphenols using Fe(III)-impregnated silica-based strips*. Chemical Papers, 2018. **72**(6): p. 1553-1559.
255. Lesniak, A., et al., *Nanoparticle Adhesion to the Cell Membrane and Its Effect on Nanoparticle Uptake Efficiency*. Journal of the American Chemical Society, 2013. **135**(4): p. 1438-1444.
256. Verma, A. and F. Stellacci, *Effect of surface properties on nanoparticle–cell interactions*. Small, 2010. **6**(1): p. 12-21.
257. Hoshyar, N., et al., *The effect of nanoparticle size on in vivo pharmacokinetics and cellular interaction*. Nanomedicine, 2016. **11**(6): p. 673-692.
258. Chithrani, B.D., A.A. Ghazani, and W.C.W. Chan, *Determining the size and shape dependence of gold nanoparticle uptake into mammalian cells*. Nano letters, 2006. **6**(4): p. 662-668.
259. Yoshimura, T., et al., *Bio-based polymer networks by thiol–ene photopolymerizations of allyl-etherified eugenol derivatives*. European Polymer Journal, 2015. **67**: p. 397-408.
260. Guzmán, D., et al., *New bio-based materials obtained by thiol-ene/thiol-epoxy dual curing click procedures from eugenol derivatives*. European Polymer Journal, 2017. **93**: p. 530-544.
261. Donovan, B.R., et al., *Thiol–ene adhesives from clove oil derivatives*. RSC Advances, 2014. **4**(106): p. 61927-61935.
262. Liu, H. and H. Chung, *Visible-Light Induced Thiol–Ene Reaction on Natural Lignin*. ACS Sustainable Chemistry and Engineering, 2017. **5**: p. 9160-9168.

263. Das Gupta, V. and K.A. Bomer, *Quantitative determination of phenol in phenolated calamine lotion USP*. J Pharm Sci, 1975. **64**(7): p. 1199-200.
264. Hernández-Sánchez, P., et al., *Complexation of Eugenol (EG), as Main Component of Clove Oil and as Pure Compound, with β - and HP- β -CDs*. Food and Nutrition Sciences, 2012. **3**: p. 8.
265. Shuyun Bi, L.Y., Yu Wang, Bong Pang, Tianjiao Wang, *Spectroscopic study on the interaction of eugenol with salmon sperm DNA in vitro*. Journal of Luminescence, 2012. **132**(9): p. 2355-2360.
266. Chen, K.L. and G.D. Bothun, *Nanoparticles meet cell membranes: probing nonspecific interactions using model membranes*. Environ. Sci. Technol., 2014. **48**(2): p. 873-880.
267. Yi, P. and K.L. Chen, *Interaction of multiwalled carbon nanotubes with supported lipid bilayers and vesicles as model biological membranes*. Environmental Science & Technology, 2013. **47**(11): p. 5711-5719.
268. Frost, R., et al., *Structural rearrangements of polymeric insulin-loaded nanoparticles interacting with surface-supported model lipid membranes*. Journal of Biomaterials and Nanobiotechnology, 2011. **2**(02): p. 180.
269. Hasan, I.Y. and A. Mechler, *Formation of planar unilamellar phospholipid membranes on oxidized gold substrate*. Biointerphases, 2016. **11**(3): p. 031017.
270. Reimhult, K., et al., *Characterization of QCM sensor surfaces coated with molecularly imprinted nanoparticles*. Biosensors and Bioelectronics, 2008. **23**(12): p. 1908-1914.
271. Johannsmann, D., I. Reviakine, and R.P. Richter, *Dissipation in films of adsorbed nanospheres studied by quartz crystal microbalance (QCM)*. Analytical chemistry, 2009. **81**(19): p. 8167.
272. Yu, Z., et al., *Supramolecular hydrogel microcapsules via cucurbit[8]uril host-guest interactions with triggered and UV-controlled molecular permeability*. Chem Sci, 2015. **6**(8): p. 4929-4933.
273. Beisl, S., A. Friedl, and A. Miltner, *Lignin from Micro- to Nanosize: Applications*. International Journal of Molecular Sciences, 2017. **18**(11): p. 2367.
274. Walsh, S.E., et al., *Activity and mechanisms of action of selected biocidal agents on Gram-positive and -negative bacteria*. Journal of applied microbiology, 2003. **94**(2): p. 240-247.
275. Renders, T., et al., *Lignin-first biomass fractionation: the advent of active stabilisation strategies*. Energy & Environmental Science, 2017. **10**(7): p. 1551-1557.
276. Tuck, C.O., et al., *Valorization of Biomass: Deriving More Value from Waste*. Science, 2012. **337**(6095): p. 695-699.
277. Nakamura, R., et al., *Enzymatic polymerization of coniferyl alcohol in the presence of cyclodextrins*. Biomacromolecules, 2006. **7**(6): p. 1929-1934.
278. Holladay, J.E., et al., *Top value-added chemicals from biomass-Volume II—Results of screening for potential candidates from biorefinery lignin*. 2007, Pacific Northwest National Lab.(PNNL), Richland, WA (United States).
279. Mita, N., et al., *Enzymatic oxidative polymerization of phenol in an aqueous solution in the presence of a catalytic amount of cyclodextrin*. Macromolecular Bioscience, 2002. **2**(3): p. 127-130.

280. Okano, L., et al., *Effect of cyclodextrin complexation on the photochemistry of the lignin model α -guaiacoxycetoveratrone*. Canadian journal of chemistry, 1999. **77**(8): p. 1356-1365.
281. Khan, M.A., et al., *Effect of Confinement in Nanopores on RNA Interactions with Functionalized Mesoporous Silica Nanoparticles*. The Journal of Physical Chemistry B, 2020. **124**(39): p. 8549-8561.
282. Prevette, L.E., et al., *Deciphering the Role of Hydrogen Bonding in Enhancing pDNA–Polycation Interactions*. Langmuir, 2007. **23**(19): p. 9773-9784.
283. Alatorre-Meda, M., et al., *DNA– Poly (diallyldimethylammonium chloride) Complexation and Transfection Efficiency*. Journal of Physical Chemistry B, 2010. **114**(29): p. 9356-9366.
284. MicroCal, *ITC data analysis in Origin: Tutorial Guide*. MicroCal LLC, Northampton, MA, 2004.
285. Bouchemal, K., *New challenges for pharmaceutical formulations and drug delivery systems characterization using isothermal titration calorimetry*. Drug discovery today, 2008. **13**(21-22): p. 960-972.
286. Velazquez-Campoy, A., *Geometric features of the Wiseman isotherm in isothermal titration calorimetry*. Journal of Thermal Analysis and Calorimetry, 2015. **122**(3): p. 1477-1483.
287. Hansen, L.D., G.W. Fellingham, and D.J. Russell, *Simultaneous determination of equilibrium constants and enthalpy changes by titration calorimetry: Methods, instruments, and uncertainties*. Analytical biochemistry, 2011. **409**(2): p. 220-229.
288. Turnbull, W.B. and A.H. Daranas, *On the value of c: can low affinity systems be studied by isothermal titration calorimetry?* Journal of the American Chemical Society, 2003. **125**(48): p. 14859-14866.
289. De, M., et al., *Biomimetic interactions of proteins with functionalized nanoparticles: a thermodynamic study*. Journal of the American Chemical Society, 2007. **129**(35): p. 10747-10753.
290. Liu, Y., et al., *Spectrophotometric study on the controlling factor of molecular selective binding of dyes by bridged bis (β -cyclodextrin) s with diselenobis (benzoyl) linkers*. The Journal of Physical Chemistry B, 2005. **109**(21): p. 10717-10726.
291. Zhang, H., et al., *Molecular recognition in different environments: β -cyclodextrin dimer formation in organic solvents*. The Journal of Physical Chemistry B, 2012. **116**(42): p. 12684-12693.
292. Zakzeski, J., et al., *The catalytic valorization of lignin for the production of renewable chemicals*. Chemical reviews, 2010. **110**(6): p. 3552-3599.
293. Poór, M., et al., *Interaction of ochratoxin A with quaternary ammonium beta-cyclodextrin*. 2015. **172**: p. 143-149.
294. Signoretto, M., et al., *TiO₂–MCM-41 for the photocatalytic abatement of NO_x in gas phase*. Applied Catalysis B: Environmental, 2010. **95**(1–2): p. 130-136.
295. Soto-Cantu, E., et al., *Synthesis and rapid characterization of amine-functionalized silica*. Langmuir, 2012. **28**(13): p. 5562-5569.

296. Cao, H., et al., *Fabrication of cyclodextrin-functionalized superparamagnetic Fe₃O₄/amino-silane core-shell nanoparticles via layer-by-layer method*. Applied Surface Science, 2009. **255**(18): p. 7974-7980.
297. Santos, E.C.d.S., et al., *AMF-responsive doxorubicin loaded β -cyclodextrin-decorated superparamagnetic nanoparticles*. New Journal of Chemistry, 2018. **42**(1): p. 671-680.
298. Zhang, L.-f., et al., *A facile immobilization approach for perfunctionalised cyclodextrin onto silica via the Staudinger reaction*. Tetrahedron letters, 1999. **40**(9): p. 1815-1818.
299. Ezzeddine, Z., et al., *Divalent heavy metals adsorption onto different types of EDTA-modified mesoporous materials: Effectiveness and complexation rate*. Microporous and Mesoporous Materials, 2015. **212**: p. 125-136.
300. Na, H.-K., et al., *Efficient Functional Delivery of siRNA using Mesoporous Silica Nanoparticles with Ultralarge Pores*. Small, 2012. **8**(11): p. 1752-1761.
301. Kondo, H., H. Nakatani, and K. Hiromi, *Interaction of cyclodextrins with fluorescent probes and its application to kinetic studies of amylase*. The Journal of Biochemistry, 1976. **79**(2): p. 393-405.
302. Nishijo, J., et al., *Interaction of 6-*p*-toluidinylnaphthalene-2-sulfonate with β -cyclodextrin*. Journal of pharmaceutical sciences, 1995. **84**(12): p. 1420-1426.
303. Topuz, F. and T. Uyar, *Cyclodextrin-functionalized mesostructured silica nanoparticles for removal of polycyclic aromatic hydrocarbons*. Journal of colloid and interface science, 2017. **497**: p. 233-241.
304. Rabadiya, B., V. Thakkar, and P. Rabadiya, *Drug-excipients interaction and solubility enhancement study of simvastatin*. Int. J. Pharm. Res. Bio-Sci, 2013. **2**: p. 168-185.
305. Dernaika, H., et al., *Spectroscopic identification of neurotoxin tetramethylenedisulfotetramine (TETS) captured by supramolecular receptor β -cyclodextrin immobilized on nanostructured gold surfaces*. Journal of Nanomaterials, 2014. **2014**.
306. Wang, C., et al., *Targeted delivery and pH-responsive release of stereoisomeric anti-cancer drugs using β -cyclodextrin assembled Fe₃O₄ nanoparticles*. Applied Surface Science, 2015. **357**: p. 2077-2086.
307. Banerjee, S.S. and D.-H. Chen, *Magnetic nanoparticles grafted with cyclodextrin for hydrophobic drug delivery*. Chemistry of Materials, 2007. **19**(25): p. 6345-6349.
308. Jayalath, S., S.C. Larsen, and V.H. Grassian, *Surface adsorption of Nordic aquatic fulvic acid on amine-functionalized and non-functionalized mesoporous silica nanoparticles*. Environmental Science: Nano, 2018. **5**(9): p. 2162-2171.
309. Zhu, X., J. Sun, and J. Wu, *Study on the inclusion interactions of β -cyclodextrin and its derivative with dyes by spectrofluorimetry and its analytical application*. Talanta, 2007. **72**(1): p. 237-242.
310. Arslan, M., S. Sayin, and M. Yilmaz, *Removal of carcinogenic azo dyes from water by new cyclodextrin-immobilized iron oxide magnetic nanoparticles*. Water, Air, & Soil Pollution, 2013. **224**(5): p. 1-9.
311. Samanta, A., N. Guchhait, and S.C. Bhattacharya, *Preferential molecular encapsulation of an ICT fluorescence probe in the supramolecular cage of*

- cucurbit [7] uril and β -cyclodextrin: an experimental and theoretical approach.* The Journal of Physical Chemistry B, 2014. **118**(46): p. 13279-13289.
312. Samanta, A., B.K. Paul, and N. Guchhait, *Studies of bio-mimetic medium of ionic and non-ionic micelles by a simple charge transfer fluorescence probe N, N-dimethylaminonaphthyl-(acrylo)-nitrile.* Spectrochimica Acta Part A: Molecular and Biomolecular Spectroscopy, 2011. **78**(5): p. 1525-1534.
 313. Frijlink, H., J. Visser, and B. Drenth, *Determination of cyclodextrins in biological fluids by HPLC with negative colorimetric detection using post-column complexation with phenolphthalein.* J. Chromatogr, 1987. **415**: p. 325-333.
 314. Fuhrer, R., et al., *Immobilized β -cyclodextrin on surface-modified carbon-coated cobalt nanomagnets: reversible organic contaminant adsorption and enrichment from water.* Langmuir, 2011. **27**(5): p. 1924-1929.
 315. Mazzaferro, S., et al., *Bivalent sequential binding of docetaxel to methyl- β -cyclodextrin.* International journal of pharmaceutics, 2011. **416**(1): p. 171-180.
 316. Couto, V.M., et al., *Capsaicin-Cyclodextrin Complex Enhances Mepivacaine Targeting and Improves Local Anesthesia in Inflamed Tissues.* International Journal of Molecular Sciences, 2020. **21**(16): p. 5741.
 317. Glasmästar, K., et al., *Protein adsorption on supported phospholipid bilayers.* 2002. **246**(1): p. 40-47.
 318. Huang, C.-J., et al., *Natural zwitterionic organosulfurs as surface ligands for antifouling and responsive properties.* 2014. **9**(2): p. 029010.

VITA

Mahsa Moradipour

EDUCATIONAL INSTITUTIONS AND DEGREES

1. University of Kentucky (UKY), Lexington, KY, USA December 2021
Ph.D., Chemical Engineering
2. Sharif University of Technology (SUT), Tehran, Iran May 2015
B.Sc., Chemical Engineering

PROFESSIONAL POSITIONS HELD

1. Research Assistant, University of Kentucky, United States. January 2017-August 2021
2. Teaching Assistant, University of Kentucky, United States January 2017-May 2017

SCHOLASTIC AND PROFESSIONAL HONORS

1. Awarded a National Science Foundation (NSF) Graduate Research Fellowship at Department of Chemical Engineering, UKY, 2017
2. Awarded the Conference Award from the Graduate Student Congress (GSC), UKY, 2020
3. Awarded the Outstanding Poster Presentation at Super Collider through the EPSCoR (Established Program to Stimulate Competitive Research) conference, 2018
4. Awarded The Laura Bassi Scholarship publication support and partial fee waivers for editorial assistance, 2019
5. Awarded Full scholarship to study at Sharif University of Technology for Undergraduate Program, Tehran, Iran, 2011
6. Ranked 374th in the Iranian National Universities Entrance Exam out of 400,000 participants, Tehran, Iran, 2011

PROFESSIONAL PUBLICATIONS

Journal Publications

Published

1. **Mahsa Moradipour**, Emily Chase, M. Arif Khan, Shadrack O. Asare, Bert C. Lynn, Stephen E. Rankin and Barbara L. Knutson, "Interaction of eugenol and lignin dimer-functionalized silica nanoparticles with lipid bilayers.", *Colloids and Surfaces B: Biointerfaces* (2020).

2. **Mahsa Moradipour**, Xinjie Tong, Brian Novak, Poorya Kamali, Shadrack O. Asare, Bert C. Lynn, Dorel Moldovan, Stephen E. Rankin, and Barbara L. Knutson, "Interaction of lignin dimers with model cell membranes: A quartz crystal microbalance and molecular dynamics simulation study.", *Biointerphases* (2021).
3. Xinjie Tong, **Mahsa Moradipour**, Brian R. Novak, Poorya Kamali, Shadrack O. Asare, Barbara L. Knutson, Stephen E. Rankin, Bert C. Lynn, and Dorel Moldovan. "Experimental and Molecular Dynamics Simulation Study of the Effects of Lignin Dimers on the Gel-to-Fluid Phase Transition in DPPC Bilayers." *The Journal of Physical Chemistry B* (2019).
4. C. Ethan Byrne, Carlos E. Astete, Manibarathi Vaithyanathan, Adam T. Melvin, **Mahsa Moradipour**, Stephen E. Rankin, Barbara L. Knutson, Cristina Sabliov, Elizabeth C. Martin, "Lignin-graft-PLGA Drug Delivery System Improves Efficacy of MEK1/2 Inhibitor in Triple Negative Breast Cancer Cell Line." *Nanomedicine* (2020).
5. M. Arif Khan, Maelyn R. Kiser, **Mahsa Moradipour**, Emily A. Nadeau, Ramy W. Ghanim, Bruce A. Webb, Stephen E. Rankin, and Barbara L. Knutson. "Effect of Confinement in Nanopores on RNA Interactions with Functionalized Mesoporous Silica Nanoparticles." *The Journal of Physical Chemistry B* (2020).

CONFERENCE PRESENTATIONS

Oral Presentations

1. **Mahsa Moradipour**^(†), Xinjie Tong, Poorya Kamali, Shadrack O. Asare, Bert C. Lynn, Dorel Moldovan, Stephen E. Rankin, Barbara L. Knutson, *Experimental and Computational Studies of Interfacial Interactions of Lignin Dimers with Lipid Bilayers*, 2018 AIChE Annual Meeting, Pittsburgh, PA, USA.
2. **Mahsa Moradipour**^(†), Emily Chase, M. Arif Khan, Shadrack O. Asare, Bert C. Lynn, Stephen E. Rankin, Barbara L. Knutson, *Interaction of Lignin Oligomer Functionalized Silica Nanoparticles with Model Cell Membranes*, 2019 ACS Colloids and Surface Science Symposium, Atlanta, GA, USA.
3. **Mahsa Moradipour**^(†), Emily Chase, M. Arif Khan, Shadrack O. Asare, Bert C. Lynn, Stephen E. Rankin, Barbara L. Knutson, *Interaction of Eugenol and Lignin Dimer Grafted Silica Nanoparticles with Lipid Bilayers*, 2019 AIChE Annual Meeting, Orlando, FL, USA.
4. **Mahsa Moradipour**^(†), Xinjie Tong, Poorya Kamali, Bert C. Lynn, Dorel Moldovan, Stephen E. Rankin, Barbara L. Knutson, *Thermodynamics of Lignin Dimers and β -Cyclodextrin Complexes*, 2020 AIChE Annual Meeting, Online.
5. M. Arif Khan^(†), Ramy Ghanim, Joshua Garay, Aniruddha Shirodkar, Yuxin He, **Mahsa Moradipour**, Barbara L. Knutson and Stephen E. Rankin, *Mesostructure thermal transformation kinetics and mechanism for the synthesis of SiO₂-TiO₂ mixed thin films with sub-3 nanometer vertical pore channels*, 2018 AIChE Annual Meeting, Pittsburgh, PA, USA.
6. Ethan Byrne^(†), Carlos E. Astete, Manibarathi Vaithyanathan, Adam T. Melvin, **Mahsa Moradipour**, Stephen E. Rankin, Barbara L. Knutson, Elizabeth C. Martin, Cristina Sabliov, *Novel lignin-conjugated PLGA drug delivery system improves efficacy of MEK1/2 inhibitor in triple negative breast cancer*, 2019 AACR-NCI-EORTC International Conference on Molecular Targets and Cancer Therapeutics, Boston, MA, USA.
7. Xinjie Tong^(†), **Mahsa Moradipour**, Brian Novak, Bert C. Lynn, Stephen E. Rankin, Barbara L. Knutson, and Dorel Moldovan, *Interaction of lignin dimers and derivatives with cyclodextrin*, 2019 SERMA, Savannah, GA, USA.

Poster Presentations

1. **Mahsa Moradipour^(†)**, Audrey Fetsko, M. Arif Khan, Barbara L. Knutson, and Stephen E. Rankin, *Interfacial Interactions of Lignin Dimers with Lipid Bilayers*, 2017 NSF EPSCoR Annual Conference, Frankfort, KY, USA.
2. **Mahsa Moradipour^(†)**, Emily Chase, M. Arif Khan, Barbara L. Knutson, and Stephen E. Rankin, *Interaction of Eugenol and Novel Lignin Grafted Silica Nanoparticles with Synthetic Lipid Bilayers*, 2018 NSF EPSCoR Annual Conference, Baton Rouge, LA, USA.
3. **Mahsa Moradipour^(†)**, Emily Chase, M. Arif Khan, Barbara L. Knutson, and Stephen E. Rankin, *Interaction of Lignin Oligomer Functionalized Silica Nanoparticles with Model Cell Membranes*, 2018 NAMS Annual Conference, Lexington, KY, USA.
4. **Mahsa Moradipour^(†)**, Audrey Fetsko, M. Arif Khan, Barbara L. Knutson, and Stephen E. Rankin, *Interfacial Interactions of Lignin Dimers with Lipid Bilayers*, 2017 Materials and Chemical Engineering (MACE) Symposium, Lexington, KY, USA.
5. **Mahsa Moradipour^(†)**, Audrey Fetsko, M. Arif Khan, Barbara L. Knutson, and Stephen E. Rankin, *Interfacial Interactions of Lignin Dimers with Lipid Bilayers*, 2018 NSF EPSCoR Super Collider, Lexington, KY, USA.
6. **Mahsa Moradipour^(†)**, Emily Chase, M. Arif Khan, Barbara L. Knutson, and Stephen E. Rankin, *Investigating the interaction of Eugenol and Lignin dimer Functionalized Silica Nanoparticles in Presence of Model Cell Membranes*, 2019 NSF EPSCoR Annual Conference, Frankfort, KY, USA.
7. **Mahsa Moradipour^(†)**, Emily Chase, M. Arif Khan, Barbara L. Knutson, and Stephen E. Rankin, *Investigating the Behavior of Lignin Oligomer Functionalized Silica Nanoparticles in Presence of Model Cell Membranes*, 2019 The National Association of Graduate-Professional Students, Lexington, KY, USA.
8. **Mahsa Moradipour^(†)**, M. Arif Khan, Poorya Kamali, Bert C. Lynn, Barbara L. Knutson, and Stephen E. Rankin, *Thermodynamic Interactions of Lignin Dimers with β -Cyclodextrin*, 2020 NSF EPSCoR Annual Online Conference, Lexington, KY, USA.
9. Audrey Fetsko^(†), **Mahsa Moradipour**, Stephen E. Rankin, and Barbara L. Knutson, *Interfacial Interactions of Lignin Dimers with Lipid Bilayers*, 2017 AIChE Annual Meeting, Minneapolis, MN, USA.
10. Emily Chase^(†), **Mahsa Moradipour**, Stephen E. Rankin, and Barbara L. Knutson *Interactions of Lignin Dimer-Grafted Particles with Supported Lipid Bilayers*, 2018 AIChE Annual Meeting, Pittsburgh, PA, USA.
11. Rami Ghanim^(†), M. Arif Khan, **Mahsa Moradipour**, Stephen E. Rankin, and Barbara L. Knutson *Novel Strategy for Functional Oligopeptide Conjugation inside the Mesopores of Silica Nanoparticles*, 2019 AIChE Annual Meeting, Orlando, FL, USA.

^(†)Presenting Author

Mahsa Moradipour

September 13, 2021